Diesel Fuel droplet impingement on heated surfaces

MEng. Hesamaldin Jadidbonab

School of Engineering and Mathematical Science

This thesis is submitted for the fulfilment of the requirements for the degree of Doctor of Philosophy

April 2018

“The knowledge of anything, since all things have causes, is not acquired or complete unless it is known by its causes”

(Avicenna)

Contents

List of Tables

List of Figures

Acknowledgment

Firstly, I would like to thank Professor M. Gavaises as my supervisor, for his continuous professional and human support during the time towards completion of my PhD. Furthermore, I am very grateful that he not only found the funding and provided the freedom, but also supported many opportunities for me to pursue my research work, despite enormous number of difficulties during my PhD period. His continuous pressing for more “accurate” measurements made me explore and learn new, very useful, experimental techniques.

I would like also to thank Dr. N. Mitroglou who is my second supervisor and supported me along the way in all possible ways, but especially with his tremendous knowledge on experimental techniques in general. I was so lucky to have him in daily basis during my first year of study and received a lot of courage and knowledge.

In addition, I would like to thank Dr. I. Karathanassis and Ilias Malgarinos for their valuable ideas and suggestions during the write up of the scientific papers and the final thesis.

Moreover, I thank Dr. J. M Nouri and Dr. Y.Yan for their useful theoretical and practical support in various stages of this work.

In addition, I thank Mr. Nikolaos Chatziarsenis for his continuous administrative support; thank you for all of those refreshing coffee breaks during all these years.

A special thank you goes to Mr. J. Ford for his technical support. Any parts of this work would have been impossible without the help of this wizards of electronic.

A very big and warm thank you goes to my friends and colleagues in the City University research group and London, in general; Dr Fivos, Dr Talal, Milad, Mahmoud, Homa, both Kostis, Nikos, Aakis, Alvaro, Carlos, Gorgia, Mitun, Statis and Max.

I also wanted to thank my close friends Hesam, Siavash and Kiarash who supported and helped me in various ways during these all years living in UK!

Last, but not least, I would like to thank my parents and my two brothers who managed to deal with my crazy behaviour for all these years and still keep on loving me.

Declaration

I hereby declare that the presented work in this thesis is my own or was developed in a joint effort with other members of the research group as it is stated and referenced in the text accordingly!

I grant powers of discretion to the University Librarian to allow this thesis to be copied in whole or in part without further reference to me. This permission covers only single copies made for study purposes, subject to normal conditions of acknowledgement.

London_____

_____

(Hesamaldin Jadidbonab)

Abstract

The present study is the result of 4 years experimental research study aimed at understanding the hydrodynamic and heat transfer phenomena of a Diesel fuel droplet during the impact process with a heated flat and spherical surface. Such a phenomena are of a direct relevance to many engineering problems such as IC engines and fluid catalytic cracking (FCC). Due to the fact that the spray systems in the aforementioned applications may be comprised of millions of interacting droplets that prohibit detailed identification of the flow conditions during the impact of individual droplets, the current study focus on the characterisation of the impact dynamics of single droplets under well-controlled conditions. Several parameters, such as droplet velocity and diameter, liquid physical properties, surface conditions and geometry, wall surface temperature and ambient pressure are of key importance for the deformation of droplets upon impact and thus, define the impact outcome.

An experimental investigation of micrometric Diesel droplets impacting on a heated aluminium and a millimetric brass particle surface was carried out. Dual view high-speed imaging has been employed to visualise the evolution of the impact process at various conditions. The parameters investigated include wall surface temperature ranging from room temperature to above Leidenfrost temperature (~420°C), impact Weber, and Reynolds numbers and ambient pressure of 1 and 2 bar. The observed post-impact outcome regimes are defined by means of hydrodynamic regimes and droplet morphology (stick, splash, break-up and rebound); then for each surface geometry, the identified impact outcomes were illustrated on regimes maps as a function of surface temperature and impact Weber number. Comparisons with the available experimental data for the single component fluids clearly shows significant differences, especially in terms of transition to Leidenfrost and breakup regimes; differences in liquid composition and non-homogeneity of the Diesel fuel droplet at the temperature above any of

its component's boiling temperature, results in different flow process and evaporating behaviour during the impact, and consequently the final outcome.

Moreover, the temporal variation of the apparent dynamic contact angle and spreading factor has been determined as a function of the impact Weber number and surface temperature. The experimental results were compared against available numerical simulations, performed using a two-phase flow model with interface capturing, phase-change and variable physical properties in order to fully understand the physical mechanism behind the observed results; Increased surface temperature resulted to different spreading dynamic, in particular induced quicker and stronger recoiling behaviour, mostly attributed to the change of liquid viscosity. It has been also shown that the extension of the lamella spreading diameter on a spherical surface is larger than on a flat surface, which is due to the presence of the gravitational and centrifugal forces; yet the centrifugal force is the dominant effect.

In addition, a series of experimental results focusing on: (i) the effect of physical properties and additives on isothermal impact of fuel droplets onto the flat and inclined substrates and (ii) oblique droplet-particle impact, are reported. These parts of the work are included in the appendices as such results were known already from the literature (Appendix A and B), or a pilot study and thus not conclusive (Appendix C) to be presented in the main body of the thesis.

Nomenclature

Latin characters

Symbol	Description	Unit
C_d	Drag Coefficient	-
c_p	Specific heat capacity	J/kgK
$Ca = \mu_l u / \sigma$	Capillary Number	-
c	Speed of sound	m/s
D	Droplet Diameter	m
D_{max}	Maximum spreading diameter	m
DTP	Droplet-to-particle size ratio	-
E_K	Kinetic Energy	J/kg
E_σ	Capillary Energy	J/kg
E_μ	Viscous Energy	J/kg
h_f	Liquid Film Thickness	m
$h^*=h_f/D_0$	Dimensionless film thickness	-
k_{cond}	Effective conductivity	W/mK
p	Pressure	Pa
$Oh = We^{1/2}/Re$	Ohnesorge number	-
r	Rim axisymmetric distance	m
R_0	Droplet Radius	m
$Re = \rho u D/\mu$	Reynolds number	-
R_a	Surface roughness	m
R^2	Coefficient of determination	
S	Spreading coefficient	-
t	Time	s
T	Temperature	^{o} C
u	Velocity (its components)	m/s
u_c	uncertainty	-
V	Volume	m^3
$We = \rho_l u D/\sigma$	Weber number	-
$t^* = tu/D$	Non-dimensional time	-

Greek characters

Symbol	Description	Unit
θ_D	Dynamic contact angle	^{o}

θ_s	Static contact angle	^{o}
μ	Dynamic viscosity	kg/ms
ρ	Density	kg/m^3
σ	Surface tension coefficient	N/m
α	Spreading angle	^{o}
β	Spreading factor	-
β_{max}	Maximum spreading factor	-

Superscripts and subscripts

Symbol	Description
d	Droplet
BP	Boiling point
CHF	Critical heat flux
dyn	Dynamic
eq	Equilibrium
g	Gas
int	interface
l	Liquid
L	Leidenfrost
lv	Liquid-vapour
max	Maximum
o	Initial
P	Particle
sl	Solid-liquid
sv	Solid-vapour
sat	Saturated
W	Wall surface

Abbreviations

Symbol	Description
CFD	Computational Fluid Dynamics
CoG	Centre of geometry
DTP	Droplet to particle ratio
ICE	Internal combustion engine
IR	infrared
VOF	Volume of Fluid

1. Introduction

1.1. Background and motivation

Understanding liquid spray impact onto solid surfaces is important in a number of industrial applications such as IC engines, fire suppression, thermal power plants, microprocessor cooling, and ink printing among others.

In particular, the development of compact high-speed direct-injection diesel engine has stimulated the interest on the phenomena associated with the impact of sprays on solid walls. Due to the short distance between the injection nozzle and the piston head, and the high injection pressures, the fuel spray may impinge on walls before it is fully vaporized and mixed with air. Spray-wall interaction has become an important phenomenon; as on one hand, it accelerates the second atomization which enhances the mixture of fuel and air and subsequently the combustion efficiency, on the other hand, a thin oil film is formed on the surface of cylinder and piston head which may prevent the evaporation of spray and cause lube dilution. Soot and unburned HC was also observed after spray-wall impingement. The deposit formation in the imposed wall-surface of the engine's cylinder and piston, is significantly depend on a combination effects of droplets pre-impact velocity and diameter of the droplets within the spray, fuel composition, surface material and temperature, and cylinder pressure and temperature. It has been shown already that the wall-surface temperature is the paramount parameter to control the fuel deposition prior to the combustion [1].

In addition, the impact of the fuel spray on the heated chamber walls, which have a temperature above the boiling or even the Leidenfrost point [2], may control to a large extent the impact outcome. When the engine warms up, fuel vaporisation is enhanced and thereby, the mechanisms of liquid disintegration are altered [3]; the latter is empirically defined by the size and number of post-impact droplets formed that remain on the wall surface or rebound from it.

The splashed droplets can be easily vaporised and enhance the fuel-air mixture. However, the wall film, which is simultaneously formed from the deposited droplets, has a significant influence on engine-out emissions and fuel economy [4]. Due to the fact that the aforementioned spray systems may be comprised of millions of interacting droplets that prohibit detailed identification of the flow conditions during the impact of individual droplets, many studies focus on the characterisation of the impact dynamics of single droplets under well-controlled conditions. However, the impact of a single droplet onto a solid wall is still not fully understood, especially in presence of heat transfer and evaporation during the impingement process. The lack of knowledge about the most influential parameters dominating the hydrodynamic and heat transfer on the small scales also complicate the design of the technical process. In general, the design process with regards to the relevant application, is based on purely empirical principles, using advanced optical diagnosis techniques. However, this design methods could also be accelerated by understanding the underlying physics of the phenomena.

This thesis aims to investigate how the post-impact regime and spreading dynamic of a multi-component hydrocarbon fuel droplet onto the flat and non-flat surfaces depends on aforementioned parameters. Therefore, at first, a proper literature review will aid the formulation of the thesis objectives, as well as the gaps in the knowledge and advancements that requires to be done.

1.2. Literature review of the relevant studies

The fluid dynamic interaction between a single droplet and a solid surface, when the droplet impinges onto the surface is subject to many parameters associated with the interface. For example, the physical and molecular properties of the solid surface and the droplet, the impact condition and the temperature. As a droplet impacts onto a surface, it behaves differently,

depending on the boundary conditions at impact including liquid and surface properties. One of the solid surface properties affecting the reaction between the liquid and surface is the surface temperature. In the literature, the droplet impact phenomenon is broadly divided into cold and heated surface impacts. The heated surface interaction mechanism is principally more complex than the cold surface impact regimes due to vapour pressure force at solid-liquid interface and in general, the hydrodynamic and thermodynamic effects. Heated surface impacts can also occur at isothermal (surface without temperature drop) and non-isothermal conditions. The works of [3], [5], [6] provide summaries of the numerical and experimental studies on droplet impact onto solid surfaces for isothermal and non-isothermal conditions.

In this chapter, the existing literature on the interaction between a droplet and solid surface is discussed in details; however, the focus remains on the experimental observations rather than numerical modelling of the phenomena.

1.2.1. Isothermal droplet impact

Drop impacting has many different outcomes depending on the properties of drops (impact speed, geometry of the drop, surface tension, viscosity, etc.), the impacted surface (dry and wet solid surface, liquid pool, roughness of the impacted solid surface, and wettability), and the surroundings (ambient pressure and temperature).

The shape of the drop varies during the impact process. In most experiments or simulations, the drop is considered as to be spherical. However, it also might be elliptic due to oscillation [7], [8], or a random deformed shape [9], or with a shield of surfactants [10]–[12]. Different drop shapes result in various impact behaviours. According to the direction in which the drop impacts, scenarios of drop impact could be either normal or oblique. Numerous experimental and numerical studies were carried out to understand the normal impact [13]–[18], whereas studies of oblique impact of single drops are scarce [19]–[23]. Even though the oblique drop

impact is not a rare event in technical applications, the consequences of oblique impacts are still insufficiently studied and understood. It is generally considered that the impingement angle (the angle between the velocity vector of the drop and the normal vector to the surface) plays an important role in results of the oblique impact. Nonetheless, a general model implying the effect of impact angle on the outcome of oblique drop impact is still unclear.

It have shown that the normal velocity component and the droplet size govern the deposition ratio (ratio between deposited liquid to total liquid impacting on the wall) [24]. The oblique drop impact is of considerable interest in agricultural spraying, where low impact angles on leaves can lead to diminished deposition on the surface. Fuel injection sprays impacting obliquely on combustion walls or droplet impacting onto airplane wings, considered for icing studies exhibit considerably higher Weber number [25].

The study of [26] performed an experimental study on water drops oblique impacts in order to analyse the droplet outcome in case of hydrophobic and superhydrophobic substrates, varying the substrate tilt angle. They observed six different outcomes; (a) Deposition, when the whole drop remains stuck close to the impact point. This regime corresponds to the so-called ‘‘spread’’ in [27]. (b) Rivulet, when the drop slides downhill while spreading, recoil does not occur. (c) Sliding, when the entire drop (thus, including both uphill and downhill contact point edge) moves downhill and, at the end of the recoil phase, the entire liquid mass (i.e., the main part plus possible tiny secondary droplets) remains attached to the surface. (d) Rolling, when the drop rolls downhill, typically preserving high contact angles and thus a reduced contact area. (e) Partial rebound, when a part of the drop pinches off from the surface, while the other remains stuck (and eventually flows downhill afterward). (f) Rebound (or complete rebound), when the entire drop detaches from the surface.

1.2.1.1. Mechanism of interaction

In the case of droplet impact on a solid-surface, since the influences of the surface roughness and the surface wettability are involved, drop impacts are more complicated compared with the ones on the liquid surface.

Several parameters are of key significance in the outcome regime of drops upon impact. For a better understanding of these factors, it is necessary to isolate each parameter and study its effect individually. Among these parameters are the droplet velocity, diameter and angle of impact [28], liquid physical properties [29], [30], surface condition [25], [31], wall surface temperature (Tw) [32]–[34], and ambient pressure [35]–[37] which are defining the impact outcome. In the literature, in case of isothermal conditions, the post-impact outcome regimes are generally illustrated on regime maps as a function of influential parameters, in particular impact Weber, Reynolds, Capillary and Ohnesorge numbers. Such a maps can be found in the work of [21], [38]–[40].

When a drop impinges on a solid surface, phenomena like splashing and fingering could occur under certain conditions. Such conditions make the drop's behaviour difficult to predict. Some research investigated the formation and instabilities of fingering [41]–[43]. Some research [12], [44] has developed correlations in terms of the Reynolds and Weber numbers for the splashing threshold. Surface conditions such as surface roughness are also found to affect the splashing threshold. The work of [45] reported that the splash limit is typically determined by Weber number and reported the effect of surface roughness on this limit, with a rougher surface having a lower Weber number splash limit. For a non-splashing case, the overall impingement process includes initial impact, advancing and receding. In most of the studies, the main parameters that have been used to describe and predict the impingement dynamics include maximum spreading diameter, crown evolution, and dynamic contact angle. The work of [46] studied the impingement of single droplets onto a flat surface experimentally, and compared the results

with a simple theoretical model. The results showed that the non-dimensional parameters which only regard the physical conditions of the droplets, such as Reynolds number and Weber number, cannot fully explain the dynamics of droplet impingement. In addition, the effects of the surface conditions also need to be included. Furthermore, a discussion of the impingement process based on non-dimensional parameters, mentioned above, has been used to describe the process [45]. When the droplet diameter is scaled by the impact diameter and the time scaled by the impact diameter divided by the impact velocity, a typical time to reach maximum spreading is on the order of 1-10 times the time scale depending on the droplet impact Weber number. The larger the Weber numbers the shorter the time to reach maximum spread. Droplets will rebound after initial spreading and once reaching an equilibrium diameter will oscillate with a transient contact angle, as shown by [47]. This complex process results in transient film thickness near the contact line that is expected to alter the local transient heat transfer rate. The work of [41] studied the impact of single water droplets impinging on a liquid film. Crown diameter (inner and outer), elevation, size and grow rate were studied quantitatively and the results were compared with existing empirical models.

The detailed reviews of the post-impact regimes are provided in the studies of [48]–[54] for various single component liquids. However, a classical characterization of the impact regimes of the phenomena considers an appropriate time scale to identify the outcome regime as in [29] and shown in Figure 1.1. The study of [55] characterized the phenomena by the impact kinetic energy of the droplet. On a dry and non-heated surface, depending on impact kinetic energy and other parameters as mentioned earlier, impingement of droplet may result into four major outcomes: a) sticking or deposition b) spreading and recoiling c) disintegration/splash and d) rebound.

Further studies of the droplet impact regimes have resulted in a number of intermediate phases. For example, the work of [29], added an intermediate state called fingering, which is a

metastable phase between spreading and disintegration and has been included as one of the subcategories of disintegration/splash. They have also subcategorized the 'splash' into four disintegration mechanisms: (c-i) prompt splash, (c-ii) corona splash, (c-iii) receding breakup, and c-iv) partial rebound.

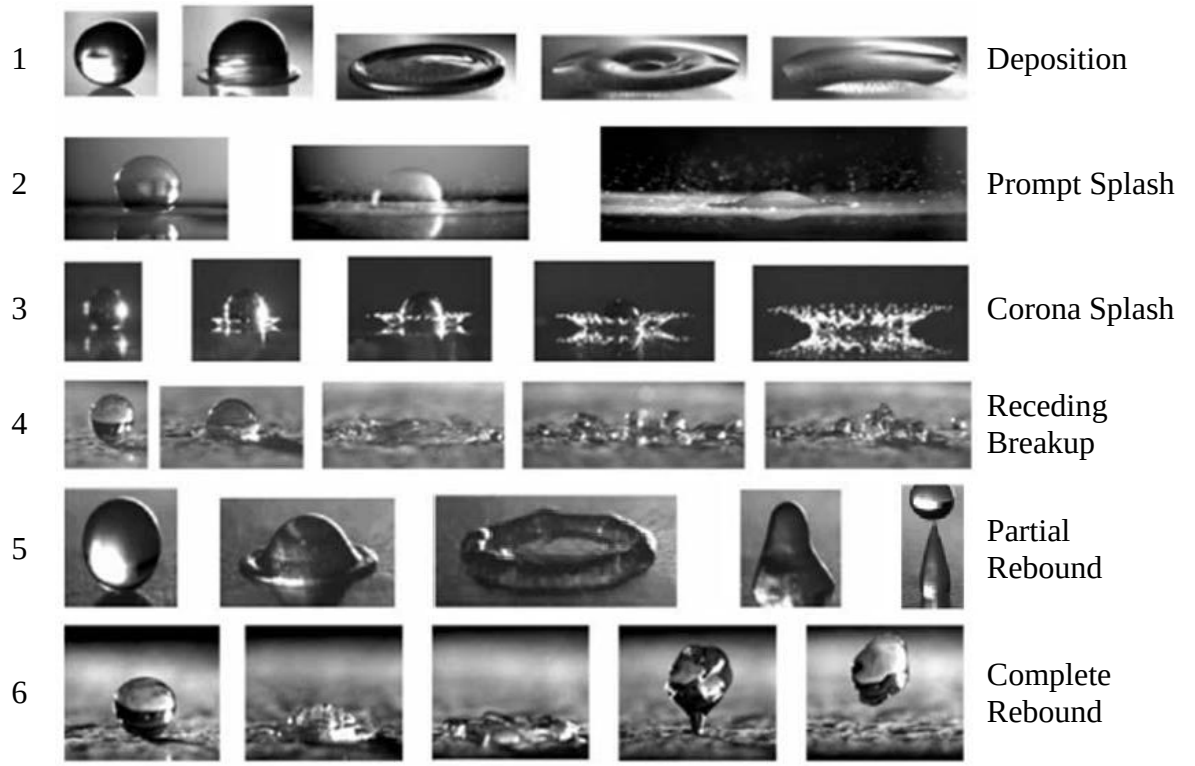

Figure 1.1: A variety of morphologies of liquid drop impact on to a non-heated, dry surface [29].

More recently, the experimental work of [56], added a phase called 'finger breakup' as shown in These fingers break-up are usually observed when the droplets impacting onto smooth surfaces, $R_a/R_0 < 3.4x10^4$, where R_a/R_0 is the dimensionless surface roughness. The occurrence of fingers breakup is either due to capillary effects at later stages of spread, or during recoil if the surface energy is not enough to keep cohesion of the receding fingers when transposing surface roughness grooves.

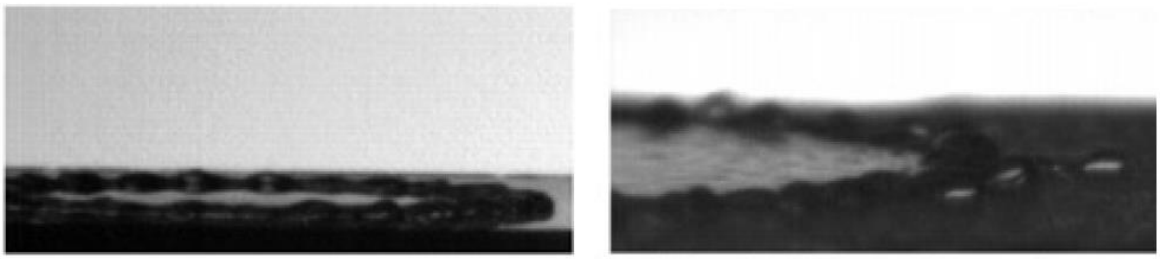

Figure 1.2: Fingering and finger break up of a single droplets impacting onto non-heated dry surface [56].

To study the droplet-solid surface interactions it is convenient to use of suitable dimensionless numbers such as Reynolds number (Re), Weber number (We), Ohnsesorge number (Oh) and Capillary number (Ca) to represent the underlying competing forces such as inertia, surface tension force, viscous force and gravity force, and their relative dominance over the dynamics. These parameters are frequently used to macroscopically characterise the impact process. Description of these dimensionless numbers as a ratio of relevant forces and associated expressions are given below:

$$Re = \frac{d_{d,0} v_{d,0}}{\mu_d} = \frac{inertial\ force}{viscous\ force} \qquad 1.1$$

$$We = \frac{\rho v_0^2 d_0}{\sigma} = \frac{inertial\ force}{surfacetension\ force} \qquad 1.2$$

$$Oh = \frac{\sqrt{We}}{Re} = \frac{viscous\ force}{\sqrt{surfacetension\ force\ \times inerial\ force}} \qquad 1.3$$

$$Ca = \frac{\mu v_0}{\sigma} = \frac{viscous\ force}{surfacetension\ force} \qquad 1.4$$

(where ρ is the liquid droplet density, σ the liquid vapour surface tension, μ the viscosity, D_0 the initial droplet diameter and V_0 the impact velocity).

1.2.1.1.1. Sticking / Deposition

Sticking or deposition of droplet on the surface occurs when the energy at impact is very low, the droplet sticks to the wall but, as impact energy increases, a lamella forms which spreads and recoils until all the energy is dissipated. The shape of a deposited droplet in this state, neglecting the impact inertia, is governed by a balance between gravity (hydrostatic pressure) and surface tension force [57].

In the "stick" regime, the entire mass of the droplet is deposited on the wall surface upon impact and the droplet spreads on the surface. The initial kinetic energy of the droplet is completely lost in viscous dissipation during this spreading. This regime occurs for Weber numbers below the splash threshold and when the heat transfer is not enough to induce breakup or rebound.

1.2.1.1.2. Spreading and recoiling

When the impact energy is higher than when the droplet sticks to the surface of the solid, a lamella forms which spreads and recoils until all the impact energy is dissipated. In other words, at impact energy lower than limit of disintegration, upon impact, droplet momentum directed normal to solid surface gives rise to a purely radial flow driven by inertia in body of the impinging droplet. This radial flow causes the droplet to spread over the surface to an extent in which the mass of the droplet gathers in a toroidal rim shape.

In this case the surface tension force is strong enough that does not allow the droplet to splash. It should be noted that the centreline height of the droplet is lower than the surrounding rim.

1.2.1.1.3. Disintegration / Splash

"Splash" or "disintegration" occurs when Weber number is high enough so the droplet inertial force becomes significantly larger than the viscous forces and the surface tension forces and finally droplet becomes unstable, deforms and smaller droplets disintegrated from the moving edge of the spreading lamella.

The splashing phenomenon is largely controlled by the effects of surface tension and viscosity. While a high surface tension limits the splashing, as fluid lamella extend increasing the surface area and hence surface energy, the high viscosity acts to delay the progressing front of the outward flowing fluid lamella more than the trailing portions. This interaction between the surface tension and the viscosity forces creates a kinematic discontinuity which stimulates the instability within the outwardly progressing liquid lamella and consequently results in splashing [58]. A brief description of different disintegration mechanisms are provided below:

- Prompt splash

This type of splash is preliminary caused by the impact of a large diameter droplet at high impact velocity over a relatively rough surface. The phenomenon is mainly observed immediately after a droplet impacts on a surface where a very thin liquid lamella emerges from below the droplet and expands radially away when the edge of the lamella is still in contact with the solid surface.

- Corona splash

This behaviour is typically observed when the droplet impacts a smooth solid surface and often attributed to the higher system pressure hence higher density of the ambient gas which exerts restraining pressure on the expanding lamella. The corona splash can be controlled by decreasing the pressure of the surrounding gas [36], which points at an important role of gas in

triggering perturbations of the spreading lamella in addition to those due to the direct effect of wall roughness.

- Receding breakup

The behaviour of the droplet in this mechanism is mainly governed by the droplet, solid surface contact angle. During receding breakup the droplet remains intact in contact with the solid surface until it has reached to its outermost extent projecting fingers at the rim. While the droplet is spreading the surface tension forces act on the lamella to pull its edges back to minimise surface energy however surface roughness hinders motion of the small portions of the lamella while the main mass of the droplet continues to recede. If the liquid-solid contact angle $\theta_s < 90°$, neighbouring fingers along the edges of the spreading liquid sheet tend to merge with each other and disappear. However, if $\theta_s > 90°$, as is the case with droplet impact on super-hydrophobic surfaces, the fingers do not disappear and grow longer as the liquid recedes [57].

- Fingering

In contrast to receding breakup wherein the peripheral fingers disintegrate during receding/recoiling state, at moderate impact velocities, the rim of the lamella may destabilize at the beginning of the spreading phase and form regular structures called fingers, which grow ahead of the contact line and further breakup during the last stages of spreading [59]. These structures are studied by several authors, however, a detailed review of the fundamentals of the fingering mechanisms is reported in [5].

1.2.1.1.4. Rebound

For a surface characterised by a non-wetting, low surface energy with contact angle higher than 90°, at relatively low impact velocity, rebound might occur in isothermal condition; the kinetic energy might not be fully dissipated by the viscous effects at the end of the spreading/recoil phase and lift the liquid upward from the surface. This rising liquid might be levitate on top of

the surface, fully detached from the surface, namely, fully rebound (Figure 1.1 6th row), or it might be partially detached from the surface and eject one or more secondary droplets, called partial rebound (Figure 1.1 5th row). Partial rebound is enhanced by decreasing the viscosity or increasing the contact angle between the liquid and the solid surface [60]. If prior to rebound, the capillary wave which propagated along the liquid surface cause the droplet to pinch off so a part of droplet stays on the surface and the other part rebound (partial-rebound regime). If the impact energy is high enough that generates strong perturbation in the liquid droplet, it will break into several smaller droplets. Then it either stays in contact with the surface (breakup-stick) or rebound from it (breakup-rebound). Extend of rebound increases with increase in surface tension of the liquid material and surface static contact angle [57].

1.2.1.2. Effect of liquid physical properties

Impact of a drop on a solid surface can be visualized as interplay of three parameters, namely as: (i) inertia of the drop or its kinetic energy, (ii) surface tension and (iii) viscous dissipation. Surface tension and viscosity of the liquid tend to oppose spreading. Prior to impact, if the drop is nearly spherical, the pressure inside is higher than the surroundings and the difference is given by the Young-Laplace equation:

$$\Delta P = \frac{2\sigma}{R_0} \qquad 1.5$$

As the drop hits the surface, the initial point of contact becomes a stagnation point, due to which high pressure develops there. A displacement wave then travels opposite to the velocity direction, into the drop. This high pressure and change of momentum causes the bottom part of the drop to spread out rapidly as a thin layer called the lamella. This initial phase where the lamella is barely visible, is called the ‘kinematic phase’ and is governed by inertia and the geometry of the drop rather than surface tension and viscosity [62]. The remaining drop remains unchanged and keeps moving at nearly the impact speed. Due to its thinness, the radial

speed of the lamella can be several times higher than the impact speed. As the lamella grows in the ‘spreading phase’, surface tension and viscosity rapidly decelerate its growth, causing it to thicken near the contact line to form a rim [62]. With drop spreading, the rim grows in thickness as it is fed liquid from the thin lamella. Near maximum spread, spreading is said to be in a ‘relaxation phase’ and the contact line speeds approach zero. Once the maximum diameter is attained, waves are reflected inwards from the rim and liquid from the rim travels back towards the centre, ultimately resulting in the final static shape. This last phase is called the wetting or equilibrium phase [62]. If the surface tension of the liquid is strong enough, the contact line might recede to a smaller final diameter. For fully wetting liquids, a thin precursor film [58], usually only several hundred angstroms in thickness, moves ahead of the macroscopic contact line due to intermolecular forces, and the spread diameter keeps increasing with time. Thus, the initial kinetic energy of the drop gets converted into surface energy and viscous dissipation [62].

Quantification of the droplet’s spreading rate and wetting behaviour are often studied. Understanding of the spreading behaviour is essential towards the determination of the wetting dynamics and thus the impact outcome. According to [63], [64] the dynamic contact angle and spreading factor have been employed extensively to study droplet dynamic wetting behaviour onto solid. The value of contact angle changes during drop spreading and can be measured from the images of the droplet’s profile at the moving contact line. The flow in the contact line and the macroscopic hydrodynamics determine the value of dynamic contact angle, contribute to the drag force and influence the spreading rate [65]. It should be noted that this contact angle is different from the so-called static (equilibrium) contact angle [15] which is generally a function of surface property. Several experimental studies have been carried out recently to measure the temporal variation of contact angle and the spreading factor under isothermal condition (selectively [30], [25], [31], [65], [66] among many other). Additionally, a higher

viscosity liquid (ethanol) was found to splash more readily compared to a lower viscosity liquid (methanol) [36], [67]. However, observations of [68] about the non-occurrence of splashing even for a splash ratio of 3.5 ($\frac{\Sigma_G}{\Sigma_L} = \frac{P_T}{\sigma}\sqrt{\gamma M_G}\sqrt{\frac{R_0 V_0}{2TK_B}}\sqrt{\nu_L}$, where σ and ν_L are the surface tension and kinematic viscosity of the liquid, respectively, R_0 and V_0 are the initial radius and velocity of the droplet, M_G is the actual mass of one molecule of the gas, γ is the ratio of its specific heats, k_B is the Boltzman's constant, T is the temperature and PT is the splash threshold pressure [36]) were due to a regime change, and not a behaviour caused due to high pressures.

All the latter observation proves that the physical properties of the liquid have a paramount role not only on determining the droplet spreading dynamic, also the post impact outcome of the droplet.

1.2.1.3. Effect of droplet pre-impact condition

As mentioned earlier the post-impact regime is sensitive to the impact velocity and droplet diameter and surface roughness. If the droplet impacts into the surface with a finite velocity, the liquid spreads out after formation of the contact between the liquid and the solid surface. The initial kinetic energy, namely inertia, of the droplet plays a paramount role during the flow process of the spreading/recoiling, and thus the final outcome. Upon the impact, the liquid drop is compressed and a shock wave is generated from the impact point. The pressure rise, results from the impact, can be approximated by ρcu, where ρ is the liquid density, c is the sound speed in the liquid, and u is the impact velocity. The flow process at the initial time of the impact is characterised by density, compressibility, and impact velocity and droplet diameter. At the end of the initial stage, the shock wave is completely separated from the triple contact point; then the sideways jetting appears in form of thin lamella. The behaviour of this generated lamella results in either spreading (low impact energy) or splashing (high impact energy).

1.2.1.4. Effect of surface wettability

Wettability can be defined as the tendency of the liquid droplet to spread on a solid surface [69]. It describes the extent of intimate contact between a liquid and a solid [70]. In general, there are two parameters to characterise the wettability of a liquid on a solid [71], [72], namely as: (i) degree of wetting and (ii) rate of wetting. The degree of wetting is generally indicated by the contact angle formed at the interface between solid and liquid. In the equilibrium case, it is governed by the laws of thermodynamics. It is dependent on the surface and interfacial energies involved at the solid/liquid interface. The rate of wetting indicates that how fast the liquid wets the surface and spreads over the same. It is guided by number of factors such as the thermal conditions of the system, capillary forces, viscosity of the liquid, the chemical reactions occurring at the interface, etc. Whenever a drop of liquid is placed on a solid substrate surface any of the following phenomena may take place either alone or in combination depending on the properties of the spreading liquid and/or substrate, system/environmental conditions, etc [73].

- The drop of liquid may spread continuously to cover the whole substrate surface completely by a thin film. This is generally known as complete wetting.
- The liquid drop may spread partially to some extent and come to rest within a short period of time—a case generally referred as partial or incomplete spreading.
- The liquid may spread a little or may not spread at all. A highly lyophobic surface such as the behaviour of lotus leaf against water shows this type of behaviour.
- The spreading liquid may stop its movement due to solidification.
- The liquid may evaporate over a period of time. This generally takes place in case of volatile liquids or when it is placed on a heated surface.
- The spreading liquid may be consumed by the substrate by chemical reaction/diffusion—the phenomenon of reactive wetting.

- The liquid may get adsorbed and subsequently absorbed by the substrate. Porous substrates generally behave in this manner.

The latter possible scenarios clearly indicate the complexity of the wetting process and respective engaged forces. In the simplest case of spreading of a non-reactive liquid on smooth and inert solid only surface tension and viscous forces act upon and determine the equilibrium state. However, the real situation is quite complex as already pointed out and a great number of factors affect the process and in most cases do not allow the equilibrium to achieve.

When a liquid sits on a solid surface, it will spread to some extent on the surface and then comes to rest making an angle with it as shown in the Figure 1.3. The angle between the tangent drawn at the triple point between the three phases (solid, liquid and vapour) and the substrate surface is known as contact angle. Under equilibrium conditions this angle is decided by the surface and interfacial energies. Contact angle has been widely used for characterizing interfacial phenomena, wetting/dewetting of solid surfaces, capillary penetration into porous media, coating, painting, etc. [71], [72].

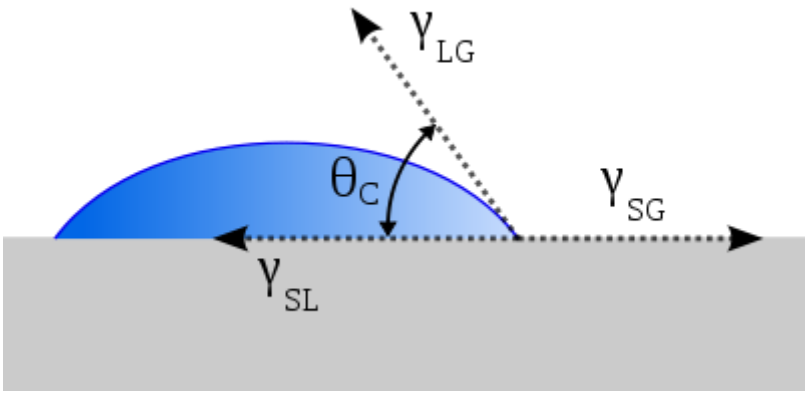

Figure 1.3: Schematic definition of the contact angle

The droplet considered to wet the solid completely only when the contact angle is zero or (σ_{sv}-σ_{sl}>σ_{lv}), where σ_{sv}, σ_{sl} and σ_{lv} are the interfacial tensions between solid-vapour, solid-liquid and liquid-vapour, respectively [74]. Therefore, the droplet tends to spread completely on the solid.

However, when contact angle is zero, Young's equation ($\sigma_{sv} = \sigma_{sv} + \sigma_{lv}cos\theta_s$) is unable to hold and the imbalance of surface free energies is given by spreading coefficient, S, defined as follows:

$$S = \sigma_{sv} - (\sigma_{sl} + \sigma_{lv}) = \sigma_{lv}(cos\theta_s - 1) \qquad \textit{Equation 1.6}$$

The distinction between different states can be made with the help of spreading coefficient defined above. It is negative for partial wetting state since the sum of solid/liquid and liquid/vapour interfacial tensions is greater than the solid/vapour tension and hence, it is unfavourable to replace the solid/vapour interface. On the other hand, for complete wetting the spreading coefficient is zero or positive [74] and cannot be used to study the spreading. All the possible scenarios of the wetting, from non-wetting condition (θ=180°) to complete wetting condition (θ=0°), can be seen schematically in Figure 1.4.

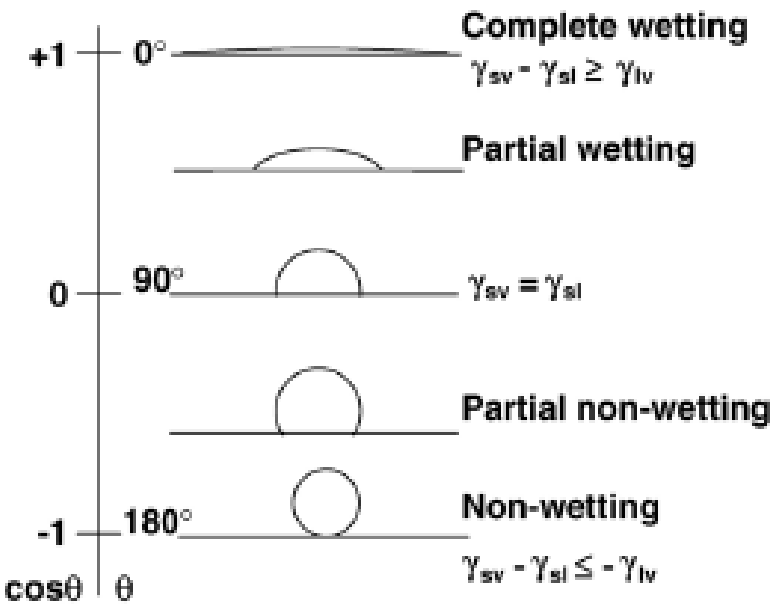

Figure 1.4: liquid droplet on a solid surface under various wettability [73]

The derivation of Young's law is made under the assumptions of spreading of nonreactive liquid on an ideal (physically and chemically inert, smooth, homogeneous, and rigid) solid. Further it is also assumed that the contact angles are large enough to allow accurate

measurement [74]. The condition is rarely met in the practical situations due to presence of thermal, surface roughness, oxidation, and compressibility effects. However, Young's equation is the most fundamental starting point for understanding of the complex field of wetting.

The quantification of the droplet spread, wettability, on solid surface and effect of all the governing factors on the surface wetting process due to its importance in variety of industrial applications has been investigated by a significant number of studies; for example, [3], [5], [6], [30], [64], [75]–[86]. There are a number of parameters should be taken into account when the wettability of a solid surface is studied. The effects of inertial, viscous, and surface forces, heterogeneity of the surface, quantity, or volume of fluid spreading, reaction between the fluid and surface of substrate and dynamic contact angle are the main measures to represent surface wettability. Therefore it is difficult to reproduce the values of the contact angle in any systems, as the number of system parameters or variables are too large to control; this explains the discrepancies of the reported contact angle values in the literatures.

The work of [31] systematically studied the effect of surface wettability, for dynamic contact angles between 5˚to 160˚, on droplet (viscosity: 1- 100 mPa.s) impacting at a velocity range of 0.5 – 5.0m/s, and spreading on the substrate using high speed cinematography. The dynamic contact angle was noted to remain almost constant during the spreading phase due to competition between the surface tension and the viscosity. The energy balance model suggested in [87] was modified with inclusion of the average value dynamic advancing contact angle to predict maximum spread diameter which was shown to produce good agreement with the experimental data in particular at low Reynolds number.

A considerable amount of experimental works can be found in literature, where the effect of basic parameters such as droplet basic properties (viscosity, density, and surface tension), droplet size, impact velocity, solid surface roughness and wettability on droplet spreading are

investigated explicitly. Recent studies focus on the dynamic impact of droplets on super-hydrophobic and complex surfaces [63], [88], as there is a great challenge in studying the behaviour of droplets coming in contact with such substrates.

The significance of the surface wettability is more important in analytical and numerical modelling of the droplet behaviour on a heated solid surface as the contact angle has a dynamic behaviour compared to a classical static contact angle assumption. Advancements in high–speed photography allow the dynamic contact angle to be investigated more explicitly. The study of [89], using a "droplet impingement imaging system" managed to digitize the shape of the droplet at each time instant during the spreading process extrapolating considerable information about its variation as function of the rim velocity. Selective experimental works depicting this change of contact angle values during the spreading period can be found in the following works [30], [31], [65], [66].

1.2.1.5. Effect of ambient pressure

Ambient pressure and air has been added to the list of influential parameters in droplet impact on solid surfaces. Recent experiments using high-speed imaging show that indeed, the liquid drop does not make contact with the surface on the impact axis as had been assumed in this classical paradigm [6], [90]. Rather, the drop is deformed by the air into a non-convex geometry preceding impact [36], [91]–[95]; thus, the stress singularity is resolved in the air before liquid-solid contact initiates. In a typical impact event contact initiates at the boundary of this dimple; as a result, a bubble of air is trapped in the liquid [91], [92]. However, the most striking demonstration of the importance of air in the impact process is the suppression of the splashing phenomenon with a reduction in ambient pressure, as shown in Figure 1.5 [36]. While a critical ratio of stresses in the gas and stresses restraining the liquid was suggested to define the threshold for splashing or not for the highest velocity impacts studied [36], the underlying mechanism for the splash remained an open discussion.

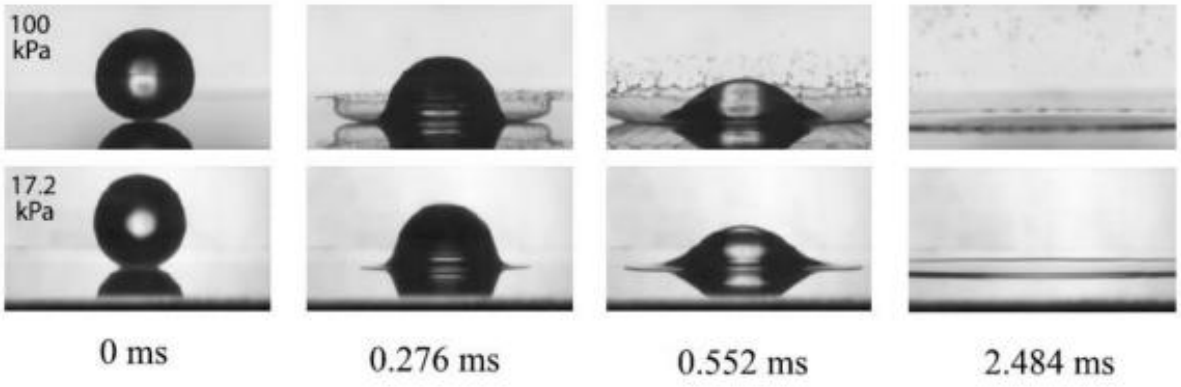

Figure 1.5: Impact of a drop under different ambient pressure and associated collapse of splashing threshold data [36]. *At ambient pressure, a mm-scale drop will emit a sheet when impacting with sufficient velocity, as can be seen in the top row of images. When the air pressure is slightly reduced, the same drop will deposit on the surface, as can be seen in the bottom row of images.*

The work of [67], performed a series of impact experiment for droplet with size ranging from 2.1 to 2.7 mm with impact speeds of 0.7-3.5 m/s to study the effect of chamber pressure on impact dynamic. In the range of pressures tested (1 bar < P < 10 bar), spreading was found to be unaffected by chamber pressure. Spread factors for propanol and diesel didn't show significant deviation at high pressures (<10bar) from the values at atmospheric pressure at isothermal condition. Additionally, in their splash tests, threshold pressure and splash ratio, as proposed by [36], were found to increase sharply at low impact speeds suggesting that much higher pressures are required to induce splashing at low speeds. It could be concluded that drop kinetic energy is more vital for splashing compared to gas pressure. Splashing was found to be affected by drop shape or curvature. Surrounding air entrainment and stronger displacement waves could be possible explanations for this observation. For instance, if the droplet is oblate, the compressed air has a narrow channel to escape and hence gets further compressed. As this compressed air tries to escape just before impact, it entrains the liquid and ejects secondary droplets upon impact [97]. On the other hand, for a high curvature drop, there is a wider space available for the air to escape. The air is less compressed and can escape freely. Such air entrainment has been reported in [98] as a possible cause of splashing. At the instant of impact, the air between the drop and the surface, gets accelerated to speeds around ten times the impact

speed. This accelerating air could cause instabilities in the liquid near the impact point which grow, resulting in droplet ejection; thus, the work of [37] suggested Kelvin-Helmholtz to be the instability mechanism rather than the Rayleigh-Taylor instability. The effect of shape on splashing, as reported in the work of [67], certainly supports the above theory.

1.2.1.6. Maximum spreading diameter

Understanding maximum spreading of drop impact is key to control the drop dynamics in several applications [17], [29]. For instance, in the case of fuel drop impact on the imposed surface of the piston in diesel engines, the evaporation intensity of the liquid directly related to the maximum spreading [3]. It is generally agreed on that the spreading is limited by either viscosity or surface tension. Therefore, a key issue is to define which of these is dominant. Different models have been proposed for the maximum spreading ratio. Studies distinguish two main domains: the capillary regime at low impact velocity and the viscous regime at high impact velocity [22], [99]–[102]. Assuming an inviscid liquid, the maximum spreading is limited by the surface tension. Balancing the Laplace pressure force with the inertial deceleration of the drop, a scaling of $\beta_{max} \sim We^{1/4}$ is obtained [99], [103]. This scaling is remarkably robust [99], [104], [105] in the capillary regime. Another limiting case is to completely ignore surface tension and assume that the maximum spreading radius is limited by the viscous dissipation during droplet spreading. Based on energy balance between kinetic and viscous dissipation energy, a scaling of βmax with $Re^{1/5}$ is found [14]. Based on an energy approach for a cylindrical disk-shaped droplet at maximum spreading, including kinetic and surface energy before impact and surface energy and viscous dissipation at maximum spreading, a scaling with $Re^{1/4}$ is found [30]. The work of [106] showed that, even though the scaling with $We^{1/4}$ seems consistent for some liquids, such as water, it is not for other liquids, such as non-Newtonian liquids; this can be attributed to the fact that Weber number does not contain the viscosity value. Based on energy balance between kinetic and surface energy, a

scaling of β_{max} with $We^{1/2}$ is found [107], [108]. However, [106] showed that none of their data scaled with the dependencies reported in literature ($Re^{1/4}$, $Re^{1/5}$, $We^{1/4}$ and $We^{1/2}$). Therefore, they proposed a solution that introduces a broad crossover regime between the low and high impact velocities by interpolating between $We^{1/2}$ and $Re^{1/5}$. The interpolation between the two scaling laws showed a good agreement with experimental data. This method thus demonstrated clearly that droplet spreading could not be predicted simply by equating kinetic energy either to capillary energy or viscous dissipation, since, in most cases of practical interest, all three energies are important.

In addition, none of the aforementioned correlations have taken the heat transfer effect into accounts. This is attributed to the shorter time scale of the maximum spreading dynamic compared to the heat transfer. This reduce the dominancy of the heat transfer, thus variable physical properties, on the spreading of the droplet in the initial stages [101].

1.2.2. Non-isothermal droplet impact

In contrast to isothermal condition, the nature of the collision of the droplet with the heated surfaces exhibits great diversity in hydrodynamic and thermodynamic properties, such as droplet splash and rebound, wetting or non-wetting contact, nucleate boiling or film boiling, and Marangoni effect, depending on the ratio between the time scales associated with momentum transfer and heat transfer. The droplet shape, the contact area and the cooling effectiveness during the impact not only depend on such dynamic forces as the inertia, pressure, surface tension and the viscosity forces but also on the surface and droplet temperature [109]. When the initial droplet temperature is below the liquid saturation temperature, which represents most of the practical applications, since the temperatures of the liquid droplet evolved from liquid spray are usually equal to that of the ambient condition to which the droplet is exposed. An important issue for developers of flow models is the ability to accurately introduce thermal

induced effects on the hydrodynamic mechanisms of interaction addressed in isothermal conditions. These effects are reviewed in this section.

The difference between the phenomena of non-isothermal droplet impact and the one for isothermal impact, arise from added influential factors related to heat transfer process, evaporation and temperature dependence of the liquid physical properties. When $T_W<T_{BP}$, the heat transfer does not affect the phenomenon at the beginning of the droplet impact process [77], where the inertia is the dominant factor. However, later on during spreading, the temperature rise in the droplet alters the evaporation process and the physical properties of the droplet (i.e. surface tension and viscosity); this may result in modification of the spreading rate.

Different heat transfer regimes occur based on the degree of wall-superheat, which are usually associated with the temperature dependence of the heat removed by a droplet gently deposited onto a hot surface, or conversely, by the droplet lifetime [76], [110]–[112]. Four regimes can be identified, as shown in Figure 1.6.

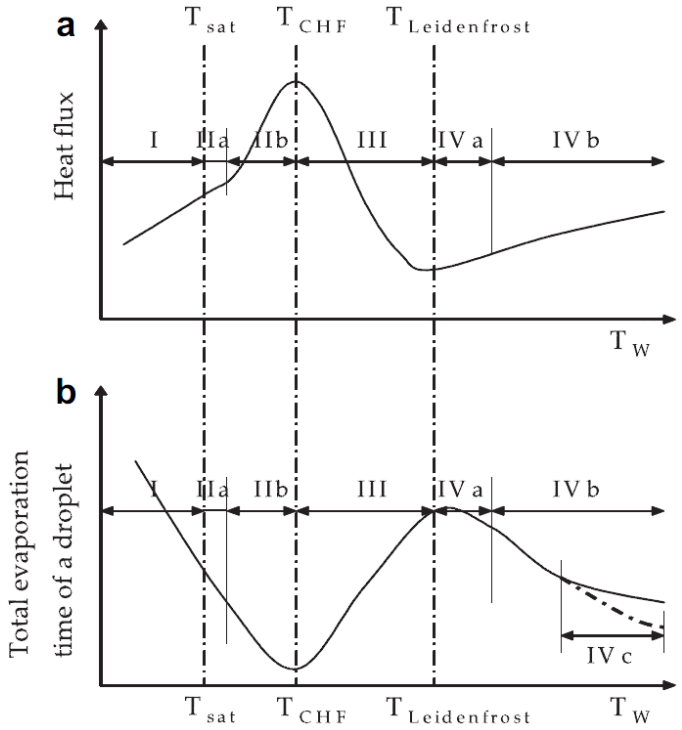

Figure 1.6: Boiling and lifetime curves of a droplet gently deposited on a heated surface. The four heat transfer regimes are associated to the segments of the curves representing the wall

heat flux or the total evaporation time of the droplet as a function of the surface temperature, T_W [3]

- single phase/film-evaporation ($T_w < T_{sat}$): heat transfer occurs mainly by conduction and free convection, without phase change;
- Nucleate boiling ($T_{sat} < T_W < T_{CHF}$): vapour bubbles form close to the wall (region IIa) and move by buoyancy up to the liquid–air interface (region IIb). The heat is removed by vaporization and increases with the surface temperature up to a maximum at the Critical Heat Flux Temperature (T_{CHF}) [113];
- transition ($T_{CHF} < T_W < T_L$): as initially the vaporization rate increases, an insulating vapour layer forms at the liquid–solid interface and then consequently the heat flux decreases down to a local minimum at the Leidenfrost temperature [114];
- Film boiling/Leidenfrost regime ($T_W > T_L$): a stable vapour layer forms, which precludes contact between the droplet and the surface and through which heat is transferred by conduction. Radiation starts to play a non-negligible role only at higher temperatures (region IVb), and in the case of fuel droplets, ignition may also occur, after which a slight decrease in droplet lifetime curve occurs [110].

The work of [115] showed that these heat transfer regimes cannot be clearly associated with corresponding hydrodynamic regimes, for ease of analysis, it is often convenient to follow the picture given by [116], that the evaporation and nucleate boiling regimes are associated with a wetting regime, while the film boiling regime is associated with a non-wetting regime (Leidenfrost). In the transition regime, the droplet contacts with the surface intermittently, with partial contact only.

The experimental work in [117], is among the first attempts to systematic study of the droplet impingement on a heated surface. They have studied the behaviour of a 2mm droplet upon impact on a polished gold surface, heated above Leidenfrost temperature. As the temperature increased, the physical contact of the droplet with the surface reduced. For low impact Weber numbers (We<30), the droplet rebounded from the surface. By further increasing the impact Weber to around 80 they have observed partial integration, while for We>80, complete disintegration occurred. The resident times of the droplet on heated surface was computed

based on the first order vibrational period of the droplet which agreed well for the low Weber number cases.

The work of [109] studied the dynamics of 24°C n-heptane droplet impacting on metallic surface with the Weber number equal to 43. The transition from nucleate boiling to film boiling was identified when the surface temperature rises from the boiling point (170°C) to above the Leidenfrost temperature (200°C) of n-heptane. The contact angle of the liquid to the surface was also reported to increase with an increase in the surface temperature, and reach 180° in the film boiling condition. They have provided detail information of temporal variation of the droplet during the deformation process. They have reported similar spreading dynamic of the droplet impacting onto both dry and wet heated surface at early stages; this was due to neglected effect of surface tension and viscosity. The occurrence of a single bubble has been reported for low surface temperature. The number of bubbles has been increased by increasing the surface temperature. The experimental values of the maximum spreading factor were in good agreement with the proposed one dimensional energy balance model [109].

In [118], the temperature drop of a stainless steel surface was measured during the impact of the subcooled water and n-heptane droplets in low gravity. They found that when the surface temperature is above the superheat limit (How high a temperature of a liquid be raised beyond its boiling point without vaporizing), the temperature drop of the surface is relatively small for the impact of an n-heptane droplet (less than 20 °C); however, for the impact of the water droplet, the temperature drop of the surface can reach 150 °C, which is due the fact that the surface tension and liquid-solid contact angle of water being much higher than that of n-heptane.

The disintegration dynamic of a water droplet impact onto various metallic surface, for above the Leidenfrost temperature of water, have been investigated in [119]. As the other relevant

studies, the spreading dynamic in the early stages is similar for all the cases and independent from the surface condition. Lowering the thermal conductivity of the surface material, results in larger value of Weber number to induce breakup. They have also observed receding breakup for low Weber number cases, while for higher Weber number cases, the droplet integrated during the early stages of spreading.

The dynamic process of bubbling and convection cells within a spreading ethanol droplet on a heated surface have been studied in [120]. The growth velocity and maximum bubble diameter before collapsing have been measured and characterised based on the impact Weber number and surface temperature. The life time, size and collapsing behaviour of the respective bubbles ultimately change the droplet breakup regime.

The experimental study of [78], [121] reported the equilibrium and dynamic advancing and receding contact angles of water droplet impacting on copper and stainless steel surfaces with wall temperatures ranged from 120-200 °C. They observed significant change in dynamic receding contact angle with respect to surface temperature and noted it as an indicative parameter of change in boiling regime. It is suggested by [76] that the rapid evaporation at the edges of the spreading droplet causes it to curl back and increase the dynamic contact angle. In [122], [123] spreading dynamic of the water droplet on a heated hydrophilic and a hydrophobic textured surface have been examined and strong influence of surface temperature on droplet spreading factor for the hydrophilic surfaces observed.

One of the few experimental investigation on Diesel fuel droplet impacting on a heated surface (460°C), tilted at different angles, has been reported in [81]. The droplet sizes are in micro-metric scale and the Weber number ranged from 3.5 to 47. Both Rebound and Rebound with disintegration of secondary droplets have been observed. The ability of Weber number to predict the droplet breakup behaviour has been discussed and they have concluded that other

important parameters such as: liquid viscosity, heat transfer mode and surface and vapour film properties should be considered as well.

A series of experiment have been performed to investigate the impact of water droplet onto smooth heated nickel plate, employing high speed shadowgraphy [32]. Three major impact outcome have been identified, namely as: deposition, splash, and rebound. The latter regimes occurred based on variation of surface temperature, impact angle and droplet pre-impact velocity and diameter. Additionally the inner droplet temperature variation has been measured by LIF technique (Laser Induced Fluorescence).

Recently, a comprehensive review of a drop impact on a heated surfaces have been given in [124]. The latter reviewed the published studies concerning the hydrodynamic and heat transfer mechanism of liquid droplet impingement on a heated surface. All four possible different heat transfer scenarios namely as: film evaporation, nucleate boiling, transition boiling, and film boiling have been discussed in details. It has been concluded that the differences in the underlying physics arise from the differences in the implemented experimental methods in each investigation. In addition, the wide range of operation conditions in terms of droplet and surface material properties and impact conditions, results in different observation. Despite the enormous attempts to fully understand the interfacial behaviour of the droplet impact dynamic, employing recent diagnosis methods (i.e. total internal reflection, Schlieren and interferometric high speed imaging), yet there are several inconsistencies for the most important features of the aforementioned phenomena such as Leidenfrost regime, effect of liquid composition, transition boiling and critical heat flux [124].

1.2.2.1. Classification of the droplet post-impact outcome on heated surfaces

In general, the post-impact outcome regimes can be illustrated on regime maps as a function of surface temperature and impact Weber number. Such regime maps are found in the studies of [50], [53], [54], [125] for various single component liquids, where the main difference relies on the criteria used by the authors to define the transitions between the regimes. In [54], the impact outcomes are defined by means of hydrodynamic regimes and droplet morphology (stick, splash, break-up and rebound),while in the rest, more attention is given to the heat transfer associated with the corresponding boiling modes (film evaporation for $T_W<T_{BP}$, nucleate boiling for $T_{BP}<T_W<T_L$ and film boiling for $T_W>T_L$).

Upon impacting on a heated surface with temperature much higher than liquid's boiling temperature, a thin layer of the droplet own vapour forms between the solid surface and the droplet, that is typically only a few nano-metres thick [50]; this layer may prevent the contact between liquid and solid which, in turn, decreases the heat transfer rate. If the pressure force exerted on the droplet from the vapour layer overcomes the droplet's weight, then it levitates from the surface and may rebound; this is known as the Leidenfrost regime [114]. Recently, relying on high-speed imaging techniques, different influential aspects of this transition temperature i.e. fingering patterns, vapour layer thickness and residence time have been reported in [86], [126], [127]. In [128] it was reported that the dynamic Leidenfrost temperature is influenced by the droplet size. Furthermore, the investigations of [33], [34], [50], [53], [129], [130] have reported a variable Leidenfrost temperature according to droplet impact velocity. Increasing the surface roughness is also reported to alter the Leidenfrost temperature [33], [48], [131], [132], however this temperature reduces by decreasing the impact angle, so the tangential impact velocity [125]. It can be also expected that an increase in the ambient

pressure, air density at given temperature, increases the Leidenfrost temperature, due to the change in liquid's boiling point [133] and the difference in aerodynamic and buoyancy forces.

Transition to splashing/break-up regime can be attributed to both droplet kinetic energy and heat transfer. When $T_W<T_{BP}$, the disintegration mechanism mostly observed is splashing [134]. Increasing the impact Weber number also leads to splashing; together with the Ohnesorge number, both have been broadly used to define the splashing threshold [135]. It is also known that splashing is affected by wettability and surface roughness [29]. The air density [136] around the droplet affects the aerodynamic drag of the spreading droplet/lamella; this has been shown to also affect the impact outcome during splashing (selectively among others [36], [137]). For wall surface temperatures above T_{BP}, droplet disintegration mostly originates in the vapour bubble formation and break-up at the liquid free surface of the spreading lamella, and also in the lamella break–up itself [138]. Several studies [64], [139] have been performed to characterise the thermally-induced disintegration process realised together with different heat transfer regimes. Moreover, an extensive experimental research [120] has been carried out to analyse the underlying mechanism of the latter process; the authors studied the growth rate of the bubbles, their collapse and the formation and destruction of convections cells in the spreading film. The effect of wettability has been also pointed out in various theories describing the boiling of liquids on solid surfaces [48], [132], [140], [141].

However, a general representation of the impinging regimes in terms of boiling modes, offers a good qualitative description of the heat induced phenomena as well and is systematized in Figure 1.7, as proposed in [142]. Major divergences are confirmed relatively to the criteria used to define the boundary temperatures: in [55] and [142], their definitions are based on the observations of droplet morphology, but the work of [143] considers the standard temperatures, to distinguish between the outcome regimes. In general, descriptions of some of the regimes in

non-isothermal condition are quite complex because the various phenomena observed at cold impact must be adopted into the boiling modes.

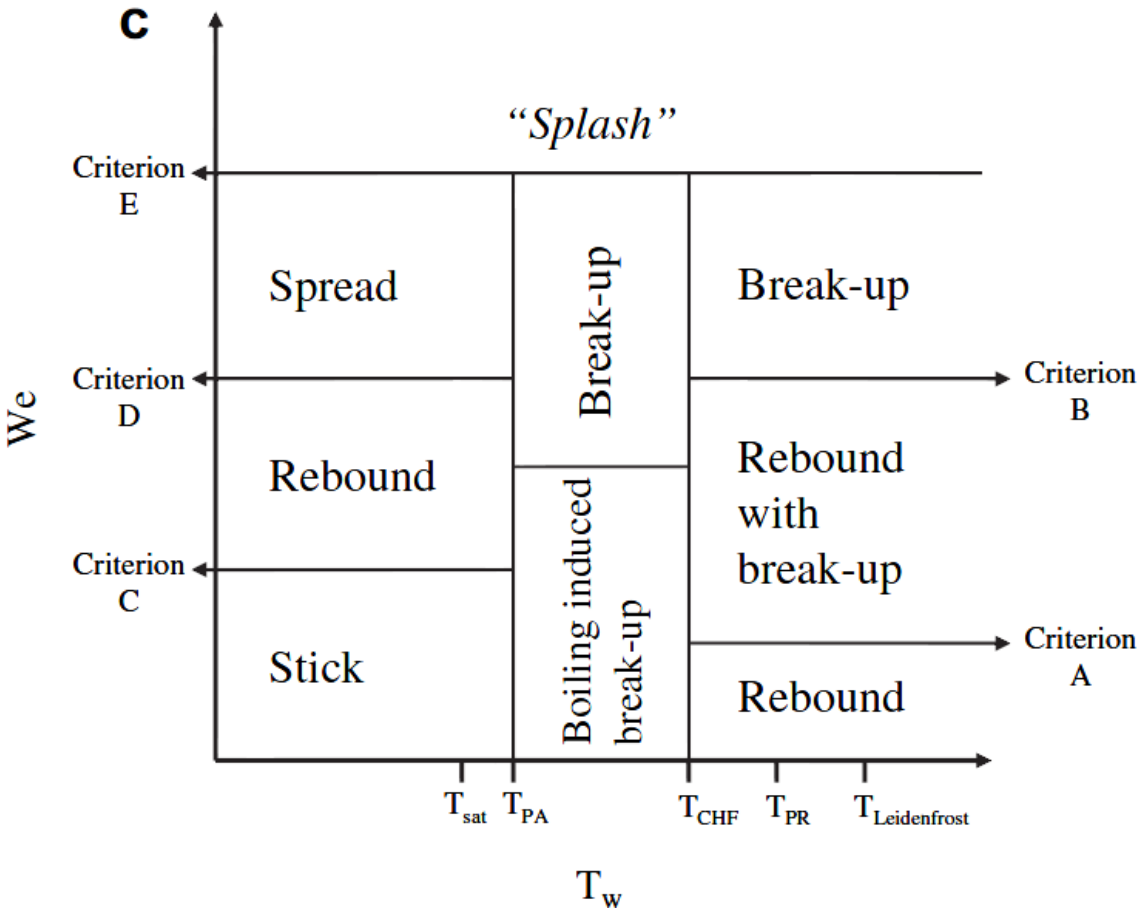

Figure 1.7: Overview of droplet global representations of the impact regimes and transition Conditions fora dry heated wall [142].

1.2.2.1.1. Nucleate boiling regime

Droplet disintegration within the nucleate-boiling regime occurs below the threshold discussed in Section 2 and is associated with the bursting of vapour bubbles formed at the solid–liquid interface. Only recently, have efforts been made to characterize this thermal induced mechanism; for example, in [56], [134], [111], and [134], [144]. Although these studies consider the impact of millmetric droplets, they provide a clear picture of the phenomena involved and of the main influencing parameters: liquid properties (primarily surface tension), surface roughness and effusivity and the impaction angle. Liquid and surface properties

produce phenomenological effects as they change the formation and growth rate of vapour bubbles and surface pressure across the vapour interface and primarily alter the size of secondary droplets; the effects of the impaction angle bear mainly on its influence on impact conditions and mostly influence the direction of ejection.

1.2.2.1.2. Transition boiling regimes

Studies of secondary atomization within the transition boiling regime are sparsely reported, mainly because the complex dependence of the dynamic Leidenfrost temperature on so many parameters introduces difficulties in establishing precise boundary conditions, or obtaining a stable film boiling regime. Nevertheless, authors agree upon the qualitative and quantitative descriptions inferred from the impact of both milli-metric [56], and sub-millimetric droplets [116], [145]: strong secondary atomization during the very intense boiling of the lamella immediately after impact, produces a large number of small, high velocity droplets. Afterward, the remaining lamella levitates and subsequent disintegration produces large, though fewer, droplets.

1.2.2.1.3. Film boiling regime

Disintegration within the film boiling regime has been reported mostly for moderate/high Weber numbers [56], [134], [138] – which however, are the most relevant in this context – and shown to occur immediately after the impact by prompt disintegration of the lamella. Although the size and velocity distributions of secondary droplets show trends similar to those observed in the nucleate boiling regime, the underlying physical mechanisms are clearly distinct. Correlations such as those reported for cold impacts are scarce, but the physical picture devised by [139], for the number, Ns, and size, SMD, of secondary droplets, is in good agreement with many experimental data [144].

1.2.2.2. Multi-component vs single component liquids

Although the work on the multi-components droplet impact started in the mid-1970s, not much has written on the behaviour of the multi-components droplets.

Reviewing the relevant available literature demonstrated that there are limited studies discussing the collision of a Diesel-fuel drop onto a flat solid surface, especially taking heat transfer into account [81]. In addition, most of past experimental investigations were focused on single-component liquids (selectively among others [33], [53]). These studies differ significantly in terms of droplet composition, droplet size and physicochemical droplet properties; thus, the corresponding regime maps and transition criteria cannot be considered applicable for Diesel which comprises of a wide range of hydrocarbons, from $C_{10}H_{20}$ to $C_{15}H_{28}$. Hydrocarbon fuel mixtures are homogeneous as long as they remain below the boiling temperature of their components [146]. Therefore it can be expected that a multicomponent fuel droplet, impacting on a heated surface to behave differently from a single component fluid when surface temperature is higher than some of the components' boiling temperatures. Indeed, no investigations to distinguish the differences, originated from the complex liquid mixtures, in terms of the post-impact outcome have not been published so far. Moreover, it is reported also in the numerical results of [147], this variation in composition of multi component fuels leads to different post-impact flow processes and a different regime map compared to single-component fuels.

The work of [148] presented a theoretical analysis of binary and single component fuel droplets impacting a hot surface, classified them into different impact regimes and explained the factors affecting the droplet's evaporation rate.

Recently, the study of [149] has experimentally studied the dynamics of a binary fuel droplet impinging on a heated surface. The concluded that, in general, mixing two different fuels, with

different boiling temperatures, may lead to significant differences in the nature of the evolving regimes that follow an impact on a heated surface. Six impact regimes, as shown in Table 1.1, were observed and identified for the examined single component and binary fuel droplets' cases and compared them with the diagrams in [146]. While some regimes were valid for both types of droplets, others were distinctive and existed only for one of them.

Impact regime	100% *n*-hexane	75% *n*-hexane 25% *n*-decane	50% *n*-hexane 50% *n*-decane	25% *n*-hexane 75% *n*-decane	100% *n*-decane
Regime # 1: wet impact, no boiling (°C)	< 70	< 85	< 90	< 95	< 175
Regime # 2: wet impact, nucleate boiling with clear droplet remaining on the surface (°C)	—	85–115	90–110	95–105	—
Regime # 3: wet impact followed by violent nucleate boiling, minimal vaporization time (°C)	70–125	—	—	—	175–240
Regime # 4: transition regime (°C)	125–135	115–130	110–120	105–115	240–250
Regime # 5: dry impact, partial film boiling followed by wet nucleation boiling (°C)	—	135–150	125–180	120–205	—
Regime # 6: dry impact, complete film boiling (°C)	> 140	> 155	> 185	> 210	> 250

Table 1.1: Classification of different impact regimes based on droplet composition and surface temperature for droplet diameter of 2.26 mm and impact velocity of 0.76 m/s [149].

Impact velocity effects on the impact regimes were also examined and it was found that changes in the impact velocity may change the boundary surface temperatures identified for some of these impact regimes; higher impact velocity led to a reduction in the surface temperature needed for Rebound regime (above Leidenfrost point) to take place.

1.2.3. Droplet impact on non-flat surface

As mentioned in the previous sections, extensive experiments were conducted to study the droplet impact on a flat surface under the isothermal and non-isothermal conditions. However, only few studies have been reported concerning the droplet impact on uneven or curved surface.

To the best of author's knowledge, the first systematic experiment investigation on droplet impingement onto a spherical surface has been published in [150]. The effect of surface curvature on splashing has been extensively studied.

Later on, the effect of variation of droplet-particle size ratio (DTP<1) on the interaction of the droplet-particle pair, and in particular the coating and disintegration regimes, has been

experimentally investigated by [151]. They have proposed an empirical coalescence parameter based on Reynolds and Laplace number, DTP, and particle wettability. It has been observed that increasing the collision angle reduces the coalescence parameter while increasing the liquid viscosity reduces it. Moreover, they have also studied the droplet-particle collision for DTP>1. The have observed four distinguished regimes, namely as: (i) coagulation, (ii) complete penetration with secondary droplet formation, (iii) formation of air bubble, and (iv) droplet disintegration. It should be noted that, the regimes of (iii) and (iv) are actually sub-category of complete penetration regime and are related to very high impact inertias. These regimes have been mapped also on a Re-We diagram.

The study of [89] conducted the experiments to study the impaction of water droplets on isothermal cylindrical wires. The effects of the impact velocity and the size of the wires were investigated and the modes of the impact outcome were classified to be disintegration and dripping. They developed a non-dimensional regime map to identify the droplet impact modes based on the droplet Weber number, the wire Bond number ($Bo = D/(\sqrt{\sigma/g\rho}$) and the size ratio of the wire diameter to the droplet diameter. Due to the difficulty in system setup and measurement, few efforts have been undertaken to study experimentally the collision between the moving particle and evaporative droplet.

The experimental study of [152], focused on droplet splashing onto the spherical particles. A map based on observed outcome regimes of splashing and coating has been developed. These two regimes were separated by a transition line which was dependent on the particle curvature.

However, more recent studies are carried out on the impact on spherical particles with focus on quantification of spatial and temporal variation of film thickness at different droplet Reynolds number and droplet-particle size ratio. For example, it has been noted in [153] that the three distinct temporal phases of the dynamics that involved an initial drop deformation

phase, the inertia dominated phase, and the viscosity dominated phase. Figure 1.8 shows a typical droplet-particle interaction observed in their work which involved formation of a liquid lamella surrounded by the rim on the particle surface at DTP<1. For a given DTP, the non-dimensional temporal variation of film thickness falls onto a single curve in the first and second stages for different viscosity values. Additionally, a simplified quasi-one-dimensional model was given to simulate the flow on the spherical target considering both inertial and viscous effects taking the gravity and the curvature of the particle into accounts. Also an analytical expression for the time-dependent film profile on the sphere was given for the inertia dominated spreading phase. By reducing the DTP, the film thinning process is getting slower with a larger film thickness.

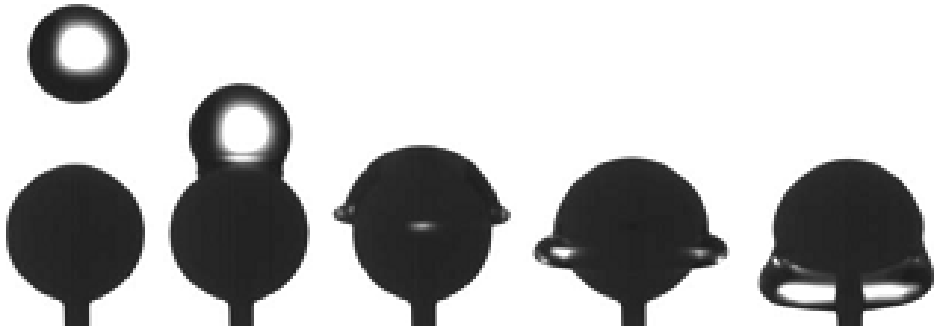

Figure 1.8: Snapshots of impact of a glycerine droplet followed by film formation on a spherical particle target [153]

Acetone droplet impact into a heated spherical brass particle, for above Leidenfrost point, has been investigated experimentally and numerically [154]. The droplet impacts particle with different distances from the particle north pole (on-axis and off-axis impact). They have observed experimentally different stages of the droplet impact dynamic such as spreading, recoiling and rebounding at film boiling mode; similar behaviour have been reproduced numerically, using the CFD simulation (see Figure 1.9).

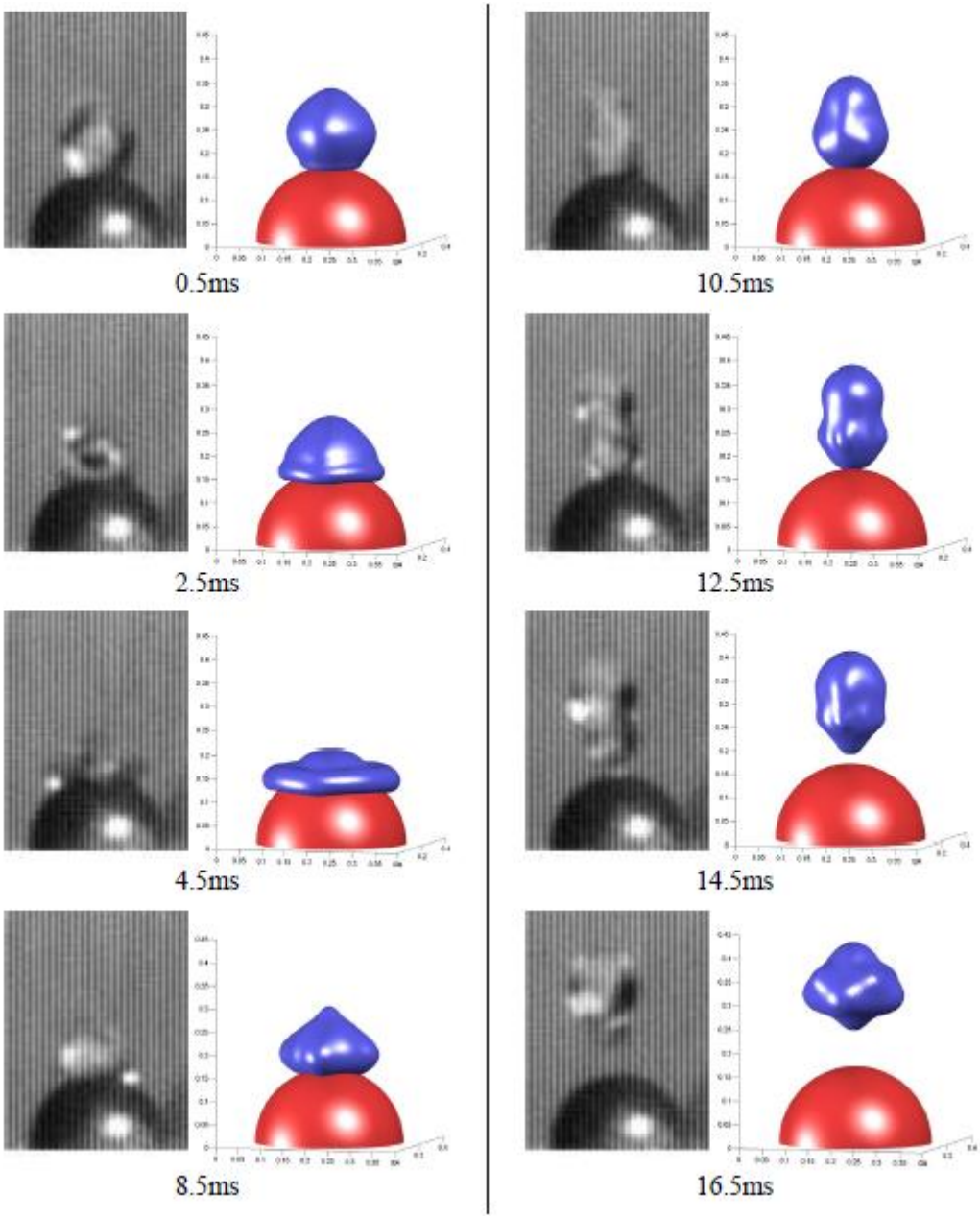

Figure 1.9: experimental and simulated images of a 1.8 mm acetone droplet impacts normally onto a 3.2 mm particle (DTP~0.56) at T_P=300°C. the impact velocity is 0.4 m/s [154]

The spreading factor, droplet-solid contact time and temperature distribution have been quantified as well. The effect of spreading factor on the heat transfer between the heated surface and the droplet has been studied; heat flux on the particle surface increases during the spreading phase, while reduces during the recoiling phase. The contact time was noted to be independent from the DTP and the impact velocity. Moreover, the extent of the spreading diameter increases with increasing the impact velocity and reducing the DTP.

Isothermal and non-isothermal ($20°C<T_P<250°C$) droplet impact on a spherical surface have been investigated numerically and experimentally in [155]. Acetone isopropyl alcohol, and water have been chosen as the fluid due to their significantly different thermos-physical properties. The experimental values of maximum spreading factor were in good agreement with the available theoretical and empirical models in the literature. The outcome regimes have been generally divided to wetting and non-wetting regimes, based on the particle temperature. The surface temperature drop has been also quantified for different droplet boiling modes.

The same authors have expanded their work, by increasing the range of impact Weber number and DTP, to study the droplet disintegration at film boiling condition [1]. A theoretical models have been developed, based on the couple effect of Reynolds and Ohnesorge number, to predict the disintegration threshold. Additionally, a theoretical model for the spreading factor was proposed using one dimensional energy balance approach considering the curvature effect; which was in good agreement with the experimental data set, especially for low impact Weber number.

The effect of surface wettability on the mid-air water droplet-particle collision for DTP=1.45, has been experimentally investigated in [156]. The impact Weber number varied in the range of 181 to 2526. Two types of material have been used to provide both hydrophobicity (Polystyrene particle) and hydrophilicity behaviour (Soda lime glass particle). Under the impact of the droplet on both hydrophobic and hydrophilic particle, 5 different outcome regimes have been observed. These regimes are schematically depicted in Figure 1.10.

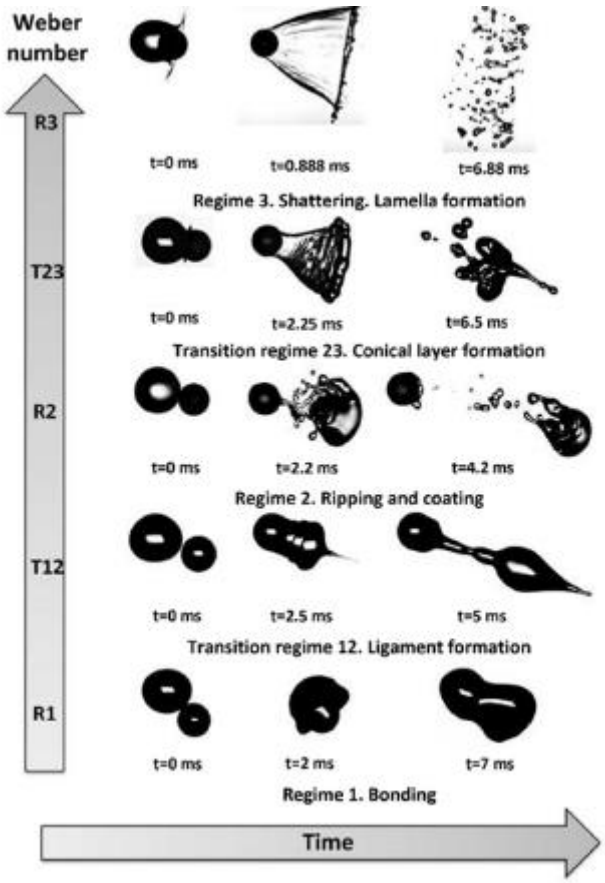

Figure 1.10: Schematic for the definition of the isothermal mid-air droplet-particle collision regimes [156]

The have also measured the structure of liquid ligaments and formation of the lamella in a systematic way.

Impact of a droplet onto a still spherical particle was experimentally investigated for a wide range impact velocity ($0.05m/s<u_0<5m/s$) and surface wettability (θ_s=70°, 90°, and 118°) at isothermal condition [157]. They have extended the impacting Weber number up to 1146 and focused on the condition where DTP>1. Geometry properties of the lamella structure have been quantified for both hydrophobic and hydrophilic surfaces. Finally, as it can be seen in Figure 1.11, they have provided an interesting comprehensive map of all the available works in drop impact on a spherical target.

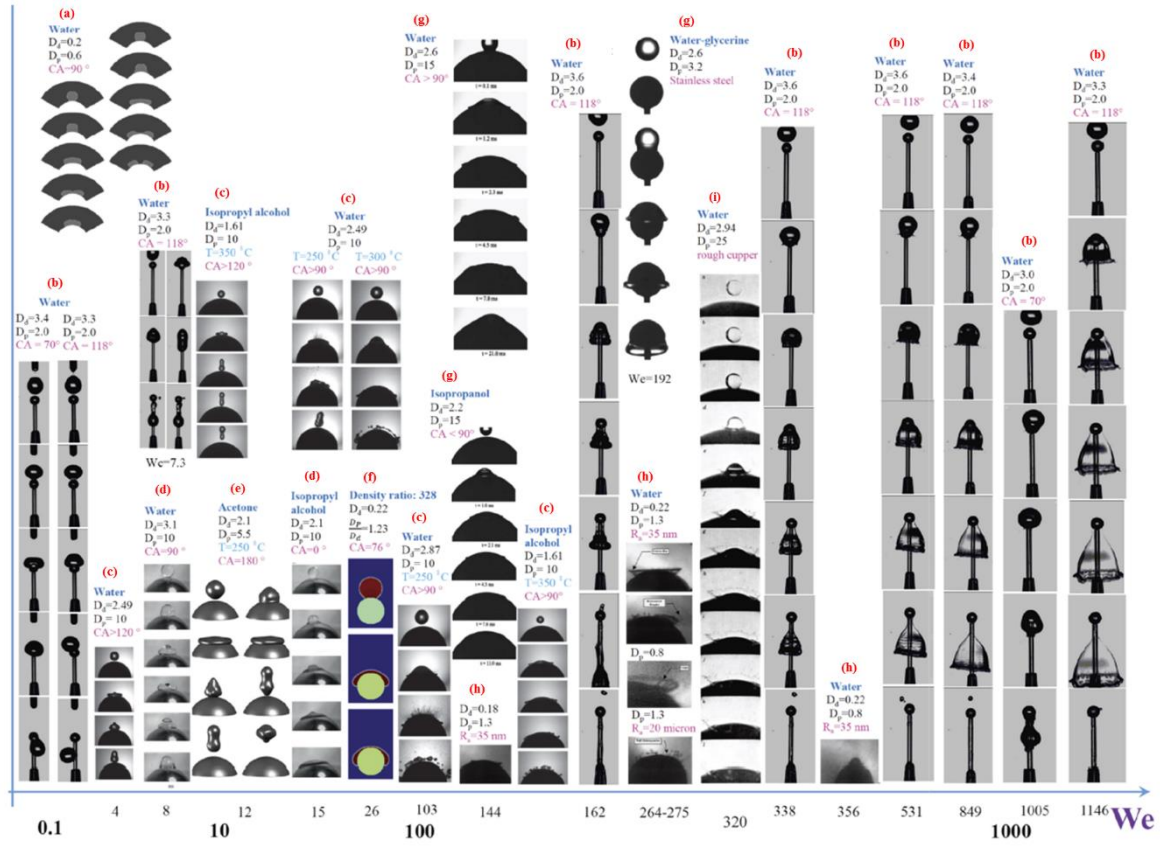

Figure 1.11: illustrative map of all available studies on droplet impact onto still spherical particle. (Ra= surface roughness, CA=contact angle; all diameters are in mm) [157]. *The presented data were extracted from: (a)* [158], *(b)* [157], *(c)* [1], *(d)* [155], *(e)* [80], *(f)* [1], *(g)* [153], *(h)* [152], *(i)* [60]

1.3. Summary

The majority of the previous experimental studies have employed water droplet with a wide range of diameters (several hundred micro-metres to several milli-metres) [84], [85]. In addition, glycerine/water mixture [138], [159], [160], alcohols [161], silicon oil [62], [162], [163], aqueous polymer solution [164], [165], single component hydrocarbons [149], [166], FC-72 [167]–[169] and non-Newtonian fluids [170] have also been used to investigate the impinging droplet phenomena. The previous experimental studies have employed single component liquids such as water [80], [171], alcohols [161], silicon oil [162] and single component hydrocarbons [166]. However, the behaviour of multicomponent hydrocarbon fuel such as Diesel can be different when the surface temperature is higher than the boiling point of

its individual components. For instance, the work of [149] confirmed that the impact outcomes of a binary fuel droplet can be different from the respective of the separate components. It is not yet clear how the contents of the multicomponent fuels can be influential on the evolving regime and the disintegration mechanism of the impinging droplet in non-isothermal conditions; therefore regime maps of single component liquids available in literature, may not be applicable for such droplets [147]. In addition, the information available characterizing the isothermal and non-isothermal droplet impact onto flat surfaces, only limited information exists regarding hydrodynamic (inertia, capillary and viscous forces) and thermal (heat flux) effects for Diesel fuel droplet impact on flat heated surfaces [147]. It should be noted that a complete impact outcome map for a wider range of Weber numbers and wall surface temperatures for Diesel droplets has not yet been presented.

Finally, the number of experimental investigations focusing on droplet impingement on non-flat surfaces and spherical particles is limited. For instance, despite the indicative numerical results which determines the effect of gravity and centrifugal on the latter phenomena, no experimental data have been provided [172].

1.4. Scope of PhD thesis

There are limited experimental studies discussing the collision of a Diesel-fuel drop onto a flat solid surface, especially taking heat transfer into account. In addition, most of past experimental investigations are focusing on single-component liquids. These studies differ significantly in terms of droplet composition, droplet size, and liquid properties from the present manuscript; hydrocarbon fuel mixtures are homogeneous as long as the temperature remains below the boiling temperature of the individual components. However, they behave differently from a single component fluid at surface temperatures higher than some of the components' boiling temperatures due to preferential vaporisation. Up to now, classification

of the post impact outcome on heated surfaces has been reported in the literature only on single component liquids; thus, the existing regime maps and transition criteria available so far are not applicable for Diesel, which comprises of more than 300 components covering light to heavy hydrocarbon molecules.

In addition, a survey of the relevant literature revealed that there are also limited studies on the topic of drop collision onto heated particles of curved surface. Recent articles are focused on either non-isothermal or just a specific regime impact of single component liquid droplets. However, none of the above studies has provided the post-impact outcome map spanning over a wide range of We-T; on the contrary, only limited We-T points were investigated. Moreover the droplet size in applications relevant to the automotive industry and especially referring to Diesel engines, are less than 100 μm in diameter; the present study focuses on droplet sizes in this micro-range. This is different when compared to droplet sizes tested in previous studies, where the smallest droplet was 2mm in diameter (as droplet size affects heating). Finally, the impact Weber-number range of the aforementioned studies is much smaller than the one used in the current work; the larger We number range tested here has demonstrated the existence of new-post impact regimes.

The research goal of this thesis is to investigate the impact behaviour of a multicomponent hydrocarbon fuel onto a solid surface, under different operation condition; surface temperature, ambient pressure, droplet size and velocity, and surface geometry are systematically alter to identify the mechanism of various post-impact outcomes and geometry parameters to characterise the spreading dynamic. In order to highlight the differences in the impact outcome of the multi- and single component fluids, new experimental data for the Leidenfrost temperature, breakup, and splash have been provided for a wide range of operation conditions for Flat and spherical surfaces and compared to those previously reported in the literature. Additionally, the effect of variable physical properties of multicomponent fuels on the

spreading dynamic have been investigated and compared with available numerical results to discover the complex physical mechanism behind it.

The current experimental data can be widely used where it is required to study the spray-wall interactions relevant to IC engine. However, as the droplet impingement onto solid surfaces is a demanding engineering subject, the presented data can be also used for the other relevant application such as droplet-particle collision in FCC (fluid catalytic cracking) reactors and spray cooling systems.

1.5. Thesis outline

In chapter 2, the experimental methods and material used in the current study are presented, followed by detail description of the test conditions and image processing methods.

In chapter 3, experimental data of micrometric Diesel fuel droplet impingement on a heated aluminium surface are presented. The post-impact regimes are identified and mapped for a wide range of Weber-T set points, by means of high-speed imaging. The temporal variation of dynamic contact angle and spreading is derived for conditions below the Leidenfrost point for which no splashing/breakup occurs. In addition, conditions leading to the onset of droplet splashing/break-up are studied and the effects of substrate temperature, We number and air density on the disintegration process are identified.

In chapter 4, the impingement of a micro-metric Diesel fuel droplet onto a brass spherical particle under elevated wall temperatures are reported. By means of high-speed imaging, different post-impact regime outcomes are identified and mapped for a wide range of Weber-T set points. The temporal variation of the dynamic contact angle and spreading factor is derived for conditions below the Leidenfrost point for which no splashing occurs. Moreover, the temporal and spatial evolution of film thickness of spreading droplet at the impact point was measured.

In chapter 5, the overall results are presented and discussed, and conclusions and future perspective are drawn.

Finally, in appendices, a series of experimental results focusing on: (i) the effect of physical properties and additives on isothermal impact of fuel droplets onto the flat and inclined substrates and (ii) oblique droplet-particle impact, are reported. These parts of the work are included in the appendices as such results were known already from the literature (Appendix A and B) or not adequate and conclusive (Appendix C) to be presented in the main body of the thesis.

2. Methodology

In this chapter, the experimental techniques implemented for visualization and quantification of the droplet impact are described in detail. Details of the deployed equipment and the physical arrangement of the experimental setup, along with the data acquisition system and image processing methodology, are presented. Backlight imaging (shadowgraphy) was used to capture the detail of the impinging droplet with high contrast and sharp outline. The dynamic of the impacting droplet was visualized at different time scales with high speed imaging method, to obtain the impact dynamic and the final impact outcome. Finally, all digitized imaging data was analysed with In-house computational imaging analysis routines to determine the required parameters with consistency and high precision.

2.1. Equipment and arrangement

In order to experimentally study the droplet impact phenomena on different surface geometry under elevated temperature and pressure, measurement technique, solid surface preparation, and droplet dispensing are of paramount importance to arrive at thermodynamically meaningful results. Therefore to achieve this target a new test rig was designed and manufactured in City University of London. The experiment performed in this study required the design, manufacture and assembly of a new test rig to suit both droplet impact onto a heated flat surface and one which also partially applicable to a heated spherical surface. The general idea of this new test-rig is to study the phenomenon of the droplet impact onto a heated flat and spherical solid surface at elevated pressure by recording the impingement process from different angles of view with high speed-high resolution photography system. Standard summer diesel fuel was used as the test fluid. Two impinging surfaces include a flat aluminium surface and a brass spherical particle. The details of the test cases are presented in the section 2.5.

The schematic of apparatus used in this study was shown in Figure 2.1 and Figure 2.2; the main components include: droplet generation system, impingement surface and heating system, imaging and lightening system, and high pressure chamber. It can be seen from the schematics that the majority of the equipment for both tests are the same. Table 2.1 summarises the names of the test rigs equipment presented in Figure 2.1 and Figure 2.2.

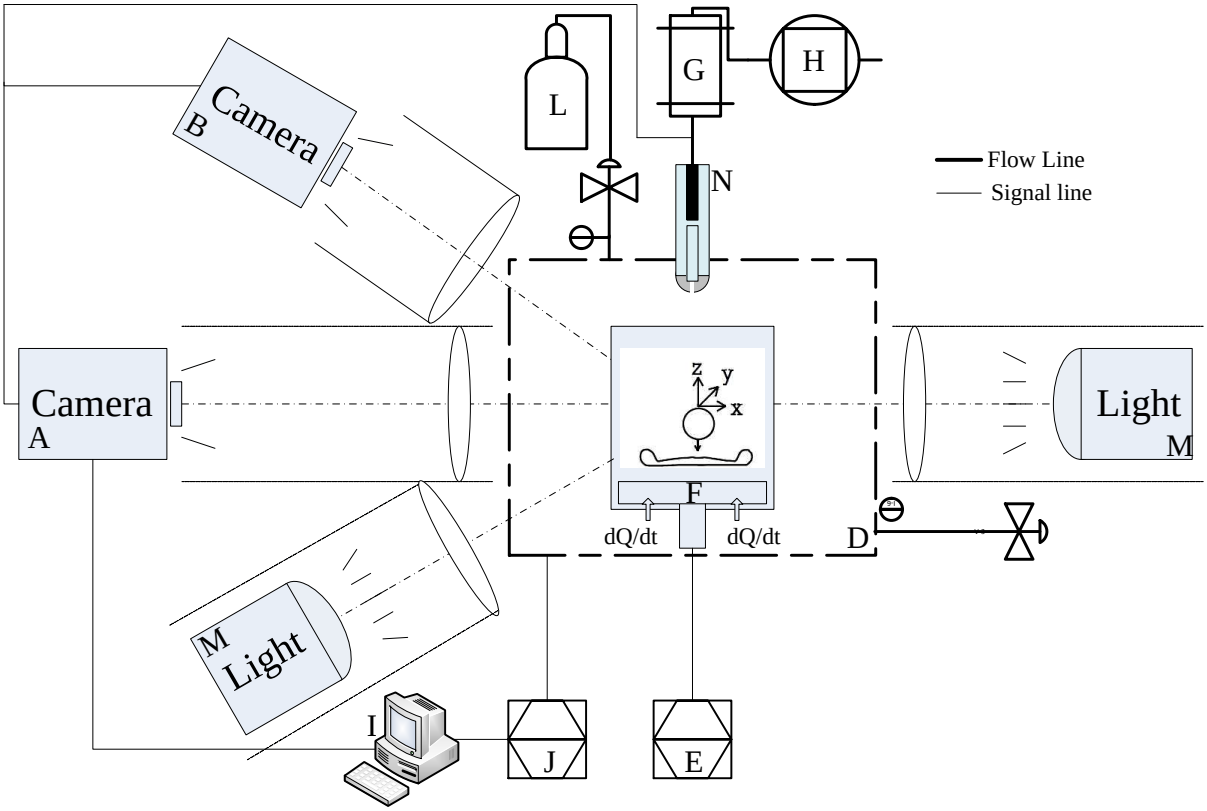

Figure 2.1 Test rig schematic of droplet impact onto a heated flat surface

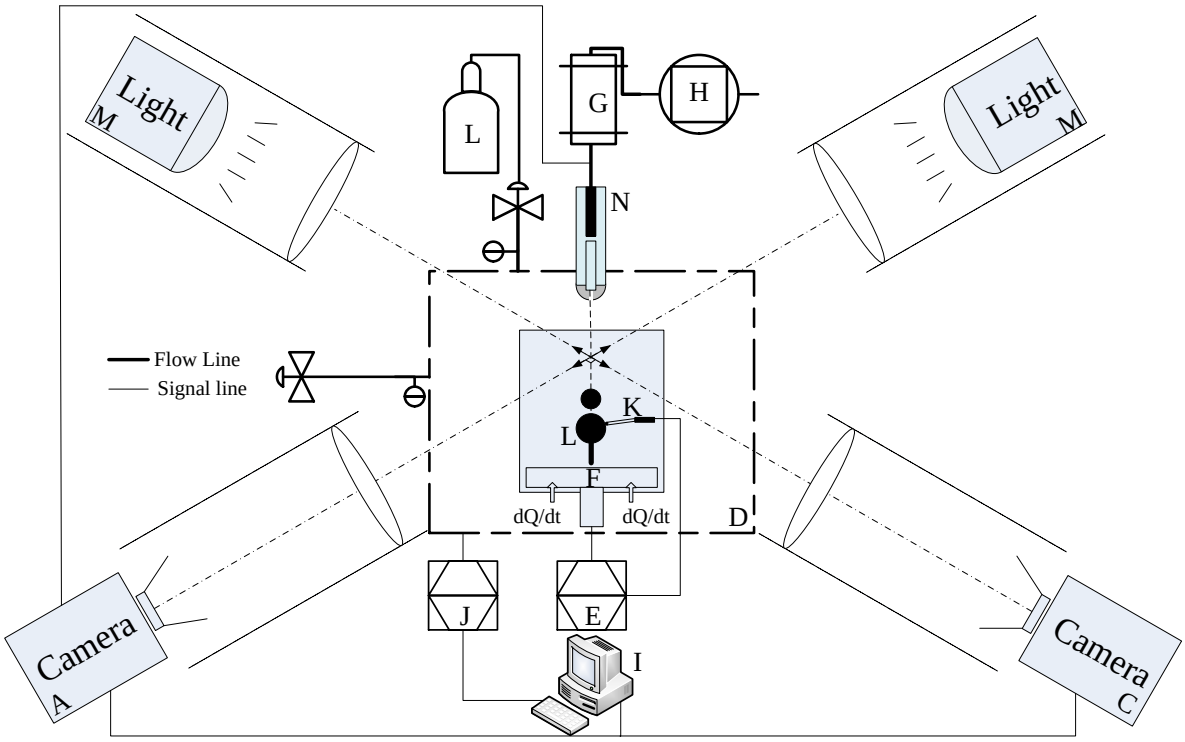

Figure 2.2 Test rig schematic of droplet impacts onto a heated spherical surface

Label	Title
A	Photron SA1.1
B	Photron ultima APX
C	Photron SA-Z
D	High pressure chamber
E	Temperature controller
F	Heated surface
G	Fuel tank
H	Compressed air
I	PC station
J	Data acquisition system and signal triggering: NI PCI 6251
K	Customised thermocouple for point measurement
L	Brass particle model
M	250W ARRI Light source
N	Micro dispenser SMD300G

Table 2.1: Names of the test rig equipment shown in Figure 2.1 and Figure 2.2

The test rigs were soak tested to confirm consistency in results for the same experiment. A micro electromagnetic droplet dispensing system was selected after in-depth research. This allows convenient integration into the high pressure chamber. All components were synchronized to achieve simultaneous droplet generation and imaging. Droplets are generated from a customized electromagnetic driven mono disperse micro valve which was controlled by actuation current. An external 5 V TTL (transistor-transistor logic) signal, produced by a NI PCI card, was responsible to synchronize both cameras and trigger the droplet generator

controller at the same time. Droplets impact onto the flat surface with embedded heaters underneath for various temperatures. In case of spherical surface, the brass particle directly attached to the flat surface using a thin (0.25 mm) drill bit to conduct the heat to the particle. Power input of the heater was controlled by a programmable power supply which was connected to three heaters positioned under the impinging surface. Two 250W ARRI metal halide continuous white light sources were used for backlighting from the opposite direction of the high speed camera. Figure 2.3 shows a photograph of the main components of the actual experimental setup. It is worth mentioning that in the case of impact onto heated flat surface a bird-eye-view was demanded; this is due to capability that this view provides to visualize the free surface of the liquid film and the air entrapped bubble dynamic in the presence of the heat transfer. Due to the hardware installation difficulties, it is more convenient to manipulate the image viewing angle by means of a mirror rather than tilting the high speed camera.

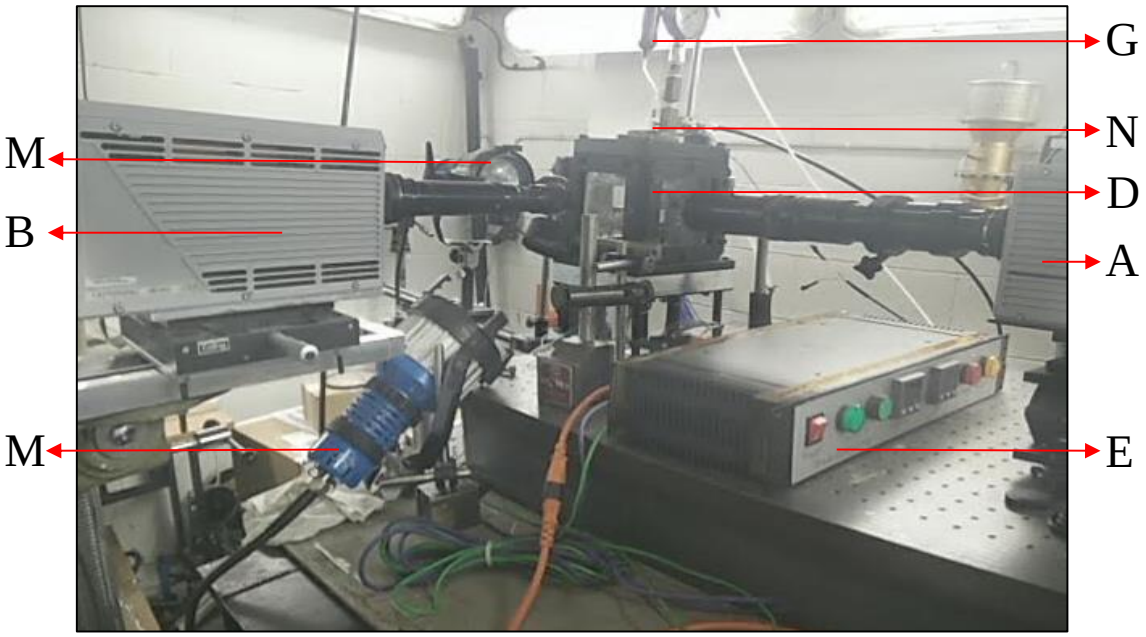

Figure 2.3: Image of actual experimental setup. Labels are explained in Table 2.1

In order to align the position of the cameras with the impact surface, they were mounted on 3D translation stages. The movements of the cameras are then accurate down to 1 µm; this provides 3 degree of freedom in order to focus on the trajectory of the droplet image and the target

impact point on the heated surface. The position of the droplet generator was fixed and sealed into the high pressure chamber; and the chamber itself was fixed up on an optical table.

Even though the majority of the materials and equipment required for this experimental investigation have been purchased for this specific project, with further modifications they can be deployed in future works. Description of the implemented components and their functionality, linked to one-another, will be discussed in detail in section 2.1.1-2.1.4.

2.1.1. Droplet generator system

In the process of conception of the experiment several droplet generation methods were reviewed which results in implementing of the particular droplet generator in this study. There exist several developed droplet generation concepts such as bubble jet, piezoelectric, acoustic, pneumatic, aerodynamic, microfluidic and needle dripping principles [173]. In this study, the operation condition of droplet generator in terms of droplet size and velocity needs to be highly flexible. On the other hand, the position of the droplet generator and imposed surface should be fixed into the high pressure chamber. Taking the aforementioned constraints into account, a customized micro electromagnetic valve (SLMD 300G, GYGER®) has been chosen. This valve is contactless micro dispensing which is suitable for miniaturisation, functional integration, and chemical inertness capable of dispensing medias with different viscosities reference.

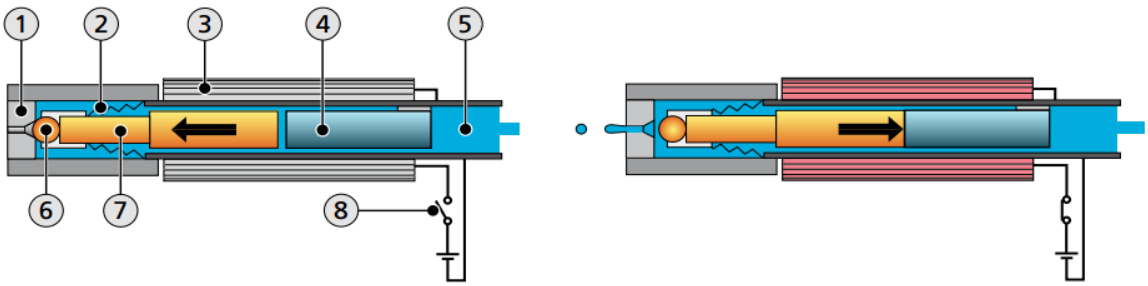

Figure 2.4 Schematic of micro electromagnetic valve dispenser: (1) Sapphire valve seat (2) closing spring (3) valve coil (4) stationary anchor (5) medium (6) Ruby valve ball (7) mobile anchor (8) switch (source: GYGER®)

Schematic description of the micro valve components illustrated in Figure 2.4. The fluid to be dispensed was pressurised inside the micro valve by compressed gas. When there is no current, the micro valve is closed and closing spring acts on the mobile anchor with the valve ball. When there is a current feed through the valve coil, the mobile anchor with the valve ball is magnetically pulled by the magnetic field of the stationary anchor. The micro valve opens and medium ejected through the valve nozzle. The hard sealing valve seat and ball structure makes precise opening strokes possible of a few hundredth of a millimetre and repeat accuracies in the range of thousandth of a millimetre and provide high chemical and mechanical resistance and compatibility values.

In order to have fine droplet from the ejected liquid mass in a certain distance from the valve, the nozzle diameter and valve ball traveling distance should be specified considering the medium physical properties; otherwise the emerged liquid mass breaks up into several satellite droplets. Table 2.2 specifies the micro valve specification for the present study.

Dispensing medium viscosity range	1-200 mPa.s
Minimal dispensing volume	Under 10 nl
Medium required pressure	1-5 bar
Temperature	Room temperature
Nozzle diameter	0.15 mm
Valve ball traveling distance	0.06 mm

Table 2.2: Micro valve specification

After determining the appropriate nozzle, it is essential to provide proper feeding pressure condition and time controlling mechanism to the micro valve. As it can be seen in Figure 2.5, the medium should be discharged from a pressure container. This reservoir was pressurised using compressed air through an air regulator/filter. If the medium takes on air, this can lead to

fluctuations in the dispensing volume as well as to satellite splatters. To prevent this, the medium and pressurising gas should be kept separately by a plastic cap.

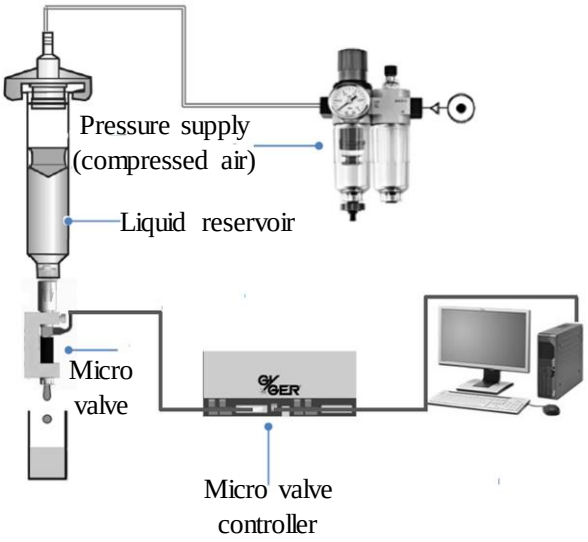

Figure 2.5 Schematic of droplet generation system (source: GYGER®)

In order to achieve minimum micro valve response times with minimum heat development, the electrical control should preferably work according to the peak and hold method. With a peak current increased for a short time, the micro valve can be opened quickly under defined timing and pressure conditions. If the micro valve is open, a lower holding current is sufficient during the remaining opening time. This has been provided by a micro valve controller. Figure 2.6 reports the required actuating current for the valve to stay open for a specified time.

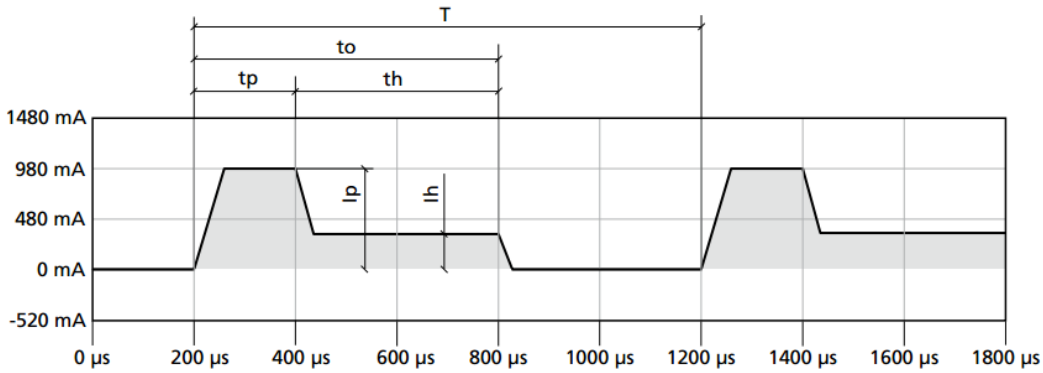

Figure 2.6 Required current for valve opening time with peak-and-hold method, t: period, t_o: valve opening time, t_p: peak time, t_h: holding time, I_p: peak current, I_h: holding current (source: GYGER®)

The waveform signal generated by the micro controller, which obtains the opening time of the micro valve, coupled with the upstream pressure at the liquid reservoir shown in Figure 2.5 are responsible to control the droplet size and velocity. The synchronization procedure of the droplet generator and the cameras were as follows: In each data set, a 5V TTL signal was generated by the PCI card and sent to the input triggering channel of the micro valve controller and the cameras.

2.1.1.1. Mapping of the droplet generator

Controllability of the droplet size and velocity dispensed from the micro valve was evaluated by four parameters; 1) upstream pressure on the liquid, 2) opening time, 3) nozzle diameter and 4) valve ball lift. These parameters should be selected based on liquids physical properties, to prevent secondary break up and appearance of satellite droplets during the injection process. According to the test liquid in the present study, the nozzle has a diameter of D_{Nozzle}=150 µm and valve ball lift of V_{Lift}=60 µm. Initially, the functionality of the micro valve was investigated under a wide range of operation conditions.

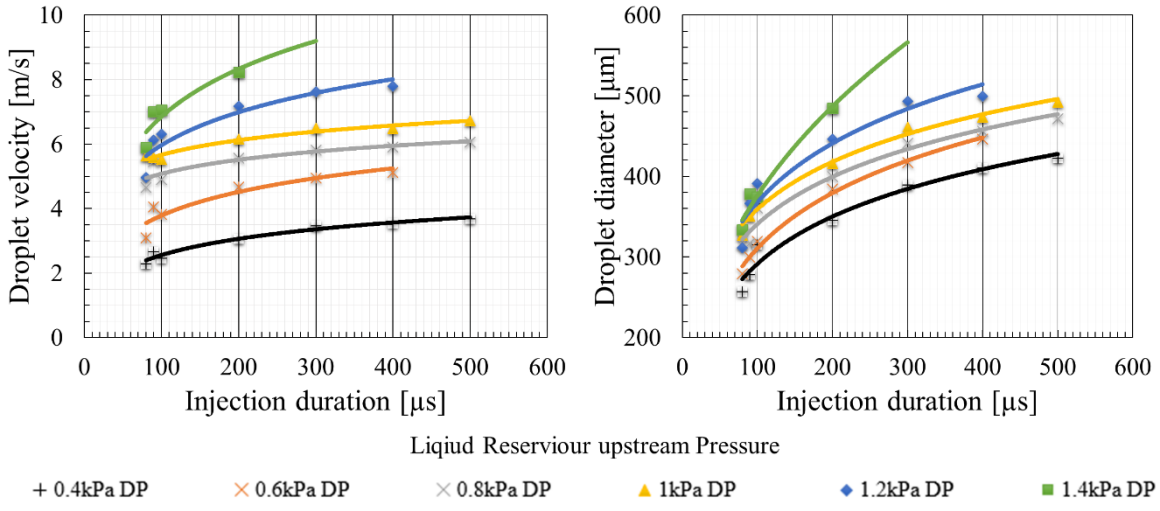

Figure 2.7 Map of the diameter and velocity of the generated droplets for injection pressure and duration range from 40-140 kPs and 80-500 µs, respectively

The procedure was as follows: The upstream liquid reservoir pressure was set to minimum value of 40 kPa and the injection duration varied from 80-500 µs where the satellite droplets

appeared. This was repeated for each stepwise up to injection pressure of 140 kPa. The droplet shape profile was visualized and processed for each data set, using the image processing routine explained in section 2.3. As it can be seen in Figure 2.7, the diameter and velocity of the droplet diameter prior to impact vary in the range of 250-500 μm and 2-9 m/s, respectively. It should be mentioned that the distance between the droplet generator and the impact surface was fixed at 150 mm. This corresponds to impact Weber number of 20-940. Figure 2.8 illustrates the dependency of impact Weber of the generated droplet to the injection pressure and duration. This map was used as operational guide to generate droplets according to test conditions.

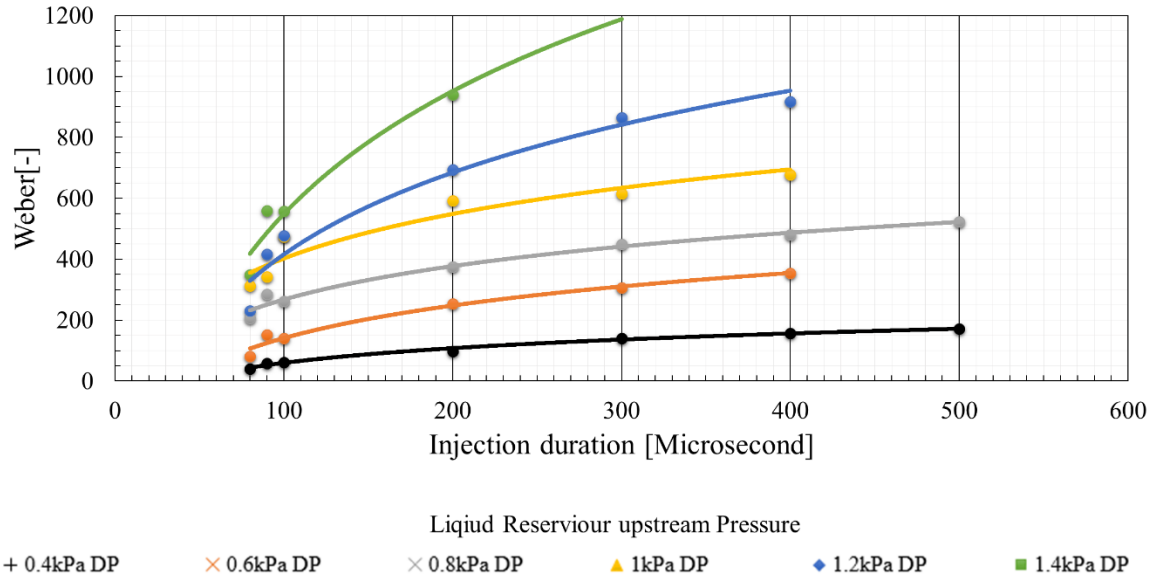

Figure 2.8 Map of Impact Weber of the generated droplets for injection pressure and duration range from 40-140 kPs and 80-500 μs, respectively

2.1.2. High pressure chamber

Quantitative and qualitative measurement of droplet impact under high temperature and pressure environment, require precise control on ambient thermodynamic conditions. For better understanding of the effects of surface temperature and ambient pressure on droplet impact dynamic, extensive shadowgraph measurements were vital. A constant volume chamber was employed for realization of the aforementioned experiments under desired operation condition. This pressure chamber was facilitated with number of inserts, specifically designed, and

implemented for the current experiment. This inserts include heater assembly, the thermocouples, pressure transducers, droplet generator, and its corresponding cooling system, air feeding and draining passages. In order to have maximum optical access into the chamber, three quartz glass windows were placed on it. Figure 2.9 depicts the 3D design of the pressure chamber.

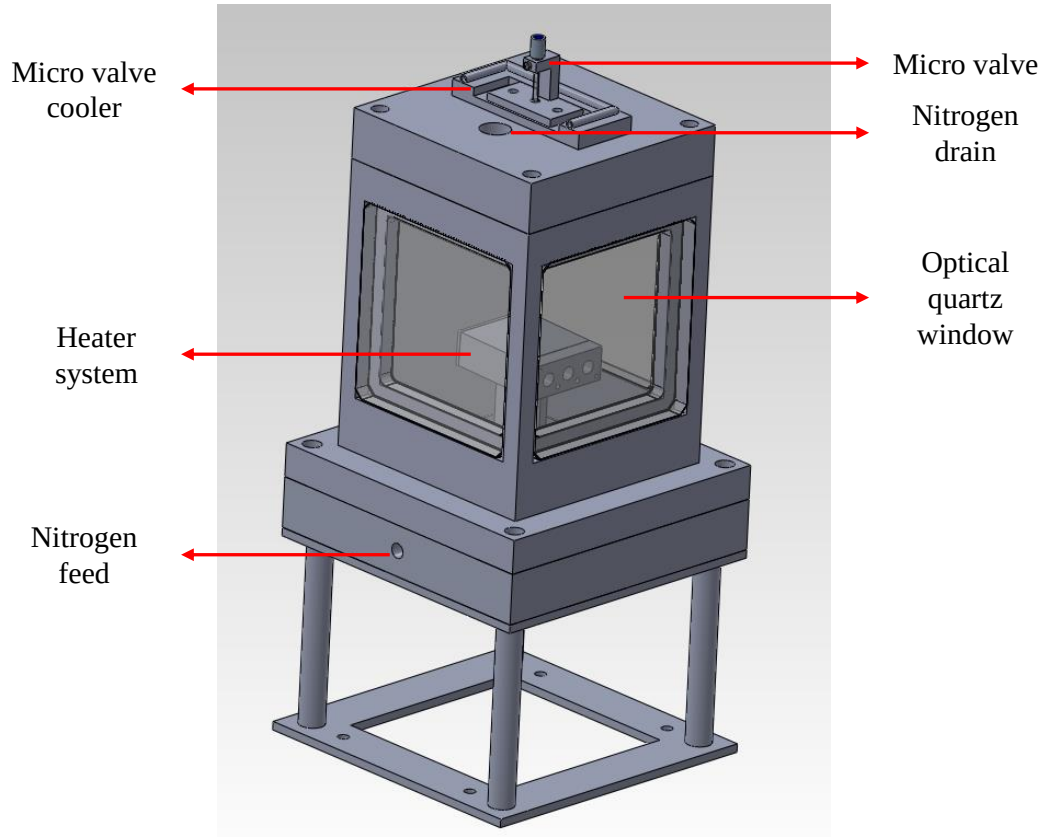

Figure 2.9 3D design of the high pressure chamber facilitated with experimental inserts

The optical chamber consisted of an aluminium cubic frame and sealed using two end aluminium plates. The optical windows were compressed with an aluminium plate and 8 M6 screws equally placed to ensure an equal compression force on the windows. A thin paper gasket was used at the gap between the each aluminium plate and the quartz window in order to seal well and avoid any nitrogen/diesel vapour leakage between intersections.

The chamber was connected to a pressurized air bottle for precise setting of the required chamber pressure (up to 12 bars). The nitrogen flow through the chamber is not continuous.

The inert flow conditions were achieved with a valve that was installed in the chamber feed and drains port; these two ports are essential equipment to discharging the chamber gas contents and purging fresh cold gas after each set of experiments. The temperature of the chamber's walls was kept at constant temperature in order to maintain homogeneous condition during the course of experiment. The injected droplet temperature was also kept at 25±1°C by means of a water heat exchanger and a layer of insulation mounted on the droplet generator system to avoid external heating of the fuel liquid from the heater.

2.1.3. Heating system and impingement surfaces

2.1.3.1. Heating system

The measurements were taken for various numbers of temperature-pressure set points. With the pressure at 1 and 2 bars, temperature values under investigation were from room temperature up to above Leidenfrost temperature. According to the reported values, the maximum temperature of the experiment design was set to 400° C to assure wide-ranging coverage of boiling phenomena of the Diesel fuel [174]. An aluminium plate, with the dimension of 50mm x 50mm with the thickness of 20 mm, was selected as the heater block. Three 250 W high performance cartridge heaters type HLP (TURK HILLINGER) with a 230V AC supply, embedded 3 mm under the impact surface. Each of the heaters has a potential heat flux of 29 W/cm^2; the actual average voltage will vary from zero to 230V.

Due to such a high temperature provided in the current experimental setup, an automatic closed loop PID controller was deployed to control and measure the temperature of the impacting surface. To have low-delay, closed loop control of the heater, the temperature needs to be sensed at a rate above 10Hz [133]. As most of the available controller modules suffer from this sampling rate, therefore a custom temperature controller was implemented. This include a

flexible programming of the PID control loop, which was extended with safety features like Emergency Stop at broken sensor or manual disable.

Using the above system allows the heater assembly to achieve heating rates of approximately 30 K/s heating rate at full power with given geometry of the heater. In order to achieve a temperature precision of 0.1 °C, the pulse width modulation (PWM) technique was implemented. Concerning the mentioned maximal heating rate, the heater power controlled with 255 steps from zero to full power. The update time of the PID controller was set to approximately t_s=100 ms.

Surface temperature measurement was carried out by using a resistor thermometer type Pt-100 integrated into the heater and two NiCr-NiAl thermocouple (type K) just under the impact surface. These thermocouples generate a voltage based on temperature difference between the measuring point and a reference, i.e. cold junction. For this purpose, three thermocouples were integrated into the heater block, under the heater cartridges and three more thermocouples were deployed to monitor the ambient temperature of different locations inside the chamber. Homogeneity of the surface temperature was estimated by numerical simulation and the estimated uncertainty in the temperature measurement was 1.1˚C or 0.4%. The PID controller adjusts the heater output power, as a ratio of the heater full power, based on the difference of the actual and set-point temperature of the target [175]:

$$P_{out}(t) = K_c[\Delta T_{out}(t) + \frac{1}{T_i}\int_0^t \Delta T_{out}(t)dt + T_d\frac{d}{dt}\Delta T_{out}(t)] \qquad \text{Equation 2.1}$$

Where T_i and T_d are the integral and derivative time and K_c is the controller gain and accounted as the PID controller input settings. The tuning process was carried out manually to achieve fast set-point response temperature adjustment without overshooting. The derivative term was off, which disable the derivative action. The setup of the other two terms was informally similar to guesstimation system for PID introduced initially by [176].

~~In order to have inclined impact condition, a tilting mechanism implemented in the junction of heated surface and the stand. To avoid heat transfer through the stand, two PTFE insulation layer of 3 mm thickness were placed in the gaps between the heater plate and the tilting stand.~~

2.1.3.2. Heated surface

The top surface of the heater block was initially machined to provide a smooth finish with average surface roughness of R_a=0.8 µm, then it was polished using abrasive paper and diamond paste to reduce the surface roughness to Ra=0.4±0.1 µm. The surface roughness was measured using a linear surf-metre (Mitutoyo Surftest-SJ-500). This surface was used for the case of impact on the flat surface.

In case of droplet-particle collision, it was required to design a particle model with diameter related to the range of generated droplet size. A 1 mm brass particle was chosen as the particle model and mounted on top of the heater using a 0.2 mm metallic stud. Figure 2.10 depicts the particle model mounted on top of the heater and its relative size scale.

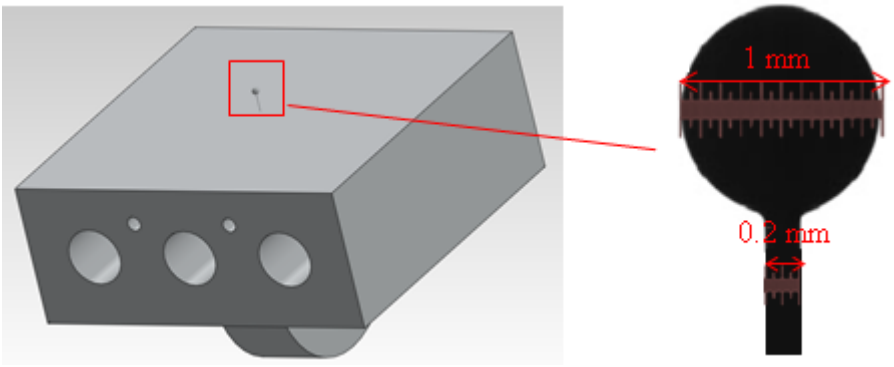

Figure 2.10 Particle model

With the purpose of accurate temperature measurement of the particle model, a customised point measuring thermocouple was employed. Due to the small diameter of the metallic stud, the heat transfer efficiency dramatically reduced and there was a significant difference between the set-point temperature of the heater and actual temperature of the particle. The temperature of particle surface was measured for each heater set temperature and a calibration curve was

derived for the entire range of heater temperature; the positioning of such a thermocouple is shown in Figure 2.2. A customised pin thermocouple, with comparable size to the particle itself, was manufactured in the workshop of the City University of London, to have much more accurate particle temperature measurement.

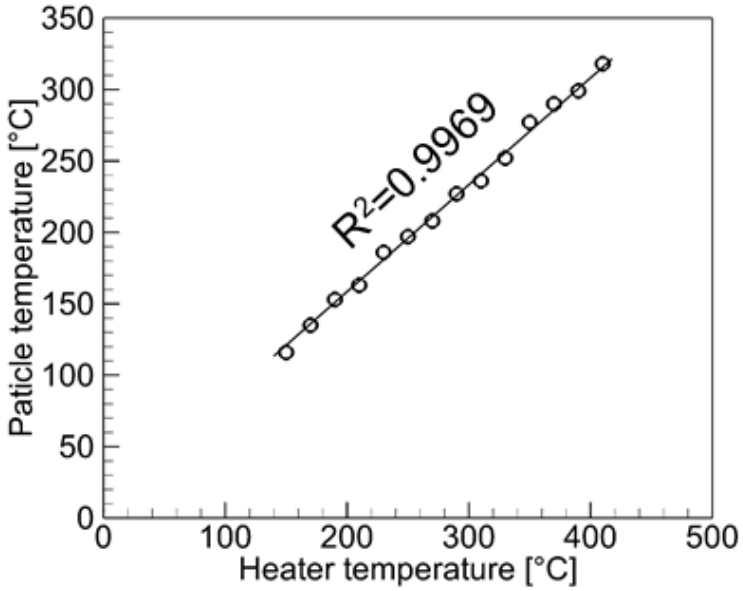

Figure 2.11 Temperature calibration chart for particle surface

2.1.4. High speed high resolution imaging technique

To fully capture different aspects of the droplet impact dynamic onto the either of heated flat and spherical surfaces, two different high speed digital video systems were set up in conjunction with the high pressure chamber as it is illustrated in Figure 2.1 and Figure 2.2.

High speed Camera	Photron Ultima APX	Photron SA1.1	Photron SA-Z
Imaging sensor chip	10-bit CMOS	12-bit CMOS	12-bit ADC
Max frame rate (@ 1024x1024 Pixels)	3000 fps	5400 fps	20000 fps
Electronic Shutter speed range	16.7 ms – 2 µs	16.7 ms – 1 µs	1 ms - 159 ns

Table 2.3: High speed cameras specification

Table 2.3 shows the specifications of the high speed cameras which were employed in the present study. It is also possible to increase the frame rate at progressively reduced resolution. In each set up, two 250W ARRI metal halide continues white light sources provided sufficient light intensity for the imaging chip of the cameras even at the highest used frame rates. The cameras were controlled by built in control units, which was derived by a special software named PFV (Photron File Viewer) installed on the image collecting computer. This special software utilises the controlling parameters of the camera such as frame rate, exposure time, resolution, and triggering signals. It should also be noted that the exposure time, which was controlled by the electronic shutter speed, can be set independently from the frame rate. After each recording session, captured images which were stored into the internal memory of the camera, transferred into the computer via a high speed Gigabit Ethernet cable connection. Since more than one high speed camera was used, the triggering signal needed to be synchronized; Synchronization was carried out by using interconnecting the control units of the two cameras which guaranteed that the images were captured at the same exact time. The significance of this technique is the ability of simultaneous imaging of the phenomena from two different angles. This provides a better understanding of the three dimensional flow patterns of spreading droplet on the heated surfaces, and the dynamic of the entrapped air bubble at the impact point.

The measurement of the diameter and velocity of the flying liquid droplet prior to the impact on heated surface is possible only via a non-invasive technique which prevents any disturbance in the shape of the droplet. Electromagnetic waves such as visible light provide the most adequate results with reference to the wavelength. Mainly because they are sufficiently fast and can be focused to allow observation of effects from outside of the high pressure chamber through the optical windows. Unlike the other complex sensors such as the high speed optics, electromagnetic sensors are not needed to be installed inside the chamber, i.e. set up is less demanding.

Due to the complexity of the interaction of the light and liquid matter, especially in the field of light scattering by small droplets, extra attention should be given to ensure a functional configuration (including testing the performance of the components). The scattering of the visible light by a small droplet can be approximated by the wave nature of light. The maximum scattering intensity occurs at zero-degree angle between the light source and the camera sensor, which is called shadowgraph and chosen for this study [177]. This method relies on placing the light source directly behind the impact surface so that the area of interest lies between the camera and light source. This enables the profile of the spreading lamella, which forms on impact, to become visible by virtue of the light it obstructs. While this method allows for the edges around the periphery to be sharp, generally information on what is occurring within the darkened area is lost.

In the test rig designed to study the droplet impact onto a flat heated surface (See Figure 2.1), the camera A was set in front view of the surface model while the camera B was mounted in side view of the model (90° angle with the front view). However this view will be altered to bird-eye-view by using a mirror mounted inside the chamber with 15° angles to the vertical axis. Because of strong light scattering inside the thick quartz windows of high pressure chamber causes blueness in the obtained images of the droplet; therefore inclination of the camera in order to obtain eye-bird-view, could not be applied. Figure 2.12 shows the visualization angle of imaging.

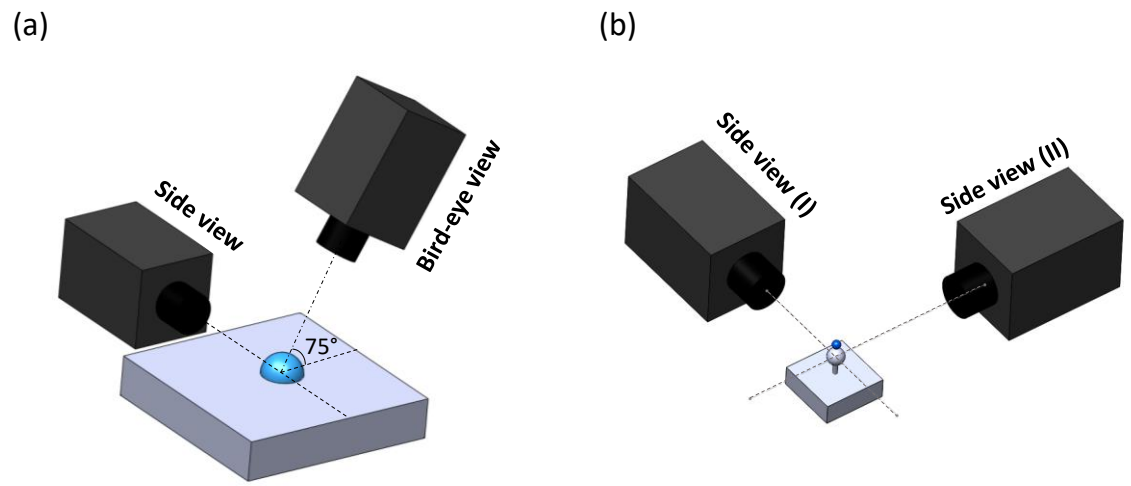

Figure 2.12: demonstration of viewing angle in case of (a) droplet impact on a flat surface, (b) droplet impact on a particle

This dual view visualization arrangement provides detailed information about the droplet spreading, rebound, and break up dynamic in case of impact on both flat and spherical surface. In case of impact onto the flat surface, the boiling condition on the both three contact line (side view) and droplet free surface (bird eye view) of the droplet will be provided as illustrated in Figure 2.12a. Moreover, due to the limited optical access into the pressure chamber, the light source should be positioned in a way that the light rays (after undergoing through number of deflections) be guided directly to the camera lens. It is worth mentioning that the top view alignment in this test rig was nearly impossible due to also the positioning of the droplet generator and limited space inside the high pressure chamber, thus the top view visualization were adjusted with the reduced angle of 75° in regards with the flat surface.

In case of droplet impact on heated spherical particle, both cameras A and C are positioned in the same level with 90° angle from each other; using this arrangement, the eccentricity of the impact with reference to the particle top dead centre (particle north pole), can be easily measured and controlled (Figure 2.12b). This will be discussed in detail in section 2.3. Final optical set up was achieved after a series of trial and error procedures, in order to overcome the obstacles and to achieve the most appropriate arrangement.

In general, there are two sources of uncertainty in raw images during the initial impact period which can significantly affect any quantitative measurement extracted from the raw images. (i) The deviation of the theoretical position of the droplet to the surface at the exact impact time (t=0), (2) The poor resolution of a thin spreading lamella thickness.

It is worth mentioning that, due to relatively small droplet size and high velocity in current study, the effect of these two uncertainties is more significant, and can be reduced by increasing both the temporal (higher frame rate) and spatial (higher pixel density) resolution, however, the temporal and spatial resolutions are restricted in the imaging setup due to requirement of relatively large field of view.

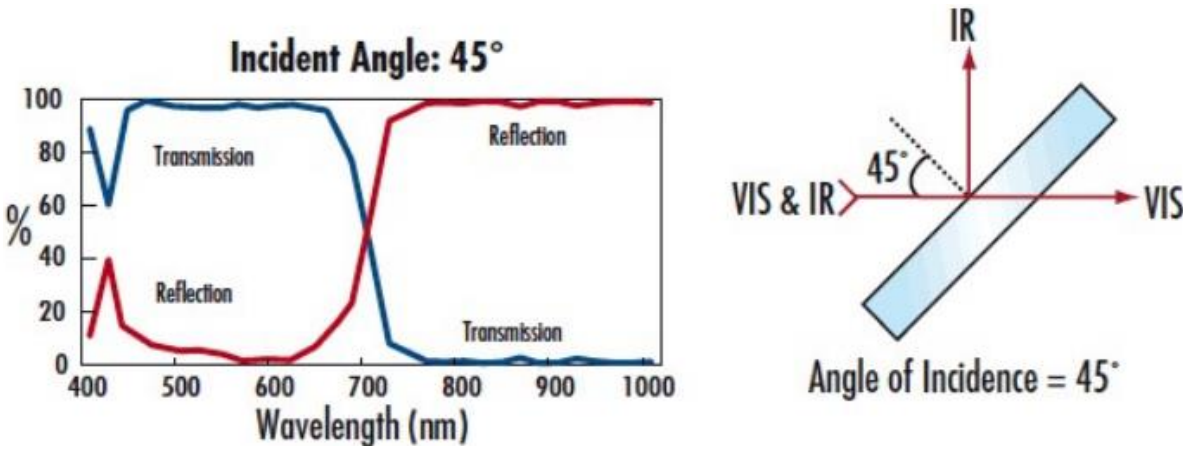

Figure 2.13 The transmission characteristics of the 45° hot mirror used to reduce the transmission of IR radiation.

Light intensity is the key factor in order to increase the frame rate which sometimes leading to the subject of examination such as droplet being affected because of the heat of the lighting. To prevent excessive heating of the droplet and surface a 45° hot mirror was used to reflect a portion of the IR radiation, with the transmission characteristics shown in Figure 2.13. This was combined with a focusing lens to reduce the amount of IR radiations reflected towards the impact surface and to maintain sufficient light intensity to facilitate the high speed imaging for maximum high frame rate. In this study, along of the maximum required frame rate,

magnification and the amount of excessive heat from the focused light at the impact area, the 250W AARI continuous white light source was selected at the most appropriate option.

For investigation of small droplets, high magnification photography was required. Additionally, the field of view should include the entire target surface. In order to magnify the field of view, it was required to couple the high speed camera with either long extension tube or specific types of camera lens known as zoom lens. However usually by using this type of lenses, the working distance between the camera and the object will be drastically reduced; therefor they are not appropriate for the case which carried out inside a closed chamber with limited access. Alternatively, long working distance microscope lenses can be used to increase the magnification and working distance (focal length). Here, two different types of long working distance lenses, i.e. an Infinity K2/distaMax long distance video microscopes and a Thorlab high magnification zoom lens were used. The maximum achievable magnification and working distance for Infinity and Thorlab objective lenses are 5.33x - 55 mm and 6.5x – 175mm respectively.

2.1.5. Alignment and Calibration

Arguably, the most important task during the experimentation is the alignment of the cameras and spatial and temporal calibration of the images. Any image that is largely out of the focus cannot be count on for further image processing, thus accurate measurement. Alignments of the cameras were achieved by focusing both cameras onto a microscopic glass calibration scale that was placed roughly at droplet impact point. As the position of the micro valve injector was fixed into the system, only the positions of the cameras could be altered. The cameras were moved via the xyz traverse systems and couple of test runs was conducted to ensure everything was in focus.

For scaling the images, a test target was recorded at the beginning of the measurement. This was done while the camera was fully adjusted with regards to the focus, exposure time and positioning of all optical components settings. In each setup, a microscopic glass calibration scale was used as calibration target, as the nominated size of the scale bar is 1mm with 100 divisions and 0.01 mm pitch size while the width of each printed line is 10 µm. The schematic and real images of the calibration scale is shown Figure 2.14a and b. The green line in Figure 2.14b marks the path along which the profile measurement was taken. Figure 2.14c illustrates the line profile of corresponding grey values. The final scale was calculated by the analogy of the pixel and real distance of the grey value 100 in pixel and real size between two successive bars.

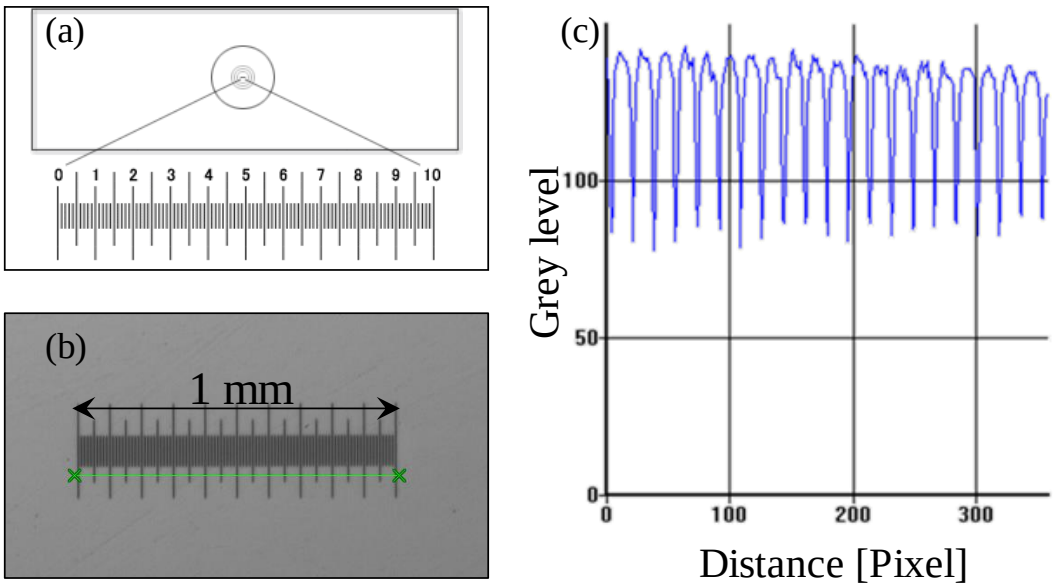

Figure 2.14 (a) Schematic of the calibration scale (b) real image of the calibration scale with the fully adjusted settings (c) grey scale line profile along the green line in (b).

The diameter of the surrounding circle in calibration scale was used to calibrate the scale itself. The nominal diameter of the circle is 4 mm. For the optical measurement, the image is prepared to facilitate the post processing. The diameter of the circle was measured again but optically via image processing tool (See section 2.3) with the preserved scaling. The recognized

boundary of the circle was taken as the optically measured diameter of the circle. The size of the circle was found to be 2% lower than the nominal value.

2.1.6. Determination of imaging parameters

Conducting any high speed/magnification imaging system requires several properties of the camera and lenses are integral in ensuring the phenomena is captured appropriately. These parameters include: (1) image resolution, (2) framing rate, (3) exposure time, (4) lens aperture and (5) lens magnification.

With regards to above considerations and the droplet pre-impact conditions such as velocity and diameter, the spatial and temporal resolution of the both test rigs were calculated and adjusted; they were adjusted based on the area that needs to be visualized and also the required imaging frequency which fully capture the deformation of droplet deformation process. Table 2.4 shows the imaging configuration of the test rigs of droplet impact on a heated flat and spherical surface.

Test rig \ Configuration	View angle	Microscopic lens	Spatial resolution [µm/Pixel]	Temporal resolution [kfps]	Exposure time [µs]	Resolution [Pixel]
Flat surface	Front	Infinity K2/distaMax	3.8	30	2.1	640x288
	Bird-eye	Thorlab zoom lens	5.6	30	4	256x256
Spherical surface	Front	Infinity K2/distaMax	4.1	80	0.25	512x424
	lateral	Thorlab zoom lens	4.9	40	3.2	384x320

Table 2.4: Imaging configuration for impact on flat and spherical surface experiment

2.2. Test liquid

Standard summer Diesel fuel was chosen as the test fluid in this experimental investigation. Diesel is a multicomponent fuel which is composed of approximately %75 saturated hydrocarbons and %25 aromatic hydrocarbons [178]. The chemical formula for standard Diesel is $C_{12}H_{23}$ [179]. Important properties of Diesel fuel are summarised in Table 2.5.

@ 0.1 MPa - 40° C	Density [kg/m^3]	Kinematic viscosity [mm^2/s]	Surface tension [mN/m]	Boiling point [°C]
Diesel	833	3.245	28.9	180-360

Table 2.5: Physical properties of standard summer Diesel fuel

Due to the heat transfer from heated wall surface to the droplet, the temperature and properties of the droplet, during the impact period are expected to change. Figure 2.15 depicts the temperature-dependent properties of the Diesel liquid for temperature in the range 0-400°C.

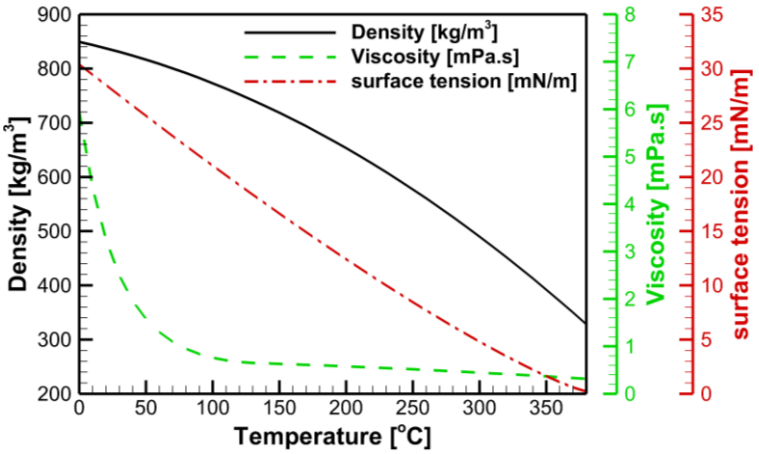

Figure 2.15 Temperature dependent properties of Diesel fuel [180]

2.3. Image analysis

Images from high speed cameras were stored into the internal memory of the cameras in RAW format and transferred to the computer hard drive by using a Gigabit Ethernet cable connection

afterwards. Post-processing of the images and extracting the quantitative measurement was carried out in MATLAB® environment. Each data set consists of a number of RAW files, and each file contains an image with specified resolution and 12-bit grey scale colour depth. An In-house MATLAB routine was applied to each frame of the data set; it detects the edges of the droplet, followed by obtaining the pre-impact parameters (D_0, V_0), spreading diameter (D(t), θ(t)) for each test condition. The results were plotted in the form of a series of graphs to compare the effects of important parameters on the droplet impact dynamic and outcome regimes. Different steps of the image processing strategy were integrated into a main MATLAB function which automatically opens, reads and processes every frame of each test condition. The final results were exported and saved into excel files for further analysis.

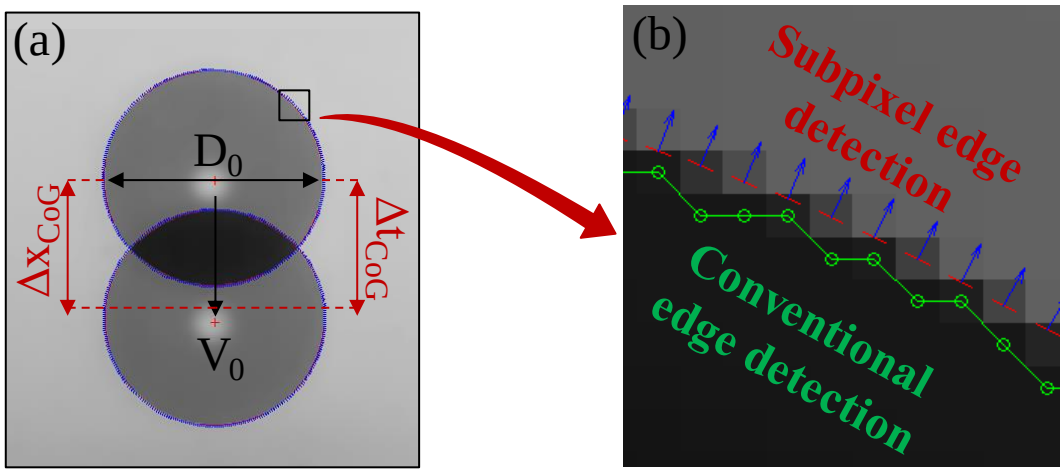

Figure 2.16 image processing procedure: (a) measurement of droplet pre-impact parameters (b) edge detection techniques

In order to measure the droplet diameter and velocity, two consecutive frames of droplet, prior to the impact, were chosen for each data set. Background subtraction and edge detection were applied to the raw images, as illustrated in Figure 2.16. Two edge detection techniques were compared and it was concluded that the subpixel edge detection is more accurate in order to detect the fine curvature of the droplet profile edge compared to the conventional canny edge detection. The subpixel edge detection routine was written based on a novel algorithm proposed

by the study of Trujillo et al. [181]. Their algorithm is based on the hypothesis of partial area effect in the acquisition process and it did not assume continuity in the intensity values of the pixels, instead it initially assumed that the edge can be approximated by straight lines in the neighbourhood of each pixel in the edge of the interest area, and then adopted to second order curves [181].

By implementing the sub-pixel edge detection algorithm, a series of points which define the shape of droplet, were extracted and thereby the droplet diameter at different directions were measured. The equivalent droplet diameter can be defined as [79]:

$$D_0=(D_v D_h^2)^{1/3} \tag{2.2}$$

Where D_v and D_h are the vertical and horizontal dimension, respectively, assuming the droplet is rotationally symmetric with respect to the vertical axis. The vertical and horizontal diameters differed by less than 1.5% for We=19 and 5% for We=490. The mean equivalent diameter in each test case was calculated with standard deviation of 2.5%.

As it can be seen in 2.3, the impact velocity was derived from the centroid values (Δx_{CoG}) in two consecutive images of the droplet and its corresponding time interval (Δt_{CoG}) which was obtained based on the high speed camera frame rate, immediately before impact.

$$V_0=\frac{\Delta x_{CoG}}{\Delta t_{CoG}} \tag{2.3}$$

The impact velocity was calculated with an accuracy of 0.07m/s at We=19 and 0.11m/s for We=490. The relative uncertainty in the calculated Weber number ranged from ±0.7 at We=19 and to ±8 at We=490.

Obtained results presented in either dimensional or non-dimensional manner. In general, the impact phenomena are governed by the initial droplet diameter (D_0), the impact velocity (V_0),

the surface tension (σ), the dynamic viscosity (μ) and the density (ρ), the spreading diameter (D(t)) and the time scale (t). As it can be seen in Table 2.6 these parameters can be grouped into the number of non-dimensional numbers.

Non-dimensional number	Name
$Re = \rho V_0 D_0 / \mu$	Reynolds number
$We = \rho V_0^2 D_0 / \sigma$	Weber number
$Oh = \sqrt{We} / Re$	Ohnesorge number
$\beta = D(t) / D_0$	Spreading factor
$t^* = t V_0 / D_0$	Non-dimensional time
$\theta(t)$	Apparent dynamic contact angle

Table 2.6: Non-dimensional numbers

The Weber and Reynolds number are the ratio between the inertial and capillary forces (kinetic and capillary energies, E_k/E_σ), and the ratio between the inertial and viscous forces (kinetic and viscous energies, E_k/E_μ), respectively. The spreading factor was also defined as the ratio between the droplet diameter during spreading and the initial droplet diameter D_0.

2.3.1. Impact on a flat surface

In case of impact on a flat surface, determination of the spreading diameter and the apparent dynamic contact angle were acquired from the image sequences after the impact. After the impact, the same routine as for Pre-impact condition was implemented to every frame to find the coordinates of each point at the spreading droplet edge. The concept of the algorithm can be perceived if Figure 2.17.

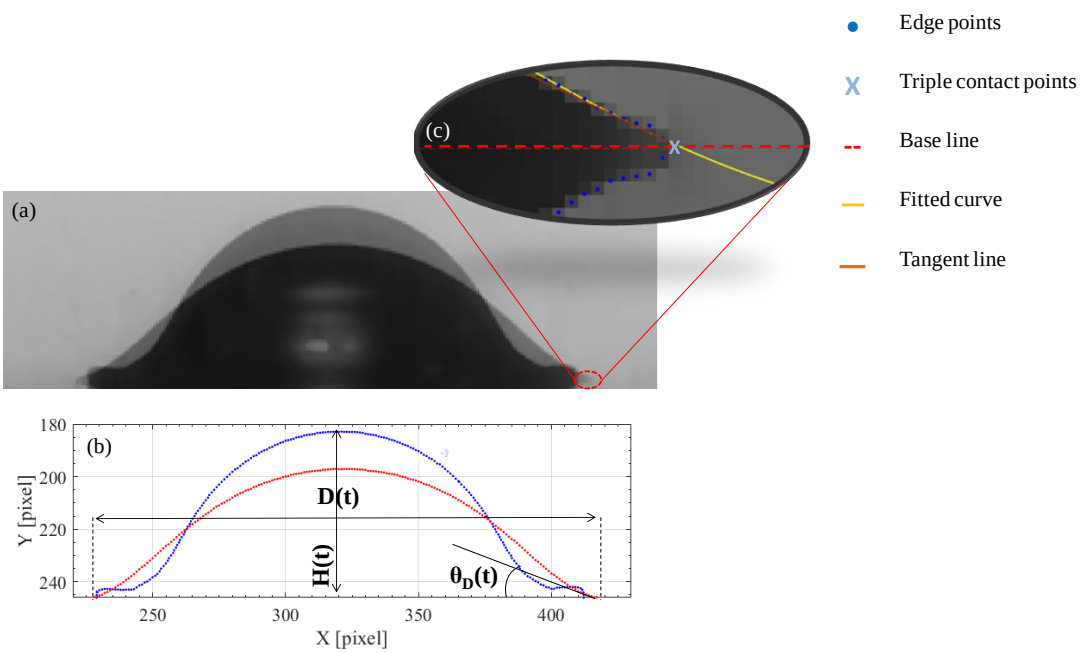

Figure 2.17 Image processing procedure (a) superimposed images of droplet at two consecutive images; (b) Extracted edge points; (c) droplet edge, triple contact point, base line and the fitted polynomial curve

Starting from the raw images shown in Figure 2.17a and using the edge detection algorithm reported in [181], the extraction of the droplet profile at two different time steps is obtained (Figure 2.17b). This method is based on the pixel intensity gradient, determining the position and orientation of the edge within each individual pixel. More specifically, initially, a threshold is specified by comparing the mean pixel intensity of the regions inside and outside of the droplet. The horizontal and vertical positions of the edge points are then registered in Cartesian coordinates. A cubic polynomial fitting curve is derived through the first 10 adjacent points on both the left and right corners near the triple contact point and at each time instant. The coefficients of determination (R^2) of the fitting curves were above 99% for all the test cases. Figure 2.17c, exemplifies the latter process, illustrating the extracted points of the droplet profile, triple contact points, base line and the fitting polynomial. The apparent dynamic contact angle $\theta_D(t)$ was measured from the tangent line drawn on the fitted polynomial at the triple contact point, with an accuracy of ±2°. To establish repeatability of the measurements, each test case was repeated up to 5 times; as the observed maximum variation was less than 2% in

dynamic contact angle and spreading factor, only the mean value of each parameter is reported here. The spreading diameter D(t) was computed as the distance between right and left triple contact points, with a maximum uncertainty of ±8μm; these values were then non-dimensionalised using the pre-impact droplet diameter D_0 and denoted as β (spreading factor). The standard deviation of measured spreading factor and non-dimensionless height in each case was less than 2.5%.

2.3.2. Impact on a particle surface

When a droplet impinges on a particle surface with the $D_0<D_{Particle}$, the momentum normal to the surface induces a tangential flow resulting in the lamella flow on surface in form of a curved disc which continues to grow until a maximum state was achieved. **Error! Reference source n ot found.** illustrates a schematic of this phenomenon with presenting the droplet state before the impact with a dotted circle in the direction of gravity (D_0, V_0) and after impact with a filled lamella indicating the droplet position at its maximum spreading (D_{max}) which spanned a half-spread angle (α) at the particle centre ($D_{Particle}$); this exemplifies the manner in which the spatial details of film spreading, thickness were obtained from the raw images at a specific time step.

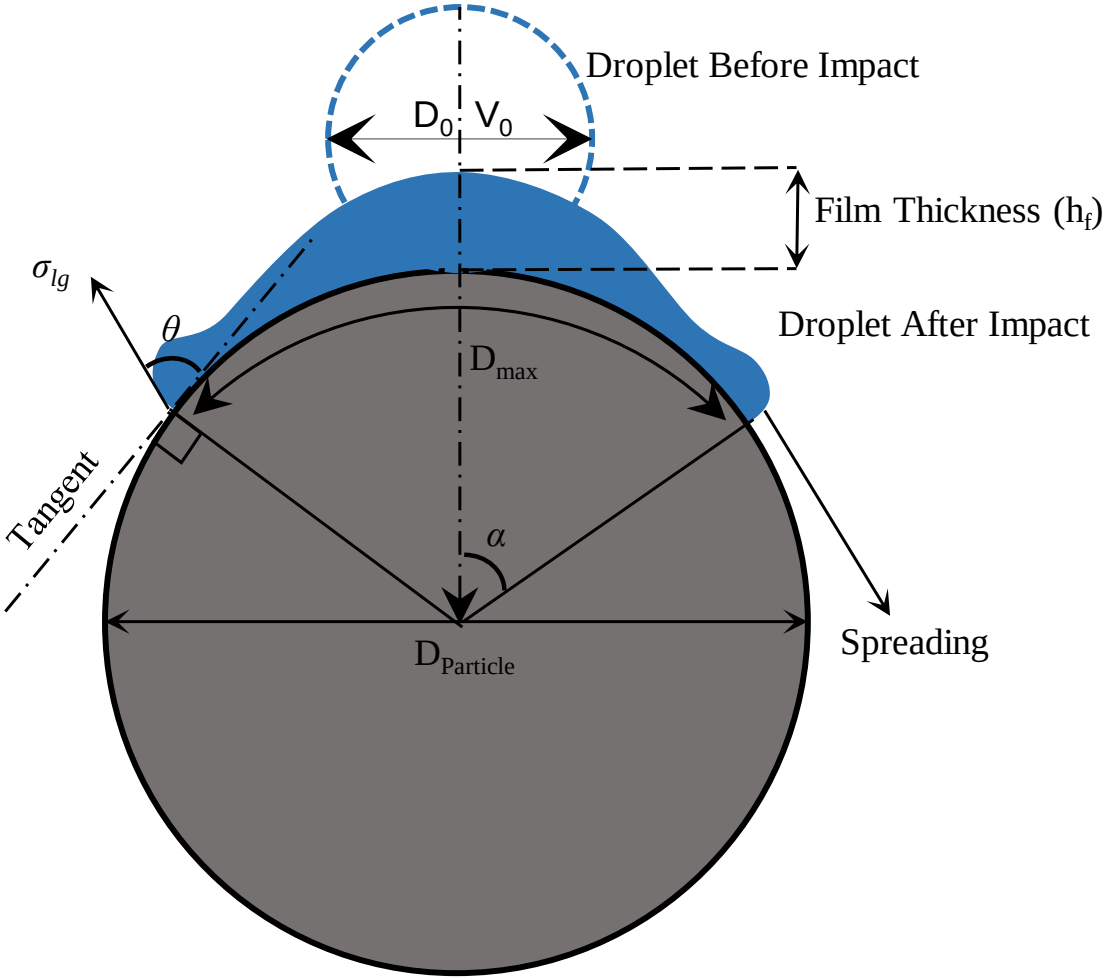

Figure 2.18: Schematic of droplet spreading on a spherical particle surface (D_0: droplet diameter, V_0: droplet velocity, $D_{Particle}$: particle diameter, Dmax: maximum spreading diameter, α: half-spread angle, θ: apparent dynamic contact angle, h_f: thickness of film, σ_{lg}: liquid–gas surface tension)

The same routine, implemented in section 2.3.1, was modified to analyse the acquired images of droplet impact on a particle surface. The pre-impact parameters (D_0, V_0) were measured with the same method explained for the flat surface. After impact, the image of the droplet lamella was isolated by subtracting the post-impingement image from the image of the particle surface alone prior to impact.

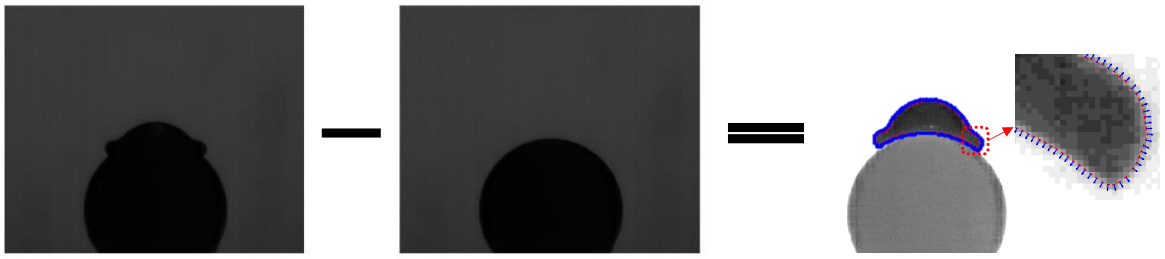

Figure 2.19 Extraction and demonstration of a flowing lamella on a particle surface by subtracting the post-impingement images from the pre-impingement image, followed by edge detection routine

As it can be seen in Figure 2.19, by subtraction of the raw image from the background image, the image of the liquid film on the particle surface can be obtained. Then from this image, the edge contour was extracted; A threshold was set by comparing the mean pixel intensity inside and outside the droplet and then the mid-plane liquid contour was estimated, using an edge detection algorithm as explained in [181]. A circle was then fitted to the particle periphery at the pre-impingement stage to calculate the diameter and centre of the particle target. In order to obtain the spatial variation of the droplet periphery shape, a spreading angle (α), generated by two vectors extended from particle centre to the left and right the triple contact points (**Error! Reference source not found.**), was initially defined as:

$$\alpha = \frac{1}{2}\cos^{-1}\frac{\overrightarrow{v_1}.\overrightarrow{v_2}}{\|\overrightarrow{v_1}.\overrightarrow{v_2}\|} \qquad \textit{Equation 2.4}$$

where, $\overrightarrow{v_1}$ and $\overrightarrow{v_2}$ are two extended vectors drawn from the particle centre to the left and the right droplet-particle intersections. This angle determines the angular position of the droplet edge profile on the particle surface. The spreading diameter was subsequently calculated, as the perimeter length spanning between the two droplet-particle intersection points, for the specified time steps, as :

$$D(t) = \alpha.D_{particle} \qquad \textit{Equation 2.5}$$

An indicative plot of the droplet lamella variation with spreading angle is presented in Figure 2.20.

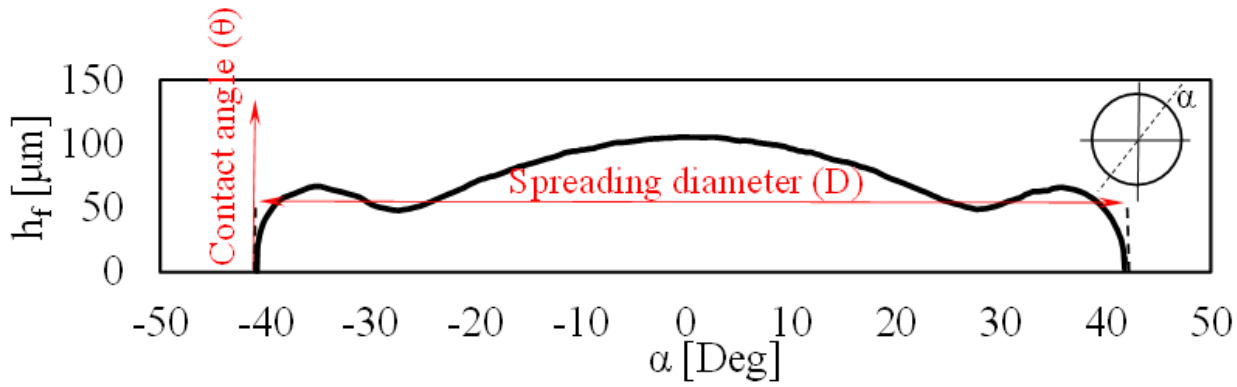

Figure 2.20 distribution of the film thickness on the particle surface as a function of the spreading angle α

This diameter and the film thickness at the north pole of the particle surface, non-dimensionalised by the pre-impact diameter D_0, constitute the spreading β factor and the non-dimensional film thickness h*, quantities suitable for the characterization of the droplet shape deformation. It should be noted that, In contrast to the impact on the flat surface, the spherical geometry of the particle surface provides the possibility to measure the film thickness of the liquid lamella after the droplet impact. In case of impact on the flat surface, this lamella was surrounded by a thick rim making it impossible to visualize it.

The contact angle was measured exactly at the intersection of the deformed droplet interface with the solid surface. The interface was approximated by a cubic polynomial and, subsequently, two vectors originating from the triple contact point and being tangent to the particle surface and the approximated interface, respectively, were drawn, so as to define the contact angle. The coefficients of determination (R2) of the fitted curves were above 99% for all test cases and the dynamic contact angle was computed with an accuracy of ±1.5°. The percentage of variation between 5 repetitions of each test case was less than 2%. Due to poor spatial resolution in the vicinity of the triple contact point for large weber numbers (extremely

thin lamella height), the contact angle measurement were carry out only for the range of low to intermediate Weber numbers.

2.4. Impact driven parameters

Based on the influential non-dimensional parameters (We, Oh), the study of [182] proposed a map which divides the driven mechanism of impact into four regimes; namely as: (I) inviscid/capillarity driven region, (II) viscous/capillarity driven region, (III) inviscid/impact driven region and, (IV) viscous/impact driven. These regions are marked in Figure 2.21. It is already known that the final shape of the droplet in all four regions can be determined, using the surface tension and dynamic contact angle. As it can be seen in Figure 2.21, on the basis of this categorization, current experimental data belong to region (III).

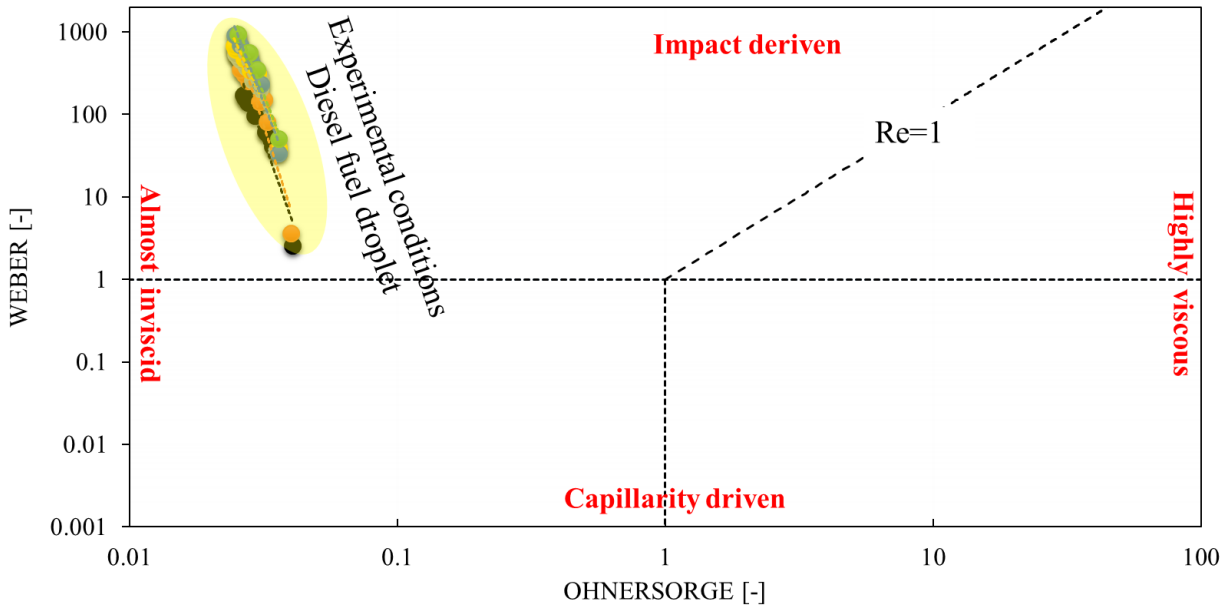

Figure 2.21: Impact regions map based on impact Weber and Ohnesorge number

The temporal evolution of the droplet impact and its spreading dynamic in the latter region can be divided into four stages as kinematic, spreading, relaxation and equilibrium stage. During the course of kinematic stage, the inertia is dominant; thus the droplet has a truncated spherical shape and the spreading factor increases according to a power law in time as shown in Equation 2.6.

$$\beta = 2.9\sqrt{t/\tau_{Kinematic}} \quad at\ 0 < \frac{t}{\tau_{Kinematic}} < 0.1 \qquad \text{Equation 2.6}$$

In the following spreading stage, the lamella forms from the base of the droplet and the dynamic pressure of the impact drives the spreading in competition with inertia. At the end of this stage, the maximum spreading diameter is reached, when the inertia is completely compensated by the viscous and surface tension forces. This value is predicted theoretically in many of the available studies, assuming the balance between the kinetic and surface energies of the droplet before and after impact; viscous dissipation term has been also added to the balance during spreading [30], [100]–[102], [109]. The maximum spreading diameter is mainly dependent to the impact Weber number, however, some of them used Reynolds, Ohnesorge and the dynamic contact angle as well. To capture the evolution of the energy spreading and the viscous force effect, it is required to assume a certain velocity profile throughout the spreading stage, which leads to a significant error for the calculated maximum spreading diameter. According to the comparisons with experimental data, these models predict the maximum spreading diameter relatively well for the intermediate impact Weber number (20<We<200).

It should be also noted that, the reproducibility of the data was guaranteed by repeating the each test condition for 5 times. In the relaxation stage, the droplet oscillation is damped out by viscous dissipation and the droplet usually recoils. The effect of surface tension force and the receding contact angle increases. Finally, the equilibrium stage follows, that spreading stops and the droplet takes the spherical cap shapes. Surface temperature can significantly changes the latter phenomenology by adding the effect boiling into the impact dynamic.

2.5. Experimental plan

In this section, the test plans and excremental procedures were introduced. It should be noted that the experiments were categorised based on the geometry of the impingement solid surface.

This research was focused on complex relationship of hydrodynamic and thermodynamic effects on the process of diesel fuel droplet impact onto a heated solid flat and spherical surface. In addition, in order to investigate the effect of the ambient pressure on droplet impingement phenomena, all the test cases for the flat surface were performed both in 1 and 2 bars chamber pressure. To simplify the problem and accomplish the purpose of the study, the test cases of each geometry were divided into the droplet spreading dynamic and mapping of the final outcome regimes [62].

It should be noted that, the reproducibility of the data was guaranteed by repeating the each test condition for 5 times.

2.5.1. Droplet impact on a flat surface

A heated aluminium surface, with temperature ranging from room temperature to Leidenfrost temperature, and standard summer Diesel fuel were used in this experimental study. Table 2.7 summaries the test conditions according to the droplet pre-impact diameter and velocity, influential non-dimensional numbers and the surface temperature. As it noted above, the chamber pressure was set to 1 and 2 bars for all test conditions.

Case No.	D_0 [µm]	V_0 [m/s]	We [-]	Re [-]	Oh [-]	T_W [°C]
1	320	1.4	20	141	0.031	
2	370	2.4	70	280	0.029	140 – 400°C
3	410	4	200	510	0.027	(varied in
4	440	5.2	360	710	0.027	10°C steps)
5	440	6.1	490	827	0.026	

Table 2.7: Table of conditions: Diesel fuel droplet impact on a heated aluminium surface

For a droplet impinging on a heated surface, after initial impact which obtains the final outcome regimes, the droplet boils and/or evaporates until the surface completely dries out. The initial impact can be referred to the period that droplet first touches the heated surface until the spreading diameter reaches a relative stable state. The impact conditions in this study were

chosen in order to characterise all possible hydrodynamic outcome regimes such as Stick, Rebound, Break up and splash. The impact Weber number was varied in the range of 20-500 while the droplet size was kept in the range of 320-440 μm. The first three cases were used to investigate the effects of impact Weber, surface temperature, and ambient pressure on spreading dynamic. These cases, in addition to the remaining cases, refer to the parametric studies of final droplet outcome regime.

On the other hand, with the specified range of surface temperatures, different types of boiling modes were observed including: nucleate, transition and film boiling. Due to broad range of boiling point of the Diesel fuel (180-360 °C); the surface temperature was varied from 140 to 400 °C in order to quantify the Leidenfrost regime.

2.5.2. Droplet impact on a heated particle surface

Droplet impact on a particle surface was also performed for a wide range of impact Weber number and particle surface temperature. The details of all cases examined in droplet-particle impact are presented in Table 2.8. Similar to the impact on flat surfaces, the test conditions were chosen in a way so a wide range of outcome regimes and boiling modes could be studied. The droplet to particle ratio (DTP) was kept constant at 0.4. The maximum achieved particle temperature was 340 °C; this temperature was adequate to shift the impact condition just above Leidenfrost regime.

Case No.	D_0 [µm]	V_0 [m/s]	We [-]	Re [-]	Oh [-]	T_P [°C]
1		1.6	30	210	0.0263	
2		2	50	267	0.0261	
3		2.4	70	309	0.0264	
4		3.2	120	423	0.0262	
5	400	3.8	160	523	0.0257	140 – 340°C (varied in 10°C steps)
6		4.5	250	590	0.0261	
7		5.9	420	781	0.0262	
8		6.8	530	900	0.0264	
9		8.6	850	1139	0.0263	

Table 2.8: Table of conditions: Diesel fuel droplet impact on a heated particle surface

2.6. Uncertainty analysis

The uncertainties of image processing are discussed in this section. In this study, all the parameters were determined based on MATLAB image processing. The uncertainty of the pixel resolution is discussed first, followed by the uncertainty estimation of image processing for each parameter.

The imaging pixel resolution of the optical setup is calculated by capturing an object with known width and measuring the width in pixels of the image as:

$$C = \frac{object\ size\ [m]}{image\ size\ [pixel]} = \frac{\Delta l}{\Delta p} = \frac{0.001\ m}{264} = 3.78\ \mu m/pixel \qquad \text{Equation 2.7}$$

And the uncertainty is calculated as below:

$$u_C = \sqrt{(\frac{\partial C}{\partial \Delta p} u_{\Delta p})^2 + (\frac{\partial C}{\partial \Delta l} u_{\Delta l})^2} \qquad \textit{Equation 2.8}$$

Where,

$$\frac{\partial C}{\partial \Delta p} = -\frac{\Delta l}{\Delta p^2} \;;\; \frac{\partial C}{\partial \Delta l} = \frac{1}{\Delta p}$$

Therefore,

$$u_C = \sqrt{(-\frac{\Delta l}{\Delta p^2} u_{\Delta p})^2 + (\frac{1}{\Delta p} u_{\Delta l})^2} = \pm 0.02 \qquad \textit{Equation 2.9}$$

In the current study, the pixel resolution is determined by capturing images of an optical grid, with the total length of 1mm and 0.1mm sub-division. The pixel resolution is calculated by capturing the images of this known lengths and analysing the images in MATLAB. These lengths were measured for several times for each of them and the mean value was used as the image line width. Therefore the uncertainty of the image line width is the standard deviation of the width measurement (±1 pixel). This gives the pixel resolution 3.78 ± 0.02μm/pixel using Equation 2.7 and Equation 2.9.

Depending on a direct or indirect measurement method, the parameters' uncertainty estimations are divided into three groups: length (droplet diameter, spreading diameter, and droplet height), velocity (impact velocity, spreading velocity), and contact angle.

The length measurement can be expressed by image distance in pixels multiplied by the pixel resolution, as in Equation 2.10. The uncertainty is determined by the standard deviation of the pixel distance measurement which is ±1 pixel and the uncertainty of pixel resolution, as discussed above. Maximum pixel distance 640pixels (the width of the image), the maximum uncertainty of length measurement, as Equation 2.11, is approximately ±12.5μm. The droplet

diameter, spreading diameter and height are much smaller than the image width, and the uncertainty of these are less; approximately ±8μm.

$$L_{Droplet} = \Delta p.C = 1540\ \mu m$$

Equation 2.10

$$u_L = \sqrt{(\frac{\partial L}{\partial \Delta p}u_{\Delta p})^2 + (\frac{\partial L}{\partial \Delta C}u_C)^2}$$

Equation 2.11

$$= \sqrt{(Cu_{\Delta p})^2 + (\Delta p u_C)^2} = \pm 8\mu m$$

Similarly, the velocity is expressed by length and time interval, as in Equation 2.12. It is determined by the uncertainties of length, time, and pixel resolution.

$$V = \frac{\Delta p.C}{\Delta t} = 6.18 m/s$$

Equation 2.12

$$u_V = \sqrt{(\frac{\partial V}{\partial \Delta p}u_{\Delta p})^2 + (\frac{\partial V}{\partial \Delta C}u_C)^2 + (\frac{\partial V}{\partial \Delta t}u_{\Delta t})^2}$$

Equation 2.13

$$= \sqrt{(\frac{C}{\Delta t}u_{\Delta p})^2 + (\frac{\Delta p}{\Delta t}u_C)^2 + (\frac{\Delta p.C}{\Delta t^2}u_{\Delta t})^2} = \pm 0.11 m/s$$

The time interval between frames is 33.33μs (this is frame rate 1/30000) with ±0.27μs uncertainty (this is calculated as the associated time of the displacement uncertainty). For an impact velocity 6.18m/s, the uncertainty is ±0.11m/s. The spreading velocity is much smaller than impact velocity and the uncertainty is less than ±0.07m/s.

The contact angle is obtained by curve fitting the drop edge profile at the near contact line region (first 10 points) and then calculating the tangential line where the drop contacts with the surface at the triple contact point. A 3th order polynomial curve fit was used in the analysis. The criteria for a good fit are the coefficient of determination and residual. The coefficient of

determination (R^2) is the statistic of curve fitting, describes how well the curve fitting is; R=1 is perfect fit. The residual is the difference between the data and fit: Residual= (data)-(fit).

The mean residual in this analysis is on the order of 0.35 pixels. The criteria were set that for R^2 greater than 99%, the curve fit power law that gives the minimum residual was chosen for contact angle calculation. The contact angle is the tangential line of the fitting curve at the surface and is expressed as below:

$$\theta = ArcTan\left|\frac{m_t - m_b}{1 + m_t m_b}\right| \qquad \textit{Equation 2.14}$$

Where m_t and m_b are the tangent lines of droplet profile and base line shown in Figure 2.22.

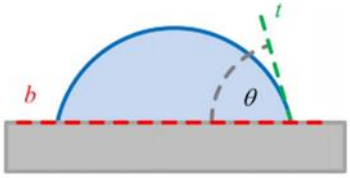

Figure 2.22: the tangent lines of the droplet and the surface

Assuming the uncertainties of the this tangent lines are,

$$u_t = \frac{\delta m_t}{m_t} \qquad \textit{Equation 2.15}$$

$$u_b = \frac{\delta m_b}{m_b} \qquad \textit{Equation 2.16}$$

Therefore the uncertainty in contact angle is:

$$u_\theta = \sqrt{(\frac{\partial \theta}{\partial m_t} u_{m_t})^2 + (\frac{\partial \theta}{\partial m_b} u_{m_b})^2} \qquad \textit{Equation 2.17}$$

By mixing the Equation 2.14 and Equation 2.17 and Equation 9 and assuming that $\delta m = \delta m_t = \delta m_b$, $|m_t| = Tan\theta$ and $u = u_t = u_b = (\delta m / m_t)$, Equation 2.17 simplifies to:

$$u_\theta = Tan\theta * \sqrt{1 + \cos^4 \theta} * u \qquad \textit{Equation 2.18}$$

Equation 2.18 is suitable to calculate the uncertainty for the angles below 80° and above 100° [183]. The value of the u can be assumed as the mean residual of the fitting which is lower than 0.35 in all cases. The maximum uncertainty calculated in current study is ±2°.

3. Droplet impingement on a flat surface

In this section, subcooled Diesel fuel droplet impact on a highly thermally conductive flat surface was investigated experimentally. Specifically the effect of impact Weber number and surface temperature on the post-impact outcome of the droplet was categorized and mapped on a We-T diagram for chamber pressure of 1 and 2 bars. In addition, the droplet shape temporal evolution and surface wetting characteristics during the early stages of the spreading was quantified in order to study the effect of heat gradients at the solid-liquid interface, the inertial force and the gas density on the spreading dynamic and the apparent dynamic contact angle. The latter parameters play paramount role in the heat transfer (mode of boiling) and consequently the post impact outcome. Maximum droplet spreading factor was measured and compared with available correlations in the literature. The rebound velocity of the satellite droplets in the breakup regime for surface temperature above Leidenfrost point was also measured. Finally, the effect surface temperature and impact Weber number on the size and life time of the entrapped central bubble at the impact time was measured investigated.

The use of a Computational Fluid Dynamics model, as developed recently by another PhD student in City University of London [184], [185] has been also employed in order to assist in the interpretation of the recorded images. This model has been validated for numerous cases of droplet impingement onto flat and spherical surfaces, with and without heat transfer. The CFD model solves the Navier-Stokes equations for mass and momentum conservation, while it employs the VOF methodology to capture the liquid-gas interface. The energy equation coupled with a species transport equation for the vapour and a local evaporation model are utilized to simulate phase change [184]. The evaporation rate is based on the kinetic theory of gases, where the driving force is the difference between the saturation conditions at the interface and the conditions on the vapour side. This model has been validated in [184] for

single droplet evaporation and impingement for an n-heptane droplet. In this work it is utilized for the simulation of Diesel drop evaporation, and validated against the experimental data of [186], [187] for Diesel. A dynamic local grid refinement technique was used to keep the computational cost at affordable levels [188]. An axisymmetric domain, along with a dynamic grid refinement technique in the liquid-gas interface, has been employed. The numerical model is used to predict the spreading dynamics for stick and breakup regimes. To capture rebound, the grid should be massively refined next to the wall surface [189] in order to resolve the thin vapour layer formed. The boundary conditions include symmetry (axisymmetric domain), pressure outlet in the open (free stream) boundaries and no-slip wall condition. A constant temperature value was applied at the wall boundary. The base grid initial grid consists of 50x50 rectangular cells. After the application of three levels of local refinement, the droplet radius was resolved by 40 grid cells. By increasing the levels of refinement 3 or above, the numerical predictions converge to a similar distribution for the temporal evolution of the spreading factor β. Further detail of employed domain used in the current study can be found in [185]. In addition, dynamic grid refinement technique was used at the liquid-gas interface at the time instant of maximum spreading. The dynamic contact angle model of Kistler was used, as implemented in [188], using the equilibrium contact angle value of 23 degrees as taken from the experiments, where it was measured at the end of relaxation phase under room temperature conditions. Although the direct imposition of the dynamic contact angle temporal evolution taken from experiments can be applied, it is not used in numerical approach, as the basic aim of the simulations is to exhibit the effect of surface temperature on the impingement dynamics. The change in liquid properties as the temperature increases, affects the contact angle variation, especially during the droplet recoiling phase, as it is shown in the following section; direct imposition of the measured contact angle variation would prevent the prediction of this behaviour. The data of the temperature dependent properties of the Diesel liquid for a

temperature range of 0-180°C i.e. up to its boiling point at 1bar pressure has were extracted from Figure 2.15. Finally, preliminary simulations have revealed that the total mass evaporated throughout the process is lower than 4% of the initial droplet mass; thus, vaporisation can be neglected for the short period during the droplet impact and spreading.

3.1. Classification of post-impact regimes

In general, under the operating conditions defined in Table 2.7 essentially six different macroscopic outcome regimes can have been identified, termed as: stick, splash, rebound, partial-rebound, breakup and breakup-rebound as illustrated in Figure 3.1. The droplet impact process and outcome regime depends on Weber number as well as the target surface temperature.

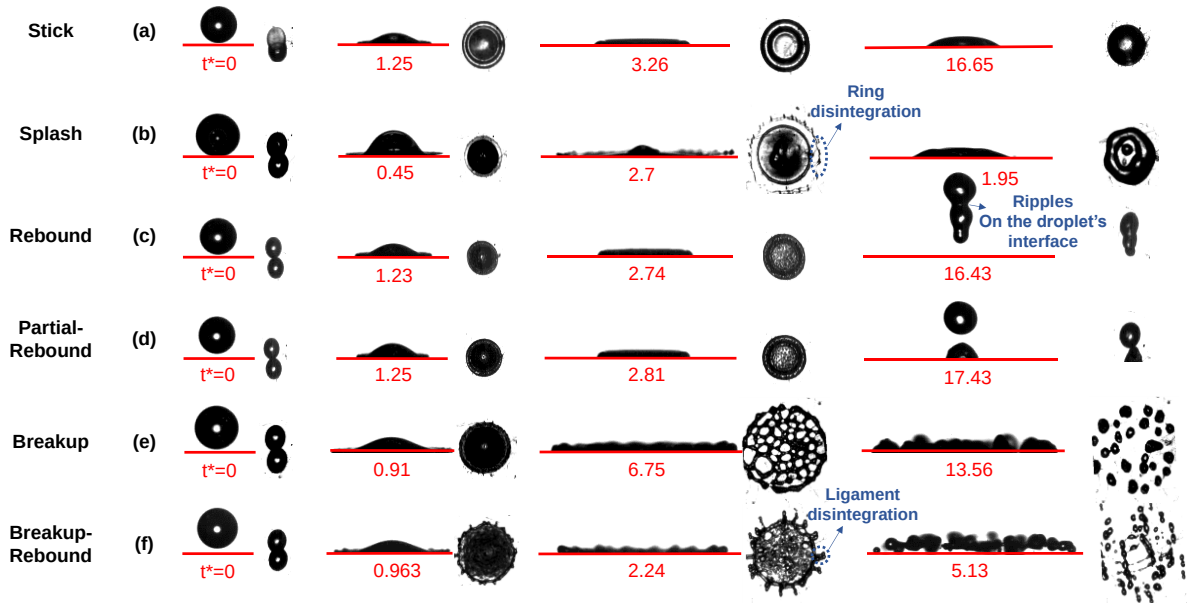

Figure 3.1: Temporal evolution of Diesel fuel droplet during impact on the heated flat aluminium surface for different values of Weber number and wall temperature; (a) stick regime at We=65, T_W=170°C; (b) splash regime at We=490, T_W=180°C; (c) rebound regime at We=65, T_W=350°C; (d) partial rebound regime at We=65, T_W=340°C; (e) breakup at We=490, T_W=340°C; (f) breakup-rebound regime at We=202, T_W=370°C

In the "stick" regime (Figure 3.1a), the entire mass of the droplet is deposited on the wall surface upon impact (t*=1.25) and spread (t*=3.26) and finally relaxed on the surface (t*=16.55). The initial kinetic energy of the droplet is completely lost in viscous dissipation

during this spreading. This regime occurs for Weber numbers below the splash threshold and/or when the heat transfer is not enough to induce breakup or rebound. In general, increased heat transfer induces local boiling within the bulk of the liquid, which is identified as one of the droplet disintegration mechanisms [134]. “Splash” (Figure 3.1b) occurs when We is high enough so the droplet becomes unstable (t*=0.45), deforms and smaller droplets are formed after the disintegration of the moving edge of the spreading lamella (t*=2.7); however, the rest of the droplet stays on the surface. Two different types of disintegration patterns were observed, namely in the form of liquid ligaments (Figure 3.1f at t*=2.24) and rings (Figure 3.1b at t*=2.7), were observed, resulting in different splash regimes. The first one is ought to instabilities developing on the liquid film forming radially outwards. The forming ligaments grow in length, their shape becomes unstable and eventually breaks up to smaller droplets. The second one is attributed to instabilities developing in the circumferential direction; as the lamella diameter increases, its thickness reduces until the formed ring at the edge of the lamella detaches and continues to expand until breaking up, eventually into smaller droplets. Similar mechanisms have been reported in [147] for both a heavy multi-component and a single component hydrocarbon fuel. In the “rebound” regime (Figure 3.1c), the droplet impacts onto the surface (t*=0), spreads (t*=1.23), recoils (t*=2.74) and finally rebounds (t*=16.43) from the surface. A vapour cushion forms between the droplet and the heated surface (t*=1.23). In this regime there is almost no direct contact between the wall surface and the liquid droplet [58]. In the partial rebound regime (Figure 3.1d), capillary waves are generated in the form of ripples on the droplet’s interface [50] due to the difference of the initial apparent (near to 180°) and the static contact angle; these propagate along the liquid surface, causing the droplet to pinch off. A part of the droplet stays on the surface and the other part rebounds (t*=17.43). If the impact energy is high enough to generate a strong perturbation, then the droplet breaks into

several smaller droplets (Figure 3.1e-f); these smaller droplets either stay in contact with the surface (breakup-stick) or rebound from it (breakup-rebound).

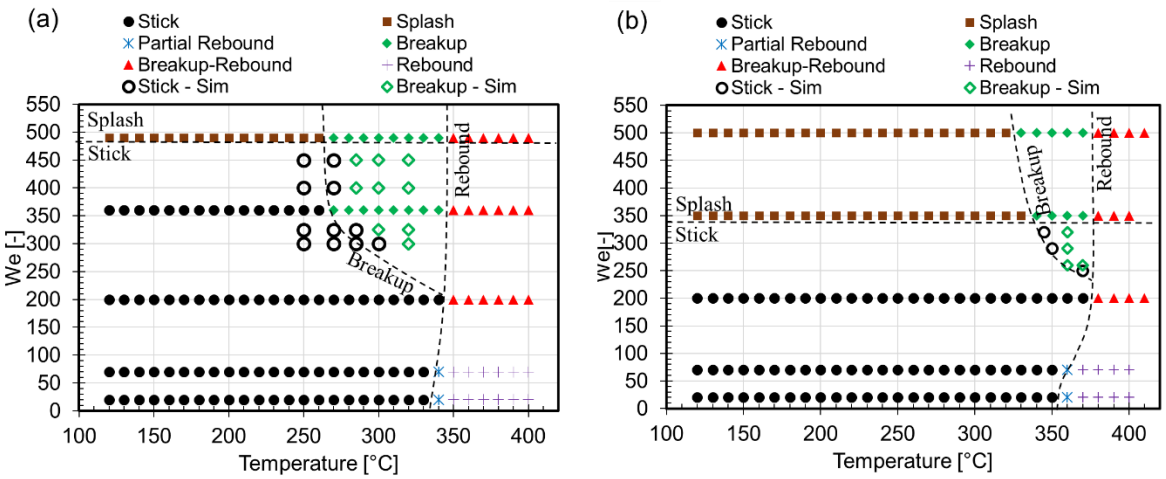

Figure 3.2: We-T regime diagram of Diesel fuel droplet impact on a heated aluminium surface at (a) P=1bar and (b) P=2bar. Empty markers show numerical results of the transition area of breakup regime have been added.

The various post-impact outcomes as identified above have been plotted on the Weber number and wall-surface temperature diagram and shown on Figure 3.2 for the two different air pressures tested. The transition boundaries (dashed lines) show where a change in the droplet impingement behaviour has been observed. It should be noted that the transition lines between neighbouring regimes were not clearly determined due to the experimental uncertainties affecting the actual We-T threshold.

At 1 bar air pressure, for temperature below the Leidenfrost point (T_L) and relatively low Weber numbers, the droplet spreads laterally over the surface up to a certain diameter (maximum spreading factor) while it stays in contact with the heated surface. Then it recoils until it relaxes into a spherical cap shape, which can be described by its geometry parameters (apparent dynamic contact angle, spreading factor). The splash regime was observed for We>490. With regards to the droplet levitation/rebound (Figure 3.1c at t*=16.43), T_L was observed around 340°C for low Weber number and increased about 10°C for We>65; this shows the dependency of the Leidenfrost regime to the impact Weber number. The breakup regime was observed for

We>350 and 270°C<T_W<T_L, however the minimum temperature of breakup regime decreases 10°C for larger Weber number. In this regime, the droplet breaks up during the retraction phase (Figure 3.1e at t*=6.75). High impact Weber number results in larger surface contact area and therefore a thinner liquid film spreads over the surface; this increases the overall heat transfer to the droplet mass, and reduces the surface tension ability to retrain the droplet shape. Thus, the liquid film ruptures and hence the droplet breaks up into smaller droplets (Figure 3.1e). For wall surface temperature above the Leidenfrost point, these smaller droplets rebound from the surface after breakup (breakup-rebound regime). The minimum surface temperature required for this regime to occur is constant over the entire range of Weber numbers. The extension of transition lines, coinciding at the point of (We=202, T_W=350°C), separates the stick, breakup and rebound regimes. The same We–T set points were also examined at chamber pressure of 2 bars (Figure 3.1b). Similar outcomes as in the 1 bar air pressure case were observed although the position of the transition lines was shifted towards higher surface temperatures and lower Weber numbers. As it is expected, the breakup and rebound regimes occur at higher temperature for increased air pressure. This can be attributed to higher Diesel components saturation point at elevated air pressure. In essence, higher wall-surface temperature is required for liquid to vaporize and the vapour layer, characteristic of the Leidenfrost point, to occur. The Leidenfrost temperature of rebound and breakup-rebound regimes were increased by 20°C and 30°C, respectively, compared to the low-pressure (1 bar) case. The transition line of breakup regime was shifted by nearly 70°C. It is already well established by experimental studies [35] that the gas flow in the vicinity of the moving edge is crucial on the splash behaviour, since increasing the air pressure and, thus, density has been found to enhance the splashing behaviour. Therefore, the splash transition line, which is independent of the surface temperature, was shifted from We=490 to We=350 by increasing the ambient air pressure from 1 to 2 bars.

CFD simulations were utilised to predict the transition line for both 1 and 2 bar conditions, as shown in Figures 6a and b, respectively. For low We numbers (200-350), the dominant mechanism that induces breakup is evaporation. As the solid surface temperature increases, evaporation intensifies and gradually results in breakup. For the range of surface temperatures simulated (250-325°C), the average droplet temperature at maximum spreading reaches around 55-65°C while at t*=10, rises up to 95-125°C; this shows that the rate of droplet heating increases for higher surface temperatures. At that moment, the droplet has lost a small portion (0.2-0.5%) of its initial mass. This might not seem as a significant amount; however, as the droplet heating rate increases, evaporation becomes more intense and this affects the post-impact regime, which changes from stick to breakup. At 2 bar air pressure, the breakup regime is limited to a small area and an average droplet temperature of approximately 135°C at t*=10 are reached for all cases.

For higher We numbers (>350), the impact kinetic energy becomes more dominant, as the transition line is almost vertical in respect to surface temperature. Droplet temperature at t*=10 is similar compared to the low We number cases (100-130°C), as well as the liquid mass evaporated (0.15-0.5%). The trend for the transition from stick to breakup mode, as predicted from CFD, is similar to the experimental one; the differences seen between experiments and predictions have been primarily attributed to the Diesel properties utilised and more specifically to the vapour pressure and fuel composition. As Diesel has been approximated as a single component fluids, its vaporisation process is inevitable different from the real Diesel fuel.

Hydrocarbon fuel mixtures, such as Diesel, are homogeneous as long as the temperature remains below the boiling temperature of the individual components. Therefore, it can be expected that a multicomponent fuel droplet, impacting on a heated surface may behave differently from a single component fluid at surface temperatures higher than some of the

components' boiling temperatures. On the other hand, classification of the post impact outcome on heated surfaces has been reported in the literature only on single component liquids; thus, the existing regime maps and transition criteria available so far are not applicable for Diesel, which comprises of more than 300 components covering light to heavy hydrocarbon molecules. In order to explore the differences in the impact outcome of the multi- and single component fluids, new experimental data for the Leidenfrost temperature, breakup, and splash have been compared to those previously reported in the literature.

In general, significant discrepancies exist in the literature with regards to the quantification of the transition between the post-impact regimes. Figure 3.3 shows the transition to the Leidenfrost temperature (based on the data extracted from the regime map depicted in Figure 3.2) as a function of impact Weber number. The Leidenfrost-temperature values of the current study are compared against those derived by the experiments carried out by [49], [50], [53], [54], [132], [169], [190] and are normalised by the respective liquid's saturation temperature ($T^*=T_W/T_{BP}$) for the pressure of 1atm (temperatures values in °C); T^* can be denoted as the degree of wall superheat. It should be noted that, as reported in [180], the so-called average boiling temperature of Diesel fuel at atmospheric pressure can be assumed to be 280°C. In general, the larger the Weber number, the higher the wall-surface temperature required to initiate the rebounding behaviour and consequently the T_L increases [96], [190]. It can be explained by comparing the inertial pressure of the drop which is proportional to We (built up in the liquid-solid interface by the impact kinetic energy) and vapour pressure which is proportional to surface temperature. For instance, considering water, several different values, ranging from 150 to 310°C, for Leidenfrost temperature have been reported in the literature [191]–[194]. The discrepancies in the reported values arise from the differences in size of the liquid mass, method of mass deposition (impact velocity), amount of liquid sub-cooling, surface roughness, initial droplet diameter, solid thermal properties, ambient pressure,

impurities and the degree of wall cooling under the droplet due to heat transfer. When the droplet impacts the hot surface, the surface temperature falls once a little owing to direct contact on the solid/ liquid interface and then rises again owing to the thermal conduction from the inner side of the solid material to the surface. At the same time, the temperature at the bottom of liquid droplet reaches the boiling point and a vapour film is formed on the solid/liquid interface. It may be natural to consider that the recovering rate of the initial surface temperature after the impact depends upon the thermal diffusivity and conductivity of the surface material. The larger value of the thermal diffusivity and conductivity reduce the time of heat recovery at the impact point, promoting the vapour film generation; it increases the rate of heat transfer from hot side to cold side of the material. This leads to isolating the liquid droplet from the solid surface through the vapour film faster [119]. The parameter β ($=1/k\rho c_p$) has been observed to be important in drop impingement for large Weber number values [192]. As the value of β decreases, the surface shows the best approximation of an isothermal surface and consequently the lowest value of the T_L. This can explain the higher required wall superheat ratios for transition to Leidenfrost in case of sapphire and silicon plates compared to aluminium plate. In addition temperature dependence contact angle is believed to be an influential parameters to control the stability of the vapour layer so the Leidenfrost temperature [195]. As the contact angle decreases, the wetted area of spreading diameter increases and larger area for heat transfer becomes available; the heat flux increases at the impact moment, so the required temperature of stable vapour layer decreases. In the present investigation, the high wettability nature of the Diesel liquid on aluminium plate, explains the lower wall superheat ratio of Leidenfrost transition. The Leidenfrost point, thus, is not a unique property of the fluid and the nature of the surface must be considered when estimating the critical temperatures such as Leidenfrost point. The heat transfer coefficient can be altered by an order of magnitude simply

by changing the properties of the surface so as to increase or decrease the Leidenfrost temperature.

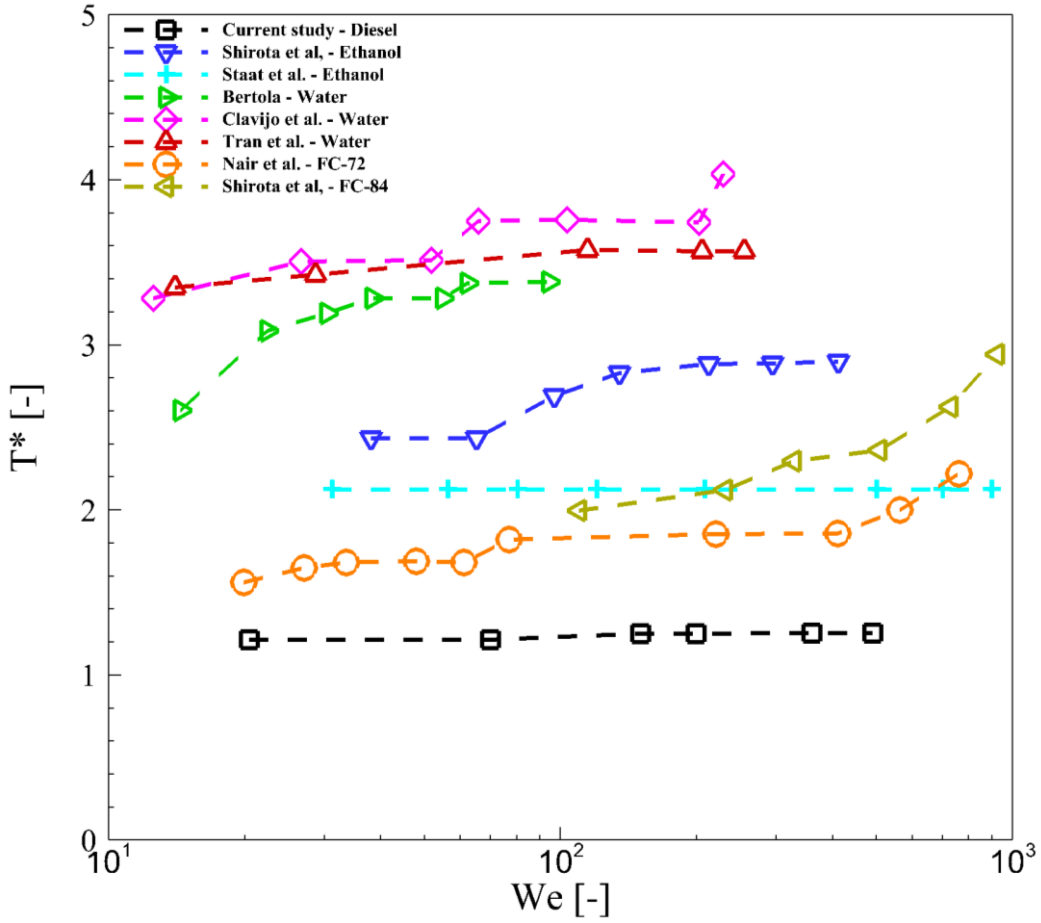

Figure 3.3: Transition temperature to the Leidenfrost temperature (T_L) as a function of We. The first data set is for the current study, followed by data representing Leidenfrost temperature values of ethanol impacting on a heated polished silicon [49] *and a sapphire glass plate* [50], *respectively. The third data set is from* [53] *and illustrates the experimental results of a water droplet impact on a heated polished aluminium surface. The next two data sets represent the impingement of a water droplet on a heated, polished silicon wafer as reported by* [132], [190]. *Finally, the last two data sets are for impact of FC-72* [169] *and FC-84 droplets* [50] *on a heated, sapphire glass plate.*

The breakup regime was not observed as a post-impact regime in the most of the studies where silicon and sapphire were used as impact surfaces due to their very low surface roughness. In order such a regime to arise, the inertial forces required to overcome the capillary pressure should be increased to values possibly outside the range of Weber and Reynolds numbers examined in the respective studies e.g. in [48], [50], [190]. Additionally, the high wettability of silicon and sapphire plates, as well as the low distribution of vapour-nucleation sites (e.g.

cracks and crevices, roughness elements) compared to a polished aluminium surface, prevent the creation of disruptive vapour bubbles that initiate the boiling-induced disintegration of the droplet [53]. This behaviour is in contrast with past studies where breakup has been observed with relatively lower Weber and surface temperature values. For instance, refer to [96], [131] discussing droplet collision onto heated metal surfaces. Figure 3.4 depicts in a comparative manner the required minimum surface temperature to initiate a droplet breakup as a function of impact Weber number, for different liquids and impact surfaces. Similar to Figure 3.3, the wall-surface temperature values were normalised by the respective liquid's boiling temperature (temperatures values are in °C). The coupled effects of heat transfer to droplet (driven by the heated surface) and impinging momentum (driven by the droplet's impact velocity) induces the breakup occurrence, overcoming the droplet surface tension forces which act to inhibit the breakup. As it can be seen, and also noted in [196], low Weber-number cases, where there is not sufficient impact energy, require higher surface temperatures in order to compensate and initiate breakup, until a certain critical value of the Weber number is reached. Beyond this value, the surface temperature required for breakup obtains a minimum value and stays roughly constant, for the We values examined. Similar behaviour has been seen in [195], where the breakup probability of a n-decane droplet impinging on a heated substrate was independent from the wall surface temperature for $T_W > 300°C$. As can be seen in Figure 3.4, the minimum wall-surface superheat ratio of breakup, for the cases of water are qualitatively similar, with some variations arising from their different impacting surface properties. The lower wall superheat ratio values in the case of water droplet impact on a silicon plate obtained by [52] compared to the respective for impact on aluminium plate are not that clear to interpret. The lower thermal conductivity which subsequently alter the local wall cooling and surface roughness of silicon plate should increase the required surface temperature and Weber number for breakup mode compared to aluminium.

However, it should be noted that the surface temperature measurement in [53] has been corrected for the difference between the substrate holder and the substrate itself; a correction that lead to increased values of the surface temperature. Lower set points of (T*, We) are related to the Diesel fuel, most probably due to the fuel composition and the surface properties. Even having the similar impacting surface, the breakup behaviour can be significantly different as the fuel composition changes, which is evident from the breakup behaviour of different mixtures of decane and hexane [149].

For breakup above the Leidenfrost point, the liquid droplet floating on the vapour film cannot uniformly spread/recoil in the radial direction. As a result, the ring structure of liquid droplet is cut off by twisting/shearing at or above a certain value of the Weber number. That is to say, the larger thermal conductivity of the surface material results in lowering the critical Weber number. It can be concluded that the heat transmission from the heated surface to the droplet bottom is more remarkable, the droplet tends to be unstable on the vapour film and break up. Therefore, the critical Weber number lowers [119].

The latter discrepancies seen in the data, explains the complex coupled effect of various parameters, especially the surface properties and liquid compositions and its component volatilities.

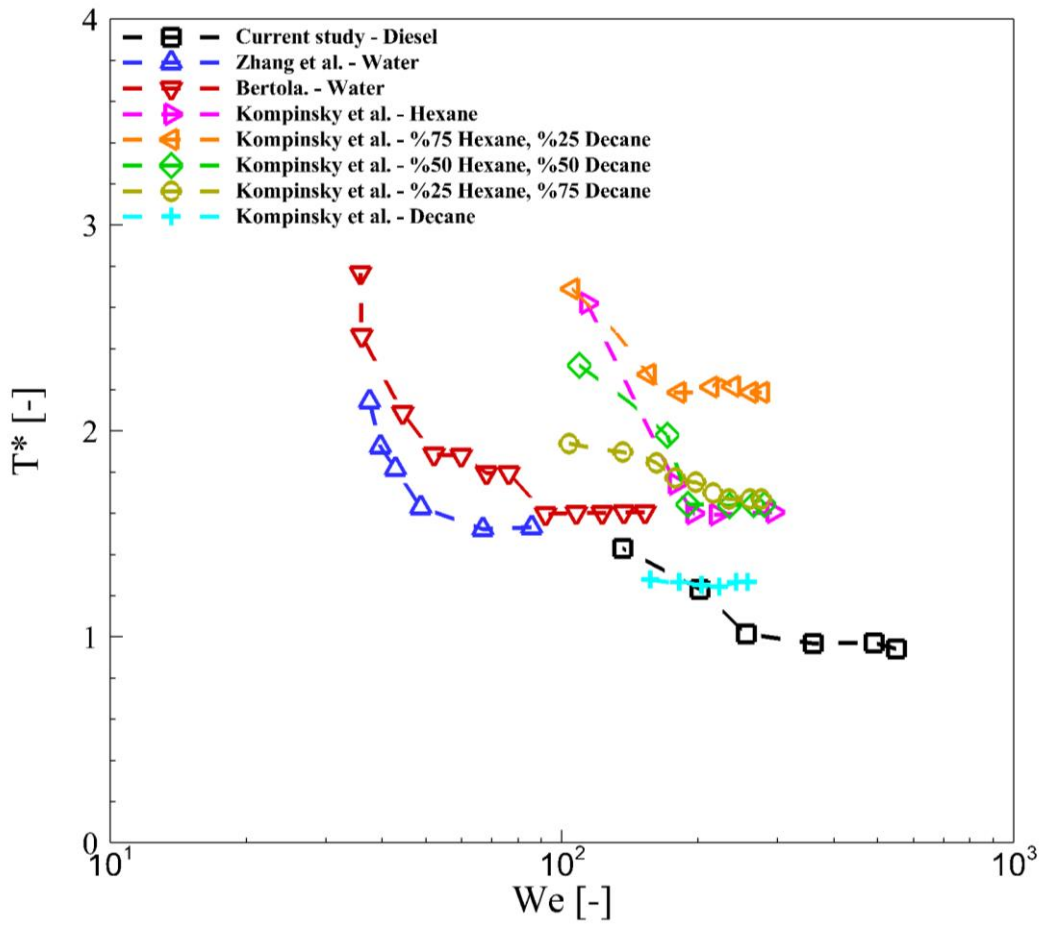

Figure 3.4: Critical surface temperature for droplet breakup as a function of Weber number. the first data set corresponds to the current study, followed by data obtained for the break up transition of a water droplet colliding on a heated silicon wafer [52] *and an aluminium plate* [53]. *The additional data sets are from* [149] *and represent the breakup transition of droplets comprising different n-hexane/n-decane mixtures colliding on a heated copper plate.*

The threshold of splashing on a smooth, flat aluminium surface has been examined under a wide impact Weber range under chamber pressure of 1 and 2 bars. Increasing impact Weber number increases the magnitude of splashing, confirming the results of previous studies. Previously, The effect of air pressure on splashing, first studied [36] has been verified to extend into super-atmospheric conditions [35]. They have derived a new semi-empirical splash threshold correlation based on the experimental data for a wide range impact conditions, considering the internal pressure generation during droplet impact and the opposing, retentive surface tension [35], as below:

$$2.84(Ca_a)^{0.54}(\frac{P}{P_0})^{0.42}=1$$ Equation 3.1

The occurrence of splashing is more attributable to the relative velocity between the spreading droplet and the surrounding gas. Thus, the air motion initiated by the impacting droplet cannot be neglected. Table 3.1 show the calculated splash threshold of the Diesel droplet onto the aluminium surface using the latter correlation against the current experimental data. It can be observed that the experimental and semi-empirical results are in good agreement and splash threshold can be well predicted by the model. It should be noted that in order to capture the splash limit experimentally, Weber number slowly increased, up to the point that the splashing observed. Only some selective points have been added to the graph.

	P= 1 bar	P=2 bar
Correlation from [35]	We=479	We=357
Current experimental data	We=490	We=360

Table 3.1: Comparison of the splash threshold between current experimental data and semi-empirical correlation from [35]

Regarding the numerical simulation of the splashing regime, this is an ongoing research subject. Only two numerical efforts have been performed up to now in order to successfully simulate this phenomenon in 3D domains [197], [198]; splashing is captured using either an initial perturbation in the velocity field, or due to small round-off errors in the pressure equation that initiate these perturbations. In a more recent paper [199], the authors manage to capture the dynamics of splashing using a grid refined at a size of 3000 equivalent cells near the contact line. The high computational effort needed make these runs unfeasible for the sake of the current study.

3.2. Dynamic behaviour of spreading receding droplet

The surface temperature and impact Weber number play paramount role in the spreading behaviour of an impacting droplet on a solid surface. This behaviour can be characterised using

the geometrical parameters of spreading factor and apparent dynamic contact angle. In addition, the effect of chamber pressure, thus the gas density in the vicinity of the droplet-solid interface, on the spreading dynamic was quantified.

3.2.1. Effect of surface temperature spreading dynamic

The effects of surface temperature and impact Weber number on spreading dynamics within the stick regime are further examined in this section. Figure 3.5 shows the sequential images of the droplet impact evolution during the spreading and receding phases for different values of the surface temperature and impact Weber number of 65. Numerical simulations are presented as well, in order to elucidate the fluid flow induced by the droplet impact.

A section view at the droplet middle plane is presented in the simulation results (Figure 3.5); the viscosity of the liquid phase and the temperature of the domain are depicted on the left and right side of the plots, respectively.

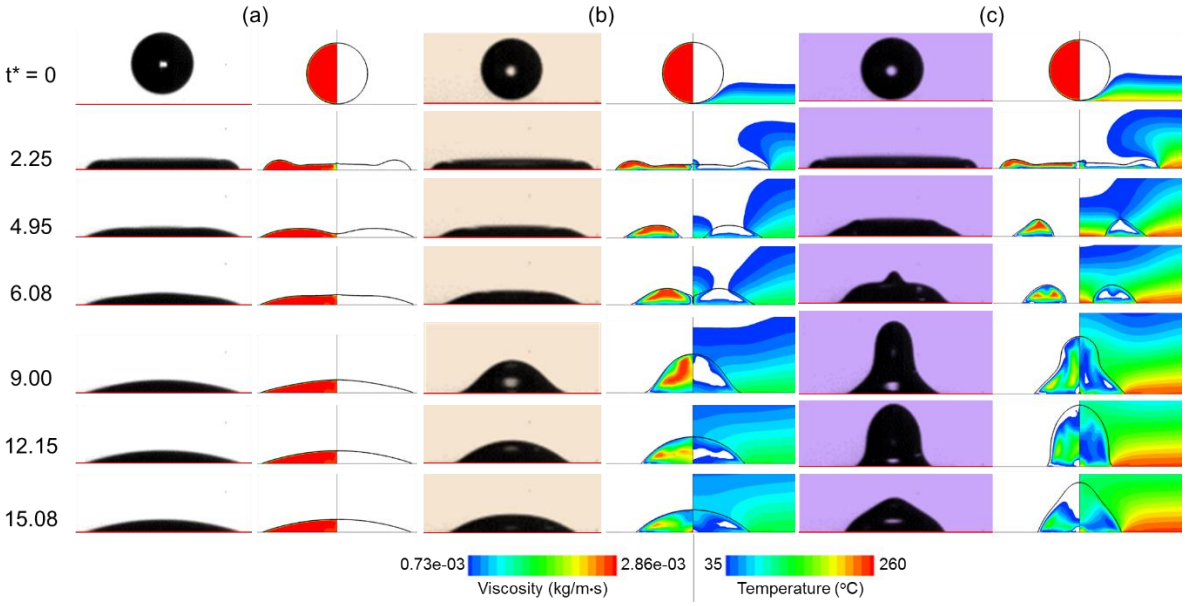

Figure 3.5: Sequential images (experiment and simulation) of Diesel fuel droplet impact on a heated aluminium surface for We=65 and P=1 bar: (a) T_W=25°C, (b) T_W=140°C and (c) T_W=260°C. For the simulation results, values of viscosity and temperature below the lower contour level are cut-off.

After impact, the droplet initially spreads on the surface with nearly the same spreading velocity for all cases (t*=2.25). After reaching maximum spreading, for impact at T_W=140°C and 260°C the droplet begins to retract (t*=4.95) towards its centre until reaching a maximum recoil position without rebounding from the surface (t*=9 and 12.15 for T_W=140°C and 260°C). Depending on the surface temperature, the droplet oscillates on the surface until it reaches to its final shape. In contrast, at surface temperature of T_W=25°C nearly no recoiling was observed and the droplet shape was not changed after the maximum spreading diameter. This can be seen in Figure 3.5a for t*>2.25. Numerical results indicate that as the temperature of the surface increases, the change in viscosity is more profound, as the droplet heats up quicker. This, as it will be further explained in the following section, is the main reason for the quicker recoiling of the drop as the surface temperature increases.

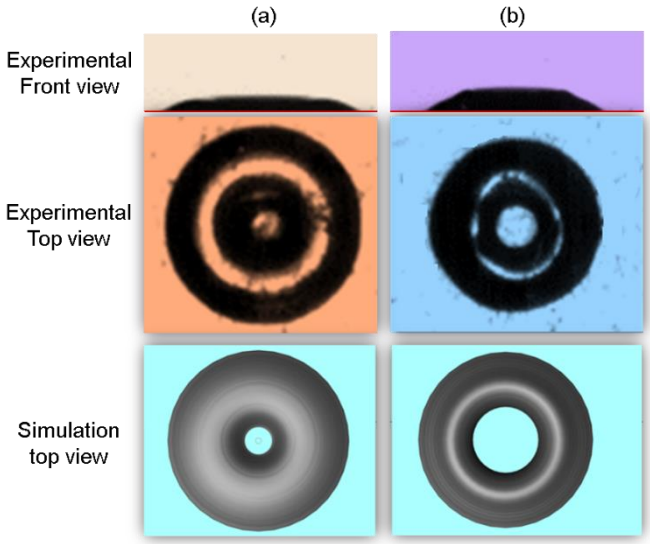

Figure 3.6: Drop break-up at impact point during recoiling, t = 4.95; (a) T_W =140°C; (b) T_W=260°C*

In Figure 3.6, the break-up of the Diesel droplet at the impact point during the recoiling phase is presented for wall surface temperatures of 140 and 260°C. Liquid break-up is adequately captured by the simulation, both qualitatively and quantitatively, at least for the case of T_W=140°C, shown in Figure 3.6a. the aforementioned breakup mode is due to the thin lamella

in the middle of the droplet and the collapse of the central entrapped bubble. It is expected that as the impact Weber number and the surface temperature increases, the probability of this mode is increases.

Figure 3.7 depicts the temporal evolution of apparent dynamic contact angle and spreading factor β= (D (t)/D0) for three different surface temperatures keeping a constant We=65. The time to reach the maximum spreading was slightly decreased by increasing the surface temperature. The droplet spreads with the same velocity approximately until t*=1, as the kinetic energy is the dominant factor in the initial spreading. By increasing the surface temperature, the droplet undergoes through stronger retraction and the maximum receding diameter decreases. The spreading factor at the end of this oscillation decreases with increasing wall temperature. A drastic decrease in dynamic contact angle is observed until t*=6 in a nearly similar manner for all surface temperatures. This shows that the decreasing dynamic contact angle during the initial phase is mainly related to the inertia of the radially spreading liquid [200]. However, during the recoiling phase, the values of the dynamic contact angle after t*=6 are significantly different for the three values of the wall temperature. The dynamic contact angle for lower surface temperature is almost constant, while it increases significantly with increasing surface temperature. The numerical results are in good agreement with the experimental measurements for the prediction of spreading diameter, maximum value and temporal evolution, as well as the drop oscillating behaviour and the quicker recoiling phase for higher surface temperatures. The equilibrium position that the droplet rests at the end of the impingement is not the same, between experiments and simulation (simulation radius is smaller), as for small contact angle values, the grid resolution should be significantly increased to capture the prescribed angle value.

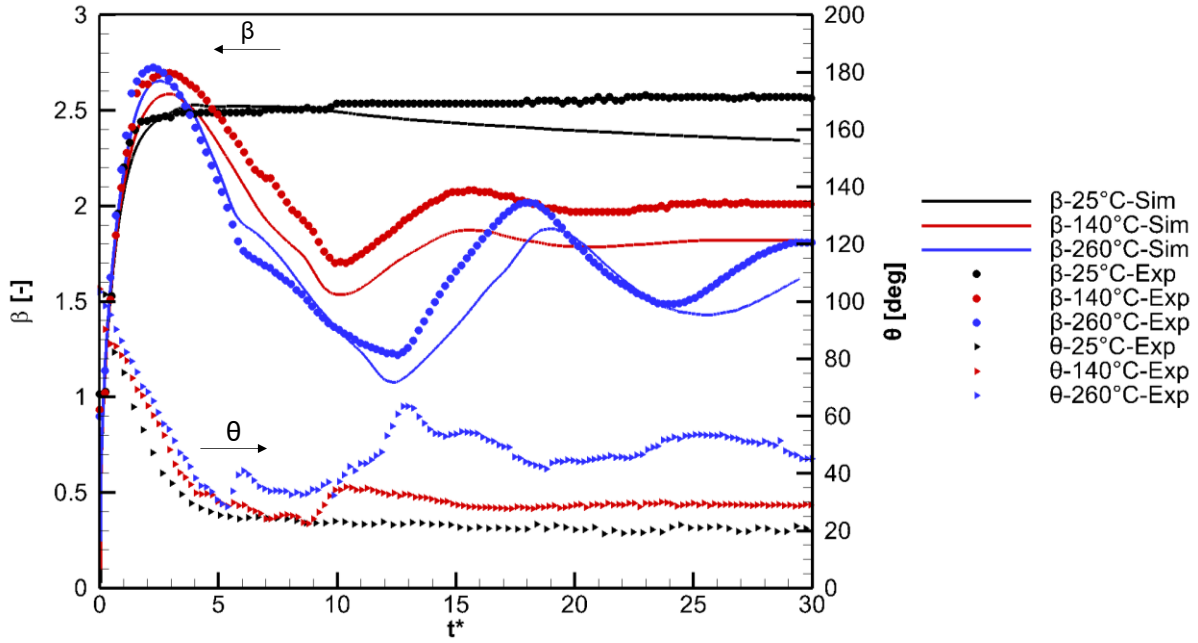

Figure 3.7: Effect of surface temperature on time evolution of dynamic contact angel and spreading factor for We=65 and 1 bar chamber pressure at T_W=25, 140, 260°C

As it can be seen from Figure 3.8, the final shape of the droplet is different for each condition at the end of spreading/recoiling phase; the respective images has been made using MATLAB® software; the outer droplet edge profile revolved around its axes of symmetry.

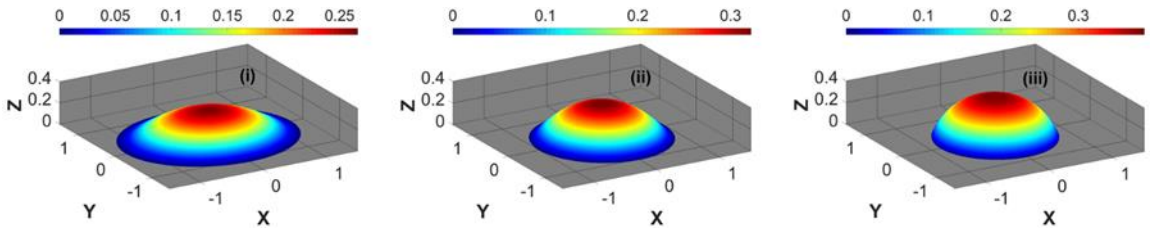

Figure 3.8: Droplet final shape at surface temperature of T_W=25, 140, 260°C for We=65 and 1 bar chamber pressure. All the dimensions were normalised by the droplet pre-impact diameter. The legend corresponds to non-dimensional height.

In Figure 3.9, the predicted viscosity of the liquid phase as the droplet spreads on the surface is presented at three different time instances close for the time instances that the drop stops spreading and starts to recoil and for three different surface temperatures. It is clear that viscosity values are lower on the liquid-solid interface as the temperature of the surface increases. This decrease in liquid viscosity induced at higher temperatures limits the liquid "friction" on the solid surface, allowing the droplet to recoil faster. Surface tension coefficient

also decreases with temperature, but the effect of viscosity is more significant. This is why the droplet forms a higher contact angle with the solid surface, a phenomenon that is captured by the simulation. In addition, as it is suggested by [78], [121], the increase in the contact angel value with surface temperature is attributed to strong evaporation at the triple contact point and indicates the transition for boiling and Leidenfrost regimes.

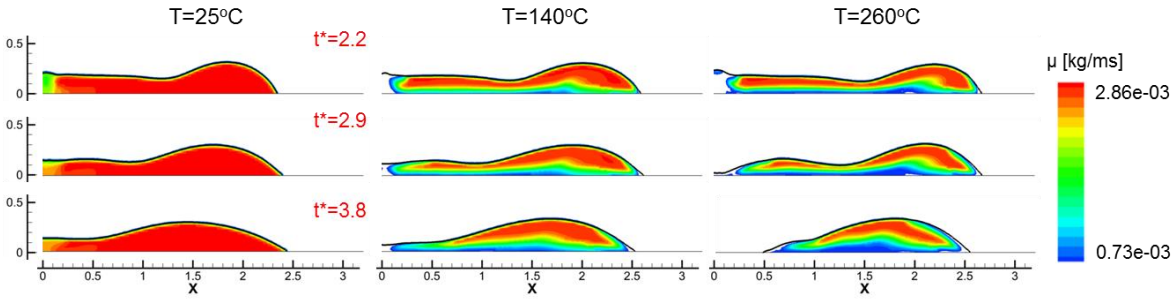

Figure 3.9: Droplet rim motion at 3 time instances (hysteresis and recoil) for 3 different surface temperatures of T_W=25, 140, 260°C, We=65 and 1 bar chamber pressure.

3.2.2. Effect of impact Weber number on spreading dynamic

Inertial force are playing a paramount role on the spreading dynamic of the impacting droplet on solid surfaces [62]. The competition of inertial kinetic energy with the surface tension and viscous forces determines the behaviour of the droplet during the spreading, until the impact energy is entirely compensated with the resisting forces.

Figure 3.10 illustrates sequential experimental and simulation images of impact on heated aluminium surface at T=140°C and 1 bar chamber pressure for different Weber numbers. All cases show similar qualitative behaviour; the drop impacts the surface, reaches its maximum spreading (t*=1.99), recoils (t*=2.91) and after oscillation (t*=5.05), relaxes to its equilibrium position (t*=10.10), which is the same for all cases. Numerical results are in good agreement with experimental measurements.

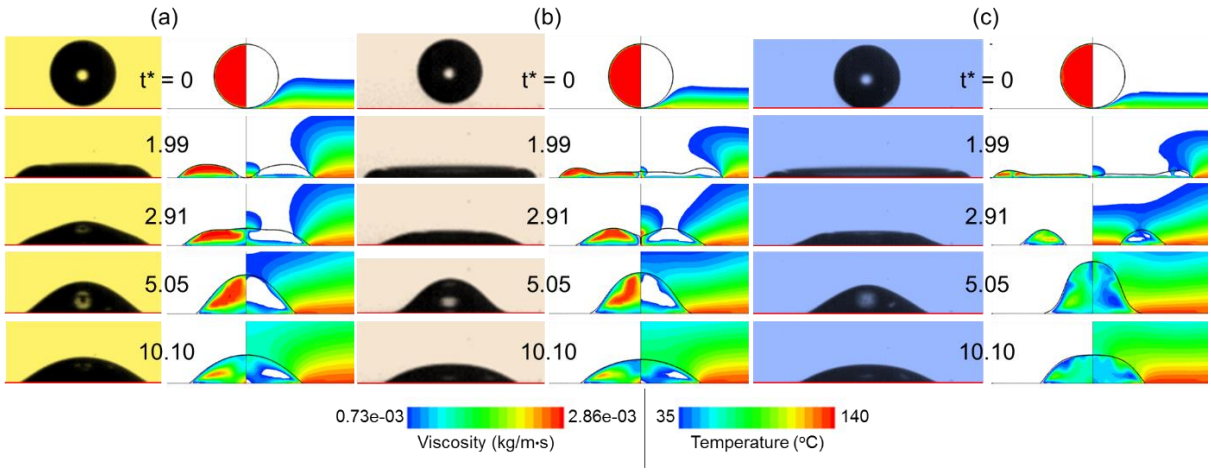

Figure 3.10: Sequential experimental and simulation images of Diesel droplet impact on heated aluminium surface at T_W=140°C and 1 bar chamber pressure; (a) We=19, (b) We=65 and (c) We=202. For the simulation results, values of viscosity and temperature below contour level are cut-off

The time evolution of dynamic contact angle and spreading factor for the conditions shown in Figure 3.10 can be seen in Figure 3.11. During the early period (t*<5) of spreading, the initially spherical droplet wets the flat surface, with the dynamic contact angle decreasing monotonically to levels approaching the equilibrium value, where both spreading factor and contact angle value became constant until the droplet relaxed on the surface; this process has a longer duration for higher impact Weber number (t*=1.4, 2.47 and 3.17 for We=19, 65 and 202, respectively). After the initial phase (t*>3.24, 9.16 and 10.74 for We=19, 65 and 202, respectively), the values of dynamic contact angle oscillate around a value approximately 20°, with different amplitudes, but similar qualitative pattern. The spreading diameter decreases during this phase.

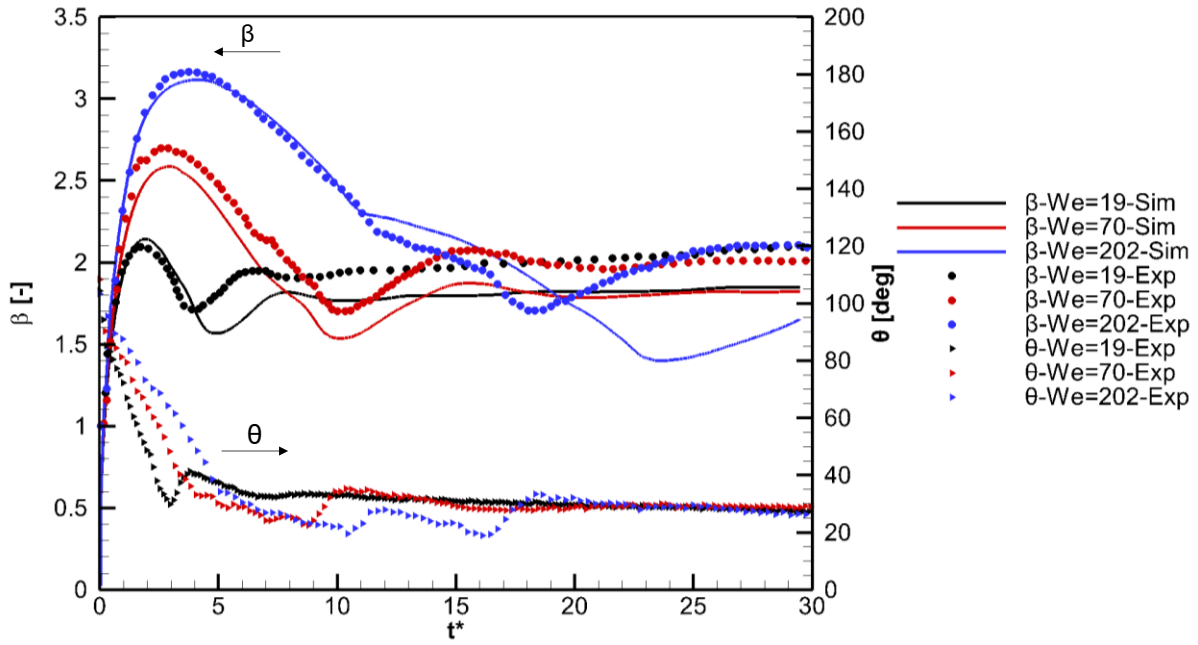

Figure 3.11: Effect of impact Weber number on time evolution of dynamic contact angle and spreading factor at surface temperature of T_W=140°C and 1 bar chamber pressure for We=19, 65 and 202

The maximum receding diameter value for all three cases is the same (ß=1.7). Although the droplets impinged with significantly different kinetic energies (by maximum factor of ~8) and spread with different contact line velocity, they all achieved nearly same final shape.

3.2.3. Effect of chamber pressure on spreading dynamic

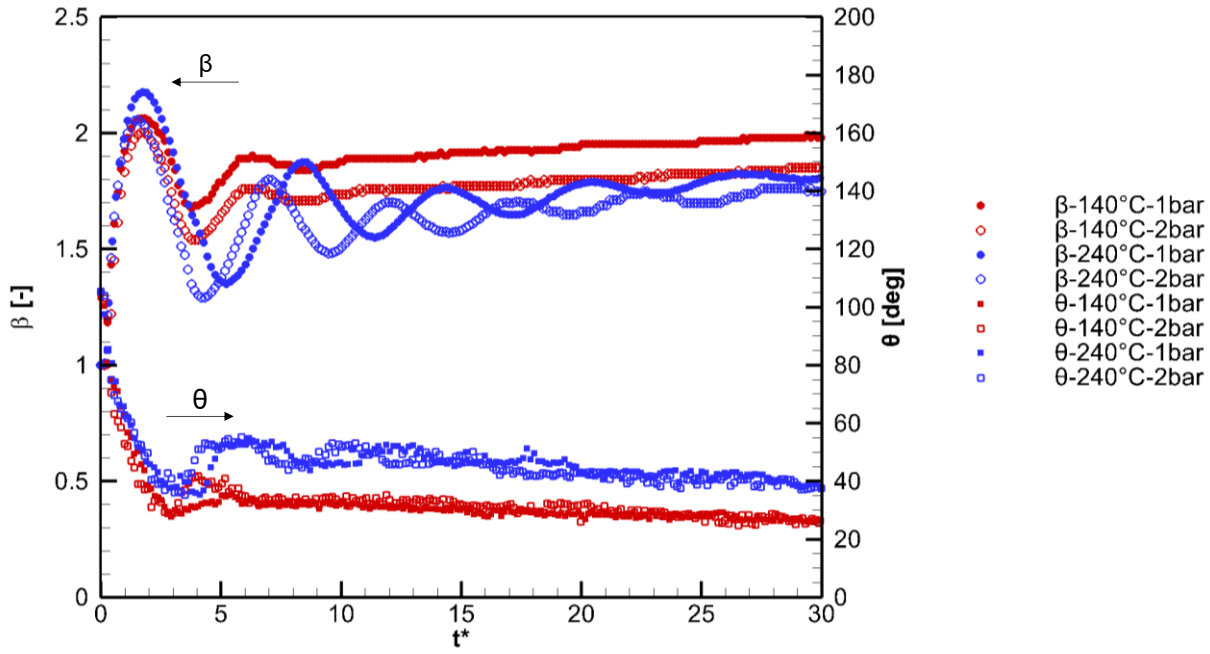

Figure 3.12: Temporal variation of (a) the dynamic contact angle θ and (b) spreading factor β for We=19 at T_W=140 and 240°C

Figure 3.12 shows the combined effect of ambient air pressure~~, impact Weber number~~ and surface temperature on the temporal evolution of the dynamic contact angle and spreading factor for We=19, ~~65~~. The oscillation frequency and amplitude seems to be only dependent on the surface temperature. The effect of the air pressure is quite insignificant for these conditions, as also reported by [67]. However, a weak suppression of the droplet spreading at P=2bar is observed, since the spreading factor β obtains a lower value compared to P=1bar test case. This can be attributed to the increased aerodynamic drag effect at the triple contact point, as the density of the ambient air is double at 2 bars chamber pressure compared to atmospheric condition; this is also reproduced by the numerical results in [35], showing that increasing the value of the ambient pressure reduces the maximum air velocity in the vicinity of the contact area.

3.2.4. Maximum spreading factor

The maximum spreading factor at the initial impact phase is one of the important parameters to characterise the heat transfer, as the contact area designates the overall heat transfer between the heated surface and the droplet. This section is devoted to quantifying the maximum spreading factor of impacting droplets for wide range of impact weber number, wall-surface temperature and chamber pressure of 1 and 2 bars. The maximum spreading factor (β_{max}) is defined as D_{max}/D, where D_{max} is the maximum spreading diameter. In Figure 3.13, a plot of β_{max} versus surface temperature for all the impact experiments obtained for various impact Weber number. All the data points were collected for impacts in the stick regime and in the course of which the droplets did not disintegrate during the expanding phase. The Weber number ranges from 19 to 360.

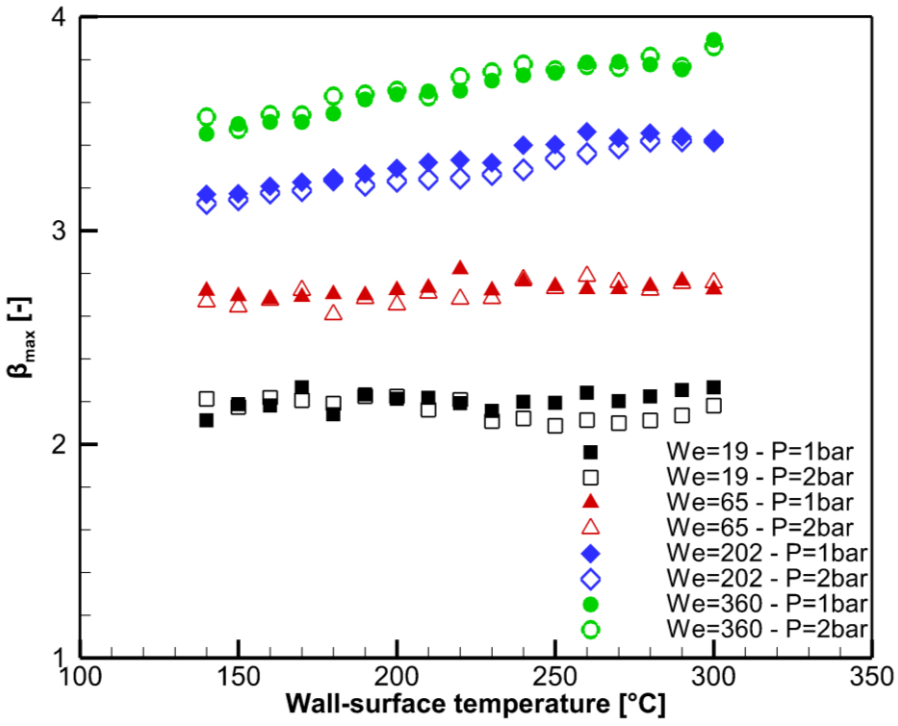

Figure 3.13: Effect of surface temperature, impact Weber number and ambient air pressure on maximum spreading diameter

Figure 3.13 shows the maximum spreading, in terms of maximum to initial droplet diameter, for different values of We and surface temperature in the range of $140°C<T_W<300°C$ at 1 and

2 bars chamber pressure. It is clear that for We<65, the maximum spreading factor does not vary significantly with increasing surface temperature. For higher values of the Weber number, there is a slight increase of the maximum spreading factor with surface temperature. On the contrary, the impact Weber number has a significant influence on the maximum spreading diameter, as increase of its value from 19 to 360 leads to a subsequent, almost double increase of the maximum spreading factor. This shows that the initial stage of the impact until the maximum spreading diameter is affected primarily by impact kinetic energy rather than thermal effects.

From the results, it's clear that the maximum spreading diameter doesn't vary much with increasing surface temperature; as it can be seen in Table 3.2, the average maximum spreading factor (β_{max}) varies for all the impact conditions not more than 12.17%. The highest variation is related to the impact Weber of 360 at 2 bars chamber pressure; a portion of this discrepancies is also attributed to the larger uncertainty values of the spreading diameter, which increases by increasing the impact Weber number. It seems that the surface temperature has little effect during initial impact stage, for the conditions studied; however it has been shown in the previous section that the surface temperature affects the recoiling behaviour, where the inertia effect significantly reduced.

Impact Weber number	19 (1bar)	19 (2bar)	65 (1bar)	65 (2bar)	202 (1bar)	202 (2bar)	360 (1bar)	360 (2bar)
Standard deviation	4.12%	4.75%	3.22%	4.84%	9.89%	9.49%	12.17%	10.97%

Table 3.2: Computed standard deviations of maximum spreading factor for Diesel fuel droplet at the surface temperature range of 140°C<T_W<300°C, impact Weber number of We=19, 65, 202 and 360 and chamber pressure of 1 and 2 bars

There are some models that predict the non-dimensional maximum spreading diameter for droplet surface impingement. Two theoretical models [100], [101] based on a surface energy analysis, are compared with the current experimental data. The difference between these

models is the way they estimate dissipation energy. In addition, two empirical correlation [99], [102], derived based on a wide range of impact conditions were added to the comparison. These correlations are listed in Table 3.3.

Correlation	Spreading factor (β_{max})
Akao [101]	$0.613We^{0.39}$
Clanet et al. [99]	$We^{1/4}$
Roisman [100]	$0.87Re^{1/5} - 0.4Re^{\frac{2}{5}} - We^{-1/2}$
Scheller et al. [102]	$0.61Re^{\frac{1}{5}}(WeRe^{-\frac{2}{5}})^{1/6}$

Table 3.3: Theoretical and empirical correlation employed to compare with the experimental data

Figure 3.14 compares the current experimental maximum spreading factor (β_{max}) with the models' predictions. For the current experimental data conditions, results show that the theoretical correlations of Akao [101] and Roisman [100], employing the surface energy analysis either over-predict or under-predict the maximum spreading factor (β_{max}). However, the empirical correlations, in particular the one for Scheller et al. [102], are in good agreement with the experimental data.

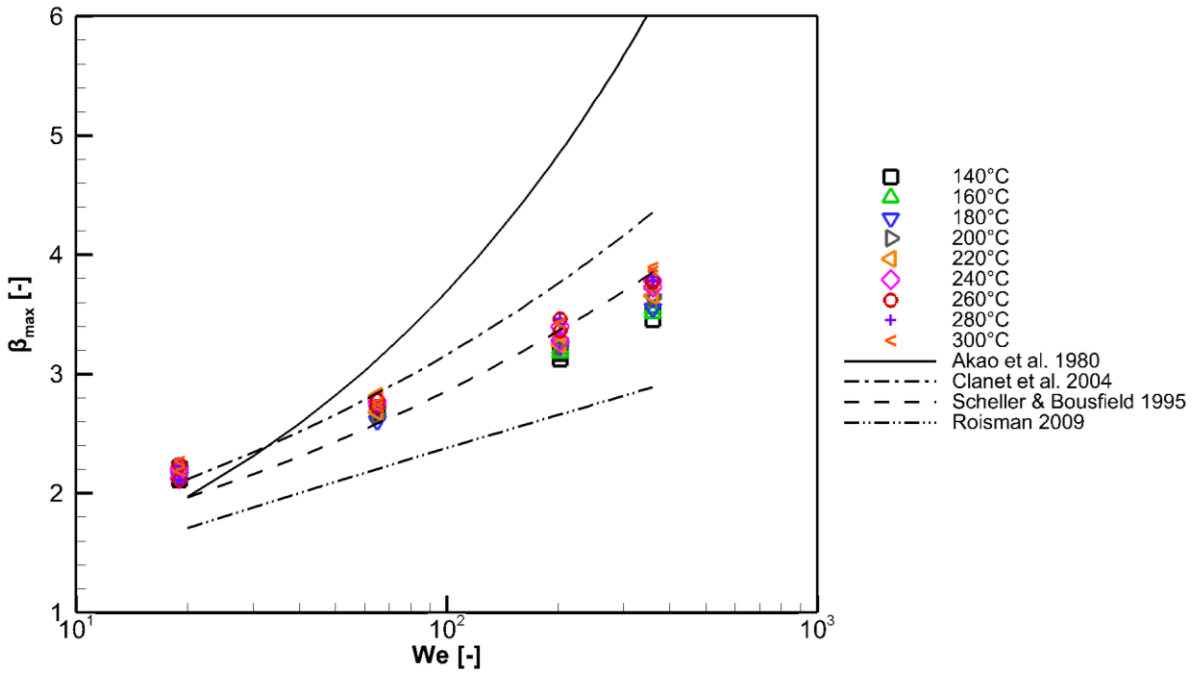

Figure 3.14: Comparison of Diesel droplet spreading characteristics at surface temperature range of 140°C<T_W<340°, Weber number of We=19, 65, 202, 360 and chamber pressure of 1 bar, with correlations of Akao [101], *Clanet et al.* [99], *Roisman* [100] *and Scheller et al.* [102]

The calculated absolute deviations of the experimental maximum spreading factor (β_{max}) at T_W=140°C, from the given correlations are presented in Table 3.4. It can be seen the lowest value of deviations are related to the correlations from [99], [102]. The large deviation observed from the theoretical predictions can be explained by the assumptions in the estimation of the energy dissipation during the impinging process; these models, for instance, has not accounted on the effect of wettability and viscous stress.

We \ Correlation		Akao [101]	Clanet et al. [99]	Scheller et al. [102]	Roisman [100]
19	1bar	6.63-12.96%	0.13-6.65%	7.05-13.34%	19.10-24.58%
	2bar	5.47-11.39%	0.04-4.96%	5.89-11.78%	18.10-23.22%
65	1bar	14.06-19.90%	2.65-7.91%	1.89-6.68%	16.64-20.71%
	2bar	15.34-23.24%	3.80-10.91%	0.51-5.63%	14.32-19.81%
202	1bar	39.78-52.69%	8.60-18.63%	0.88-5.97%	16.21-23.30%
	2bar	41.50-54.77	9.94-20.25%	0.02-7.423%	15.07-22.35%
260	1bar	56.38-76.27%	11.90-26.14%	1.01-11.58%	16.28-25.73%
	2bar	57.70-75.22%	12.84-25.38%	0.17-10.92%	16.78-25.01%

Table 3.4: Deviation of the experimental data of droplet maximum spreading factor from the correlations in Table 3.3.

3.2.5. Rebound velocity analysis

It is a well-known fact that when a droplet impacts on a heated surface with temperature above the Leidenfrost point, rebound from the surface occurs [53]. For low Weber numbers when no breakup occurs, the droplet rebounds vertically upwards without rupturing, while for higher values of the impact Weber number, the droplet breaks up during the spreading and the satellite droplets rebound with different angles depending on their distance from the axis of impact. In other words, the satellite droplets located at the axis of impact rebound vertically upwards, whereas the trajectories of those located at the rim edge have a radial outward direction. Nevertheless, the normal constituent of the droplet velocity remains constant regardless of its location and thus the droplets elevate from the surface in an identical manner; this behaviour can be seen in Figure 3.15.

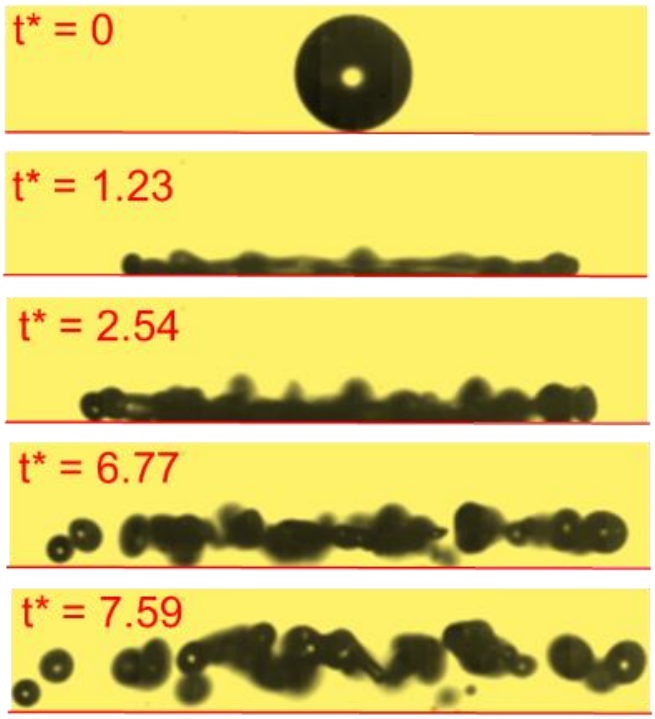

Figure 3.15: Side-view of the satellite droplet motion after their rebound from the heated surface. Droplet impact at We=202 and T_W=370°C

It can be therefore deduced that the rebound velocity is dependent on both surface temperature and impact Weber number as also illustrated by Figure 3.16. By increasing the impact weber number, the rebound velocity increases significantly for all wall-surface temperature examined. The correlation of the rebound force to surface temperature can be attributed to the so called vapour recoil force at the meniscus [201]. This term, in essence, corresponds to the buoyancy force acting on the air stream surrounding the droplet and leading to its ascending motion, which entrains the locally generated fuel vapour and forces it to an upward displacement, as well. In the designated conditions of the current study, it acts as the leading mechanism for upward movement on the satellite droplets. Increasing the surface temperature and the impact Weber number is expected to increase evaporation, so the recoil vapour force increases and leads to higher rebound velocity during the rebound process.

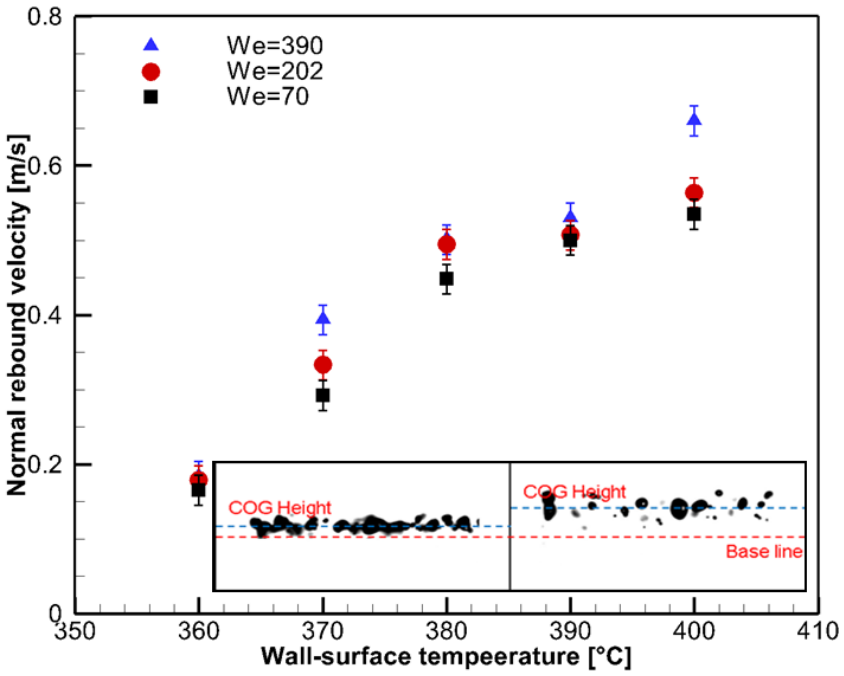

Figure 3.16: Effect of the surface temperature on the rebound velocity of satellite droplets for different values of the We number. Inset: Velocity calculation method based on the displacement of the geometric centre (COG) of satellite droplets.

3.2.6. Formation and collapse of entrapped gas bubble at impact point

As it can be seen in Figure 3.17, an air bubble entrapped in the liquid phase at the point of impact [120], [137] can be observed with the current setup and with a resolution of 3.78μm/pixel. When the droplet approaches the solid boundary, the surface is deformed due to the pressure gradient occurring at the impact point and an air bubble forms at the contact point of the droplet on the solid surface. In general, the droplet, due to its curvature, acts as a lens in front of the entrapped bubble so an accurate estimation of the bubble size is a challenging task. However, in the current study the bubble size was estimated from the top view images during the spreading phase where the free surface of the droplet lamella is nearly flat. It should be noted that this bubble has also been seen at room temperature.

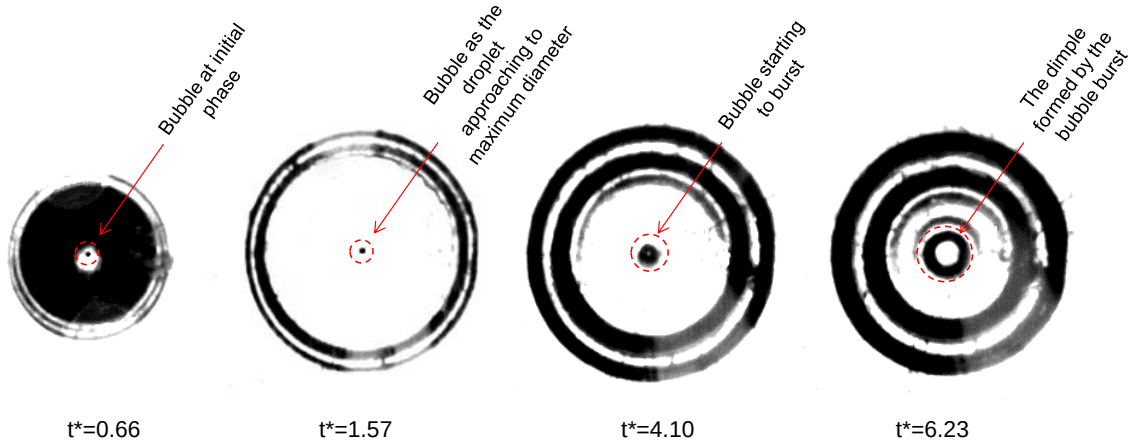

Figure 3.17: Temporal evolution of the entrapped air-bubble topology until its disappearance. Droplet impact at We=202 and T_W=180°C

Figure 3.18 shows the measured diameter of the entrapped bubble as a function of the surface temperature for three different values of the Weber numbers. The bubble diameter increases with surface temperature. Moreover, the bubble diameter is also dependent on the Weber number, since the bubble forms in the centre of the droplet spreading film, therefore its size can only reach to a certain value that compares with the film thickness. As the maximum spreading factor increases with increase of the Weber number, the film thickness is decreased and consequently the bubble diameter decreases, as well.

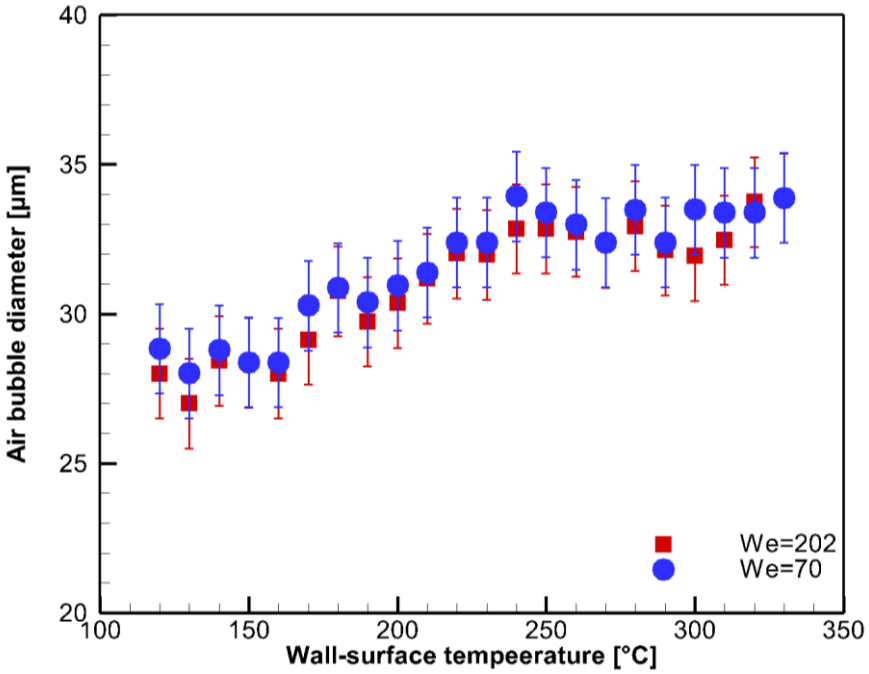

Figure 3.18: Effect of wall temperature on the measured bubble diameter for impact Weber number of 65, 202

The lifetime of the entrapped bubble after the droplet impact depends on wall temperature and Weber number, as shown in Figure 3.19. For the wall surface temperature values lying on the left hand side of the dashed line, the bubble stays in the liquid bulk for the entire duration of the impact process. The lifetime of the bubble decreases with increasing the wall surface temperature, while it increases with impact Weber number. The dependency of the lifetime to the wall temperature is more pronounced at higher impact Weber numbers. The bubble bursts as it reaches the free liquid film surface, due to the rupture of the thin separating layer between the gas inside the bubble and the ambient air. It has been verified that the time interval required the bubble to burst, considering as starting point the time of impact, coincides with the time required for the maximum droplet spreading factor to be reached, a correlation that is indicative of the effect of the droplet spreading film on the bubble bursting process.

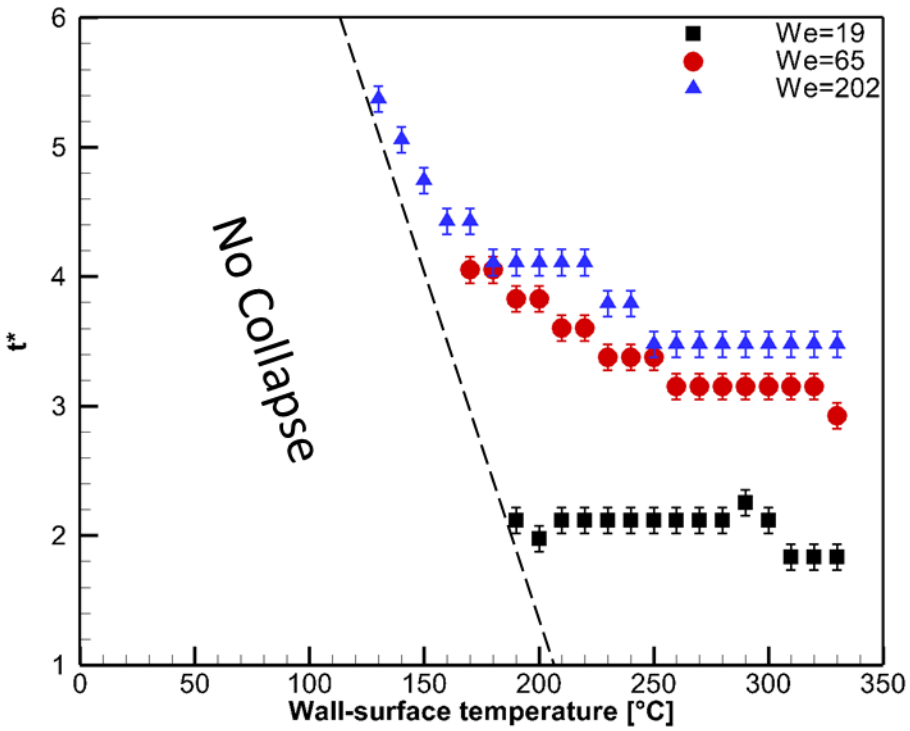

Figure 3.19: Bubble lifetime as a function of wall temperature

3.3. Summary

The impact of Diesel fuel droplets on a heated surface within a gaseous (air) environment at 1 and 2 bar has been investigated for a wide range of Weber number and surface temperature values employing both high speed visualization and CFD modelling. The We-T map for all the flow conditions has been formulated and six distinct impact regimes have been identified in the map, termed as stick, partial-rebound, breakup, breakup-rebound, splash, and rebound. Critical (We, T) value pairs have been identified, which signify the transition to the breakup, splash and rebound regimes. Additionally, The effect of wall-surface temperature and impact Weber number on wetting parameters (spreading factor and dynamic contact angle) have been numerically and experimentally assessed.

.

4. Droplet impingement onto similar size spherical heated solid surface

The phenomenon of drop impingement on a curved surface represents a complex physical problem governed by various interacting parameters, including droplet diameter and velocity, surface properties, angle of impact, liquid properties, and probably the pre-existing liquid wall film present in the case of spray impact. The latter grows into even more challenging problem if phase change occurs and theoretical approaches require proper assumption for simplifying the analysis.

The process of non-isothermal droplet-particle collision has received considerable attention among researchers recently. One of the motivations is the differences in spreading dynamic and the post impact outcome, arising from the wall-surface geometry. However, complete understanding of non-isothermal droplet-particle collision has not been fully understood yet. The outcome of a flow generated by drop impact onto a dry curved target (splash, stick and rebound) generally depends on the energy of the impacting droplet. In addition, in droplet impingement on a heated surface at given impact energy of the droplet, the surface temperature can significantly alter the impact dynamic. The latter is due to the change of the liquid physico-chemical properties at surface temperature much below the boiling temperature of the droplet liquid. When the surface temperature increases to approximately the boiling temperature of the liquid, nucleation and collapse of the disruptive vapour bubbles changes the impact dynamic. And finally for the temperatures above the boiling point, the droplet starts to evaporate already when approaching the surface. The vapour generated in the region between the drop and the surface is further compressed and at above the so-called Leidenfrost temperature, the evaporation and compression rate are sufficiently high to provide enough pressure in the vapour layer that prevents a direct contact of the droplet and surface. The droplet is then said to be in

the film boiling regime and the impact dynamics can be significantly different from the lower surface temperature. The surface then shows a hydrophobicity nature, the contact angle between the droplet and gas vapour layer increases and the droplet levitate or even rebound from the surface upon the impact. This chapter, represents new experimental data of micro-metric Diesel fuel droplet impingement on a brass spherical particle under elevated wall temperatures. By means of high-speed imaging, different post-impact regime outcomes are identified and mapped for a wide range of We-T set points. This graph is then is compared for the respective phase map of the droplet impact on a heated flat surface. The temporal variation of the dynamic contact angle and spreading factor is also derived for conditions below the Leidenfrost point for which no splashing occurs. In addition, conditions leading to the onset of droplet splashing and disintegration are studied and the effects of substrate temperature and Weber number on the splashing behaviour are discussed. Finally, the temporal and spatial evolution of film thickness of spreading droplet at the impact point was measured. It should be noted that in the current study, Reynolds and Weber numbers change only due to the droplet kinetic energy, and systematic variation of viscosity and surface tension of the tested liquid has not been considered.

4.1. Classification of post-impact regimes

During the process of droplet impingement on a heated spherical surface and for the operating conditions summarized in Table 2.8, seven distinctive outcome regimes were observed during the course of the present experimental investigation, termed as coating, rebound, splash, breakup-rebound, splash-breakup, breakup and splash-breakup-rebound. Figure 4.1 presents the characteristic images of these outcomes. The 3D reconstructed view (produced employing a dual-view optical arrangement) allows the demonstration of the impact symmetry (which is missing from the available literature). It has been shown, that in the case of asymmetric impact, the unbalance between gravitational and centrifugal forces on the droplet can significantly

change the hydrodynamic and heat transfer processes arising during the droplet impact [80], [154], [172]. The 3D reconstruction also facilitates a better illustration of secondary droplets setting in on the particle surface at breakup regime. The impact process and the post-impact regime depend on the impact Weber number, the target surface temperature, and droplet-to-particle size ratio. .

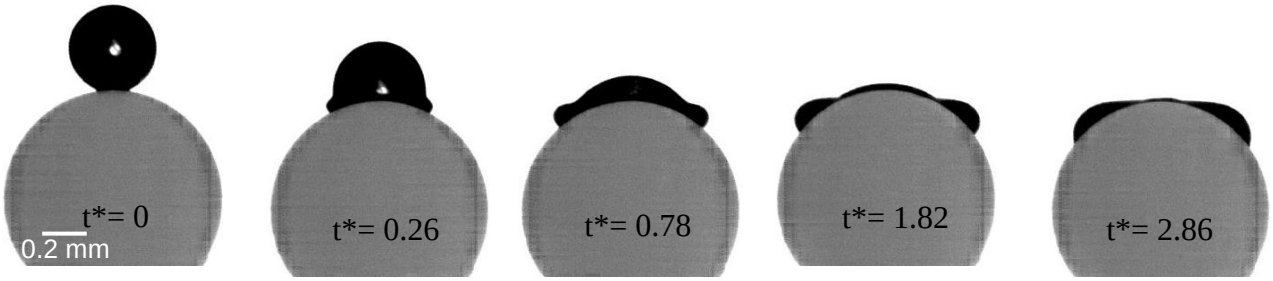

(a) 2D-front view of coating regime: We=30/TP=140°C

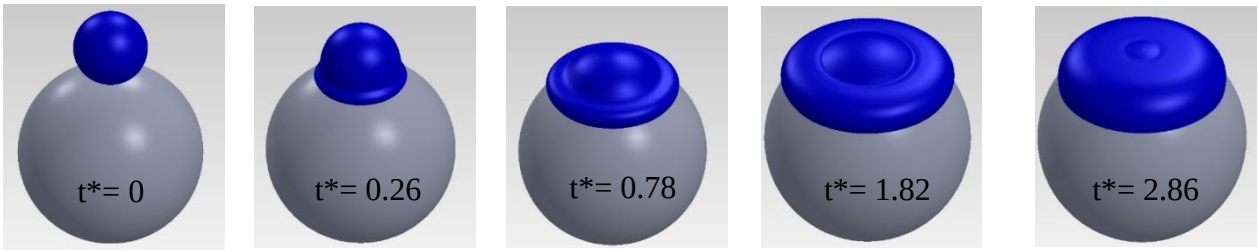

(a') 3D-Isometric view of coating regime

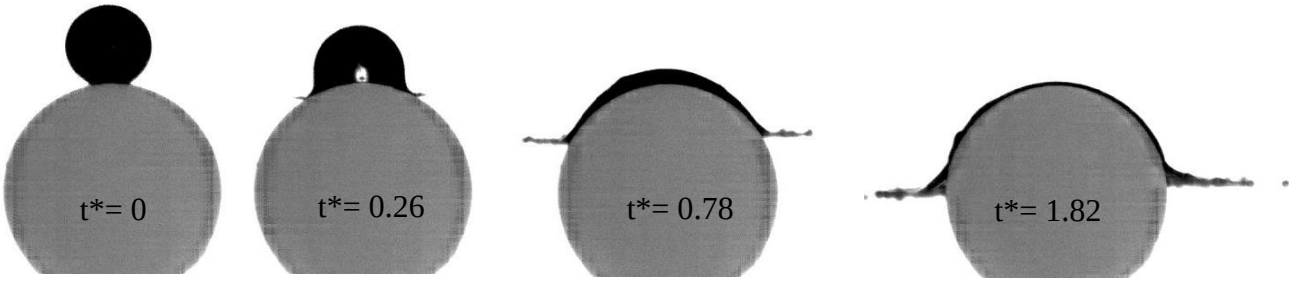

(b) 2D-front view of splash regime: We=520/TP=140°C

(b') 3D-Isometric view of coating regime Splash regime

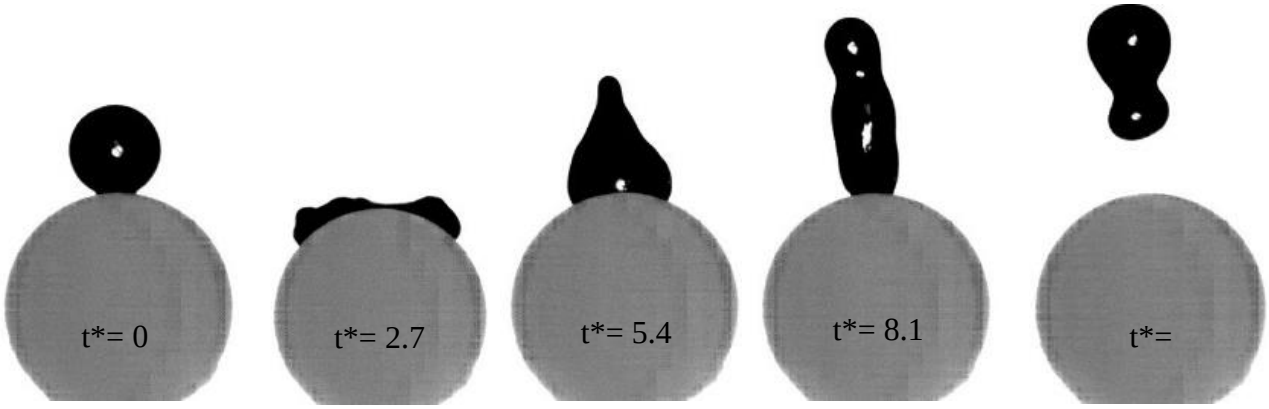

(c) 2D-front view of rebound regime: We=30/TP=340°C

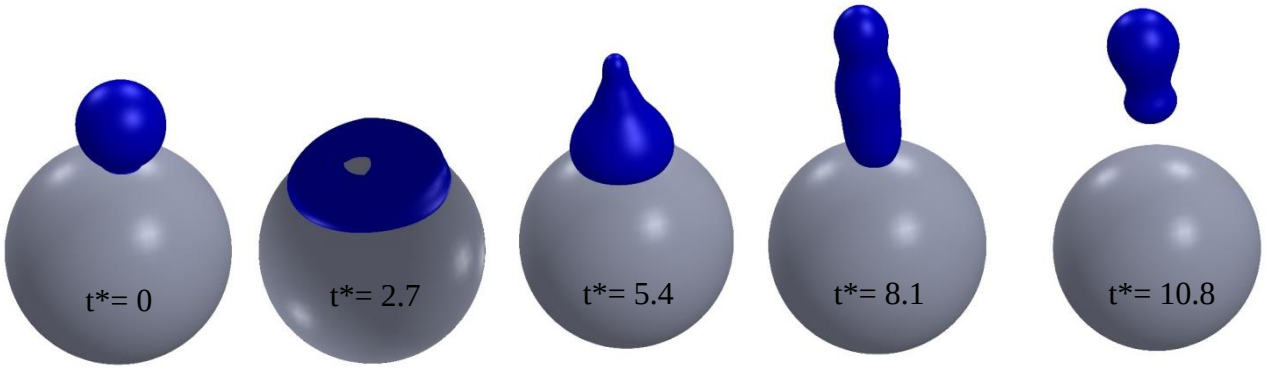

(c') 3D-Isometric view of rebound regime

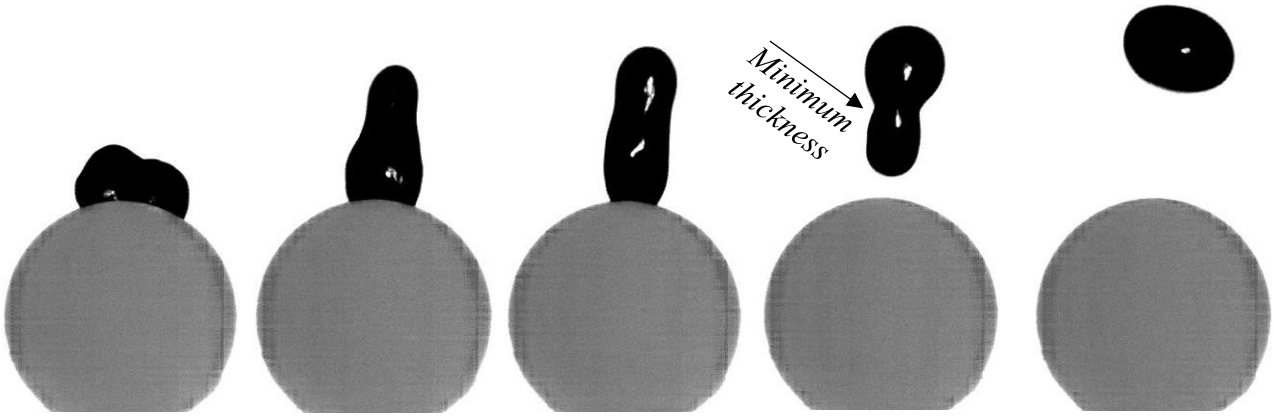

(d) 2D-front view of droplet oscillation during the droplet lift up at rebound regime

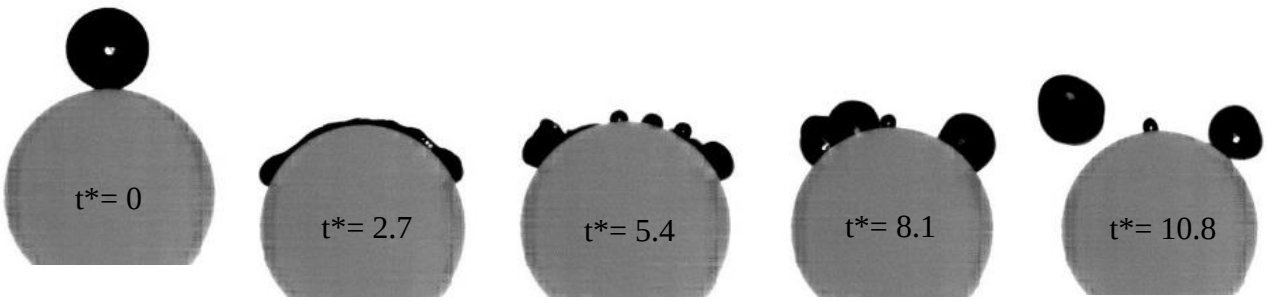

(e) 2D-front view of breakup-rebound regime: We=70/TP=340°C

(e') 3D-isometric view of breakup-rebound regime

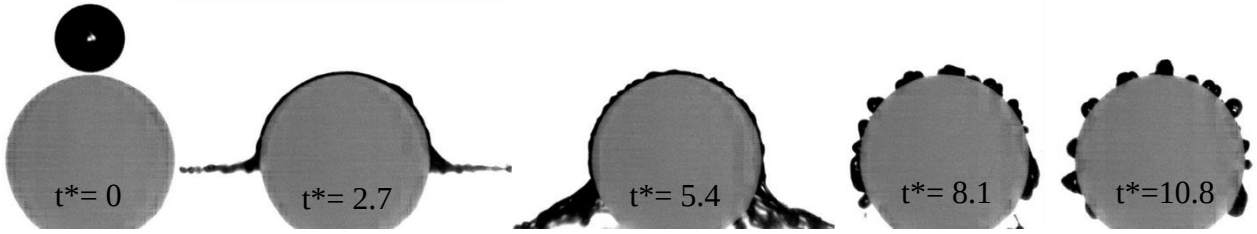

(f) 2D-front view of splash-breakup regime: We=530/TP=320°C

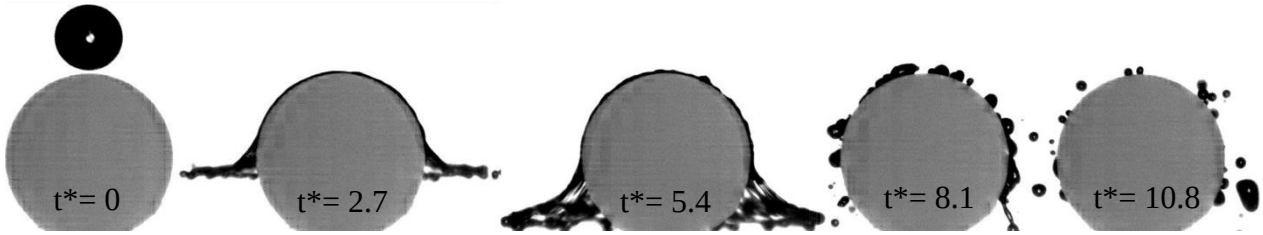

(g) 2D-isometric view of splash-breakup-rebound regime: We=530/T_P=340°C

Figure 4.1: Snapshots taken at different (non-dimentional) time instances of the impact of a Diesel fuel droplet onto a heated particle (a),(a') We=30/T_P=140°C (coating regime), (b),(b') We=520/T_P=140°C (splash regime), (c),(c') We=30/T_P=340°C (rebound regime), (d) oscillating droplet during the lift up at rebound regime, (e),(e') We=70/T_P=340°C (breakup-rebound regime) and (f) We=530/T_P=320°C (splash-breakup regime), (g) We=530/T_P=340°C (splash-breakup-rebound regime). The 3D-isometric views presented were reconstructed based on two 2D-side views. Due to droplet complex interface in (f) and (g) 3D views have not been produced.

In the coating regime (see Figure 4.1a), the entire mass of the droplet is deposited on the particle upon impact and the droplet spreads on the surface. The combined effect of gravity and initial kinetic energy force the droplet lamella to stretch until its maximum diameter, which is detected at approximately t*=2. A receding phase follows until the droplet relaxes on the particle

surface. This regime has been observed for Weber numbers below the splash threshold and when the heat transfer is not adequate to induce breakup or rebound.

Splash (see Figure 4.1b) occurs when the droplet inertia becomes significantly larger than the viscous and surface tension forces. As the droplet approaches the particle surface, a liquid film spreads radially outwards. The droplet becomes unstable, deforms and smaller droplets are detached from the moving edge of the spreading lamella, while the remaining part of the droplet sticks on the solid particle. Impact characterized by higher values of the Weber number results in a much larger droplet contact area and a thinner liquid film over the surface at $t^*=0.26$ could be detected, compared to the one in coating regime. However, this thin film, at the lower half of the droplet, remains only for a short period on the particle surface. Afterwards, it detaches from the particle surface through a flapping motion evident at $t^*=0.78$. Due to the high radial velocity of this liquid sheet, which is larger than the capillary retraction of the liquid rim, small drops are detached and ejected radially at $t^*=1.82$. This regime is very similar to corona splashing that occurs often during droplet impact on flat surfaces [21].

In rebound (Figure 4.1c), the droplet impacts onto the surface, spreads, recoils and finally levitates or rebounds from the surface. The static contact angle of the spherical particle and the Diesel fuel is around 30°, thus, the surface can be considered as hydrophilic for impact under cold condition. For low impact Weber-number values, upon the first touchdown of the droplet on the heated particle, a vapour layer forms due to the high heat transfer rate and the intense evaporation at the solid-liquid interface, as shown for $t^*=2.7$. At this time, the impact momentum forces the droplet to deform to a disk-like shape. When the inertial force pushes the droplet towards the particle surface, a relatively large pressure gradient builds up and generates a vapour flow in the spreading direction. The specific vapour flow acts as an opposing force (upward thrust), hence creates strong retraction ($t^*=5.4$), lifts up the droplet ($t^*=8.1$), until it completely rebounds from the particle surface ($t^*=10.8$). The shape deformation

continues even after the droplet rebounds (t*>10.8). As depicted in Figure 4.1d, upon the departure from the particle surface, the droplet undergoes a strong fluctuating expansion and contraction along its main axis, while the inertial force is counteracted by the surface tension force, which tends to minimize the interfacial area. In the case that surface tension does not suffice so as to maintain the droplet shape, breakup occurs at the location of minimum droplet thickness; a similar behaviour has been reported in [1] for water-glycerol mixture (35 wt.%) at T_P=~274°C and We=20.6; however, the rebounding droplet was much more elongated in the rebound direction while most of the droplet mass accumulated in the leading part of the droplet followed by a narrow connecting ligament. During the spreading and recoiling phases of the rebound regime there is almost no direct contact between the particle surface and the droplet [50].

As it can be seen in Figure 4.1e, if the impact Weber number and/or particle temperature are high enough, the droplet spreads widely over the particle periphery; then, the lamella thickness decreases significantly at the wetted area until the maximum spreading diameter is reached (t*=2.7). Irregular interface deformation is more intense due to nucleate boiling. Neck areas (locations where the liquid film ruptures) start to appear leading to the formation of small drops over the dry surface. The remaining droplet mass forms a hollow circular ring with a thick rim (t*=5.4). This ring also undergoes strong deformation and finally breaks up into three droplets (t*=10.8). Similarly to the We=30 case, these three droplets are finally lifted from the surface and rebound in different directions (t*=16.3), in the so-called breakup-rebound regime. However if the surface temperature is lower than the Leidenfrost point, the droplets remain on the surface (breakup). At this condition, the droplet impact process shows an asymmetric behaviour.

At the highest values of impact-Weber number and particle temperature (see Figure 4.1f and e), the droplet splashes at t*=2.7 with the mechanism discussed for the conditions of Figure

4.1b. Increasing the Weber number, enhances the prevalence of inertial forces during the early stages of the impact. Also, surface tension becomes less pronounced above the Leidenfrost temperature. After splashing, the remaining mass of a droplet spreads tangentially and deforms into a liquid sheet of highly complex and perturbed topology over the particle surface. The sheet then breaks up into several small droplets (t*=8.1). Depending on the temperature, the satellite droplets are possible to either stick to the particle (Figure 4.1e) or rebound from it (Figure 4.1f), as is shown in detail in Figure 4.2.

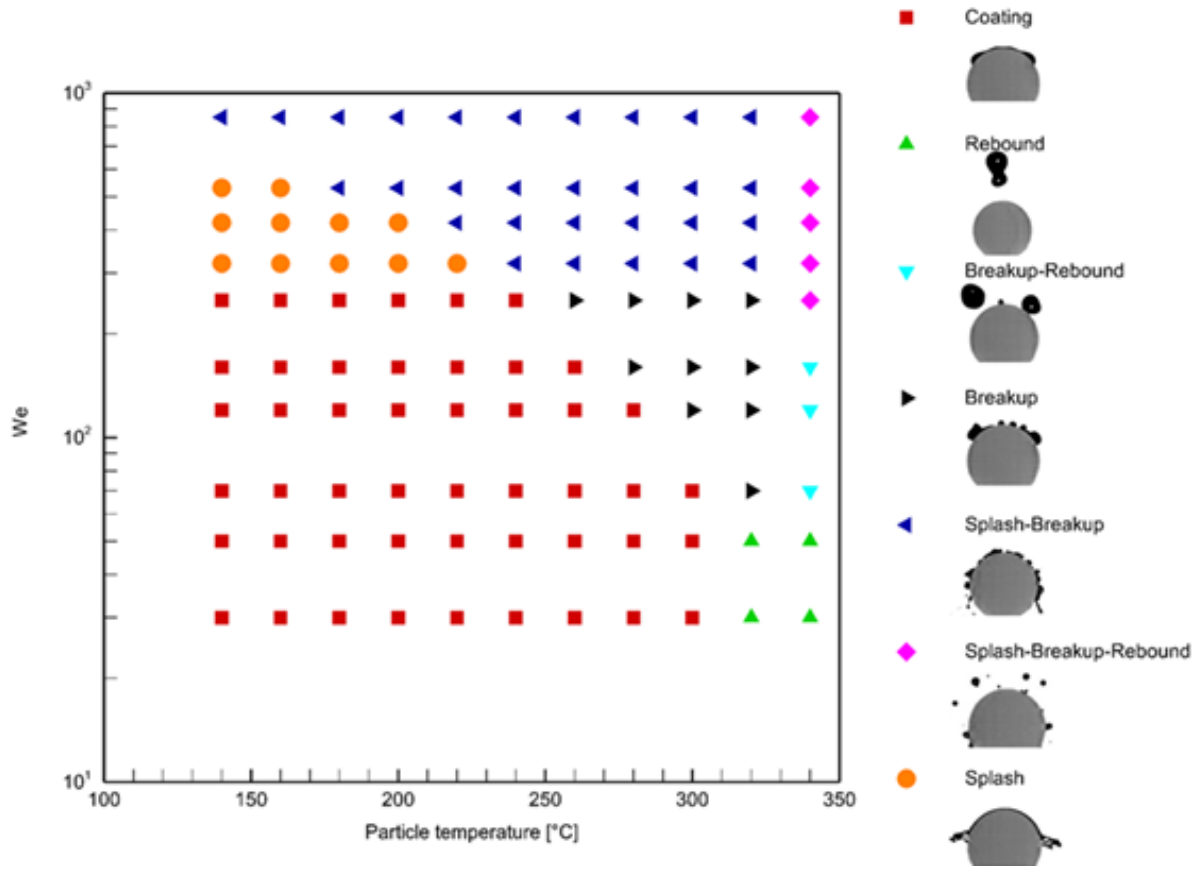

Figure 4.2: We-T regime diagrams of Diesel fuel droplet impact on a heated brass particle and Characteristic images of the outcome regimes

Figure 4.2 in particular, presents a map of the droplet-impact outcomes possible to set in for the We-T range examined. The respective characteristic droplet-shape images for each regime are also presented in Figure 4.2. In order to highlight the differences in reference to the flow phenomena arising during the impact of either single or multiple-component fuel droplets on a heated particle, a number of experimental studies referring to the regime mapping of the post-

impact processes of single-component fuel droplets have been summarized in Table 4.1. As shown in Figure 4.2, the coating regime in the present study is detected for temperatures below the Leidenfrost point and relatively low Weber numbers (We<70), while the reported values for water and isopropyl are We<50 and 80, respectively [155]. While Diesel droplets are found in this study to disintegrate at We>70 for DTP=0.4, it has been reported by [155] that water droplets disintegrate at We>50 for DTP=0.31. It has also been shown that increasing DTP significantly enhances the breakup mode for water, however this effect is less profound for isopropyl [1]. In this study, the Leidenfrost temperature was specified to be around 320°C for low Weber numbers and increased by ~20°C for We >50; this is in good agreement with the previously reported temperature (T_P=357°C), above which the Diesel fuel droplet impacting on a flat hot aluminium alloy surface starts to levitate on its own vapour layer [202]. The deviation of the reported values is attributed to the different composition of the Diesel sample, droplet deposition method, thermo-physical properties and roughness of the solid surface [96]. The dependency of the Leidenfrost temperature (T_L) to the Weber number (We) can be illustrated by comparing the vapour pressure, which increases with particle temperature and the inertial energy of the impacting droplet, which is proportional to We. In order for the droplet impact outcome to remain above the Leidenfrost temperature with increasing We, higher vapour pressure and, thus, higher target-particle temperature is required. The dependency of the Leidenfrost point to the Weber number is generally limited to 40°C for We>20 [132], [169]. However, in [190], a much stronger dependency has been reported (180°C). This could be attributed to the polished surface employed for the experiment as low surface roughness affects nucleation and thus heat transfer rate and consequently the Leidenfrost temperature. For Diesel-fuel droplet with Weber-number values above 320, a transition to the splash regime was observed for the entire temperature range examined. It is already shown by several studies (see selectively [21], [152], [203]) that the splashing threshold for different single-component

liquids depends mostly on viscosity and the DTP. The splashing threshold for a water droplet has been reported to be ~210 with DTP=0.287 [152], while it increases to We=240 with DTP=0.4 for heptane [203]. In contrast to the Leidenfrost temperature, the transition border to the splashing regime is independent of the surface temperature and it is only a function of Weber number. In the present study, a particle temperature of 320°C was required, in order to induce breakup of the droplet, for the minimum value of the Weber number (We=70) examined. Nevertheless, the minimum temperature value for breakup gradually reduced, as the impact Weber number increased from 70 to around 850 (see Figure 4.2). Similar behaviour has been manifested in [1] for water, where an increase in the particle temperature from 250°C to 350°C, has shifted the breakup We to higher values by ~6, 4 and 3 orders of magnitude for DTP=0.228, 0.249 and 0.287, respectively. This can be attributed to the effect of the particle temperature on heat transfer rate above and below the Leidenfrost point. Increase of the particle temperature for conditions below T_L enhances heat transfer and thus, promotes breakup. On the contrary, for wall temperature above T_L, the vapour layer thickness increases which hinders heat transfer [52].

Reference	System	Findings
[155]	• Water (8<We<84) • Isopropyl (14<We<136) • Acetone (13<We<130) • 25°C<T_P<250°C • DTP=0.31 and 0.21 for water and isopropyl, respectively • 10mm polished brass particle	• Water droplet coats the particle for We<50 and 20°C<T<175°C • Breakup has been observed for We>50 for water and We>80 for isopropyl and acetone • Transition to rebound regime occurs at T=250°C
[1]	• Water (3.9<We<103.6) • Isopropyl (8.6<We<194.6) • 250°C<T_P<350°C • Leidenfrost regime • DTP=0.287, 0.249 and 0.228 for water • DTP=0.212, 0.192 and 0.161 for isopropyl • 10mm polished brass particle	• No coating regime has been observed • For water droplets, the minimum We required for break up for DTP=0.228, 0.249 and 0.287 and T=250°C is equal to 16.5, 40.6 and 63.5, respectively • Increasing the particle temperature to T=350°C, has shifted the breakup We to higher values by ~6, 4 and 3 orders of magnitude for DTP=0.228, 0.249 and 0.287, respectively • For isopropyl, the minimum We for break up has been reported equal to 85.2. • Variation of the transition to breakup for isopropyl is not significantly affected by temperature and DTP.
[204]	• Water and water-glycerol • 0.9<We<47.1 • T_P=273°C • DTP~0.83-0.86 • 3mm hydrophobically coated particle	• Rebound regime has been observed for We=19.1 • Breakup has been reported for We>43.7 without rebounding of the secondary droplets.

Table 4.1: Current literature on the characterization of post-impact flow regimes for single-component liquid droplets colliding on a heated particle.

The work of [205] has ~~been~~ performed a parametric study in order to distinguish the outcome of isothermal impact of a droplet on the spherical surfaces under different impact conditions, using CFD simulation. They have indicated a critical curve which separates the rebound and coating regime based on impact Weber number and DTP; if the droplet initial kinetic energy is equal or higher than the surface energy needed to spread the film pas the particle equator, thus the following ratio equals to unity and the limiting curve is derived [205]:

$$\frac{E_{kin}}{E_{0.5surf}} = \frac{m_0 u_0^2/2}{\sigma A_{psurf}/2} = \frac{\rho_0 u_0^2 \pi D_0^3/12}{\sigma \pi D_0^2/2}$$

$$= \left(\frac{\rho_0 u_0^2 D_0}{\sigma}\right).\left(\frac{D_0}{D_p}\right)^2.\frac{1}{6} \qquad \text{Equation 4.1}$$

$$= We.DTB^2.\frac{1}{6}$$

The experimental droplet impact outcome at particle surface temperature of T_P=140°C and the latter theoretical correlation depicted in Figure 4.3. As in the experimental results, rebounds regime were absent, only coating regime were marked in the map. Additionally, for higher impact Weber, were mechanical breakup/splash were observed, part of the liquid mass stayed on the particle surface and sliding downwards, thus marking the coating regime. It can be observed that the experimental and theoretical correlations are in good agreement. Based on the theoretical correlation and the numerical results in [205], both increases of DTP and impact Weber number promote the transition from droplet rebound regime to the coating one. The effect of wettability is expected to shift the border line on Figure 4.3; in case of hydrophilic surface, the transition line is expected to be shifted towards higher Weber numbers for a the same DTP, as hydrophobicity promotes rebound over coating [205].

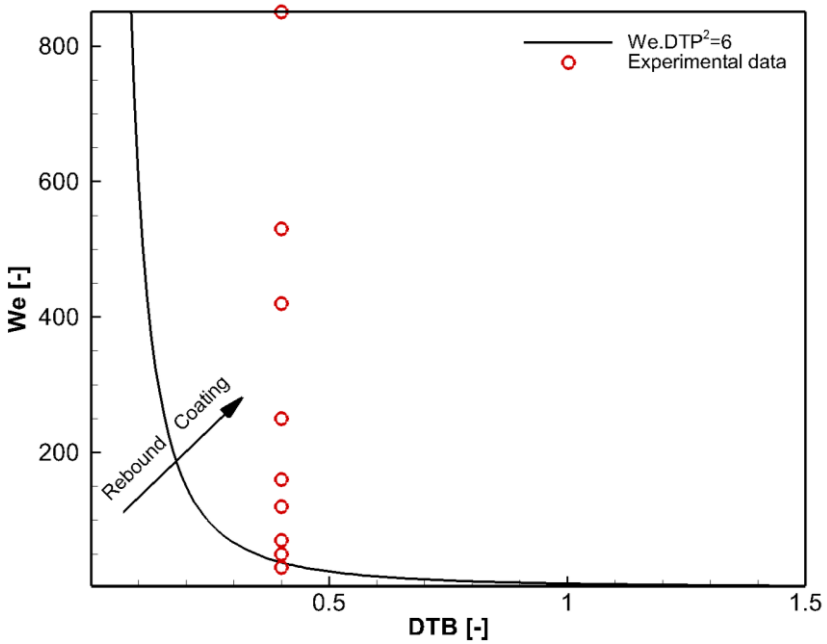

Figure 4.3: We-DTP post impact outcome map. Circle markers denote experimental coating regime

Figure 4.4 illustrates in a comparative manner the post-impact outcome regimes of drop impingement on heated flat and spherical surfaces; each line perceives a necessary condition for a regime to be reached. The coloured regions highlighting the various regimes correspond to impact on a particle. The experimental data for droplet impact on a flat surface have been acquired with the same setup explained in the material and methods section. As can been seen in Figure 4.4, the overall qualitative behaviour of the transition borders between the respective regimes are similar. However, it can be seen that the required (We, T) set points to shift the outcome is generally reduced for the impact on the spherical surface. For instance, the critical We for splashing and the Leidenfrost temperature were reduced by 160 and 20°C, respectively, compared to the respective values referring to impingement on a flat surface. A similar behaviour was also observed for the breakup limit, which is correlated to both the Weber number and surface temperature. The minimum Weber number required for break up below the Leidenfrost temperature decreased by 65% for impact on spherical surface compared to the flat one. This earlier shift could be attributed to additional droplet interface perturbations induced by the wall curvature and the additional effect of gravitational forces.

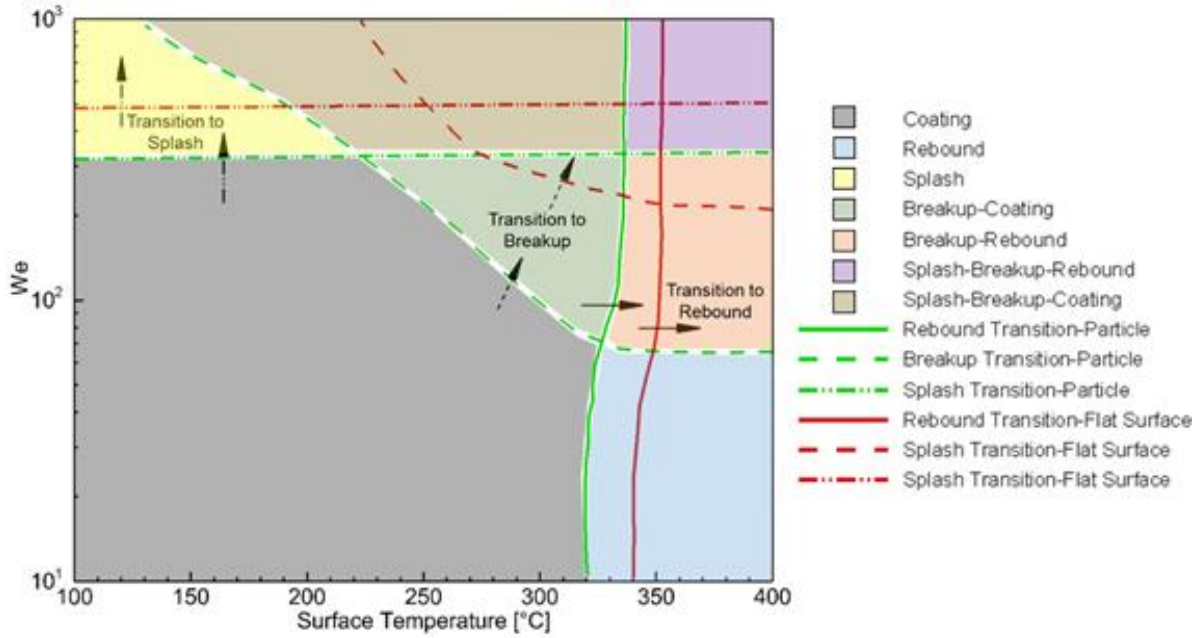

Figure 4.4: Comparison of the post-impact outcome regimes for the drop impingement on flat and spherical surfaces.

4.2. Spreading dynamic

4.2.1. Effect of impact Weber number

In this section, the effects of particle temperature and impact Weber number on the spreading dynamics are discussed.

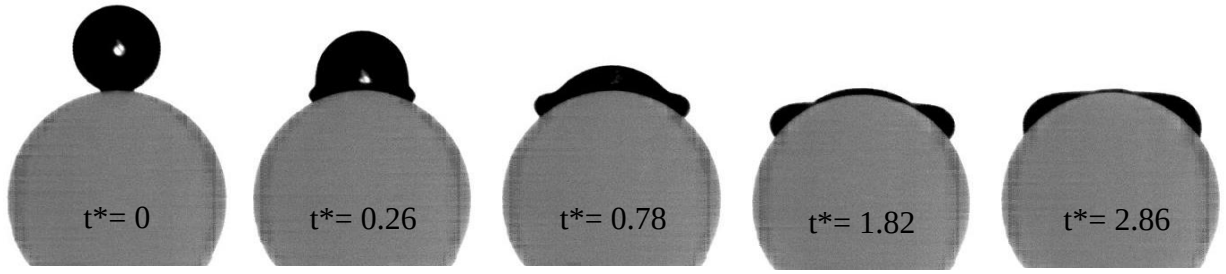

(a) We=30

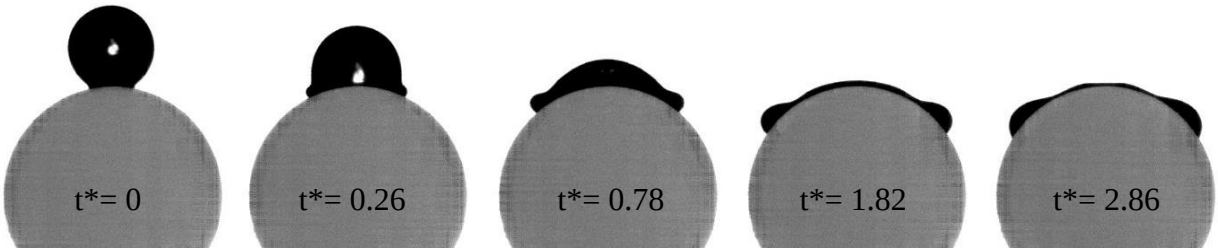

(b) We=50

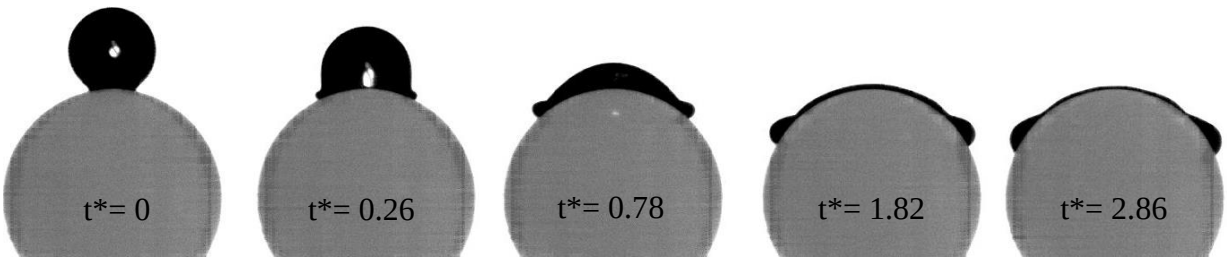

(c) We=70

Figure 4.5: Snapshots taken at different non-dimensional times for the impact of a diesel fuel droplet onto heated (T_P=140°C) spherical surface for (a) We=30, (b) We=50 and (c) We=70. Effect of surface impact Weber number on spreading dynamic.

In order to illustrate the effect of Weber number on the drop spreading dynamic, snapshots of the droplet lamella during the spreading phase at different non-dimensional times, shown in Figure 4.5, schematically compare the extent of the lamella diameter on the particle surface at three different Weber numbers of 30, 50 and 70and at wall-surface temperature of 140°C. In

case of droplet impact on a hydrophilic surface at temperature much below the boiling temperature of droplet liquid and in absence of splashing, the drop can readily spread over the surface and reach its maximum diameter and then it can retract or remains close to the stated maximum spreading diameter, depending on the particle surface temperature and DTP ratio. However, in case of droplet impact on hydrophobic or super-hydrophobic surface, the droplet receding is usually followed by a partial or complete rebound (if the droplet-surface interaction stays in Cassie-Baxter state [26]) due to remaining inertia energy at the end of spreading phase [206].

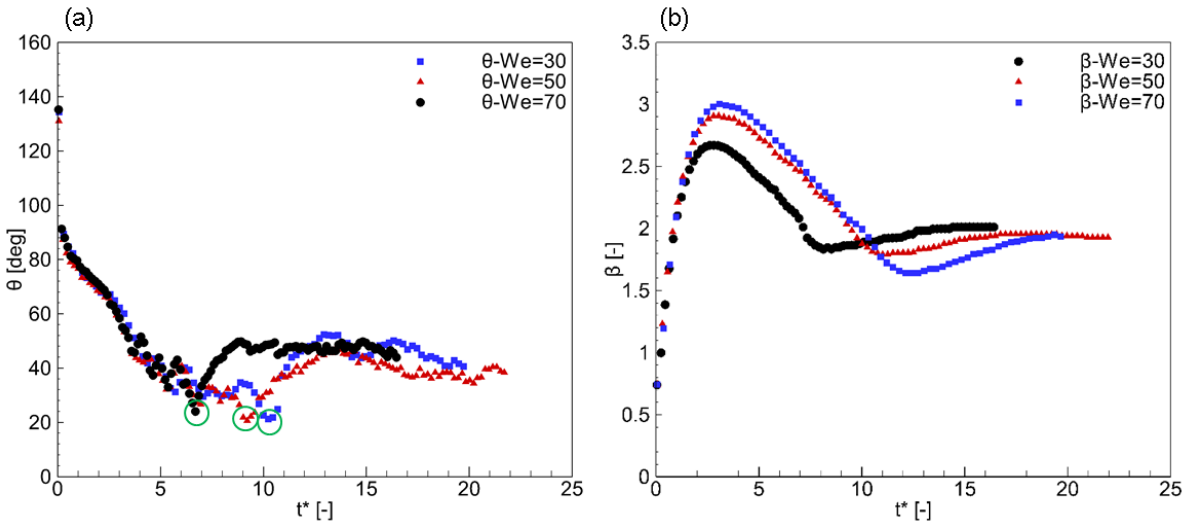

Figure 4.6: Effect of impact Weber number on (a) dynamic contact angle θ and (b) spreading factor β, for We=30, We=50 and We=70 at T_P=140°C

The effect of impact Weber number on the temporal evolution of the apparent, dynamic contact angle and spreading factor are illustrated on Figure 8. Contact-angle measurements (Figure 4.6a) were only performed for low Weber-number values (We≤70) due to insufficient resolution in the vicinity of the triple-contact point of the image processing procedure employed for higher Weber numbers during the spreading phase. This is attributed to the small thickness of the liquid film at the area of interest, which was not possible to capture. It can be noticed that for all Weber numbers, the dynamic contact angle first decreases sharply following impact, until the maximum diameter is reached (t*~3.2). After this initial stage, it oscillates

and follows a strong recoiling behaviour as indicated by the local minimum values observed at t*=7, 9, and 10 for We=30, 50 and 70, respectively. Finally, the dynamic contact angle reaches a value of approximately θ=40° (recall: θ=30° for impact on flat surface) at its equilibrium state for all cases. It is clear that the impact Weber number has insignificant effect on the dynamic contact angle; this is in agreement with the experimental results in [155], as similar results have been reported for We=42 and 84. However, its effect becomes noticeable at later stages of impact, where the duration of the oscillation increases with increasing Weber number.

Figure 4.6b illustrates the effect of the Weber number on the droplet spreading factor β. As the impact Weber increases, the droplet spreading onto the solid particle is more pronounced. The spreading behaviour for all cases is similar; the droplet shows an oscillation due to the competition between inertial, surface tension and viscous forces. This oscillating behaviour decays with time until the droplet completely rests on the surface. Initially, the droplet spreads rather fast onto the solid wall, reaching a maximum deformation and later it recoils towards its centre. It should be taken into the account that the time to reach the maximum spreading factor differs for the examined cases and as the Weber number increases, the time of reaching maximum spreading diameter decreases. After the pass of the recoiling phase, a second expansion takes place with decreasing amplitude since the available kinetic energy is gradually lost due to viscous dissipation. Finally, the droplet shape oscillates with very low amplitude until it becomes still. The frequency of the oscillations is in the order of $(16\sigma/\pi^2\rho D^3)^{1/2}$ as suggested in [207]. This results to different oscillating behaviour for the droplets examined due to the variable droplet size and variation of its surface tension and density, which are influenced by the droplet's heating rate. At the early stages of the impact, the spreading factor increases monotonically with the same rate for all Weber numbers until t*=1.2. This behaviour is similar to the droplet impingement onto a flat surface, as shown in the work of [62]. They have reported that increasing the Weber number is not influential on the spreading rate of the droplet during

the early stages of impact. Afterwards, the spreading rate decreases until the maximum spreading factor is reached at t*=2.6, 2.8 and 3.3 for We=30, 50 and 70, respectively. Then, the droplet starts to retract until the spreading factor reaches a minimum value; this value slightly reduces with increasing Weber number. The recoiling rate appears to increase with increasing values of the Weber number, however the recoiling process commences earlier for droplets characterized by lower Weber number. Higher droplet inertia urges the droplet to spread excessively to counterbalance the resulting force from the impact. Due to the increase in contact area at higher impact Weber numbers, the heat rate provided to the liquid film increases, hence the liquid viscosity and surface tension decrease. The more intense recoiling is attributed exactly to the increased heat transfer rate and surplus energy during the recoiling phase. Numerical results shown in [208], confirm that the temperature gradient at the interface of the droplet impacting with higher We, is generally greater than the respective for lower We values; this designates a higher heat-transfer rate to the droplet. For all cases, the entire mass of the droplet is deposited on top of the particle and there is no sliding towards the lower part of the particle cross-section; this shows that the gravitational energy cannot overcome the surface energy, which tends to minimize the interfacial shape of the droplet and induce tangential flow in the liquid. Finally, the droplet deformation decays and stabilizes at a spreading factor value of ~2.

The spreading ratio values have been compared to the theoretical model proposed by [101]. According to the theoretical model, if the time integral Φ* of the impact velocity is defined as:

$$\Phi^* = \int_0^t v dt / d_0 = 3\left\{\frac{1-\left(2-\sqrt{3}\right)\exp\left(-\sqrt{3}t^*\right)}{1+\left(2-\sqrt{3}\right)\exp\left(-\sqrt{3}t^*\right)}\right\}^2 - 1 \quad (4.2)$$

where t* is the non-dimensional time, d_0 is the impact diameter, and v is the impact velocity. Then, the non-dimensional lamella thickness d* and the non-dimensional spreading ratio D* for the t*<3 can be calculated as follows:

$$d^* = 1.19We^{-0.56}\Phi^*(2.26 - \Phi^*) \tag{4.3}$$

$$\beta = \left\{((2 - \Phi^*)\Phi^* + \left(\Phi^{*2}\right)(3 - \Phi^*))/3d^*\right\}^{1/2} \tag{4.4}$$

Figure 4.7 shows the comparison of the theoretical and experimental results for three different Weber numbers.

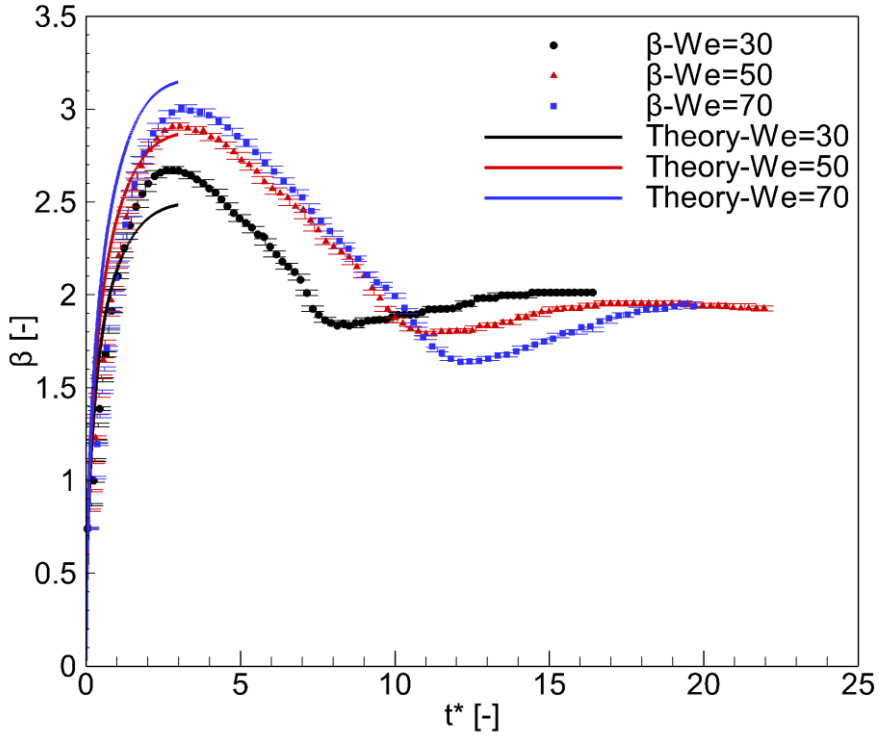

Figure 4.7: Effect of impact Weber number on spreading factor β, for We=30, We=50 and We=70 at T_P=140°C; comparison of the experimental and theoretical results

The calculated mean deviation of the experimental and theoretical values are 8.93%, 8.08% and 16.36% for We=30, 50 and 70, respectively. The model under predicts the experimental

results of maximum diameter extent for We=30 and 50, while at We=70 the model over predicts it. In general, the model gives a larger slope than the experimental results. As mentioned in [101], three key parameters affecting the dynamics of droplet spreading on a heated curved surface have been neglected namely as: (i) The gravitational effect, (ii) Loss of mass due to its vaporization and viscous effect on the lamella flow. Negligence of the aforementioned parameters in the model constitutes the possible reason of the discrepancies detected between the results.

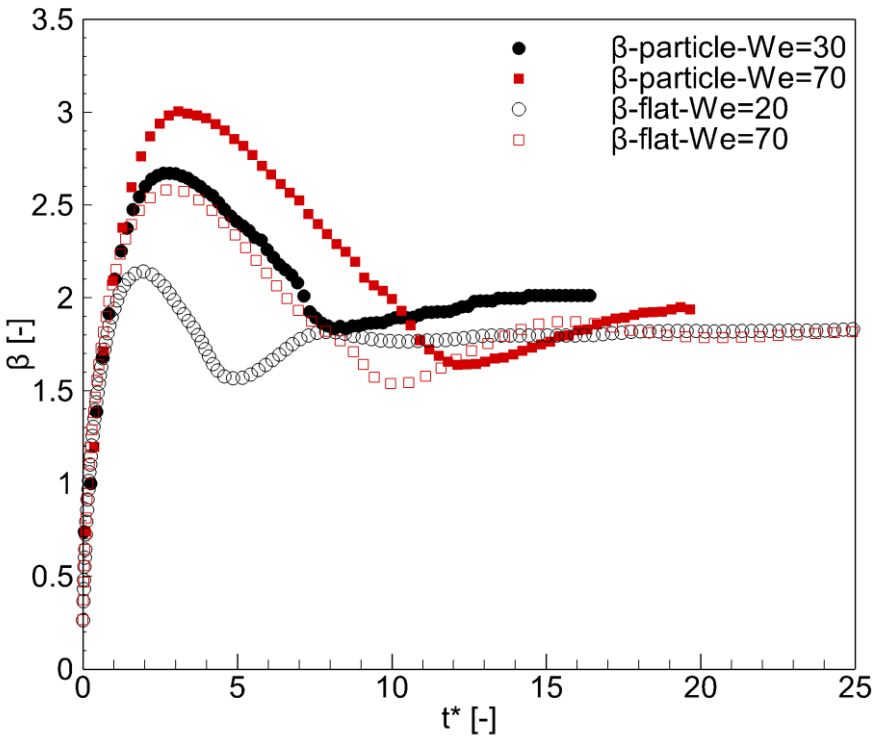

Figure 4.8: Comparison of the effect of impact Weber number on the time evolution of the spreading factor at surface temperature of T_P=140°C for drop impingement on flat and spherical surfaces.

Figure 4.8 shows the effect of impact Weber number on the temporal variation of the spreading factor at surface temperature of T_P=140°C for drop impingement on flat and spherical surfaces. It can be seen that the maximum spreading diameter is higher for the impact on a spherical surface, while the minimum recoiling diameter decreased, respectively. However, the spreading and recoiling rate stayed similar for both surfaces. Based on the numerical results

reported in [172], attention should be given to the effect of gravitational and centrifugal forces, which significantly influence the spreading dynamics of droplets impinging on spherical surfaces. It has been shown that by taking the gravity effect into account, the spreading factor increases up to 17%. In addition, centrifugal force has an even stronger influence on the droplet spreading; this effect is made more profound by increasing the DTP [172]. The presence of these additional forces are responsible for the further extension of the lamella spreading diameter on spherical surfaces compared to flat surfaces; yet the centrifugal force is the dominant effect.

4.2.2. Effect of particle temperature

Figure 4.9 presents the temporal variation of the apparent, dynamic contact angle and the spreading factor on the particle temperature for three different particle temperatures at a fixed value of We equal to 30.

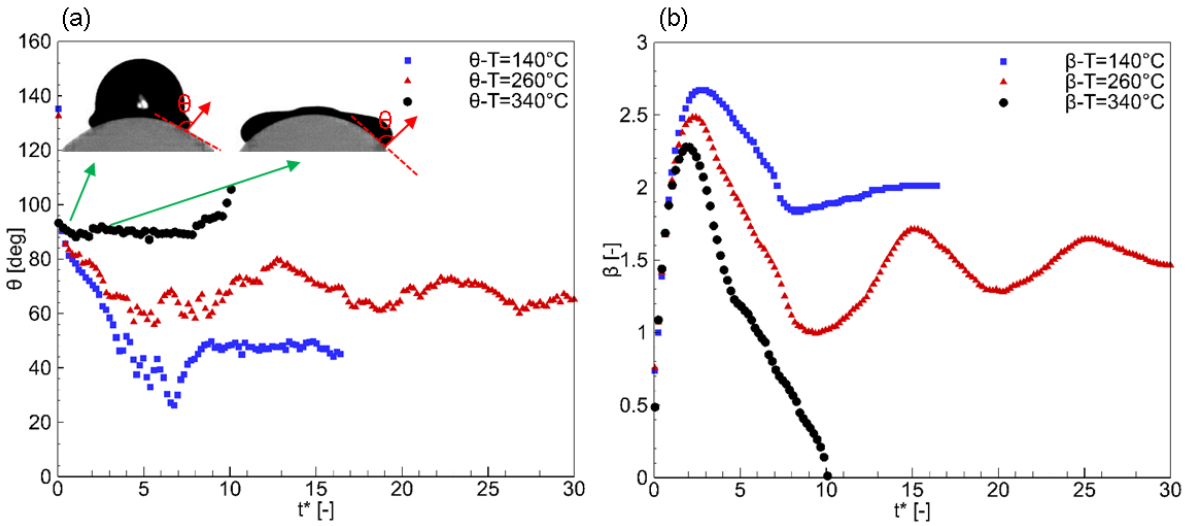

Figure 4.9: Effect of the particle temperature on (a) the dynamic contact angle θ and (b) spreading factor β, for We=30 at different temperatures.

The two lower temperature values considered correspond to the coating regime, while the highest one is actually the Leidenfrost temperature of the fuel droplet, where the droplet rebounds from the particle after the spreading-recoiling process is completed. It is obvious that

the particle temperature has a strong effect on the dynamic contact angle. For the coating regime and during the initial spreading phase, the rate of dynamic-contact angle reduction is becoming smaller as the particle temperature increases. These variations can be attributed to the transient heat transfer at the particle surface, which leads to vaporization at the advancing contact line. The intensity of vaporization depends on the particle temperature. Therefore, the vaporization rate keeps increasing as the particle temperature increases and, consequently, leads to decrease in the observed spreading ratio, high values of the dynamic contact angle and prevention of further surface wetting. During the retraction phase, the droplet vibrates; this can be perceived from the strong fluctuation in the dynamic contact angle values, after the maximum spreading diameter is reached. At T_P=140°C, the dynamic contact angle stabilizes after t*=9, while for T_P=260°C the dynamic contact angle vibrates for the entire duration of the recorded images. This is attributed to a more intense vaporization process around the triple contact point. At Leidenfrost temperature (T_P=340°C), the dynamic contact angle maintains a value ~90° until t*=8. Then, it increases slowly as the entire mass of the liquid moves vertically upward and rebounds from the particle surface; this is in agreement with the results presented in the work of [1]. In the specific study, they have also noted that the contact angle increases with further increase of particle temperature above Leidenfrost point. As it is proposed by [76], an increase in surface temperature results in higher vaporization rate near the triple-contact point, which consequently reduces wetting by increasing the contact angle. This increase in contact-angle values also indicates the transition to the boiling and Leidenfrost regimes. Therefore a contact angle value of 180° was assumed for $T_W > T_L$. This value can also be deduced from the Young's law, $\cos\theta=(\sigma_{Solid\text{-}Vapour}- \sigma_{Solid\text{-}Liquid})/ \sigma_{Liquid\text{-}Vapour}$, which relates the contact angle to the interfacial surface tension [209]. Due to the presence of a vapour cushion at the liquid-solid interface, the solid terms can be replaced by the vapour terms in the formula and thus a value of θ=180° is calculated. This value indicates that the levitating droplet in the

Leidenfrost regime takes a spherical shape in the case of gentle deposition. However, due to the impact, the droplet deforms during the spreading and recoiling, which leads to a change in the contact angle until the droplet rebounds from the surface.

As it has already been discussed for cases characterized by different Weber numbers (Figure 4.6b), the particle temperature does not affect the spreading rate during the early stages ($t^*=1.2$) of impact, while subsequently, the spreading diameter increases to its maximum value. This is expected as the motion of the droplet is dominated by the kinetic energy resulting from its impact onto the solid particle. Considering an unaltered initial droplet temperature of 25°C, it can be inferred due to the gradual and finite transfer of energy from the heated particle to the spreading liquid that the droplet has similar values of viscosity and Reynolds number at the early stages of droplet impingement for all the examined cases, regardless of the particle temperature [208]. Therefore, similar hydrodynamics are obtained. As the droplet continues to spread, the viscosity and surface tension effects of the liquid become gradually more dominant. Eventually, a maximum spread diameter is reached and the droplet retracts. By increasing the particle temperature, the droplet reaches to its maximum spreading diameter in shorter time, yet the maximum spreading factor decreases. The spreading process at higher particle temperature is hindered due to the stronger evaporation at the contact line, which leads to higher apparent dynamic contact angle values [76].

For low particle temperature ($T_P=140$°C), the droplet reaches to its final shape approximately at $t^*=15$ and the spreading factor becomes constant. For $T_P=260$°C, the spreading factor continues to oscillate (spread and recoil) with an amplitude decreasing with time. This behaviour is due to competition between inertial, viscosity and surface tension forces. As the particle temperature increases, the increasing heat transfer rate between the solid particle and liquid, results to a larger reduction rate of liquid viscosity near the solid-liquid interface [208]. The consequent decrease of kinetic-energy dissipation and the liquid friction caused by the

decrease of viscosity is responsible for the faster recoiling behaviour. As inertia eventually reaches an equilibrium to the viscous and surface tension forces, this variation decreases until spreading factor reaches to a constant value. At the Leidenfrost regime (T_P=340°C), recoiling continues until the spreading factor reaches a value of zero, which coincides with the droplet rebound from the surface [76].

4.2.3. Maximum spreading diameter

The maximum speeding factor (β_{max}) at the initial impact stage is one of the important parameters to characterise droplet impingement dynamics and subsequently the respective heat transfer in the droplet-surface interface. The maximum spreading factor (β_{max}) is defined as the maximum wetting diameter the droplet first approaches upon its impact on the surface normalised to the initial droplet diameter (~D_{max}/D_0). It usually happens at t*<3 after impact. The values of maximum spreading factor (β_{max}) at different surface temperatures (140°C<T_P<340°C) and Weber number of We=30, 50, 70, 250 were presented in Figure 4.10.

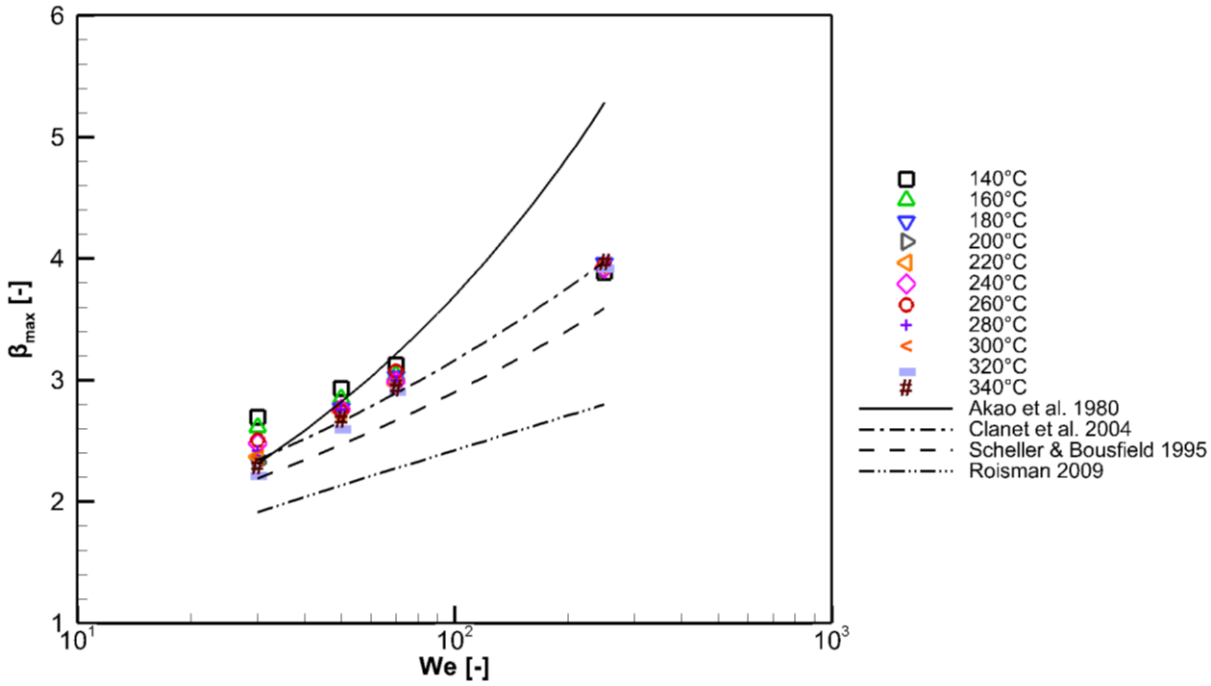

Figure 4.10: Comparison of Diesel droplet spreading characteristics at surface temperature range of 140°C<T_P<340° and Weber number of We=30, 50, 70, 250, with correlations of Akao [101], *Clanet et al.* [99], *Roisman* [100] *and Scheller et al.* [102]

In addition, the experimental data for maximum spreading factor (β_{max}) were also compared with the existing correlations of Akao [101], Clanet et al. [99], Roisman[100] and Scheller et al. [102]. These correlations are listed in Table 3.3.

It can be seen that, in general, the values of β_{max} in all these cases increases with an increase in Weber number. The observed trend can be attributed to increase in the droplet surface deformation which is driven by an increase in the impact kinetic energy. The maximum spreading factor (β_{max}) also shows higher dependency to the impact Weber number rather than to the particle temperature. The variations in β_{max} with the particle temperature can be observed especially in the low Weber number cases which indicate decrease in β_{max} with increasing surface temperature. Similar behaviour has been reported in [1]. It can be attributed to the transient heat transfer at particle surface which leads to vaporization at the advancing contact line wherein the intensity of vaporization depends on the values of the wall-surface superheat limit. The vaporization rate increases as the particle temperature increases; this prevents the surface wetting, resulting a reduction in the observed values of β_{max} [109]. These variations reduce in the larger values of impact Weber number. In the low Weber number cases, surface tension remains the dominating parameter for droplet spreading. The gradient of interfacial surface tension is larger in the flow process of droplet impingement at lower Weber numbers, due to longer contact time; thus resulting in greater heat transfer. The latter affects the spreading behaviour due to significant change of physical properties.

In the cases of higher impact Weber number as the effect of inertia compared to the heat transfer on effect become less dominant inertial force and also due to shorter impact time scale, which hinders the heat transfer effect on the variation of physical properties of the droplet liquid during the initial spreading phase. Therefore, the particle temperature effect on the values of maximum spreading factor (β_{max}) is insignificant at higher impact Weber number cases.

In order to study the effect of particle temperature on the variation of maximum spreading factor (β_{max}), the standard deviations of all observed values (Figure 4.10) were calculated for all surface temperatures at each impact Weber number (We=30, 50, 70 and 250) and listed in Table 4.2. The represented data for each Impact Weber number point out that the most of the deviations occurs in the lower impact Weber numbers (i.e. 13.04% at We=30); however, as impact Weber increases the effect of surface temperature decreases and the maximum spreading factor become approximately independent from the particle surface temperature (i.e. 2.58% at We=250).

Impact Weber number	30	50	70	250
Standard deviation	13.04%	7.71%	5.74%	2.58%

Table 4.2: Computed standard deviations of maximum spreading factor for Diesel fuel droplet at the particle surface temperature range of 140°C<Tp<340°C and impact Weber number of We=30, 50, 70 and 250

Prediction of Clanet et al. [99] correlation was in better agreement with the experimental data at all surface temperature. Deviations were lower for Clanet et al. [99] correlation compared with other correlations. These deviation are listed in the Table 4.3; a deviation range, related for the examined surface temperatures are given for each tested impact Weber number. Highest deviations are related to the higher impact Weber number. The empirical model of Akao [101] ($\sim 0.61We^{0.39}$) was also in good agreement with the experimental data, in the lower impact Weber number (We<70). The large deviation of empirical correlations from the experimental data in the cases of large Weber and Reynolds number has been also reported in [1], [21].

The most important reason of the deviations observed between the correlations and the experimental data is the ignorance of the curvature effect in the mentioned correlations where the role of gravity and centrifugal force has not been taken into the account [172]. The gravity

effect is neglected in the models for the case of impact on flat surfaces as the gravity component is zero at the advancing contact line of the spreading lamella in the radial direction.

In addition, geometric limitation of the models is another source of error; the forming of the spreading lamella on the curved particle surface takes a complex shape during spreading and specifically at the time of the maximum spreading factor occurrence. It consists of a thin central film connecting the thicker bent rim in the periphery of the droplet (See Figure 4.5c at t*=2.86). The theoretical correlations were simplified the latter complex shape with a disk with uniform thickness and curvature which is another source of error in their predictions.

Correlation / We	Akao [101]	Clanet et al. [99]	Scheller et al. [102]	Roisman [100]
30	0.62-14.22%	0.11-13.08%	2.79-18.67%	15.14-29%
50	0.97-6.98%	0.58-9.25%	6.35-15.80%	19.08-27.24%
70	2.89-9.6%	1.35-7.39%	8.98-14.56%	22.45-27.24%
250	33.05-35.69%	0.19-2.38%	7.51-9.49%	27.91-29.45%

Table 4.3: Deviation of the experimental data of droplet maximum spreading factor correlations listed in Table 3.3.

4.3. Film thickness

Figure 4.11 shows the spatial variation of the spreading lamella on the spherical particle at different spreading angles, as computed by the image processing procedure described in Figure 2.17. The various lines shown in the figure correspond to different time instances during the spreading phase. The x-axis of the figure corresponds to the circumferential angle along the particle periphery; zero value corresponds to the north pole of the particle. The profile indicates that the film thickness at the north pole of the particle initially reduces in the impact direction and increases in the polar direction; this results to thinner lamella film and thicker rim (t*=1.82 and t*=2.65). The droplet spreads symmetrically around the particle north pole during the

initial stage of the impact (t*=0.78); however the distribution becomes slightly uneven as time advances (t*=1.82, 2.65 and 3.86).

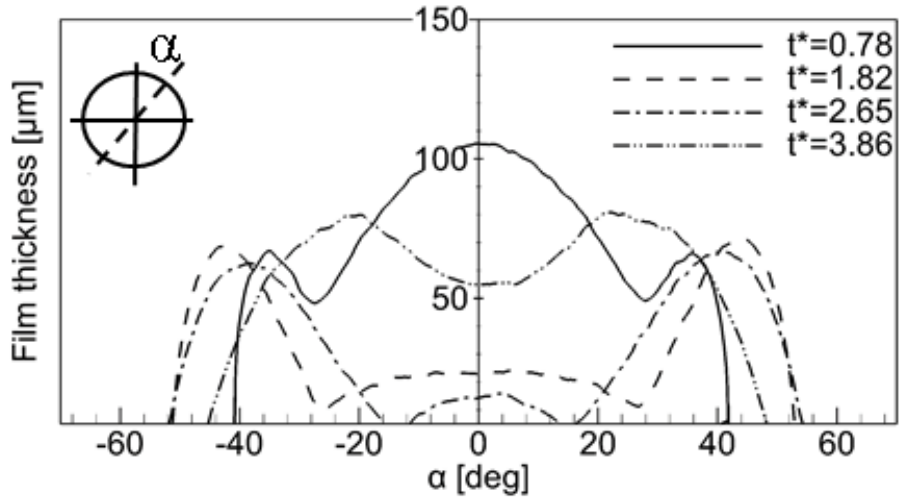

Figure 4.11: Spatial variation of the flowing lamella on the spherical target at different time steps after the droplet impact. The impact Weber number and particle surface temperature are 30 and 200°C, respectively.

The temporal variation of film thickness on the north pole of the particle (as defined in Figure 2.17c) is shown on Figure 4.12a as function of the impact Weber number at a fixed temperature of T_P=160°C on a log-log scale; Figure 4.12b shows the film thickness as function of wall temperature at a fixed We=30. As it has been proposed in [153], the time variation of the film thickness on the north pole of the particle can be divided into 3 stages termed as: (i) the initial droplet deformation stage, (ii) the inertia dominated stage and (iii) the viscosity dominated stage. In the first phase, the droplet free surface is not affected by the presence of the particle surface, meaning that the droplet half-cross section closer to the particle north pole moves downwards with the initial velocity. In the second phase, where the inertial force decreases in magnitude, the viscous forces become more influential. Finally, in the third phase, viscous, surface tension and gravity, determine the behaviour of film thickness variation.

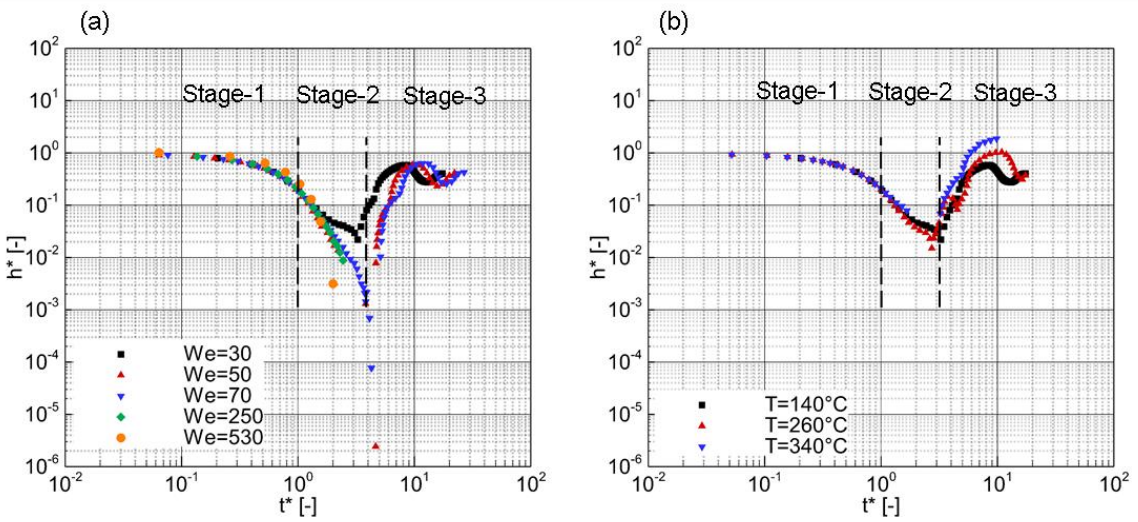

Figure 4.12: Temporal variation of spreading lamella thickness on the north pole of the heated particle (a) Effect of We at T_P=160°C and (b) Effect of surface temperature at We=30.

In the first stage (t*<1), all measured points collapse onto a single curve, an additional indication of the insignificant effect of the impact Weber number effect and particle temperature, while h* values reduce from 1 down to 0.5. Analysing this stage for different droplet-particle size ratios shows that the liquid in the north pole of the particle is not affected by the particle [153]. In the second stage (1<t*<2), the film thickness reduces at much higher rate especially for higher values of the Weber number (We>50). In the cases of We=250 and 530, this reduction continues until the film thickness becomes practically non-detectable by the visualization system. This means that the droplet deforms into a hollow ring with a dry area in the north pole of the particle surface. In the third stage (t*>2), following a strong retraction, the film thickness increases again for We=30, 50 and 70. During this stage, the droplet exhibits a weak oscillatory behaviour until the equilibrium condition is reached. The film thickness at the end of the third stage is similar for all We values tested. In the case of higher We values (We=250 and 530), the droplet breaks up during the initial stage and thus, it is no longer possible to measure the film thickness variation, as the liquid film does not have a continuous interface; this can be depicted in Figure 4.1f and 5g at t*=8.1. Figure 4.12b also emphasizes that the heat transfer at the liquid-solid interface is fairly insignificant on the film thickness at

the north pole of the particle for the first two stages, while it evolves differently in the third stage where the droplet goes to the recoiling phase; the film thickness starts to increases earlier at higher particle temperatures.

4.4. Summary

An experimental investigation of a Diesel fuel droplet impacting vertically at the north pole of a solid heated brass spherical particle has been presented in this paper. The parameters considered, in order to characterize the temporal evolution of the impact phenomenon, were the particle temperature and impact Weber number. With use of high speed imaging technique and appropriate image processing, the effect of these parameters on the dynamics of droplet spreading and the final post-impact outcome were recorded.

5. Conclusions and outlook

5.1. Conclusions

In the first part of this study, new experimental data for the impact of standard Diesel fuel droplets on a heated flat surface within a gaseous (air) environment at 1 and 2 bar pressure has been investigated for a wide range of Weber number and surface temperature values, employing high speed visualization. The six distinct impact regimes observed have been indicated on the We-T map for all conditions tested; these are termed as stick, partial-rebound, breakup, breakup-rebound, splash and rebound. Critical (We, T) value pairs have been identified, which signify the transition to breakup, splash and rebound regimes. At 1 bar air pressure, splash occurs for We>490 regardless of the wall-surface temperature value. The rebound regime transition to which, in essence, indicates that Leidenfrost condition, was observed for T_W>340°C. The breakup regime was observed for We>350 and 270°C<T_W<T_L. By increasing the ambient air pressure to 2 bars, the critical We number for splash was reduced to 350 and the Leidenfrost-point temperatures of rebound and breakup-rebound regimes were increased by 20°C and 30°C, respectively. In addition, the transition line of breakup regime was shifted by nearly 70°C. The above observation shows the significant effect of chamber pressure on the outcome regimes, especially at surface temperatures above Diesel average boiling temperature.

The effect of wall-surface temperature and impact Weber number on wetting parameters (spreading factor and dynamic contact angle) have been experimentally assessed. Experimental and available numerical results in the literature were found to be in a good agreement in terms of droplet shapes, spreading behaviour, and oscillation frequency of the droplet interface. It has also been confirmed that by increasing wall-surface temperature, the droplet exhibits a strongly oscillating behaviour during the expansion and recoil phases, due to a reduction of liquid

viscosity at higher surface temperature. This stronger recoiling behaviour also increases the value of the dynamic contact angle with the solid surface. In addition, an increase in the Weber number results in a larger value of the spreading factor while the oscillating frequency and final droplet shape remain unchanged.

To the best of authors' knowledge, this the first attempt to classify the impact outcome of a complex hydrocarbon fuel droplet on a flat heated surface. As thermal induced effects are fairly different between multi- and single component liquids. Comparisons with the available experimental data for the single component fluids clearly shows significant differences, especially in terms of transition to Leidenfrost and breakup regimes; differences in liquid composition and non-homogeneity of the Diesel fuel droplet at the temperature above any of its component's boiling temperature, results in different flow process and evaporating behaviour during the impact, and consequently the final outcome.

In the second part, an experimental investigation of a Diesel fuel droplet impacting vertically at the north pole of a solid heated brass spherical particle has been presented. The effect of particle temperature and impact Weber number on the dynamics of droplet spreading, film thickness variation and the final post-impact outcome were reported. This is the first time that the post-impact outcomes regime have been mapped for a multi-component fuel droplet impacting onto a heated particle; due to the wide range of impact Weber number and particle temperature values examined, important information on the observed outcome has been extracted. Seven distinctive outcome regimes were observed and mapped on the We-T diagram. It can be noted that the droplet disintegration was promoted by increasing the impact Weber number and the particle temperature. The dynamic contact angle generally increases with the particle temperature. The initial spreading phase, where the inertia is the dominated force, exhibits a similar temporal evolution for all the cases examined. The maximum spreading factor increases with increasing impact Weber number and decreases with particle temperature.

Also, by increasing the particle temperature, the droplet vibrates on the particle surface, which causes a weaker oscillatory variance of its shape after the maximum spreading diameter is reached. This can be explained by the change of liquid physical properties, especially the viscosity, due to heat transfer at the solid-liquid interface. The non-dimensional film thickness at the north pole of the particle was measured and the effect of particle temperature and impact Weber number were investigated; effect of We on the thickness is more profound compared to the effect of heat transfer. Due to the presence of gravitational and centrifugal forces in case of droplet impact on to a particle, the spreading factor is larger compared to flat surface case under similar conditions.

5.2. Outlook

Development of experimental data followed by CFD modelling which could allow a direct comparison, can open hidden doors that might disclose more physical problems. From an experimental and modelling perspective all the above mentioned phenomena still lack a complete and physically sound description. For instance, the range of the influential parameters should be extended to cover the operation conditions of the respective application.

High-speed micro Schlieren technique can be employed as a convenient and easy-to-setup optical system to quantify the vaporization of the impacting fuel droplet on the heated surfaces in order to validate the available evaporative CFD models for multicomponent fluids.

Oblique droplet-particle collision should be also further investigated to study the effect of obliquity on the droplet hydrodynamic and consequently the heat transfer.

Additionally, the mid-air head-on droplets collision in hot gaseous environment, will also help to address the rationale of describing spray-wall interaction based on the knowledge of single droplet impacts.

Finally, the droplet impact/mid-air breakup in presence of a well-defined cross flow rather than stagnant condition, can reveal the dynamic of the spray droplets interactions inside the combustion chamber.

Bibliography

[1] S. Mitra, T. Nguyen, E. Doroodchi, and V. Pareek, "On wetting characteristics of droplet on a spherical particle in film boiling regime," *PhD Thesis,* 2016.

[2] G. Lechner, T. Jacobs, C. Chryssakis, and D. Assanis, "Evaluation of a narrow spray cone angle, advanced injection timing strategy to achieve partially premixed compression ignition combustion in a diesel engine," *SAE Trans. J. Engines - V114-3,* 2005.

[3] A. Moreira, A. Moita, and M. Panao, "Advances and challenges in explaining fuel spray impingement: How much of single droplet impact research is useful?," *Prog. energy Combust.,* 2010.

[4] Y. Zhang, M. Jia, H. Liu, and M. Xie, "Development of an improved liquid film model for spray/wall interaction under engine-relevant conditions," *Int. J. Multiph. Flow,* 2016.

[5] A. Yarin, "Drop impact dynamics: splashing, spreading, receding, bouncing," *Annu. Rev. Fluid Mech.,* 2006.

[6] M. Rein, "Phenomena of liquid drop impact on solid and liquid surfaces," *Fluid Dyn. Res.*, vol. 12, no. 2, pp. 61–93, Aug. 1993.

[7] S. Winnikow, "Droplet Motion in Purified Systems," *Phys. Fluids,* vol. 9, no. 1, p. 50, 1966.

[8] F. Rodriguez and R. Mesler, "The penetration of drop-formed vortex rings into pools of liquid," *J. Colloid Interface Sci.*, vol. 121, no. 1, pp. 121–129, Jan. 1988.

[9] J. P. Dear and J. E. Field, "High-speed photography of surface geometry effects in liquid/solid impact," *J. Appl. Phys.*, vol. 63, no. 4, pp. 1015–1021, Feb. 1988.

[10] R. Crooks, J. Cooper-White, and D. Boger, "The role of dynamic surface tension and elasticity on the dynamics of drop impact," *Chem. Eng. Sci.,* 2001.

[11] N. Mourougou-Candoni, B. Prunet-Foch, F. Legay, M. Vignes-Adler, and K. Wong, "Influence of Dynamic Surface Tension on the Spreading of Surfactant Solution Droplets Impacting onto a Low-Surface-Energy Solid Substrate," *J. Colloid Interface Sci.*, vol. 192, no. 1, pp. 129–141, Aug. 1997.

[12] X. Zhang and O. A. Basaran, "Dynamic Surface Tension Effects in Impact of a Drop with a Solid Surface," *J. Colloid Interface Sci.*, vol. 187, no. 1, pp. 166–178, Mar. 1997.

[13] T. Okawa, T. Shiraishi, and T. Mori, "Effect of impingement angle on the outcome of single water drop impact onto a plane water surface," *Exp. Fluids*, vol. 44, no. 2, pp. 331–339, Feb. 2008.

[14] I. Roisman and R. Rioboo, "Normal impact of a liquid drop on a dry surface: model for spreading and receding," *R. ...*, 2002.

[15] Š. Šikalo, H. Wilhelm, and I. Roisman, "Dynamic contact angle of spreading droplets: Experiments and simulations," *Phys. Fluids (,* 2005.

[16] A.-B. Wang, C.-H. Lin, and C.-C. Chen, “The critical temperature of dry impact for tiny droplet impinging on a heated surface,” *Phys. Fluids*, May 2000.

[17] A. L. Yarin, “DROP IMPACT DYNAMICS: Splashing, Spreading, Receding, Bouncing…,” *Annu. Rev. Fluid Mech.*, vol. 38, no. 1, pp. 159–192, 2006.

[18] A. L. Yarin and D. A. Weiss, “Impact of drops on solid surfaces: self-similar capillary waves, and splashing as a new type of kinematic discontinuity,” *J. Fluid Mech.*, vol. 283, no. 1, p. 141, Jan. 1995.

[19] M. Bussmann, J. Mostaghimi, and S. Chandra, “On a three-dimensional volume tracking model of droplet impact,” *Phys. Fluids*, May 1999.

[20] G. LENEWEIT, R. KOEHLER, K. G. ROESNER, and G. SCHÄFER, “Regimes of drop morphology in oblique impact on deep fluids,” *J. Fluid Mech.*, vol. 543, no. 1, p. 303, Nov. 2005.

[21] C. Mundo, M. Sommerfeld, and C. Tropea, “Droplet-wall collisions: Experimental studies of the deformation and breakup process,” *Int. J. Multiph. Flow*, vol. 21, no. 2, pp. 151–173, Apr. 1995.

[22] M. Pasandideh-Fard and S. Chandra, “A three-dimensional model of droplet impact and solidification,” *Int. J.*, 2002.

[23] S. L. Zhbankova and A. V. Kolpakov, “Collision of water drops with a plane water surface,” *Fluid Dyn.*, vol. 25, no. 3, pp. 470–473, 1990.

[24] Š. Šikalo, N. Delalić, and E. Ganić, “Hydrodynamics and heat transfer investigation of air–water dispersed flow,” *Exp. Therm. fluid Sci.*, 2002.

[25] Š. Šikalo, C. Tropea, and E. Ganić, “Dynamic wetting angle of a spreading droplet,” *Exp. Therm. Fluid Sci.*, 2005.

[26] C. Antonini, F. Villa, I. Bernagozzi, and A. Amirfazli, “Drop rebound after impact: The role of the receding contact angle,” *Langmuir*, 2013.

[27] Š. Šikalo, C. Tropea, and E. Ganić, “Impact of droplets onto inclined surfaces,” *J. Colloid Interface Sci.*, 2005.

[28] S. Yao and K. Cai, “The dynamics and Leidenfrost temperature of drops impacting on a hot surface at small angles,” *Exp. Therm. Fluid Sci.*, 1988.

[29] R. Rioboo, C. Tropea, and M. Marengo, “Outcomes from a drop impact on solid surfaces,” *At. Sprays*, 2001.

[30] M. Pasandideh-Fard, Y. Qiao, and S. Chandra, “Capillary effects during droplet impact on a solid surface,” *Phys. Fluids (*, 1996.

[31] D. Vadillo, A. Soucemarianadin, and C. Delattre, “Dynamic contact angle effects onto the maximum drop impact spreading on solid surfaces,” *Phys. Fluids (*, 2009.

[32] G. Castanet, T. Lienart, and F. Lemoine, “Dynamics and temperature of droplets impacting onto a heated wall,” *Int. J. Heat Mass*, 2009.

[33] H. Staat, H. Nair, T. Tran, and A. van Houselt, “The Leidenfrost temperature increase for impacting droplets on carbon-nanofiber surfaces,” *APS Meet.*, 2014.

[34] M. van Limbeek, M. Shirota, P. Sleutel, and C. Sun, “Vapour cooling of poorly

conducting hot substrates increases the dynamic Leidenfrost temperature," *Int. J.*, 2016.

[35] J. Liu, H. Vu, S. Yoon, and R. Jepsen, "Splashing phenomena during liquid droplet impact," *At.*, 2010.

[36] L. Xu, W. Zhang, and S. Nagel, "Drop splashing on a dry smooth surface," *Phys. Rev. Lett.*, 2005.

[37] S. Yoon, R. Jepsen, S. James, and J. Liu, "Are drop-impact phenomena described by Rayleigh-Taylor or Kelvin-Helmholtz theory?," *Drying*, 2009.

[38] S. Yoon, R. Jepsen, M. Nissen, and T. O'Hern, "Experimental investigation on splashing and nonlinear fingerlike instability of large water drops," *J. Fluids*, 2007.

[39] D. Bartolo, F. Bouamrirene, E. Verneuil, A. Buguin, P. Silberzan, and S. Moulinet, "Bouncing or sticky droplets: impalement transitions on micropatterned surfaces," 2005.

[40] F. Villa, C. Antonini, I. V. Roisman, and M. Marengo, "Experimaental Analysis of High Weber Number Drop Impact onto Super-Hydrophobic and Hydrophobic Surfaces," in *Proceedings of the 15th International Heat Transfer Conference*, 2014.

[41] G. E. Cossali, G. Brunello, A. Coghe, and M. Marengo, "IMPACT OF A SINGLE DROP ON A LIQUID FILM: EXPERIMENTAL ANALYSIS AND COMPARISON WITH EMPIRICAL MODELS," *Ital. Congr. Thermofluid Dyn. UIT, Ferrara, 30 June-2 July*, 1999.

[42] E. LAJEUNESSE and Y. COUDER, "On the tip-splitting instability of viscous fingers," *J. Fluid Mech.*, vol. 419, p. S0022112000001324, Sep. 2000.

[43] N. Z. MEHDIZADEH, S. CHANDRA, and J. MOSTAGHIMI, "Formation of fingers around the edges of a drop hitting a metal plate with high velocity," *J. Fluid Mech.*, vol. 510, pp. 353–373, Jul. 2004.

[44] C. D. Stow and M. G. Hadfield, "An Experimental Investigation of Fluid Flow Resulting from the Impact of a Water Drop with an Unyielding Dry Surface," *Proc. R. Soc. A Math. Phys. Eng. Sci.*, vol. 373, no. 1755, pp. 419–441, Jan. 1981.

[45] Š. Šikalo and E. N. Ganić, "Phenomena of droplet–surface interactions," *Exp. Therm. Fluid Sci.*, vol. 31, no. 2, pp. 97–110, Nov. 2006.

[46] A. S. Moita and A. L. Moreira, "THE DYNAMIC BEHAVIOUR OF SINGLE DROPLETS IMPACTING ONTO A FLAT SURFACE," *ILASS-Europe Zaragoza*, vol. 9, 2002.

[47] J. Shen, J. Liburdy, D. Pence, and V. Narayanan, "Single Droplet Impingment: Effect of Nanoparticles," in *Volume 2: Fora*, 2008, pp. 621–628.

[48] T. Tran, H. Staat, A. Susarrey-Arce, and T. Foertsch, "Droplet impact on superheated micro-structured surfaces," *Soft Matter*, 2013.

[49] H. J. J. Staat *et al.*, "Phase diagram for droplet impact on superheated surfaces," *J. Fluid Mech.Phys. Rev. Lett. J. Fluid Mech*, vol. 779, no. 772, pp. 630–648, 2015.

[50] M. Shirota, M. van Limbeek, C. Sun, and A. Prosperetti, "Dynamic Leidenfrost effect: relevant time and length scales," *Phys. Rev.*, 2016.

[51] H. Nair, H. Staat, T. Tran, A. van Houselt, and A. Prosperetti, "The Leidenfrost

temperature increase for impacting droplets on carbon-nanofiber surfaces," *Soft Matter*, 2014.

[52] W. Zhang, T. Yu, J. Fan, W. Sun, and Z. Cao, "Droplet impact behavior on heated micro-patterned surfaces," *J. Appl. Phys.*, 2016.

[53] V. Bertola, "An impact regime map for water drops impacting on heated surfaces," *Int. J. Heat Mass Transf.*, 2015.

[54] G. Liang, S. Shen, Y. Guo, and J. Zhang, "Boiling from liquid drops impact on a heated wall," *Int. J. Heat Mass*, 2016.

[55] C. Bai and A. Gosman, "Development of methodology for spray impingement simulation," 1995.

[56] A. Moita and A. Moreira, "Drop impacts onto cold and heated rigid surfaces: morphological comparisons, disintegration limits and secondary atomization," *Int. J. Heat Fluid Flow*, 2007.

[57] S. Mitra, "Droplet particle interaction in a flowing gas stream," no. October, 2016.

[58] H. P. Kavehpour, B. Ovryn, and G. H. McKinley, "Microscopic and Macroscopic Structure of the Precursor Layer in Spreading Viscous Drops," *Phys. Rev. Lett.*, vol. 91, no. 19, p. 196104, Nov. 2003.

[59] S. S. Yoon and P. E. DesJardin, "Modelling spray impingement using linear stability theories for droplet shattering," *Int. J. Numer. Methods Fluids*, vol. 50, no. 4, pp. 469–489, 2006.

[60] P. H. Z Levin, "Levin, Z. and Hobbs, P. V., Charge separation due... - Google Scholar," *Am. Meteorol. Soc.*, vol. 51, pp. 577–586, 1970.

[61] A. Gopinath, "Droplet rebound from rigid or strongly hydrophobic sur- faces," 2005.

[62] R. Rioboo, M. Marengo, and C. Tropea, "Time evolution of liquid drop impact onto solid, dry surfaces," *Exp. Fluids*, 2002.

[63] M. Marengo, C. Antonini, and I. Roisman, "Drop collisions with simple and complex surfaces," *Curr. Opin. Colloid*, 2011.

[64] A. Karl and A. Frohn, "Experimental investigation of interaction processes between droplets and hot walls," *Phys. Fluids*, 2000.

[65] I. V. Roisman, L. Opfer, C. Tropea, M. Raessi, J. Mostaghimi, and S. Chandra, "Drop impact onto a dry surface: Role of the dynamic contact angle," *Colloids Surfaces A Physicochem. Eng. Asp.*, vol. 322, no. 1, pp. 183–191, 2008.

[66] I. Bayer and C. Megaridis, "Contact angle dynamics in droplets impacting on flat surfaces with different wetting characteristics," *J. Fluid Mech.*, 2006.

[67] N. Mishra, Y. Zhang, and A. Ratner, "Effect of chamber pressure on spreading and splashing of liquid drops upon impact on a dry smooth stationary surface," *Exp. Fluids*, 2011.

[68] Anthony Dix, "Pressure effects on drop impact with a smooth dry surface (Book, 2007) [WorldCat.org]," University of Iowa, 2007.

[69] V. H. López and A. R. Kennedy, "Flux-assisted wetting and spreading of Al on TiC," *J.*

Colloid Interface Sci., vol. 298, no. 1, pp. 356–362, Jun. 2006.

[70] P. T. Vianco and D. R. Frear, "Issues in the replacement of lead-bearing solders," *JOM*, vol. 45, no. 7, pp. 14–19, Jul. 1993.

[71] B. Wang, Y. Zhang, L. Shi, J. Li, and Z. Guo, "Advances in the theory of superhydrophobic surfaces," *J. Mater. Chem.*, vol. 22, no. 38, p. 20112, 2012.

[72] D. R. Frear, W. B. (Wendell B. Jones, K. R. (Kenneth R. . Kinsman, and M. and M. S. E. Minerals, *Solder mechanics : a state of the art assessment*. Warrendale Pa.: Minerals, Metals & Materials Society, 1991.

[73] G. Kumar and K. N. Prabhu, "Review of non-reactive and reactive wetting of liquids on surfaces," *Adv. Colloid Interface Sci.*, vol. 133, no. 2, pp. 61–89, Jun. 2007.

[74] D. Quã Erã, "Rough ideas on wetting," *Physica A*, vol. 313, pp. 32–46, 2002.

[75] C. . Pedersen, "An experimental study of the dynamic behavior and heat transfer characteristics of water droplets impinging upon a heated surface," *Int. J. Heat Mass Transf.*, vol. 13, no. 2, pp. 369–381, Feb. 1970.

[76] S. Chandra and C. T. Avedisian, "On the Collision of a Droplet with a Solid Surface," *Proc. R. Soc. A Math. Phys. Eng. Sci.*, vol. 432, no. 1884, pp. 13–41, Jan. 1991.

[77] W. M. Healy, J. G. Hartley, and S. I. Abdel-Khalik, "On the Validity of the Adiabatic Spreading Assumption in Droplet Impact Cooling," *Repr. from Int. J. Heat Mass Transf.*, vol. 44, pp. 3869–3881, 2001.

[78] S. Kandlikar, M. Steinke, and A. Singh, "Effects of Weber number and surface temperature on the boiling and spreading characteristics of impinging water droplets," *Proc. NHTC*, 2001.

[79] Š. Šikalo, M. Marengo, C. Tropea, and E. Ganić, "Analysis of impact of droplets on horizontal surfaces," *Exp. Therm. fluid*, 2002.

[80] Y. Ge and L. Fan, "Droplet–particle collision mechanics with film-boiling evaporation," *J. Fluid Mech.*, 2007.

[81] R. Chen, S. Chiu, and T. Lin, "Resident time of a compound drop impinging on a hot surface," *Appl. Therm. Eng.*, 2007.

[82] G. Strotos, M. Gavaises, and A. Theodorakakos, "Numerical investigation of the cooling effectiveness of a droplet impinging on a heated surface," *Int. J.*, 2008.

[83] K. Yokoi, D. Vadillo, and J. Hinch, "Numerical studies of the influence of the dynamic contact angle on a droplet impacting on a dry surface," *Phys. Fluids (1994-*, 2009.

[84] H. Fujimoto, Y. Oku, T. Ogihara, and H. Takuda, "Hydrodynamics and boiling phenomena of water droplets impinging on hot solid," *Int. J.*, 2010.

[85] E. Negeed, S. Hidaka, M. Kohno, and Y. Takata, "High speed camera investigation of the impingement of single water droplets on oxidized high temperature surfaces," *Int. J.*, 2013.

[86] G. Liang, X. Mu, Y. Guo, S. Shen, S. Quan, and J. Zhang, "Contact vaporization of an impacting drop on heated surfaces," *Exp. Therm. Fluid Sci.*, 2015.

[87] C. Ukiwe and D. Kwok, "On the maximum spreading diameter of impacting droplets on

well-prepared solid surfaces," *Langmuir*, 2005.

[88] C. Antonini, A. Amirfazli, and M. Marengo, "Drop impact and wettability: From hydrophilic to superhydrophobic surfaces," *Phys. Fluids (1994-*, 2012.

[89] L. Hung and S. Yao, "Experimental investigation of the impaction of water droplets on cylindrical objects," *Int. J. Multiph. flow*, 1999.

[90] M. B. Lesser and J. E. Field, "The Impact of Compressible Liquids," *Annu. Rev. Fluid Mech.*, vol. 15, no. 1, pp. 97–122, Jan. 1983.

[91] S. T. THORODDSEN, T. G. ETOH, K. TAKEHARA, N. OOTSUKA, and Y. HATSUKI, "The air bubble entrapped under a drop impacting on a solid surface," *J. Fluid Mech.*, vol. 545, no. 1, p. 203, Dec. 2005.

[92] S. T. THORODDSEN, T. G. ETOH, and K. TAKEHARA, "Air entrapment under an impacting drop," *J. Fluid Mech.*, vol. 478, Mar. 2003.

[93] M. M. M. Driscoll and S. S. R. Nagel, "No Title," vol. 107, no. 15, p. 154502, Oct. 2011.

[94] J. M. J. Kolinski, S. M. S. Rubinstein, S. Mandre, M. M. P. Brenner, D. A. Weitz, and L. Mahadevan, "No Title," vol. 108, no. 7, p. 74503, Feb. 2012.

[95] R. C. A. van der Veen, T. Tran, D. Lohse, and C. Sun, "Direct measurements of air layer profiles under impacting droplets using high-speed color interferometry," *Phys. Rev. E*, vol. 85, no. 2, p. 26315, Feb. 2012.

[96] J. Bernardin, C. Stebbins, and I. Mudawar, "Mapping of impact and heat transfer regimes of water drops impinging on a polished surface," *J. Heat Mass Transf.*, 1997.

[97] N. Mishra, "Effect of chamber pressure on liquid drop impacts on a stationary smooth and dry surface," *Theses Diss.*, Dec. 2009.

[98] S. Yoon, B. D.-A. and Sprays, and undefined 2006, "Effects of air on splashing during a large droplet impact: Experimental and numerical investigations," *dl.begellhouse.com*.

[99] C. Clanet, C. Béguin, and D. Richard, "Maximal deformation of an impacting drop," *J. Fluid*, 2004.

[100] I. V. Roisman, "Inertia dominated drop collisions. II. An analytical solution of the Navier–Stokes equations for a spreading viscous film," *Phys. Fluids*, vol. 21, no. 5, p. 52104, May 2009.

[101] F. AKAO, "Deformation behaviors of a liquid droplet impinging onto hot metal surface," *Trans. Int. Steel Inst. Japan*, 1980.

[102] B. Scheller and D. Bousfield, "Newtonian drop impact with a solid surface," *AIChE J.*, 1995.

[103] L. Cheng, "Dynamic Spreading of Drops Impacting onto a Solid Surface," *Ind. Eng. Chem. Process Des. Dev.*, vol. 16, no. 2, pp. 192–197, Apr. 1977.

[104] C. D. Stow and M. G. Hadfield, "An Experimental Investigation of Fluid Flow Resulting from the Impact of a Water Drop with an Unyielding Dry Surface," *Proc. R. Soc. A Math. Phys. Eng. Sci.*, vol. 373, no. 1755, pp. 419–441, Jan. 1981.

[105] H. Marmanis and S. T. Thoroddsen, "Scaling of the fingering pattern of an impacting drop," *Phys. Fluids*, vol. 8, no. 6, pp. 1344–1346, Jun. 1996.

[106] N. Laan, K. G. de Bruin, D. Bartolo, C. Josserand, and D. Bonn, “Maximum Diameter of Impacting Liquid Droplets,” *Phys. Rev. Appl.*, vol. 2, no. 4, p. 44018, Oct. 2014.

[107] E. W. Collings, A. J. Markworth, J. K. McCoy, and J. H. Saunders, “Splat-quench solidification of freely falling liquid-metal drops by impact on a planar substrate,” *J. Mater. Sci.*, vol. 25, no. 8, pp. 3677–3682, Aug. 1990.

[108] T. Bennett and D. Poulikakos, “Splat-quench solidification: estimating the maximum spreading of a droplet impacting a solid surface,” *J. Mater. Sci.*, vol. 28, no. 4, pp. 963–970, 1993.

[109] S. Chandra and C. Avedisian, “On the collision of a droplet with a solid surface,” *R. ...*, 1991.

[110] Z. Tamura and Y. Tanasawa, “Evaporation and combustion of a drop contacting with a hot surface,” *Symp. Combust.*, vol. 7, no. 1, pp. 509–522, 1958.

[111] B. Kang and D. Lee, “On the dynamic behavior of a liquid droplet impacting upon an inclined heated surface,” *Exp. Fluids*, 2000.

[112] S. L. Manzello and J. C. Yang, “An experimental study of high Weber number impact of methoxy-nonafluorobutane C4F9OCH3 (HFE-7100) and n-heptane droplets on a heated solid surface,” *Int. J. Heat Mass Transf.*, vol. 45, no. 19, pp. 3961–3971, 2002.

[113] S. Nukiyama, “The maximum and minimum values of the heat-Q transmitted from metal to boiling water under atmospheric-pressure,” *Int. J. Heat Mass Transf.*, vol. 27, no. 7, pp. 959–970, 1934.

[114] J. G. Leidenfrost, “On the fixation of water in diverse fire,” *Int. J. Heat Mass Transf.*, vol. 9, no. 11, pp. 1153–1166, Nov. 1966.

[115] C. C. Wang AB, Lin CH, “The critical temperature of dry impact for tiny droplet impinging onto a heated surface,” *Phys Fluids*, vol. 12, pp. 1622–1625, 2000.

[116] J. Naber and P. Farrell, “Hydrodynamics of droplet impingement on a heated surface,” 1993.

[117] L. H. J. Wachters and N. A. J. Westerling, “The heat transfer from a hot wall to impinging water drops in the spheroidal state,” *Chem. Eng. Sci.*, vol. 21, no. 11, pp. 1047–1056, 1966.

[118] Y. M. Qiao and S. Chandra, “Boiling of droplets on a hot surface in low gravity,” *Int. J. Heat Mass Transf.*, vol. 39, no. 7, pp. 1379–1393, May 1996.

[119] N. Hatta, H. Fujimoto, K. Kinoshita, and H. Takuda, “Experimental Study of Deformation Mechanism of a Water Droplet Impinging on Hot Metallic Surfaces Above the Leidenfrost Temperature,” *J. Fluids Eng.*, vol. 119, no. 3, p. 692, 1997.

[120] H. Chaves, A. Kubitzek, and F. Obermeier, “Dynamic processes occurring during the spreading of thin liquid films produced by drop impact on hot walls,” *J. heat fluid flow*, 1999.

[121] S. Kandlikar and M. Steinke, “Contact angles and interface behavior during rapid evaporation of liquid on a heated surface,” *Int. J. Heat Mass Transf.*, 2002.

[122] A. Alizadeh Vaibhav Bahadur Sheng Zhong Wen Shang Ri Li, “IdeaExchange@UAkron Temperature Dependent Droplet Impact Dynamics on Flat

and Textured Surfaces."

[123] J. H. Moon, M. Cho, and S. H. Lee, "Dynamic wetting and heat transfer characteristics of a liquid droplet impinging on heated textured surfaces," *Int. J. Heat Mass Transf.*, vol. 97, pp. 308–317, 2016.

[124] G. Liang and I. Mudawar, "Review of drop impact on heated walls," *Int. J. Heat Mass Transf.*, vol. 106, pp. 103–126, Mar. 2017.

[125] C. Tang, J. Zhao, P. Zhang, and C. Law, "Dynamics of internal jets in the merging of two droplets of unequal sizes," *J. Fluid Mech.*, 2016.

[126] J. Burton, A. Sharpe, R. van der Veen, and A. Franco, "Geometry of the vapor layer under a Leidenfrost drop," *Phys. Rev.*, 2012.

[127] M. Khavari, C. Sun, D. Lohse, and T. Tran, "Fingering patterns during droplet impact on heated surfaces," *Soft Matter*, 2015.

[128] S. Nishio and M. Hirata, "Direct contact phenomenon between a liquid droplet and high temperature solid surface," *Sixth Int. Heat Transf.*, 1978.

[129] G. Celata, M. Cumo, A. Mariani, and G. Zummo, "Visualization of the impact of water drops on a hot surface: effect of drop velocity and surface inclination," *Heat mass Transf.*, 2006.

[130] C. Zhang and H. Liu, "Effect of drop size on the impact thermodynamics for supercooled large droplet in aircraft icing," *Phys. Fluids*, 2016.

[131] J. BERNARDIN, C. Stebbins, and I. Mudawar, "Effects of surface roughness on water droplet impact history and heat transfer regimes," *Int. J. Heat*, 1996.

[132] C. Clavijo, J. Crockett, and D. Maynes, "Hydrodynamics of droplet impingement on hot surfaces of varying wettability," *Int. J. Heat Mass*, 2017.

[133] I. Buchmüller, "Influence of pressure on Leidenfrost effect," *PhD Thesis*, 2014.

[134] A. Moreira, A. Moita, E. Cossali, and M. Marengo, "Secondary atomization of water and isooctane drops impinging on tilted heated surfaces," *Fuel*, 2007.

[135] R. Rioboo, C. Bauthier, J. Conti, M. Voué, and J. De Coninck, "Experimental investigation of splash and crown formation during single drop impact on wetted surfaces."

[136] G. Riboux and J. Gordillo, "The diameters and velocities of the droplets ejected after splashing," *J. Fluid Mech.*, 2015.

[137] W. Bouwhuis, R. van der Veen, T. Tran, and D. Keij, "Maximal air bubble entrainment at liquid-drop impact," *Phys. Rev.*, 2012.

[138] G. E. Cossali, M. Marengo, and M. Santini, "Secondary atomisation produced by single drop vertical impacts onto heated surfaces," *Exp. Therm. Fluid Sci.*, vol. 29, no. 8, pp. 937–946, 2005.

[139] S. Akhtar, G. Nasr, and A. Yule, "Characteristics of water droplet impaction behavior on a polished steel heated surface: Part II," *At. Sprays*, 2007.

[140] V. Carey, "Liquid-vapor phase-change phenomena," 1992.

[141] S. Olek, Y. Zvirin, and E. Elias, “The relation between the rewetting temperature and the liquid-solid contact angle,” *Int. J. Heat Mass Transf.*, 1988.

[142] S. Lee and S. Ryu, “Recent progress of spray-wall interaction research,” *J. Mech. Sci. Technol.*, 2006.

[143] M. Rein, “Interactions between drops and hot surfaces,” *Drop-Surface Interact.*, 2002.

[144] G. E. Cossali, M. Marengo, and M. Santini, “Thermally induced secondary drop atomisation by single drop impact onto heated surfaces,” *Int. J. Heat Fluid Flow*, vol. 29, no. 1, pp. 167–177, 2008.

[145] A. J. Yule, “Droplet Impaction on a Heated Surface at High Weber Numbers,” no. SEPTEMBER 2001, 2015.

[146] D. Segawa, T. Kadota, S. Nakaya, and K. Takemura, “A liquid film or droplet of miscible binary fuel burning on a heated surface at elevated pressures,” *Proc. Combust. Inst.*, 2009.

[147] A. Mahulkar, G. Marin, and G. Heynderickx, “Droplet–wall interaction upon impingement of heavy hydrocarbon droplets on a heated wall,” *Chem. Eng. Sci.*, 2015.

[148] W.-J. Yang, “Theory on vaporization and combustion of liquid drops of pure substances and binary mixtures on heated surfaces,” 1975.

[149] E. Kompinsky, G. Dolan, and E. Sher, “Experimental study on the dynamics of binary fuel droplet impacts on a heated surface,” *Chem. Eng. Sci.*, 2013.

[150] Z. Levin and P. Hobbs, “Splashing of water drops on solid and wetted surfaces: hydrodynamics and charge separation,” *Proceeding R. Soc. A*, 1971.

[151] V. V. Dubrovsky, A. M. Podvysotsky, and A. A. Shraiber, “Particle interaction in three-phase polydisperse flows,” *Int. J. Multiph. Flow*, vol. 18, no. 3, pp. 337–352, May 1992.

[152] Y. Hardalupas, A. Taylor, and J. Wilkins, “Experimental investigation of sub-millimetre droplet impingement on to spherical surfaces,” *Int. J. heat fluid*, 1999.

[153] S. Bakshi, I. Roisman, and C. Tropea, “Investigations on the impact of a drop onto a small spherical target,” *Phys Fluids*, 2007.

[154] Y. Ge, “3D numerical study on droplet-solid collisions in the Leidenfrost regime,” 2005.

[155] S. Mitra, M. Sathe, E. Doroodchi, and R. Utikar, “Droplet impact dynamics on a spherical particle,” *Chem. Eng.*, 2013.

[156] V. Sechenyh and A. Amirfazli, “An experimental study for impact of a drop onto a particle in mid-air: The influence of particle wettability,” *J. Fluids Struct.*, vol. 66, pp. 282–292, Oct. 2016.

[157] S. A. Banitabaei and A. Amirfazli, “Droplet impact onto a solid sphere: Effect of wettability and impact velocity,” *Phys. Fluids*, vol. 29, no. 6, p. 62111, Jun. 2017.

[158] and S. M. W. Y. E.Wang, J. H. Zhou, Y. L. Qin, P. L. Li, M. M. Yang, Q. Han, Y. B.Wang, “Numerical simulation for behavior of a droplet impacting onto a target spherical surface,” *J. Vib. Shock*, vol. 31, pp. 51–56, 2012.

[159] M. Driscoll and S. Nagel, “Ultrafast interference imaging of air in splashing dynamics,” *Phys. Rev. Lett.*, 2011.

[160] S. Jung and I. Hutchings, “The impact and spreading of a small liquid drop on a non-porous substrate over an extended time scale,” *Soft Matter*, 2012.

[161] G. Liang, Y. Guo, Y. Yang, S. Guo, and S. Shen, “Special phenomena from a single liquid drop impact on wetted cylindrical surfaces,” 2013.

[162] T. Gilet and J. Bush, “Droplets bouncing on a wet, inclined surface,” *Phys. Fluids*, 2012.

[163] C. Stevens, “Scaling of the splash threshold for low-viscosity fluids,” *EPL (Europhysics Lett.*, 2014.

[164] V. Bertola, “Dynamic wetting of dilute polymer solutions: the case of impacting droplets,” *Adv. Colloid Interface Sci.*, 2013.

[165] H. Fujimoto, S. Watanabe, T. Okamoto, and T. Hama, “Photographic study of hydrodynamics of drops of aqueous polymer solution impinging on hot solid,” 2015.

[166] A. Moita and A. Moreira, “Development of empirical correlations to predict the secondary droplet size of impacting droplets onto heated surfaces,” *Exp. Fluids*, 2009.

[167] A. Moita and A. Moreira, “The deformation of single droplets impacting onto a flat surface,” 2002.

[168] S. Herbert, S. Fischer, and T. Gambaryan-Roisman, “Local heat transfer and phase change phenomena during single drop impingement on a hot surface,” *Int. J. Heat Mass Transf.*, 2013.

[169] H. Nair, H. Staat, T. Tran, A. van Houselt, and A. Prosperetti, “The Leidenfrost temperature increase for impacting droplets on carbon-nanofiber surfaces,” *Soft Matter*, 2014.

[170] J. Moon, D. Kim, and S. Lee, “Spreading and receding characteristics of a non-Newtonian droplet impinging on a heated surface,” *Exp. Therm. Fluid Sci.*, 2014.

[171] A. Alizadeh, V. Bahadur, S. Zhong, and W. Shang, “Temperature dependent droplet impact dynamics on flat and textured surfaces,” *Appl. Phys.*, 2012.

[172] D. Khojasteh, A. Bordbar, R. Kamali, and M. Marengo, “Curvature effect on droplet impacting onto hydrophobic and superhydrophobic spheres.”

[173] N. Ashgriz, *Handbook of atomization and sprays: theory and applications*. 2011.

[174] T. Y. Xiong and M. C. Yuen, “Evaporation of a liquid droplet on a hot plate,” *Int. J. Heat Mass Transf.*, vol. 34, no. 7, pp. 1881–1894, Jul. 1991.

[175] C. National Instrument, “LabVIEW™ PID Control Toolkit User Manual.” National Instruments, Corp., Austin, TX, USA., 2008.

[176] J. Ziegler and N. Nichols, “Optimum settings for automatic controllers,” *trans. ASME*, 1942.

[177] C. Tropea and F.-T. Ari, “Optical Particle Characterization in Flows,” *Annu. Rev. Fluid Mech*, vol. 43, pp. 399–426, 2011.

[178] H. Well, “Agency for Toxic Substances and Disease Registry (ATSDR),” 2015.

[179] A. Date, *Analytic combustion: with thermodynamics, chemical kinetics and mass transfer*. 2011.

[180] N. I. Kolev, “Thermodynamic and transport properties of diesel fuel,” in *Multiphase Flow Dynamics 3*, Berlin, Heidelberg: Springer Berlin Heidelberg, pp. 269–302.

[181] A. Trujillo-Pino, K. Krissian, M. Alemán-Flores, and D. Santana-Cedrés, “Accurate subpixel edge location based on partial area effect,” *Image Vis. Comput.*, vol. 31, no. 1, pp. 72–90, Jan. 2013.

[182] S. Schiaffino and A. A. Sonin, “Molten droplet deposition and solidification at low Weber numbers,” *Phys. Fluids Appl. Phys. Lett. J. Vac. Sci. Technol. B Fluids J. Appl. Phys. Phys. Fluids*, vol. 9, no. 9, pp. 3172–161609, 1997.

[183] C. W. Extrand, “Uncertainty in contact angle measurements from the tangent method,” *J. Adhes. Sci. Technol.*, vol. 30, no. 15, pp. 1597–1601, Aug. 2016.

[184] I. Malgarinos, N. Nikolopoulos, and M. Gavaises, “Numerical investigation of heavy fuel droplet-particle collisions in the injection zone of a Fluid Catalytic Cracking reactor, Part I: Numerical model and 2D simulations,” *Fuel Process. Technol.*, vol. 156, pp. 317–330, 2017.

[185] I. Malgarinos, N. Nikolopoulos, M. Marengo, C. Antonini, and M. Gavaises, “VOF simulations of the contact angle dynamics during the drop spreading: Standard models and a new wetting force model,” *Adv. Colloid Interface Sci.*, vol. 212, pp. 1–20, 2014.

[186] X. Ma, F. Zhang, K. Han, B. Yang, and G. Song, “Evaporation characteristics of acetone–butanol–ethanol and diesel blends droplets at high ambient temperatures,” *Fuel*, vol. 160, pp. 43–49, Nov. 2015.

[187] K. Han, B. Yang, C. Zhao, G. Fu, X. Ma, and G. Song, “Experimental study on evaporation characteristics of ethanol–diesel blend fuel droplet,” *Exp. Therm. Fluid Sci.*, vol. 70, pp. 381–388, Jan. 2016.

[188] G. Strotos, G. Aleksis, M. Gavaises, K.-S. Nikas, N. Nikolopoulos, and A. Theodorakakos, “Non-dimensionalisation parameters for predicting the cooling effectiveness of droplets impinging on moderate temperature solid surfaces,” *Int. J. Therm. Sci.*, vol. 50, no. 5, pp. 698–711, 2011.

[189] L. Villegas, S. Tanguy, G. Castanet, and O. Caballina, “Direct numerical simulation of the impact of a droplet onto a hot surface above the Leidenfrost temperature,” *Int. J.*, 2017.

[190] T. Tran, H. Staat, A. Prosperetti, C. Sun, and D. Lohse, “Drop impact on superheated surfaces,” *Phys. Rev. Lett.*, 2012.

[191] T. Xiong and M. Yuen, “Evaporation of a liquid droplet on a hot plate,” *Int. J. Heat Mass Transf.*, 1991.

[192] K. Baumeister, R. Henry, and F. Simon, “Role of the Surface in the Measurement of the Leidenfrost Temperature,” 1970.

[193] V. Borishansky, “Heat transfer to a liquid freely flowing over a surface heated to a temperature above the boiling point,” *Probl. heat Transf. Dur. a Chang. state (ed.*, 1953.

[194] H. Blaszkowska-Zakrzewska, “Rate of Evaporation of Liquids from a Heated Metallic Surface,” *Bull. Int. VAcademie Pol.*, 1930.

[195] R. Chen, M. Lu, V. Srinivasan, Z. Wang, and H. Cho, “Nanowires for enhanced boiling

heat transfer," *Nano Lett.*, 2009.

[196] A. Wang, C. Lin, and C. Cheng, "Pattern analysis of a single droplet impinging onto a heated plate," *Heat Transf. Res.*, 2005.

[197] M. Bussmann, S. Chandra, and J. Mostaghimi, "Modeling the splash of a droplet impacting a solid surface," *Phys. Fluids*, vol. 12, no. 12, pp. 3121–3132, Dec. 2000.

[198] K. Yokoi, "A practical numerical framework for free surface flows based on CLSVOF method, multi-moment methods and density-scaled CSF model: Numerical simulations of," *J. Comput. Phys.*, 2013.

[199] Y. Guo, Y. Lian, and M. Sussman, "Investigation of drop impact on dry and wet surfaces with consideration of surrounding air," *Phys. Fluids*, vol. 28, no. 7, p. 73303, Jul. 2016.

[200] J. Lee and S. Lee, "Dynamic wetting and spreading characteristics of a liquid droplet impinging on hydrophobic textured surfaces," *Langmuir*, 2011.

[201] S. Kim, J. Kang, H. Ahn, and H. Jo, "Study of leidenfrost mechanism in droplet impacting on hydrophilic and hydrophobic surfaces," *Int. J. Air-Conditioning Refrig.*, 2013.

[202] Y. M. Arifin and M. Arai, "The effect of hot surface temperature on diesel fuel deposit formation," *Fuel*, vol. 89, no. 5, pp. 934–942, 2010.

[203] G. Liang, Y. Guo, X. Mu, and S. Shen, "Experimental investigation of a drop impacting on wetted spheres," *Exp. Therm. Fluid Sci.*, 2014.

[204] S. Mitra, G. M. Evans, E. Doroodchi, V. Pareek, and J. B. Joshi, "Interactions in droplet and particle system of near unity size ratio," *Chem. Eng. Sci.*, 2017.

[205] I. Malgarinos, N. Nikolopoulos, and M. Gavaises, "A numerical study on droplet-particle collision dynamics," *Int. J. Heat Fluid Flow*, vol. 61, pp. 499–509, 2016.

[206] Z. Wang, C. Lopez, A. Hirsa, and N. Koratkar, "Impact dynamics and rebound of water droplets on superhydrophobic carbon nanotube arrays," *Appl. Phys. Lett.*, vol. 91, no. 2, p. 23105, Jul. 2007.

[207] L. Wachters, L. Smulders, and J. Vermeulen, "The heat transfer from a hot wall to impinging mist droplets in the spheroidal state," *Chem. Eng.*, 1966.

[208] M. Gumulya, R. Utikar, and V. Pareek, "Evaporation of a droplet on a heated spherical particle," *Chem. Eng.*, 2015.

[209] T. Young, "An essay on the cohesion of fluids," *Philos. Trans. R. Soc.*, 1805.

[210] M. Pasandideh-Fard, Y. M. Qiao, S. Chandra, and J. Mostaghimi, "Capillary effects during droplet impact on a solid surface."

[211] V. Konduru, "Static and dynamic contact angle measurement on rough surfaces using sessile drop profile analysis with application to water management in low temperature fuel cells."

Contribution

1. Journal Papers:

- Jadidbonab H., Malgarinos I., Karathanassis I., Mitroglou N., and Gavaises M. "We-T classification of Diesel fuel droplet impact regimes". Revised version submitted in Proceeding of Royal Society A.
- Jadidbonab H., Karathanassis I., Mitroglou N., and Gavaises M. "Experimental study of Diesel fuel droplet impact onto similar size polished spherical heated solid particle". Revised version submitted in Langmuir.
- Jagadeesh C., Gowree E. R., Jadidbonab H., and Atkin C. J. "on the temporal analysis of acoustic waves using Schlieren imaging" Measurement, Elsevier (2017) In Press.

2. Conference Papers:

- Jadidbonab H., Mitroglou N., and Gavaises M. "Diesel fuel drop impingement on a heated surface at elevated pressure". ILASS – Europe 2016, 27th Annual Conference on Liquid Atomization and Spray Systems, Brighton, UK.

3. Posters:

- Jadidbonab H., Mitroglou N., and Gavaises M. "Experimental study on diesel fuel droplet impingement on spherical heated surface". 5th IICR Workshop (2016), Chania, Greece.
- Jadidbonab H., Karathanassis I., Mitroglou N., and Gavaises M. "Diesel Fuel Drop Impingement on a Heated Surface at Elevated Pressure". 4th IICR Workshop (2016), Chania, Greece.

Appendices

In the appendices, a series of experimental results are reported as follows:

A. Effect of additives on Diesel fuel wetting characteristics
B. Effect of physical properties on isothermal impact of millimetric droplet onto solid surfaces
C. Oblique droplet-particle collision

The obtained results presented in appendix A and B, were already well-stablished in the literature for single component liquids, and were in good agreement with the available studies (selectively among others [25], [210]).

In appendix C, the results of a pilot study on oblique droplet-particle collision at above Leidenfrost temperature have been presented and are in good agreement with numerical study of [154]. The obtained indicative results show that obliquity results in asymmetric flow process and might affect the hydrodynamic and heat transfer during the collision. However, a significant development would be required in order to further investigate the effect of obliquity.

A. Effect of additives on Diesel fuel wetting characteristics

A.1. Introduction

In present section, the effect of additives on the below two main phenomena were experimentally investigated:

- Wettability (by employing the spreading geometry parameters)
- Fuel drop impact characteristics on wetted surface

Wettability studies usually consist of the three phase contact angle as a primary data which is an indication of wetting degree when a solid and liquid are in contact.

The contact angle is defined as the equilibrium angle between the contact point of the liquid-vapour and the liquid-solid interface. This interface where the liquid, solid and gas meet each other, is called contact angle. Generally small contact angles (<<90°) related to high wettability (hydrophilic surface) while large contact angles (>>90°) corresponds to low wettability (hydrophobic surface). Figure A.1 explore the wetting and non-wetting condition based on their contact angle.

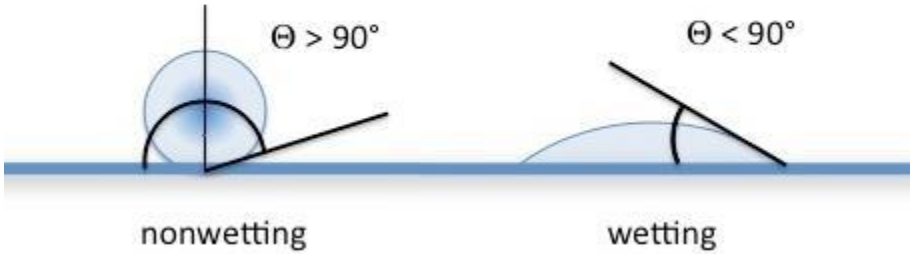

Figure A.1: Wetting and non-wetting condition

The ideal way to define the droplet shape is using surface tension of the liquid. Surface tension is the intension of the liquid to voluntarily contract its surface area to have the lowest surface free energy by being pulled inward by neighbouring molecules. Based on this definition, bubbles and droplets are ideally assumed spherical, as the best shape to keep the surface area in its minimum value for a fixed volume. Therefore the shape of any liquid or bubble can be defined based on its surface tension. In reality, due to the gravitational force the spherical shape is fairly deformed. So the contact angle determination is performed by means of a combination of liquid surface tension and external forces.

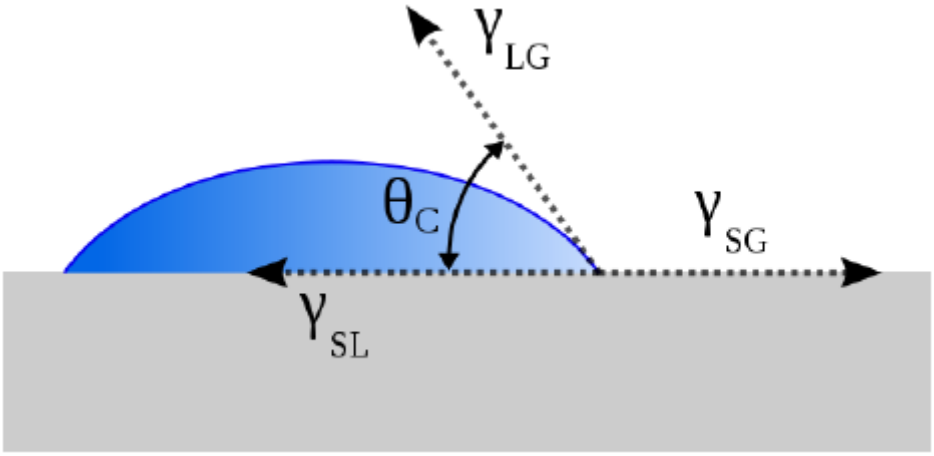

Figure A.2: Three phase contact angle

As Thomas Young described for the first time in 1805, the contact angle is a mechanical equilibrium of the drop under the interaction of three different interfacial tensions (Figure A.2):

$$\sigma_{lv} cos\theta_Y = \sigma_{sv} - \sigma_{sl} \qquad \textit{Equation A. 1}$$

Where, σ_{lv}, σ_{sv} and σ_{sl} are the liquid-vapour, solid-vapour and liquid-solid interfacial tension, respectively, and is the Young contact angle. If the contact line is in motion the terms "dynamic" is added to the contact angle and it is deviated from the actual equilibrium contact angle. This wetting process is dependent on the material properties of all the media which are in contacts and also the parameters characterising the flow. Pre-impact flow field influences not only the onset of air entrainment, but also the value of the dynamic contact angle and spreading behaviour (on dry clean surface) and rebound\deposition regime (on wet surface). A set of non-dimensional parameters, Reynolds, Weber and capillary number, can be used to characterise the droplet as defined in section 2.1.6.

The experimental procedures are explained in chapter 2. Base and additised Diesel fuel, are selected as the test liquids (see Table A.1).

@ 0.1 MPa - 40° C	Density [kg/m^3]	Kinematic viscosity [cSt]	Surface tension [mN/m]	Boiling point [°C]
Base Diesel	833	3.245	28.9	180-360
Additised Diesel	832.9	3.150	27.616	180-360

Table A.1: Properties of standard summer Diesel fuel

The temperature of the substrate surface as well as liquid deposited in the syringe is monitored continuously and kept around 25°C to avoid the effect of temperature on the liquid droplet physical properties, employing two heat filter glass in front of the light source. Table A.2 presents the test conditions.

Experiment \ Configuration	Substrate Configuration			Operation condition
	Angle	Material	Condition	
Spreading dynamic	15° Levelled	Steel & Perspex	Dry	5, 10, 15, 100 mm needle height
Outcome regime	15° Levelled	Steel & Perspex	Wet 100μm Diesel film	5-100 mm (Every 1 mm)

Table A.2: Test condition

Raw captured images are required to further process by means of In-house MATLAB routine to obtain the geometry parameters of the impact. This is done by balancing between surface tension and external forces like gravity which is mathematically expressed by the so called Laplace equation [27]. This equation is corresponded to the pressure gradient between liquid-fluid interface to the curvature of the interface and surface tension:

$$\sigma\left(\frac{1}{R_1}+\frac{1}{R_2}\right)=\Delta P \qquad \textit{Equation A. 2}$$

Where σ is the liquid-fluid is surface tension, R_1 and R_2 and are the two radii of curvature, and is ΔP the pressure difference along the interface. There is linear relation for the pressure difference in absence of external forces except gravity:

$$\Delta P = \Delta P_0 + (\Delta\rho)gz \qquad \textit{Equation A. 3}$$

Where ΔP_0 is the reference pressure difference at the surface, Δρ is the density difference of the liquid and surrounded gas, g is the gravity, and z is the vertical height of the contact point from the reference point. Therefore for a set of known physical properties, the shape of drop can be determined.

Ideally, by integration of the Laplace equation (Equation A. 2) is a direct approach just for the well-defined cylindrical menisci, where either R1 or R2 is zero, but for the irregular shapes mathematical operation would be a difficult approach. In case of axisymmetric drops (rest on well levelled surface) the position of the axial symmetry is convenient and mathematical approach can be obtained from specific numerical procedure. This can be done by matching the calculated theoretical profiles from Laplace equation and the captured shape of the drop. In present case by calculating the surface tension and the principal radii of the drop menisci, the equation can be integrated to obtain the contact angle [211].

Dynamic contact angle is calculated for a set of images recorded for 5 sec event with the rate of 5000 frames per second. The first 6ms is not considered as the Young-Laplace method can be applied at the end of initial spreading phase. A typical processed data is shown in Figure A.3.

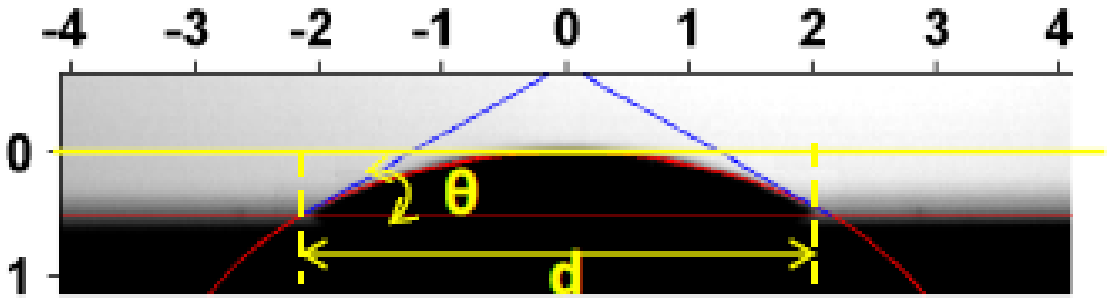

Figure A.3: Contact angle and spreading diameter calculated from Laplace equation in case of normal impact

In the incline case, the Young-Laplace equation was not performed due to the asymetric shape of the droplet and instead the spherical cap method is carried out. In this case, droplet is split in two halves, from the apex point, and two individual circles are fitted to the droplet halves. Two different values are measured for the contact angle which is corresponded to the advance (front) and receding (rear) contact angles concerning the direction of droplet spreading. The spreading diameter is measured from the distance of the contact points. Figure A.4 illustrates the latter parameters in a raw image data.

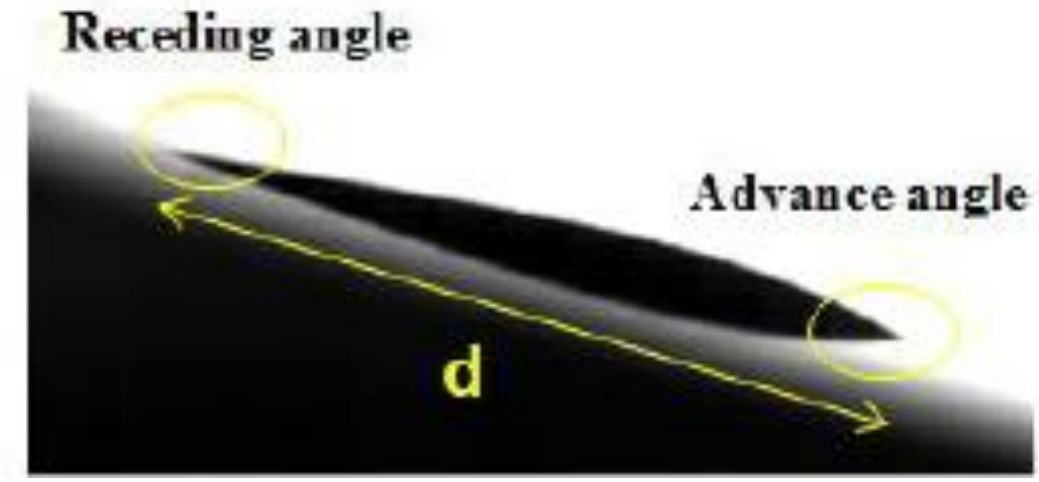

Figure A.4: Contact angle and spreading diameter calculated from Laplace equation in case of oblique impact

A.2. Result and discussion

A.2.1. Spreading Dynamic

In the case of droplet impact onto the dry clean surface, two geometric parameters of spreading droplet is measured and extracted:

- Apparent dynamic contact angle
- The diameter of the wetted area on the wall surface

The usual assumption for the spreading dynamic is based on a balance between the spreading forces and viscosity. But resistance of the inertia towards the motion change this classical dynamics law. It is believed that a microscopic precursor film moves ahead of macroscopic droplet which is spreads on the substrate and wetted it. The droplet first reshape by the gradient of the curvature and Laplace pressure which is due to the interfacial surface tension of gas-liquid interface. In the later stage gravity becomes the dominant spreading force. As time passes by, these two driving force are getting weaker and weaker so the contact line velocity and spreading rate decrease. Inertial forces (increase as the impact velocity increases) are the driven force for the spreading behaviour at initial phase, as its magnitude is much larger than the surface tension and viscous forces. High deformation and waviness motion is the energy dissipation source for the initial forces. When the deformation is reached to its maximum value, recoiling happens due to the surface tension forces. After complete dissipation of initial energy, capillary energy is becoming the driven forces. Its time period is much shorter than the capillary and viscous time.

In the current study, due to hydrophilic nature of all tested surfaces and Diesel fuel, despite of the range of Weber number values examined, the only observed regime was deposition. Thus all the measurements are started after 6 ms to skip the complex transient behaviour of impact. This transient behaviour has been discussed in chapter 3. In Figure A.5 the experimental results for the spread diameter and apparent contact angle on Perspex plate are shown for two Weber

number values (We=3, 15). The time window is set in order to capture the phenomena up to the equilibrium phase.

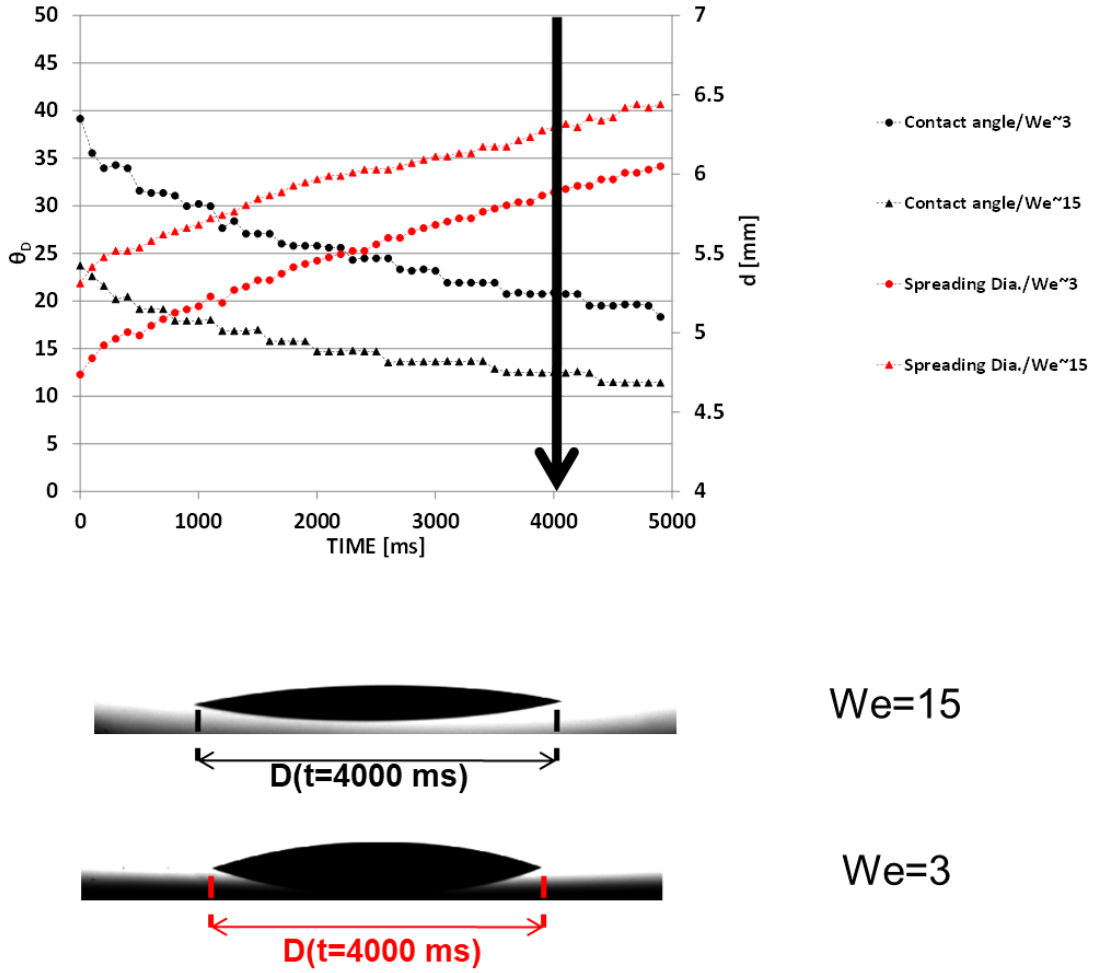

Figure A.5: Dynamic contact angle and spread diameter of Base fuel droplet on levelled Perspex substrate for We=3 and 15

The general behaviour of the apparent dynamic contact angle is similar for both Weber number values. It can be divided in two main stages. In the initial stage of spreading (t<30ms), which is not shown in the graphs, the wetting contact angle decreased rapidly from 180º then from this point the droplet shows more gentle behaviour and continue to spread to its minimum contact angle and maximum spreading diameter. This time is highlighted as the transition limit of inertia driven spreading and surface tension driven spreading.

The spreading diameter is increased for larger Weber number values. The influence of Weber number, in particular, appears in the first stage, however the importance of surface tension and

viscous forces increases in the second stage. Therefore, as shown in Table A.3, the maximum spreading diameter becomes significantly larger and dynamic contact angle becomes smaller for higher impact velocity (higher Weber number) for each specific time step.

We	Dynamic contact angle θ [°]	Spreading diameter d [mm]
3	35.8-20.5	4.67-5.84
9	32.3-18.8	5-5.96
15	30.3-14.4	5.26-6.19
130	11	6.4

Table A.3: Dynamic contact angle and spreading diameter range for additised fuel droplet on the steel surface

Around 70% of the wetting is achieved in the first stage for and this value increased by increasing the Weber number. Similar behaviour can be seen in previous studies [182] up to the Weber number of We=12. The contact angle and spreading diameter values for the case of We=130 are constant for t>30ms; the droplet diameter extents to its maximum at the early stages. It should be noted that noted that studying the initial stage of impact requires different optical setup.

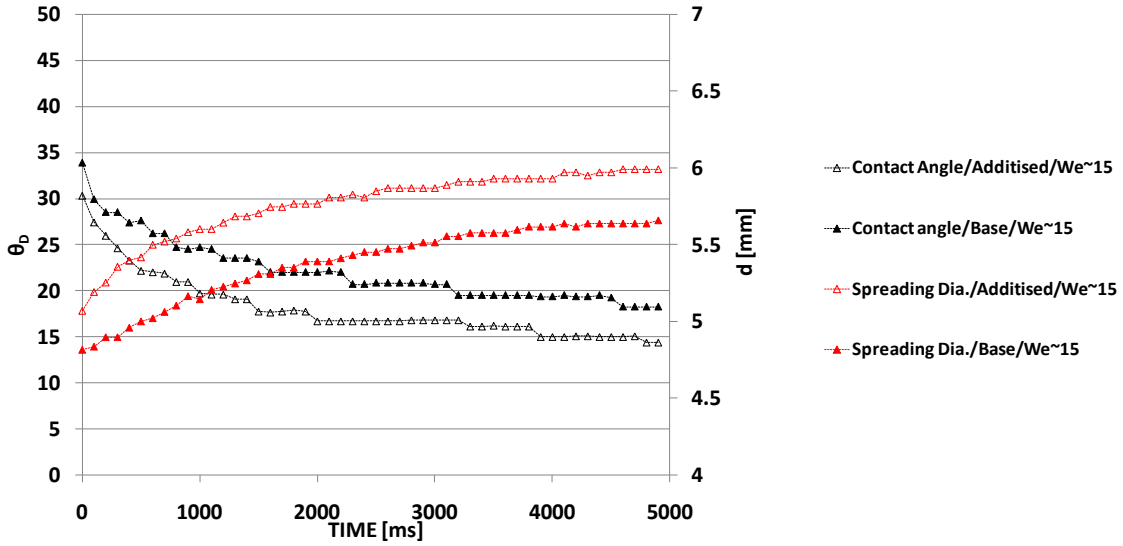

Figure A.6: Comparison of additised and base Diesel fuel droplets on levelled steel substrate for We=15

Figure A.6 shows the effect of additives on spreading behaviour of the two different fuels. Comparison of the spreading diameter and dynamic contact angle clearly shows the influence of the additive on the impact dynamic. The lower contact angle of the additised fuel, leads to larger droplet wetting diameter compared to the base fuel. Slightly difference of the surface tension and kinematic viscosity of these two fuels is the reason of this behaviour.

As expected, the dynamics rate is slower for the drops of higher viscosity (Base fuel). The influence of the additives and physical properties of the liquids are negligible at very high Weber number as the spreading diameter and dynamic angle values are falling into the same curve for both fuels (We=130). This is attributed to the dominated influence of the kinetic energy rather than surface tension and viscous forces in high Weber number cases.

Figure A.7 shows the time variation of the contact angle and spreading diameter of the additised Diesel fuel droplet, deposited and spreading on both substrates. Spreading rate for the Perspex surface is significantly increased. It can be seen that the surface energy of the Perspex surface is higher than steel, so the droplet shows stronger wettability behaviour on Perspex.

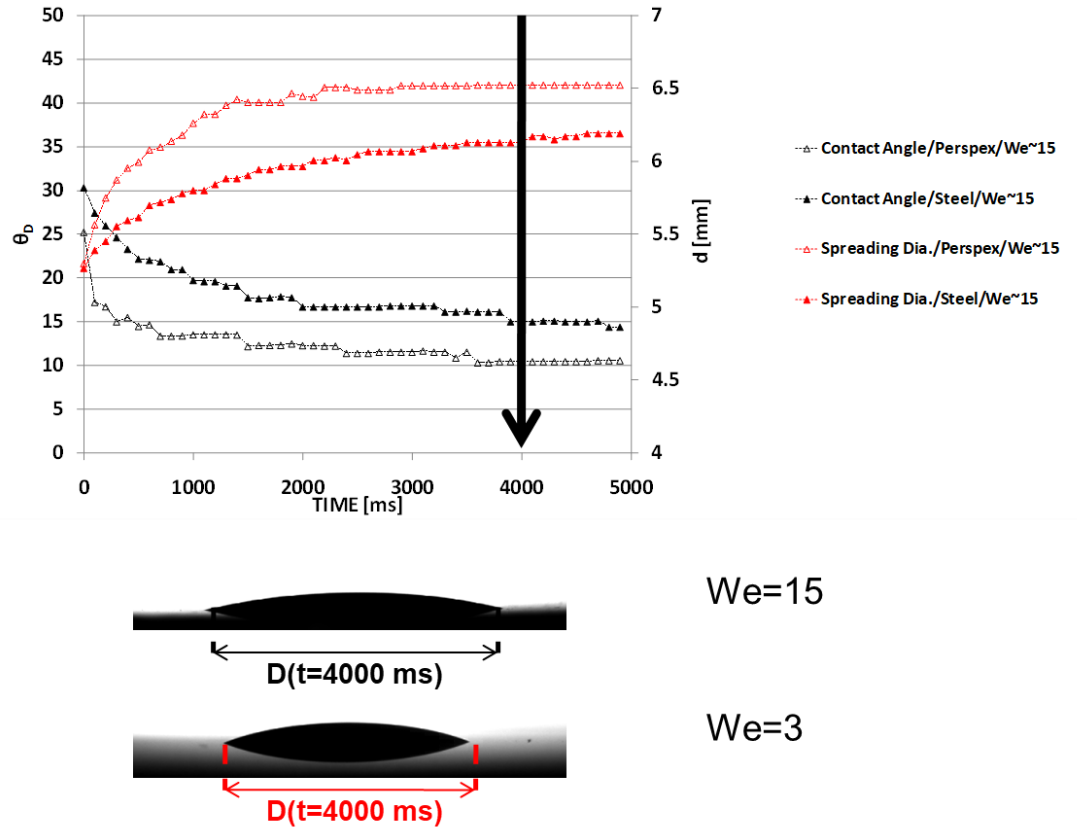

Figure A.7: Dynamic contact angle and spread diameter of additised fuel droplet on levelled steel and Perspex substrate for We=15

As it can be seen Figure A.8, Diesel base fuel droplet spreading rate is fairly linear with the constant slope foe all Weber number examined. This might be attributed to faster overcoming of the viscous forces to the initial forces, so capillary forces start to drive the spreading in advance.

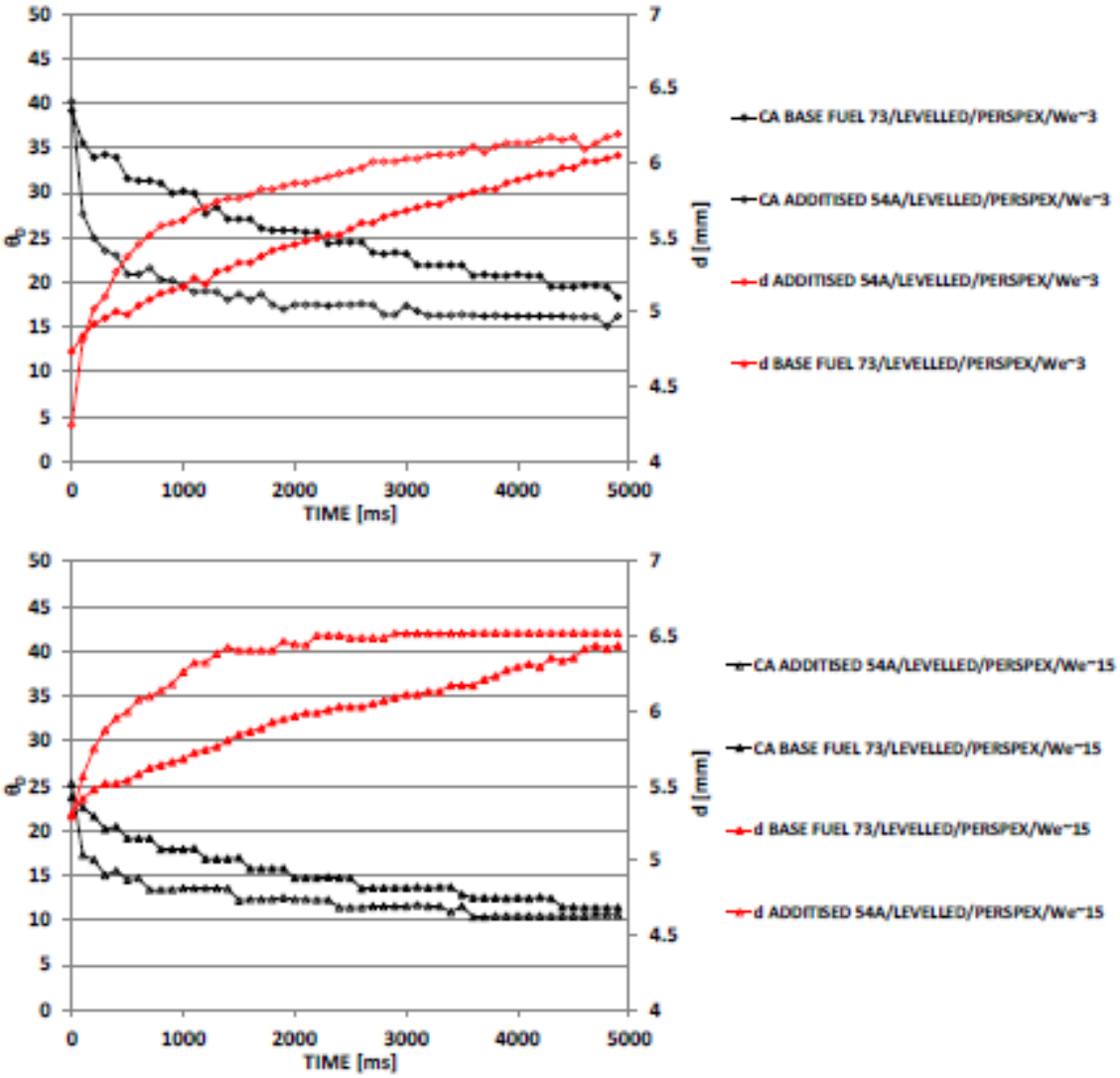

Figure A.8: Comparison of additised and base fuel drops on levelled Perspex substrate for low and medium Weber number

In case of tilted substrate, after the gravity is one of the dominant parameters and forces the droplet to continuously move in the direction of the inclination. The advance contact angle is reduce sharply to approximately 22º for both Weber number and remains approximately constant for t>1000ms, but spreading was increasing constantly with a constant advance contact angle and decreasing receding contact angle (See Figure A.9).

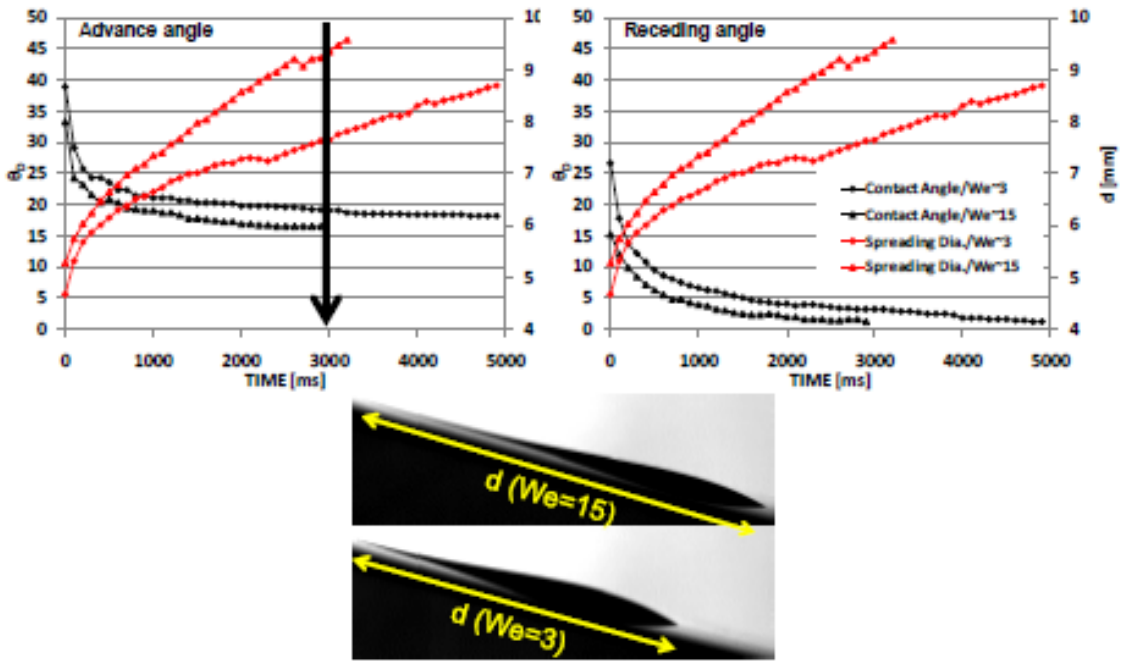

Figure A.9: Advance/Receding dynamic contact angle and spread diameter of additised fuel droplet on incline Perspex substrate for We=3, 15

Therefore it can be concluded qualitatively and quantitatively that the droplet is spreading and no slippery effect is observed. This should be also noted that for very thin tail part of the droplet in rear contact point, with very low receding contact angle, there is a probability of the artefacts due to the threshold sensitivity. It means that the real contact point is not accurately.

Figure A.10 illustrates the effect of the substrate wettability on the spreading behaviour. Droplet continues to spread on the substrate with advancing front contact point while the rear point stays fix on Perspex substrate. But in case of steel surface, the receding contact angle is not decreased from a certain point and instead the rear contact points also pulled down with the bulk of the droplet mass. This also explains lower surface energy of the steel substrate compare to the Perspex one.

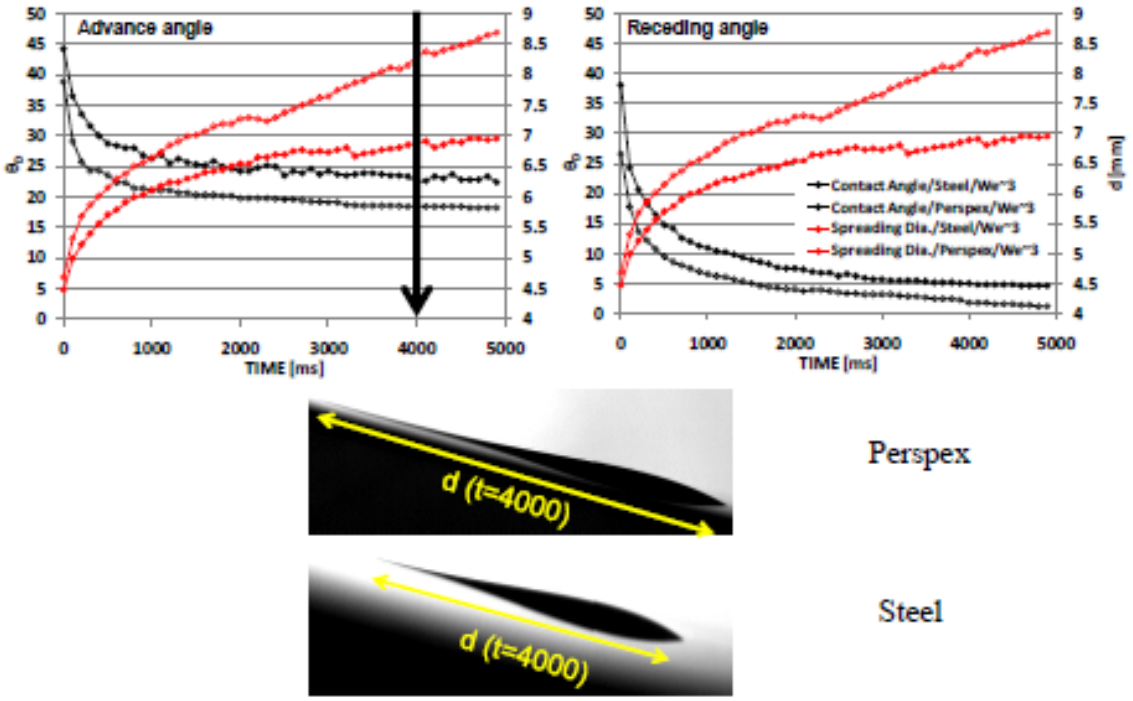

Figure A.10: Advance/Receding dynamic contact angle and spread diameter of additised fuel droplet on incline steel and Perspex substrate for We=3

Higher tendency of the droplet to spread on the Perspex is similar to the Levelled condition. Higher spreading rate observed for the inclined surface is due to the constant effect of gravity on the phenomena. Due to the high quality surface machinery for steel and polishing for Perspex, the hysteresis is decreased to a very low value. It means there are no pinning and unpinning of the moving contact points while it is spreading on the surface; therefore there is no oscillation on the measured contact angle.

Figure A.11 presents the effect of the additives on the dynamic contact angle for the Perspex substrate. There has been a minor change on the spreading dynamic in presence of the additives. This effect is even more suppressed for higher impact velocity. As gravity effect on the droplet dynamic is overcoming the other influential forces, the behaviour is becoming more or less similar. On the other hand, the effect of the impact velocity on contact angle is much lower than the one in levelled case. The reason lies in the fact that the equilibrium cannot met due the eternal presence of gravity which is acting on the droplet continuously.

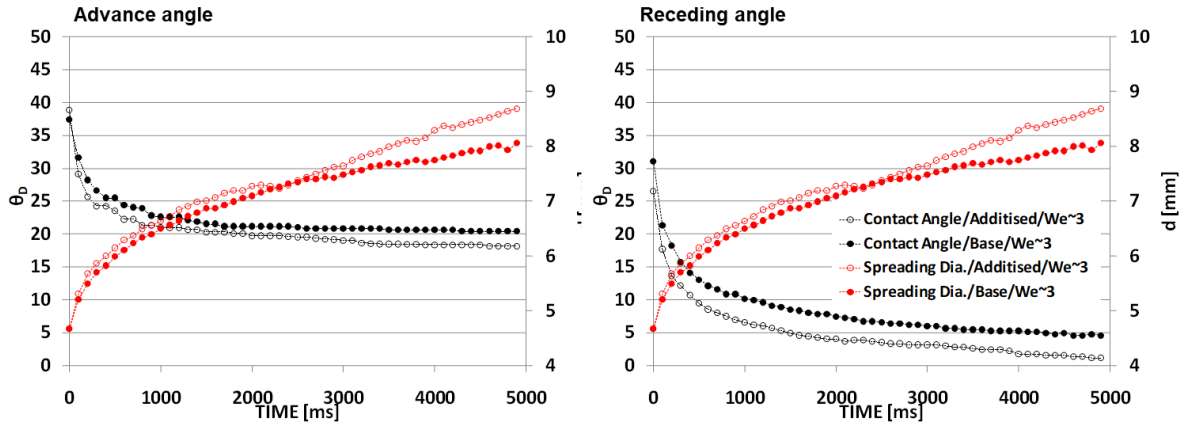

Figure A.11: Advance/Receding dynamic contact angle and spread diameter of additised and base fuel droplet on incline Perspex substrate for We=3

A.2.2. Droplet impact outcome on a wetted surface

When a liquid droplet impacts onto a liquid pool, film or another droplet, several phenomena can be seen. It can deposit or rebound, remain in one piece or split in smaller satellite droplets. This phenomenon is strongly depended on the air entrainment between the droplet and the liquid film. If the kinetic energy of the impact droplet can drains the air layer, deposition happens otherwise the droplet rebound using the translational kinetic energy. In Rebound, due to the existence of this air interlayer and its relative lubrication force, the contact between two liquids never met therefore the droplets deform to dissipate the kinetic energy from the impact.

Figure A.12 show sequences of 4 identical droplets impacting onto a levelled substrate. All the parameters are the same except for the Weber number, which is varied for a range of 1.2 to 15.5. At impact time, a set of capillary waves rises from the base of the droplet to form a pyramidal structure (t=3.6ms). These large amplitude waves then reshape the droplet into a pancake (t=5.6ms). These phases are identical for all 4 droplets. The following phases are depends significantly on the impact Weber number.

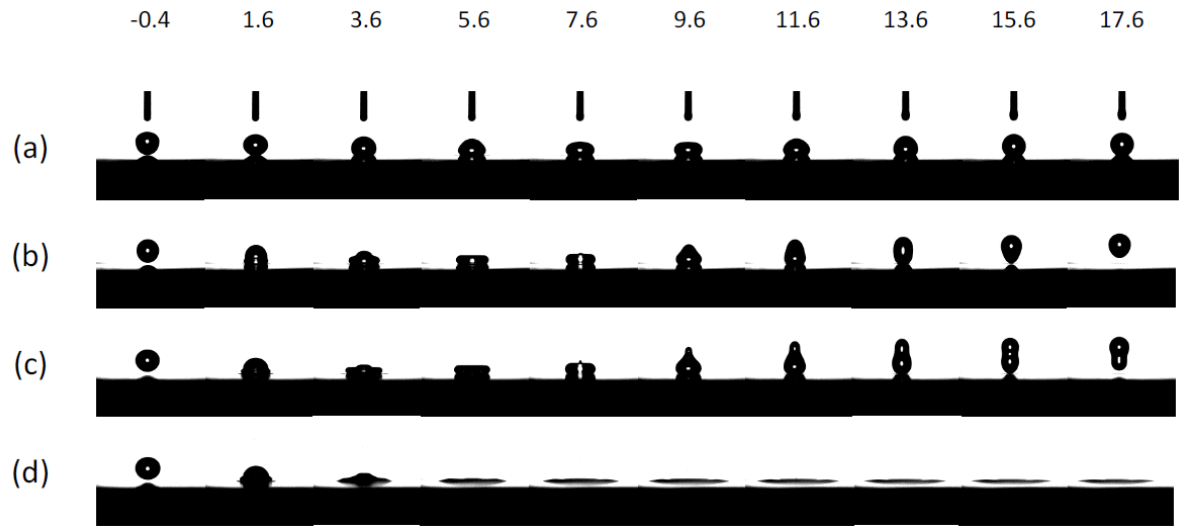

Figure A.12: Drop impact of the base fuel on the level substrate (a) We=1.15 (b) We=6.2 (c) We=11.2 (d) We=15.3. The images are taken at identical times after the impact for every 2ms

For We<7 (Figure A.12a and b), the air layer survives the impacting droplet, so there is no deposition. The droplet deforms, then recoils and recovers its initial spherical shape. This regime is called complete rebound. For the We>15 (Figure A.12d), the air layer raptures and total deposition occurs between the droplet and the underlying film. The intermediate phenomena between these two regimes are can be complex and is not only related to the impact velocity but the surface tension of the liquid. In Figure A.12c the air layer survives from impacting droplet like the complete rebound regime. The only significant difference is, a very strong Worthington jet that tries to pinches off the droplet into two or even smaller satellite droplets. But the surface tension forces are overcome this jet and keep the droplet as one piece. Splitting is not seen for the examined cases but stronger temperature gradient on the surface and fuel droplet enhances can promote the splitting.

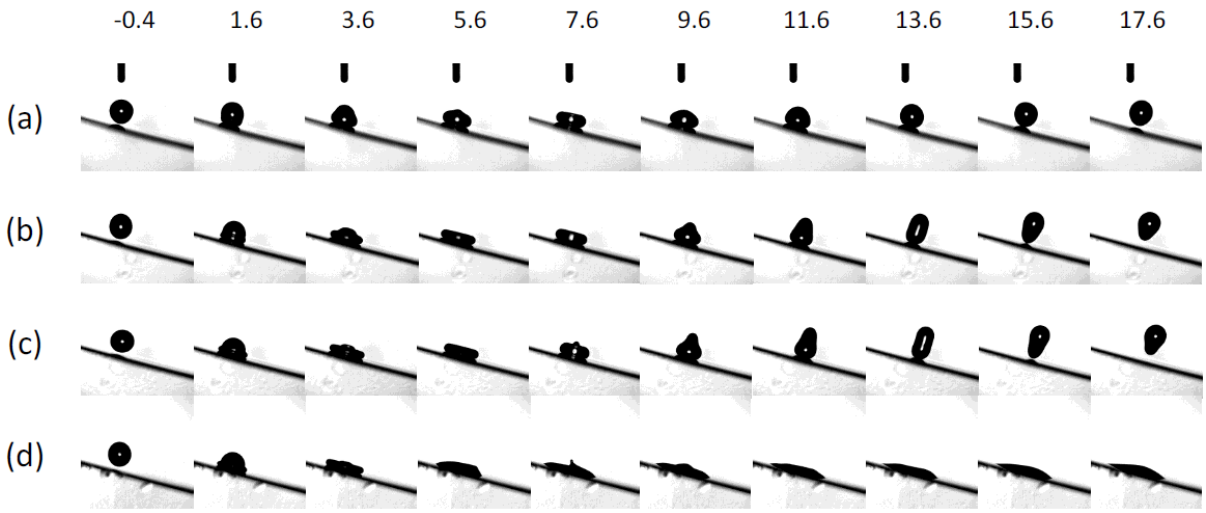

Figure A.13: Drop impact of the base fuel on the incline substrate (a) We=0.8 (b) We=5.7 (c) We=10.6 (d) We=14.5. The frames are taken at identical times after the impact every 2ms

As it is observed from the time frame sequences in Figure A.13, the inclinations were not altered the impact dynamic. For each tested Weber number, similar behaviour was observed for both substrates' positioning. In addition, the drop deformation is followed the same pattern as the levelled surface case.

In this section, a comprehensive regime map for the impacting fuel droplet is introduced. During the recoiling process of the droplet, kinetic energy will be partly transferred from the surface energy to the translational kinetic energy. If this energy is sufficient, the droplet rebounds from the surface. Some of the kinetic energy also remains as internal oscillation and dissipates by deformation of the droplet shape.

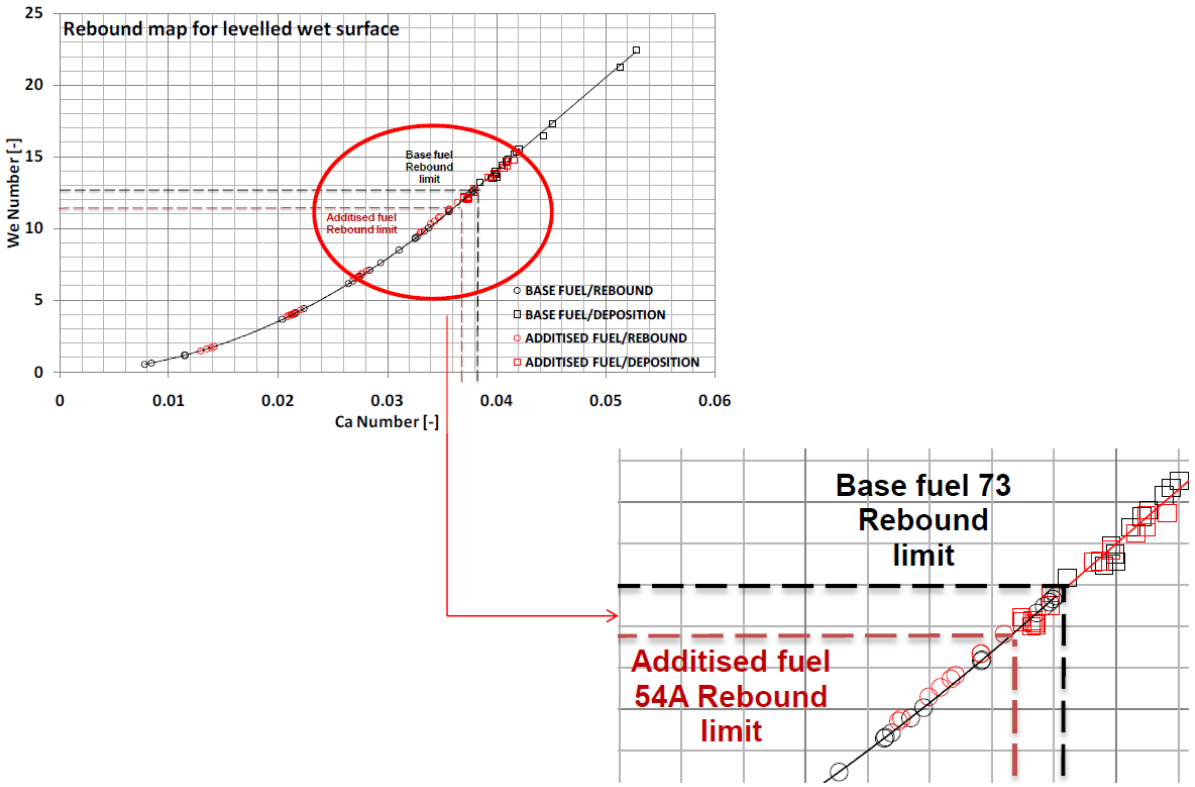

Figure A.14: Rebound map of the droplet impact on levelled substrate

Figure A.14 shows the critical Weber number of transition from deposition to rebound regime versus the capillary number on the levelled wet substrate. By increasing the Weber number, the tendency of the droplet to merge to the film increases. The transition of the rebound/deposition regime for the additised fuel is in lower Weber number. This is attributed to the lower surface tension and viscosity of this fuel sample. The contact time of the droplet on the surface is shortened fairly by increasing the impact velocity.

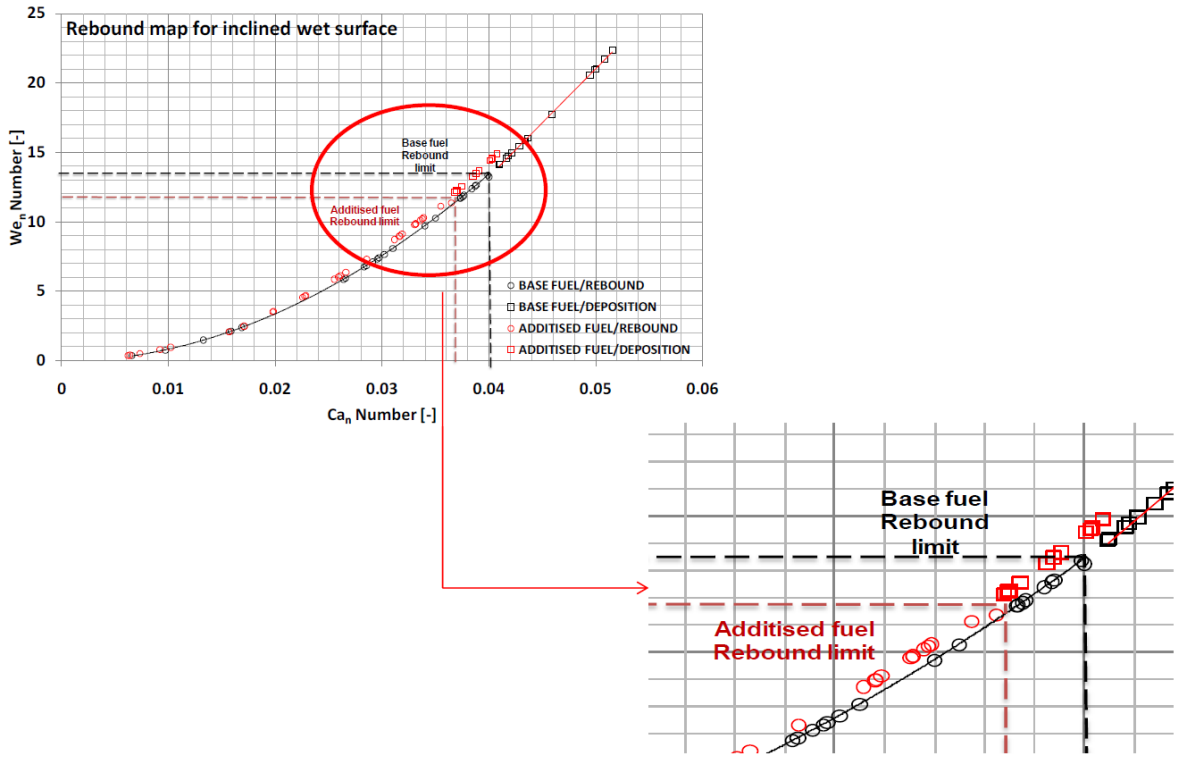

Figure A.15: Rebound map of the droplet impact on levelled substrate

Although the critical Weber number cannot be clearly identified due to its sensitivity of the droplet dispensing methods and film thickness, however critical Weber number for base fuel is slightly higher than for the additised one. The base fuel starts to deposit on the surface from approximately We=13 while this value for the additised one is around We=11.5. In the inclined surface the same trends is observed. Figure A.15 shows the results for the droplet impact on wet inclined substrate (α=15º) for both fuels. No sliding behaviour was observed during the impact for the incline surface. In general, sliding increases the contact time of the droplet on the surface and the probability of the air layer breaking.

Figure A.16 reveals the effect of the substrate angle on droplet rebound map for both fuels. It can be seen that substrate angle shifts the deposition regime to the higher impact Weber numbers.

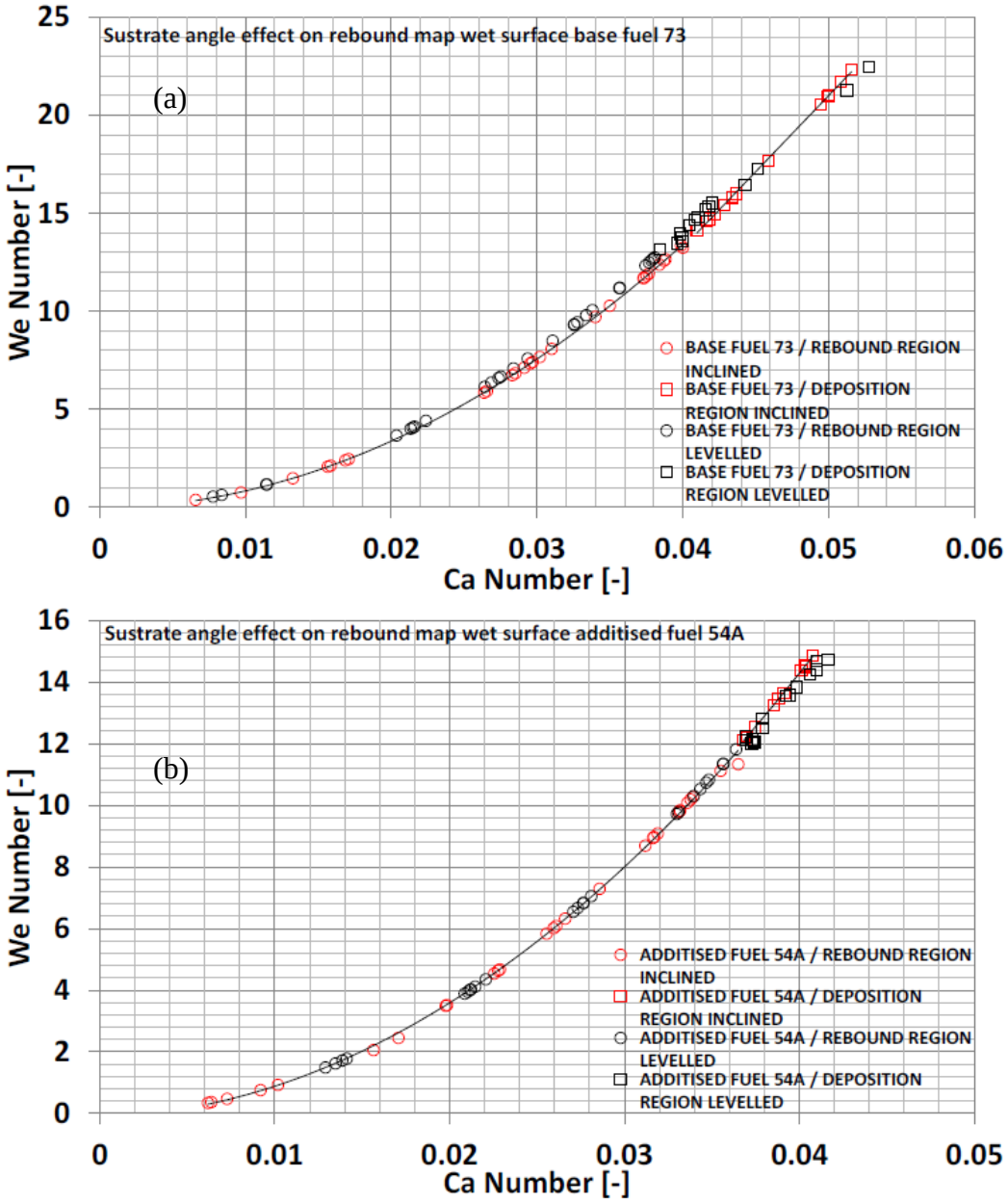

Figure A.16: Substrate angle effect on rebound regime (a) base fuel and (b) additised fuel

B. Isothermal impact of millimetric droplet onto solid surfaces; effect of physical properties

B.1. Introduction

The dynamic behaviour of an individual droplet impacting onto a solid surface includes several individual phenomena, such as deformation, fingering, splashing, and rebound. The onset and physical description of those phenomena are usually characterized based on dynamic similarity arguments making use of dimensionless numbers characterizing the relative magnitude of the forces acting upon the surface of the droplet (Reynolds, Weber and Ohnesorge numbers). Estimative of these dimensionless numbers were, in turn, obtained by scaling the forces (surface tension, shear and gravity) with physical properties of the liquid (density, viscosity and surface tension) and considering all lengths proportional to the diameter and velocity at the instant of impact, respectively. However, the physical properties of the impacting surface such as temperature, roughness, or inclination alter the boundaries of the problem under study and similarity arguments cannot be applied.

The fact that the properties of the impact surfaces influence droplet dynamic behaviour and don't allow to apply similarity arguments is the reason why it appears, from the reviewed literature that it is not possible to correlate the several phenomena occurring during droplet deformation with proper dimensionless numbers. The present study is part of a research study aimed at to account for the complexity introduced by the influence of non-scaled parameters on the description of droplet impact.

This section reports an experimental analysis of droplet deformation on dry cold flat surfaces of different materials. The experiments were carried out for different regimes commonly characterized by non-dimensionless numbers. The analysis considers different fluid properties,

namely and Diesel and Iso-octane fuel and droplet velocity at impact to vary the Weber and Reynolds numbers. Experimental results are analysed in terms of the influence of liquid properties, surface material on the spreading dynamic.

The experimental arrangement and image processing are similar with the procedure explained in chapter 2. Cold dry flat steel and Perspex surfaces, employed along with standard summer Diesel and Isooctane fuel to investigate experimentally the effect of liquid and surface properties and the Pre-impact droplet velocity on the spreading dynamic. Table B.1 summaries the test conditions according to the droplet pre-impact diameter and velocity, influential non-dimensional numbers and the fuels physical properties.

Case	Fuel	Surface Material	D0 [mm]	V0 [m/s]	We [-]	Re [-]	Static CA	ρ [kg/m3]	σ [N/mm]	μ [cP]
1	Diesel	Steel	2.181	0.34	7.8	234				
2	Diesel	Steel	2.161	0.92	56	626	16			
3	Diesel	Steel	2.162	1.82	215	1236		833	28.9	2.706
4	Diesel	Perspex	2.149	0.37	8.23	246				
5	Diesel	Perspex	2.167	0.91	54	617	13			
6	Diesel	Perspex	2.161	1.81	216	1230				
7	Iso-Octane	Steel	2.072	0.3	7.2	919				
8	Iso-Octane	Steel	2.075	0.86	56	2595	<10			
9	Iso-Octane	Steel	2.041	1.69	216	5040		692	18.7	0.475
10	Iso-Octane	Perspex	2.121	0.32	8.1	999				
11	Iso-Octane	Perspex	2.072	0.87	58	2652	<10			
12	Iso-Octane	Perspex	2.01	1.72	219	5033				

Table B.1: Table of conditions; Diesel and Iso-octane droplet impact on steel and Perspex cold dry flat surface

B.2. Result and discussion

When the drop hits the substrate, a fast spread occurs and is characterized by an increase in the contact diameter coupled with significant deformation of the free surface. Usually, the evolution of the contact diameter D(t) is employed to describe the drop evolution, but this view does not depict the full evolution of the drop as the free surface (can be illustrated from top view) can take various shapes for different experimental conditions in terms of impact velocity, surface wettability, fluid viscosity, and fluid surface tension [211]. The spreading mechanism

of a drop onto a solid surface is described in detail in the literature [62] and the evolution of the contact diameter is divided in four phases respectively called kinematic phase, spreading phase, relaxation phase, and wetting phase. Figure B.1 presents the sequence of images of Diesel and Iso-octane drops spreading onto steel solid surface.

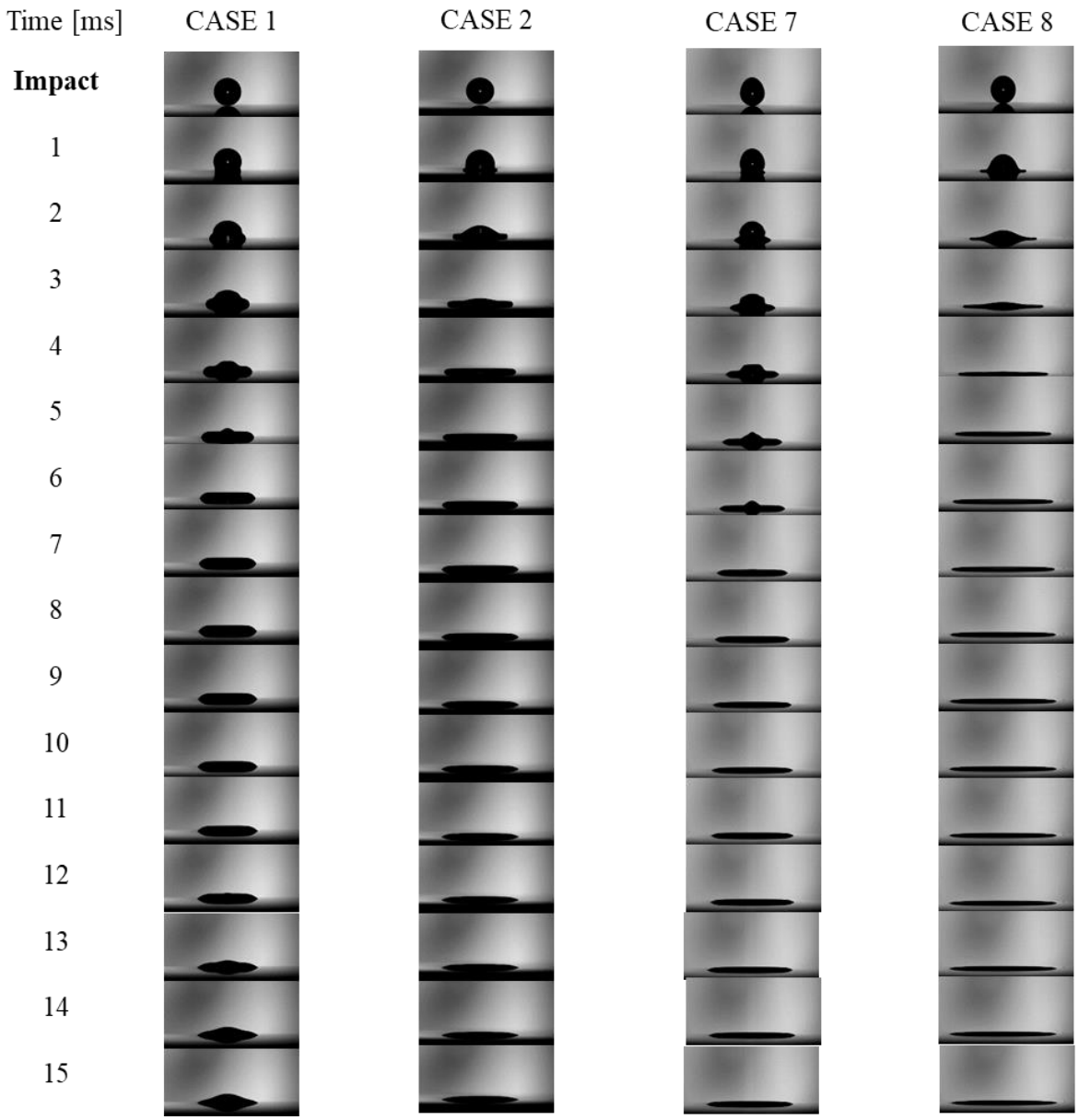

Figure B.1: Photographs of droplets impacting on smooth surfaces with the conditions listed in Table B.1.

During the kinetic phase, the drop does not show any deformations of its free surface, it keeps its form of a truncated sphere, and no lamella spreads on the surface yet. Generally, this phase continues until 0.1t*.

Most of the spreading occurs during the spreading phase, which is governed mostly by inertia. The surface tension and viscosity of the fluid act together against the drop spreading until the contact line stops. In all the cases of drops spreading, capillary wavelets develop on the free surface from the contact line to the upper part of the drop. At the end of the spreading phase, inertia, viscosity, and surface tension compete toward the stop of the contact line and the droplet reaches its so-called maximum spreading diameter (β_{max}).

During the relaxation phase, the surface tension tends to minimize the free surface of the drop. Depending on the maximum spreading in comparison with the final equilibrium diameter, the contact diameter could either show no motion or a de-wetting of the surface. Regarding spreading and relaxation, in many cases the drop diameter evolution is determined by the motion of the rim, which is formed by capillary forces, which certainly contribute to the major part at the shape of the free surface at the contact line.

The fourth phase was defined as wetting phase. During this phase, when the equilibrium state has not been reached yet, the surface tension acts against the viscosity in order to spread the liquid onto the substrate. This phase has been completely investigated in Appendix A1.

Figure B.2 shows the time variation spreading factor and apparent dynamic contact angle of a Diesel and a Iso-octane fuel droplet impacting onto a smooth steel surface (Ra<1μm) with the condition listed in Table B.1. The Iso-octane droplet has a higher Reynolds number, of about 919, while the Diesel droplet has a lower Reynolds number, of about 234. The results in the Figure B.2a show the periodic deformation of the Iso-octane droplet, expanding and recoiling, while the diesel droplet shows a free surface oscillation with the pinned contact points.

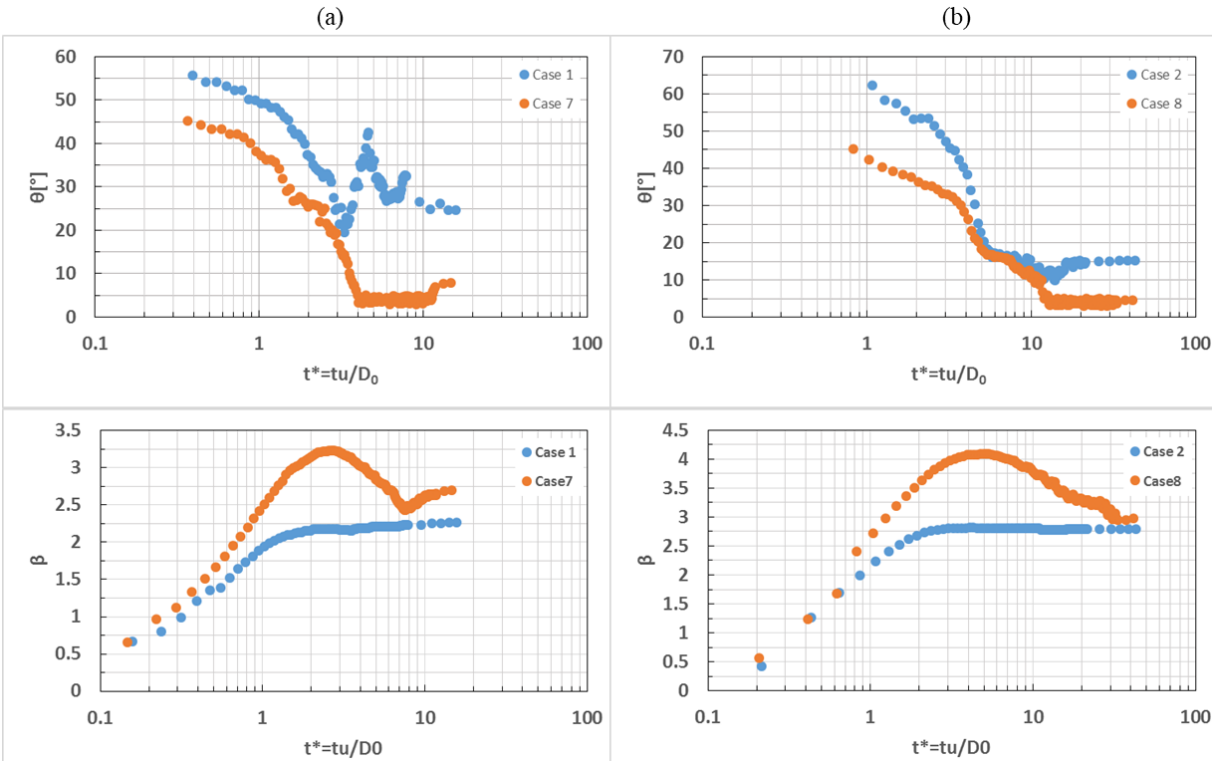

Figure B.2: Time variation of the spread factor and apparent dynamic contact angle for (a) We~7 and (b) We~56

The differences observed in the behaviour of the two droplets may be explained, in part, by the lower surface tension of the Iso-octane, which may not be large enough to bring the liquid back to the central region of the droplet. Also, it seems that the system Iso-octane/steel surface has a higher wettable liquid/solid interaction, so the liquid film progression is easier. The influence of viscosity does not seem to be important during the first stage of spreading, since inertial forces are dominant. However, the higher dissipation due to shear forces may explain the absence of recoiling stage of the Diesel oil droplet with lower Reynolds number, compared to Iso-octane droplet.

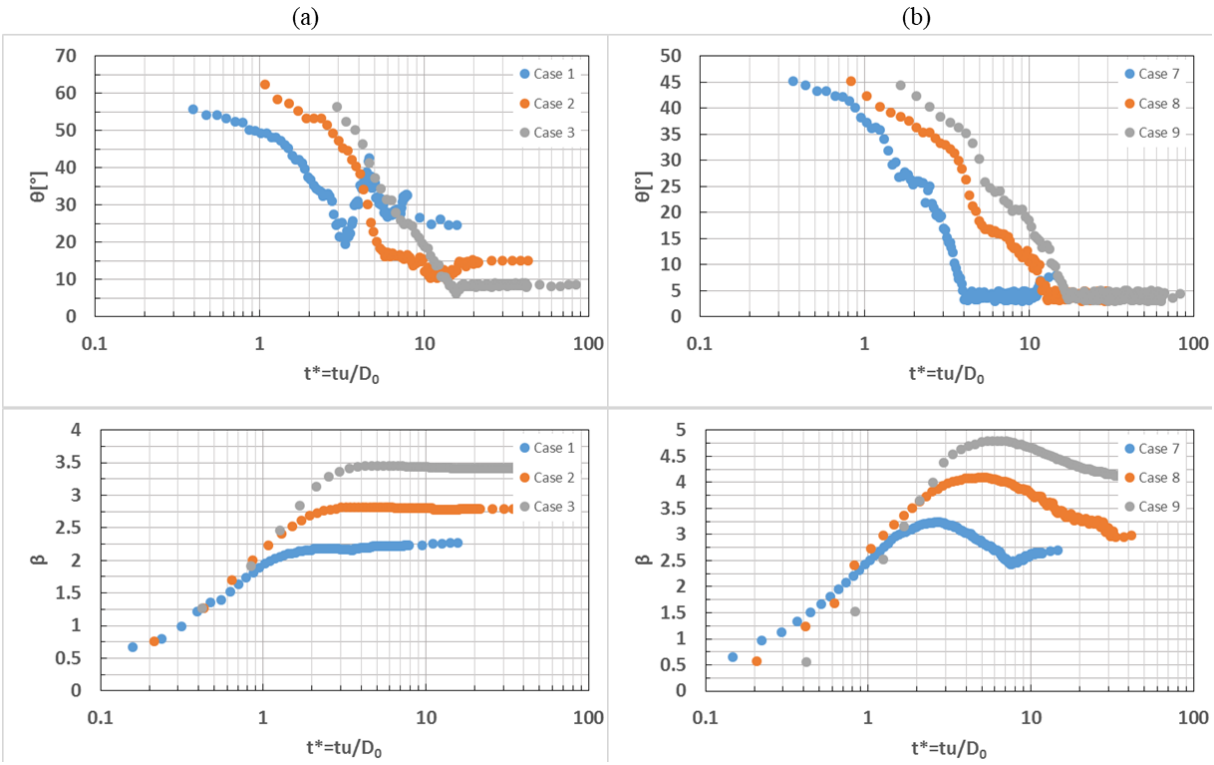

Figure B.3: Time variation of the spread factor and apparent dynamic contact angle on steel and Perspex substrate for (a) Diesel and (b) Iso-octane

Figure B.3 depicts the influence of the impact velocity on the spreading dynamic of Diesel and Iso-octane droplet on both steel substrate. The effect of inertial forces on the spreading dynamic can be clearly seen. As the impact kinetic energy (proportional to We) increases, the extend of the spreading also increases; this results in lower contact angle for Diesel fuel droplet cases, however contact angle variation of the Iso-octane cases were not affected by inertial forces.

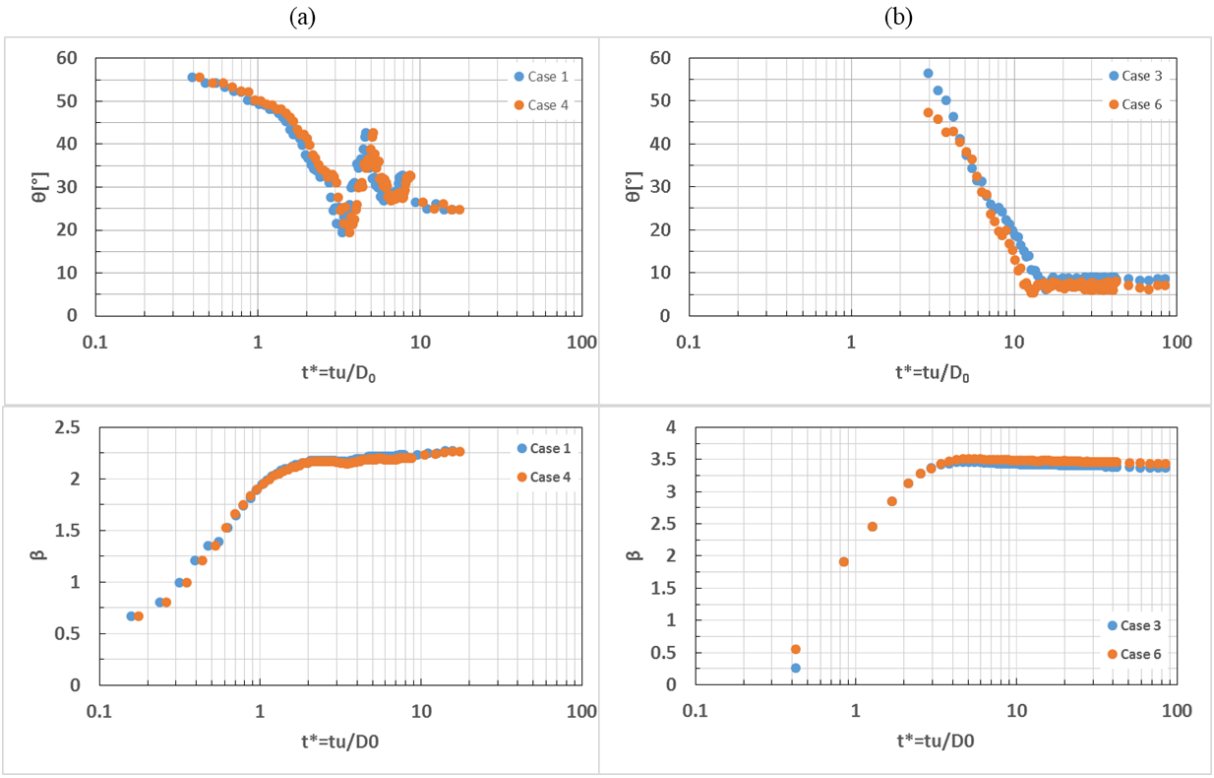

Figure B.4: Effect of surface material on the spreading dynamic of Diesel substrate for (a) We~8 and (b) We~215

It is also interesting to investigate the influence of surface material on droplet spreading. Figure B.4 and Figure B.5 shows the time evolution of the spread factor and dynamic contact angle of Diesel fuel and Iso-octane droplets impacting onto a steel and a Perspex surface with surface roughness of R_a<0.1 . In each case the droplets have nearly the same diameter and the same impact velocity, so the little changes in the` behaviour may be attributed to surface properties only.

The results show similar qualitative and quantitative trends for all coupled cases shown in each graph of Figure B.4 and Figure B.5. The effects of surface roughness seems to be negligibly small in the initial stage (t*<0.5), which is in accordance with the fact that the initial rate of change depends more on the kinetic. Further, the maximum spread is also similar for coupled cases on both surfaces. This shows that the surface roughness is a dominant factor rather than the surface material for the examined cases.

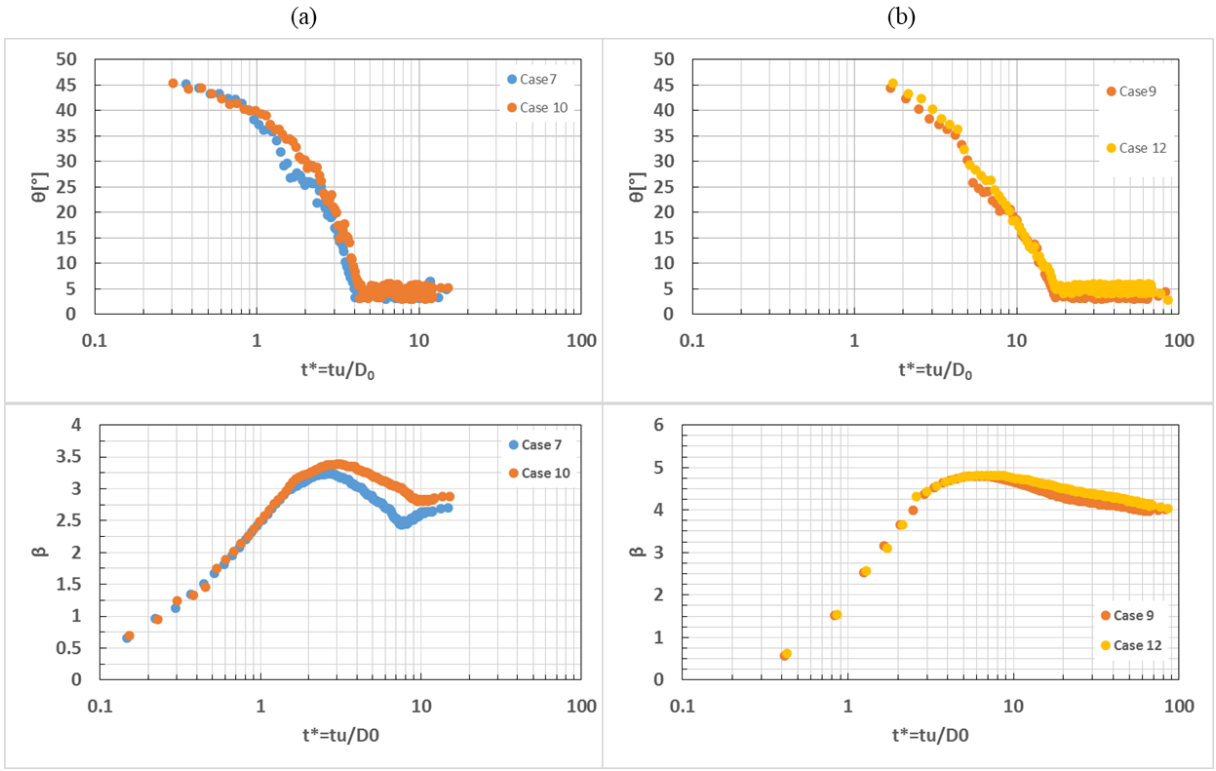

Figure B.5: Effect of surface material on the spreading dynamic of Iso-Octane substrate for (a) We~8 and (b) We~215

C. Oblique droplet-particle collision at above Leidenfrost temperature

C.1. Introduction

Droplet impact onto non-flat solid surfaces, in particular spherical particles, has a wide range of applications in IC engines, chemical and petrochemical industries (e.g. fluid catalytic cracking, FCC). In case of head-on droplet-particle collision, the liquid flow on the particle surface will be symmetrical around the axis of impact, and the influence of the gravity and centrifugal forces will be entirely balanced over the droplet mass; this can simplify the analysing of the impact dynamic, due to the similarities with the droplet impact onto flat surface scenario. When the particle surface temperature is above the Leidenfrost point, the impact morphology resembles the behaviour of a droplet impact on a super-hydrophobic surface, where the only impact outcome is normal rebound, opposed to the impact direction. An extensive literature review focusing on head on droplet-particle impact has been reported in chapter 1.

However, considering the oblique collision between a droplet and a particle, there is no axis of symmetry for the flow. This will add more complexity to the phenomena, especially with the presence of the heat transfer effect. The effect of obliquity on the momentum and energy changes of the droplet during the collision significantly affects the heat transfer and the contact time [80].

The experiments were performed employing the exact setup as explained in chapter 2. The impact Weber number was fixed at 30, while the particle temperature is around 340°C (above the Leidenfrost point). The droplet and particle diameter were 0.4 and 1 mm, respectively; this results to a droplet to particle ratio of 0.4. Sixty different impact, with random obliquity, were

recorded from two front and side view; the acquired images from this two views were further analysed to reconstruct the 3-Dimensional positioning of the droplet at each time step of the impact process. The 3D offset values of the droplet to the north pole of the particle, as the reference point, at the beginning of the impact and at time of t*=12.5 (when the droplet completely detached from the surface) were measured; this two offset values were plotted to show the effect of impact obliquity on the final direction of the droplet after rebound.

C.2. Results and discussion

Figure C.1 shows a set of experimental photographs of a droplet impacting on a heated particle with We=30 at T=340°C with impact obliquity of 0.111mm taken from both front and side view. In the first stage of the impact (t*<2.4), the droplet spreads out right after the contact in a manner similar to the normal collision, and the location of the centre of the disk-like liquid film shifts along the particle surface away from the initial contact point. When the droplet reaches the maximum diameter at t*=2.4, the liquid film starts to retreat back to its centre (2.4<t*<7.5) due to the surface tension force induced from the periphery of the droplet. During this process, the droplet continues slipping on the particle surface and the offset values increases gradually. After the droplet rebounds from the particle surface (t*>7.5), the displacement of the droplet from its initial collision position is significant, even in the case of low impact obliquity values. This can be considered as evidence of the indirect contact of the liquid and solid at Leidenfrost condition, which gives a free-slip boundary condition on the particle surface. Similar behaviour has been reported in the numerical study of [80].

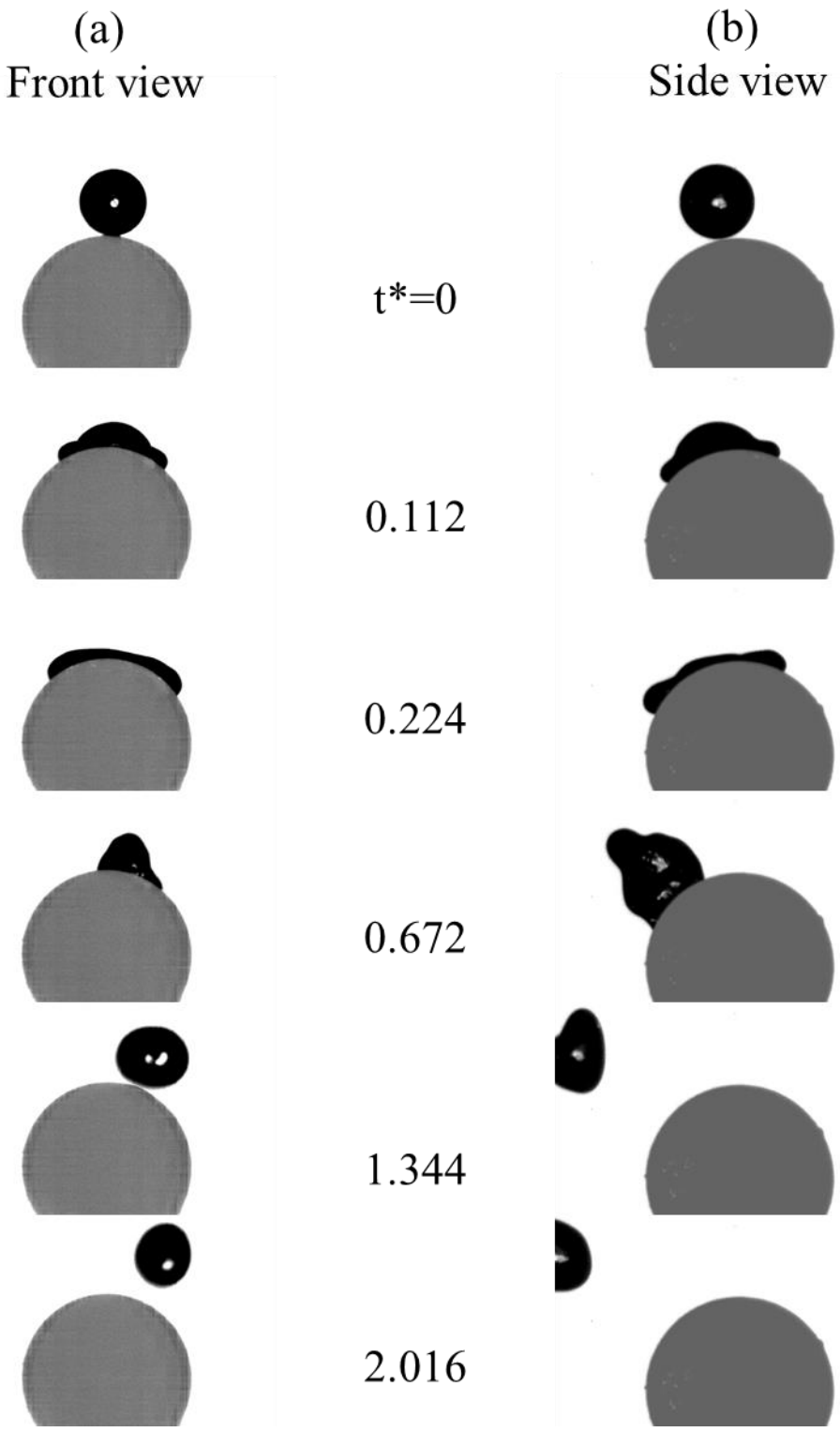

Figure C.1: Experimental photographs of droplets impacting on a heated particle with We=30 at T=340°C with impact obliquity of 0.111mm taken from (a) front and (b) side view.

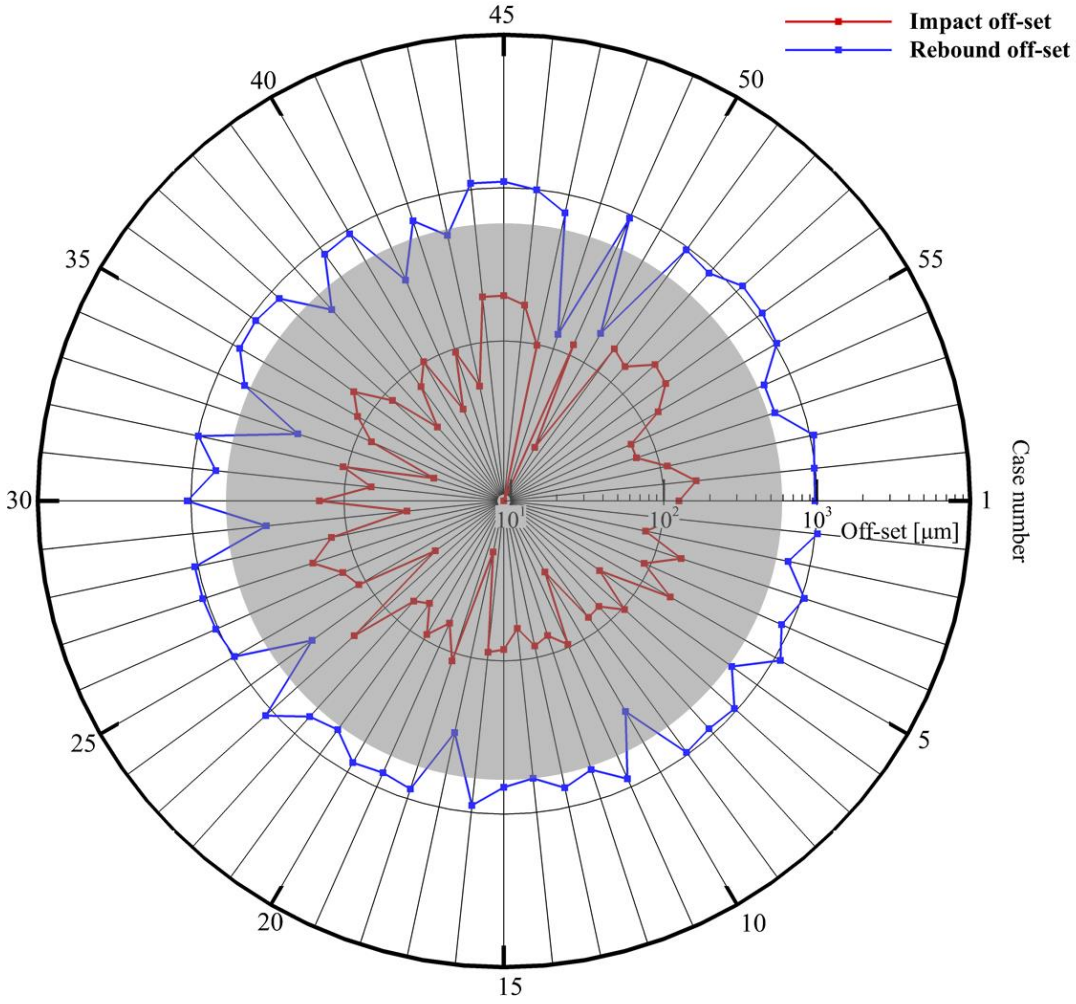

Figure C.2: the off-set values of the droplet centre of geometry from the particle north pole at impact and rebound. The grey sphere resembles the top view of the particle

Figure C.2 depicts the off-set values of the droplet centre of geometry from the particle north pole at impact and rebound time for all the cases examined. Each pair of red and blue set points is representing the impact and rebound off-sets of the droplet for each test case. It can be clearly seen that the by increasing the impact off-set the rebound off-set is also increasing. The work of [154] has numerically shown that as the obliquity increases, both the contact area and the contact time decreases. They have also reported that the temperature drop of the heated particle is larger for lower impact offset cases.

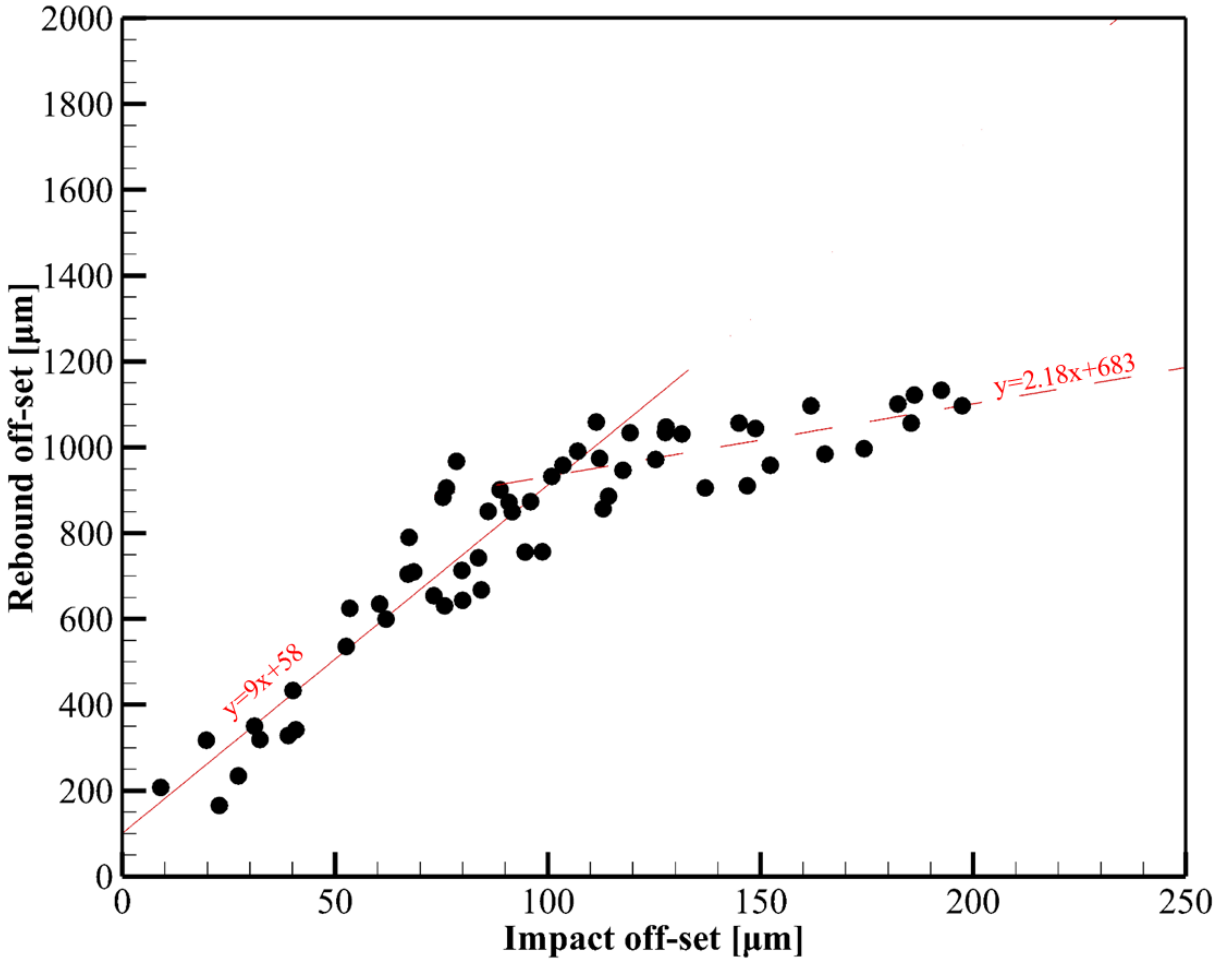

Figure C.3: the rebound offset changes of the droplet during the collision as a function of obliquity

The effect of impact off-set value on rebound off-set values of the droplet is illustrated in Figure C.3. The change of droplet rebound off-set is monotonically increases with an increase in the impact obliquity. For impact off-set values lower than 100µm, the rebound off-set are increasing with the rate of 9. However, this rate reduces for larger impact off-set values; this is attributed to the increase effects of gravity and centrifugal forces during the spreading, which lower the available energy of rebound at the end of retraction phase. Figure C.4 shows the variation of the maximum spreading factor as function of impact off-set. As it can be seen the maximum spreading factor values are not significantly affected as the impact off-set increased for the cases examined; as the impact energy of all the examined cases are the same and the

fact that inertial forces are dominant in the initial spreading phase, thus the maximum spreading factor is independent from the impact off-set.

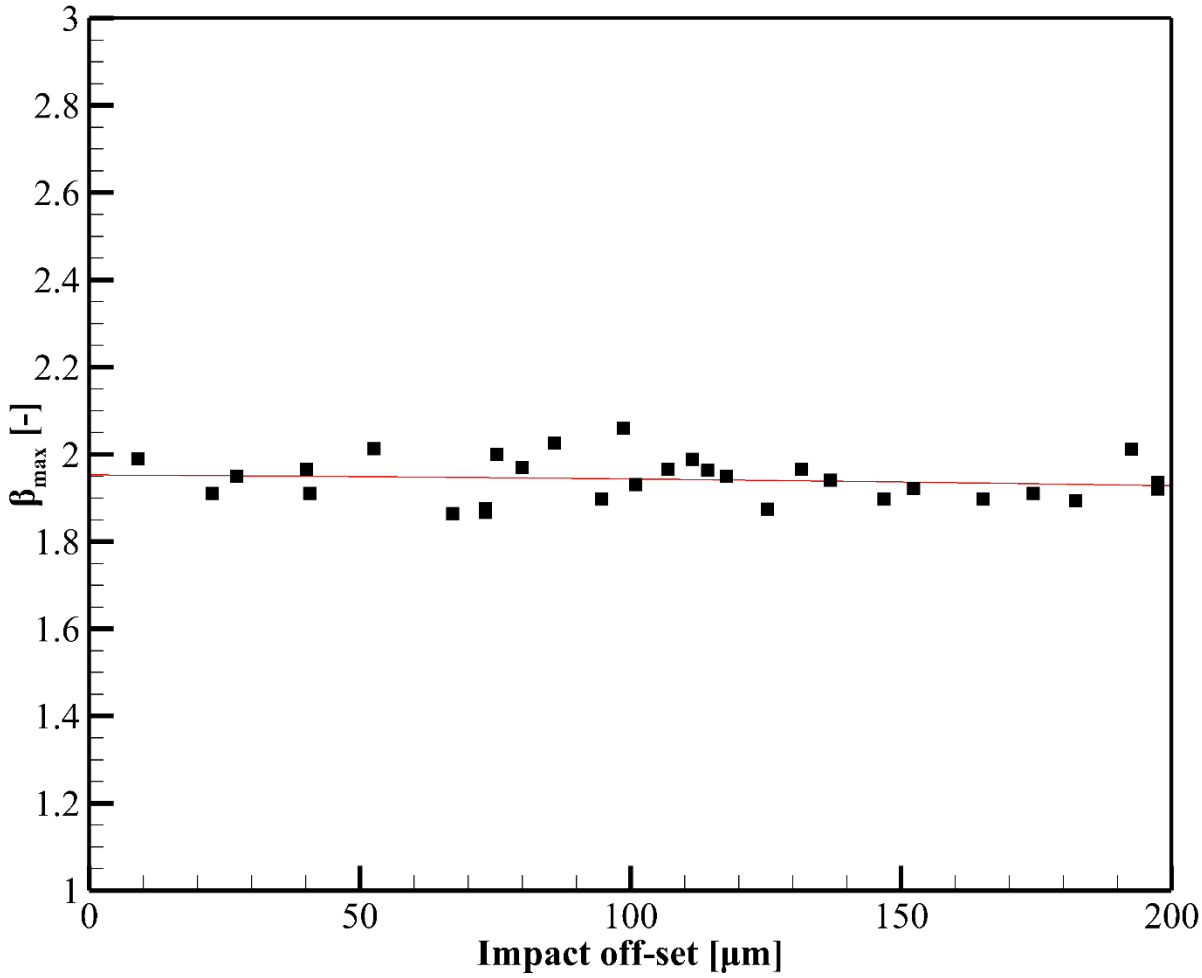

Figure C.4: The variation of maximum spreading factor as a function of impact off-set value